M. E.

MECHANICAL ENGINEERING
SEP 13 1961
LIBRARY

JOURNAL OF THE

AEROSPACE SCIENCES

VOLUME 28 SEPTEMBER 1961 NUMBER 9

PURDUE UNIVERSITY
SEP 11 1961
LIBRARY

CONTENTS

The Oscillation and Noise of an Overpressure Sonic Jet ..... ANDREW G. HAMMITT 673

Velocity and Range Considerations for the Attainment of Given Intercept Angles ..... WAYNE H. TEMPELMAN 681

Aerodynamic Noise in Supersonic Wind Tunnels ..... JOHN LAUFER 685

Transfer From an Arbitrary Initial Flight Condition to a Point Target ..... HARVEY L. ROTH 693

A Theory of Ring-Stiffened Cylinders ..... R. J. DUFFIN 702

Vortex Containment for the Gaseous-Fission Rocket ..... JACK L. KERREBROCK AND ROBERT V. MEGHREBLIAN 710

Torsional Analysis of Thin-Walled Shells With Many Closely Spaced Spar Webs ..... DAVID W. FOX AND ROBERT M. RIVELLO 725

Frequency-Response Functions of Orthotropic Sandwich Plates ..... M. P. BIENIEK AND A. M. FREUDENTHAL 732

Readers' Forum 736

Published by
INSTITUTE OF THE AEROSPACE SCIENCES, INC.

JOURNAL OF THE AEROSPACE SCIENCES

Editor: W. R. SEARS
Director, Graduate School of Aeronautical Engineering, Cornell University

Associate Editor: ROBERT R. DEXTER *Editorial Production Manager:* VEHIG S. TAVITIAN

Editorial Assistant: CAROL A. SCHAU

IAS Aerospace Technology Panels

Paul J. Burr, Technical Services Director, Coordinator

The members of the IAS Aerospace Technology Panels shown here are to be available, collectively or as individuals, to assist and advise IAS Committees, Sections, and staff members as to currently interesting and important technical topics related to their specialties and as to people most qualified to speak or write on such topics. The panels will also stimulate thought and scientific papers of potential value for the future, and they should be sensitive to technical activity of other professional groups, seeking through joint action the enlightenment of all having professional aerospace interests. Panel chairmen are indicated with an asterisk (*).

Aerodynamics and Fluid Mechanics
Lester Lees*
Seymour M. Bogdonoff
Dean R. Chapman
Antonio Ferri
Paul Germain
Wayland C. Griffith
Hans W. Liepmann
C. C. Lin
Henry T. Nagamatsu
W. R. Sears
John R. Sellars
R. T. Whitcomb
Hideo Yoshihara

Aeroelasticity
R. L. Bisplinghoff*
Y. C. Fung
I. E. Garrick
Martin Goland
Kurt H. Hohenemser
J. C. Houbolt
W. P. Jones
W. J. Mykytow
Robert F. Speaker

Biomedical Sciences
Brig. Gen. D. Flickinger, USAF*
W. Ross Adey
Capt. Wm. Augerson, USA
Hilding Bjurstedt
Stuart Bondurant
A. Scott Crossfield
Cdr. J. H. Ebersole, USN
W. R. Lovelace, II
Capt. Bruce Pinc, USAF
Stanley Roscoe

Communication
P. C. Sandretto*
K. C. Black
James M. Bridges
Harvard L. Hull
Leonard Jaffe
David S. Little
Lt. Com. M. M. Macomber
Cdr. D. O. Mann, USN
Paul Rosenberg
William Sen
Arnold Shostack
Teck A. Wilson

Control and Guidance
Robert N. Brown*
B. Paul Blasingame
S. F. Eyestone
C. E. Gallagher
Percy Halpert
B. J. O'Connor
Robert L. Roderick
S. F. Schmidt
O. Hugo Schuck
H. Philip Whitaker

Energy Conversion
David Altman*
Robert Bromberg
M. U. Clauser
J. Preston Layton
Frank Marble
G. H. Markstein
A. M. Rothrock
Milton M. Slawsky
Martin Summerfield
T. Y. Toong

Flight Mechanics
H. J. Kelley*
Malcolm J. Abzug
H. Julian Allen
A. E. Bryson, Jr.
T. N. Edelbaum
William C. House
George Leitmann
Bernard Maggin
Angelo Miele
John D. Nicolaides
Charles B. Westbrook

Instrumentation
Paul F. Bechberger*
J. M. Hungerford
Mac Lowy
Walter McKay
M. David Prince
Charles P. Sonet
George I. Toumanoff
William A. Wildhack

Management
Edward A. Ledeen*
Garrett C. Covington, Jr.
Maj. Gen. Marvin C. Demler, USAF
Richard G. Folsom
Joel M. Jacobson
Boyd C. Myers
Sidney M. Robbins
Lewis A. Rodert
John H. Sidebottom
R. C. Siebold
Paul Torda

Meteorology
Thomas F. Malone*
Robert D. Fletcher
Henry T. Harrison
Joseph Kaplan
Donald T. Perkins
Herbert Riehl
Morris Tepper
Clayton Van Thullenar
Harry Wexler

Nuclear Applications
J. Donald Rauth*
Jack L. Armstrong
Robert W. Bussard
H. M. Dieckamp
Capt. R. L. Duncan, USN
Harold B. Finger
Donald J. Keirn
Frank E. Rom
Raymer E. Schreiber
D. Roy Shoults
T. B. Taylor

Operations
Richard V. Rhode*
Maj. Gen. Otis Benson, USAF (MC)
Ernest A. Cutrell
Capt. E. E. Fawkes, USN
Melvin N. Gough
Franklin W. Kolk
Col. J. L. Marinelli, USA
W. E. Rhodes
M. B. Spaulding, Jr.
Maj. Gen. D. Yates, USAF

Propulsion Systems
Bruce T. Lundin*
Robert H. Boden
George W. Brady
David Cochran
Elliot Mitchell
Perry W. Pratt
C. C. Ross
John G. Wilder, Jr.
Maurice J. Zucrow

Space Physics
John C. Evvard*
Herbert Friedmann
Leo Goldberg
C. F. Hansen
Arthur Kantrowitz
Bruno Rossi
S. F. Singer
Leo Steg
Fred L. Whipple

Structures and Materials
Nicholas J. Hoff*
Samuel B. Batdorf
Bruno A. Boley
Pol Duwez
R. R. Heldenfels
Samuel Levy
George N. Mangurian
S. S. Manson
Nathan E. Promisel
Ernest E. Sechler

Support
Ernest G. Stout*
Albert D. Brown
Edward I. Brown
Col. Paul T. Cooper, USAF
P. J. Daniel
Paul Hartline
Donald R. Hill
Capt. N. D. Hodson, USN
Lt. Col. George L. Lovett
R. R. Malik
John McKenna
Gilbert Rolan
Richard A. Schmidt
William R. Owens

Vehicle Design
C. E. Pappas*
Ralph Alex
Adolph Burstein
C. H. Christenson
A. J. Eggers, Jr.
Robert Lichten
E. V. Marshall
Rene H. Miller
John R. Ragazzini
George S. Schairer
George S. Trimble, Jr.

SUBSCRIPTION RATES

JOURNAL OF THE AEROSPACE SCIENCES, Published Monthly. United States and Possessions: 1 Year, $15.00; Single Copies, $1.50. Foreign Countries Including Canada (American Currency Rates): 1 Year, $16.00; Single Copies, $1.50.

AEROSPACE ENGINEERING, Published Monthly. United States and Possessions: 1 Year, $5.00; Single Copies, $0.50. Foreign Countries Including Canada (American Currency Rates): 1 Year, $6.00; Single Copies, $0.50.

Notices of change of address, which should be sent at least 30 days prior to actual change of address, and correspondence regarding subscriptions should be sent to the Circulation Department, JOURNAL OF THE AEROSPACE SCIENCES, 2 East 64th Street, New York 21, N.Y.

Manuscripts for publication, proofs, and all correspondence should be addressed to the Editorial Office of the JOURNAL.

© Copyright, 1961, by the Institute of the Aerospace Sciences, Inc.

Publication Office, 20th and Northampton Sts., Easton, Pa. Second-Class Mail Privileges Authorized at Easton, Pa. Acceptance for mailing at a special rate of postage provided for in Section 1103, Act of October 3, 1917, authorized April 29, 1937.

JOURNAL OF THE AEROSPACE SCIENCES

VOLUME 28 SEPTEMBER 1961 NUMBER 9

The Oscillation and Noise of an Overpressure Sonic Jet†

ANDREW G. HAMMITT*

General Applied Science Laboratories, Inc.

Summary

A series of experiments on plane, two-dimensional, overpressure sonic jets has been performed to study the oscillating behavior of the jet and accompanying sound field. Shadowgraphs were obtained which show the oscillations and generation of sound waves in some detail. Measurements from these pictures show that the oscillating jet and sound fields can be described in terms of the length of the shock-wave cells. The importance of the sound waves acting upon the base of the jet is demonstrated and it is found that the jet can be stabilized by shielding its base from these sound waves.

Symbols

a	=	speed of sound in atmosphere around jet
C_0, C_1, C_2	=	constants of proportionality
d	=	width of jet
l	=	distance from origin of jet to source of sound waves
L	=	length of shock-wave cells
M	=	Mach number
n	=	frequency of oscillation
P_a	=	atmospheric pressure
P_c	=	stagnation pressure to cause critical flow
P_0	=	stagnation pressure
St	=	Strouhal number
η	=	wavelength of jet oscillations
λ	=	wavelength of sound waves

Introduction

A HIGH-VELOCITY JET OF AIR has been observed to be a source of considerable noise. In general, this noise covers a broad range of frequencies. For the particular case of an overpressure jet issuing from a sonic orifice, a single-frequency tone is sometimes heard which predominates over the other noise. This generation of a pure tone has been called jet screech. The purpose of this study is to obtain fundamental information on the mechanism of the jet screech phenomenon.

Experimental Investigation

The experimental investigation to be described was carried out at Princeton University using the facilities of the Gas Dynamics Laboratory. A settling chamber was built to provide a low-turbulence, low-noise-level supply for various jet orifices during operation from an available 3,000-psi air supply. Since maximum pressures in the settling chamber of the order of 100 psi were desired, a mechanism had to be provided to throttle the 3,000-psi air supply without the introduction of turbulence or noise. To accomplish this throttling, a valve followed by two pieces of porous stainless steel was used. A drawing of this settling chamber together with the nozzles used is shown in Fig. 1. Two plane, two-dimensional slit-type jet nozzles were used, one with the jet originating at the face of the flange and the other with a tube or spout so that the jet originates away from the face of the flange. Both nozzles were of the converging type.

Studies of the jets were made using flow visualization techniques and microphone pressure measurements of the sound field. The shadowgraph technique for visualizing the second derivative of the density field was used extensively. The sensitivity of this system can be adjusted by placing the film at different distances from the phenomena being observed, the greater the distance the more sensitive is the system. Pictures near the jet show the stronger phenomena more clearly

Received May 11, 1960. Revised and received August 2, 1960.

† The work was sponsored by OSR, ARDC under Contract AF 49(638)-194.

* Formerly, Sr. Research Associate, Princeton University, and Consultant, General Applied Science Laboratories, Inc.; now, Head, Aerodynamics Research Section, Space Technology Labs., Inc., Los Angeles, Calif.

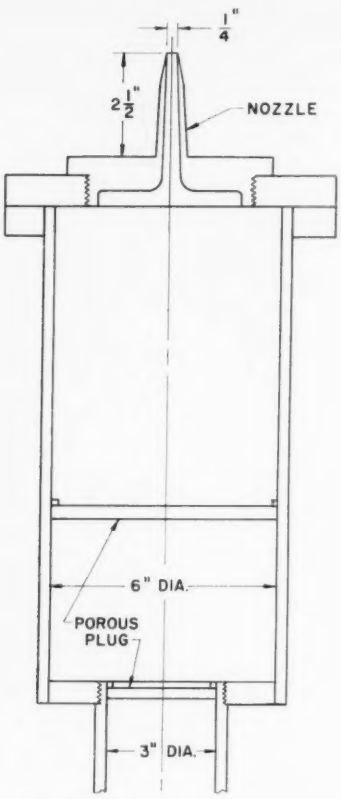

FIG. 1(a). Settling chamber used in jet-noise studies.

while those further away emphasize the weaker phenomena. A high-voltage spark with a duration of about 1 microsecond was used as the light source, and proved adequately fast to stop the motion.

The microphones used were a Massa Type M-141 crystal microphone having a frequency range to 30 kc and a General Radio Rochelle-salts microphone with a frequency range to 10 kc. The Massa microphone was used for obtaining all data presented except that shown in Fig. 8. In this latter case, the higher response of the Rochelle-salts microphone was required.

Experimental Results

Optical Studies

A series of shadowgraphs of the nozzle with spout taken looking at the narrow edge of the jet, is shown in Fig. 2. These shadowgraphs were taken with the film at two distances from the jet, 5 in. and 4 ft. The 5-in. pictures show the jet structure, while the 4-ft pictures show the sound field. The shadowgraphs shown are for a range of stagnation pressures varying from 30 to 64 psia.

At 30 psia just the 5-in. picture is shown, since the jet is stable at this condition. In the object just to the right of the jet are two small holes 1 in. apart which furnish a reference scale for these pictures. The object appearing on the right side of the picture is a microphone. Fig. 1(b) shows the jet at 39 psia from both the near and the far positions. At this pressure, the jet is violently unstable. The closeup shows the oscillations of the jet structure, and the distant view shows the sound waves spreading away from the jet. It is interesting to note the much more rapid spread of the jet at this pressure than at the 30 psia condition. This rapid spreading is characteristic of the oscillating jet. Figs. 1(c) at 54 psia and 1(d) at 64 psia show the same phenomena as 1(b) except that the sound waves are stronger and of lower frequency. Figs. 1(c) and 1(b) also show a series of waves with small curvature lying in the horizontal plane. These waves are the reflections from the flange on the settling chamber at the base of the nozzle.

The predominant waves originating from the jet can be seen to be approximately semicircular and to originate alternately from each side of the jet. The sources of these waves on each side of the jet seem to be located at about the same height. A detailed examination of the pictures presented here, and of others as well shows that apparently some weaker waves originate from other heights also, in the same alternating fashion. An examination of the pictures of the jet structure shows that the regular jet shock pattern can be seen through the third cell and that the jet is relatively stable up to this point. After the third cell, the violent oscillations take place and the predominant sound waves are emitted near the top of the third cell.

Pictures of this oscillating jet at various times during a complete cycle would be useful in determining the manner in which the sound waves originate. The jet is oscillating at between 5,000 and 10,000 cycles per second, and since several pictures per cycle are necessary, a frame speed of about 50,000 frames per second would be required. A camera of this speed was not available, and so a different technique was used. A series of pictures was taken of the jet at one stagnation pressure. These pictures, having their own built-in clock in the position of the sound waves, could then be arranged in chronological order. Fig. 3 shows a series of such pictures taken at $P_0 = 64$ psia and arranged in this manner. The time intervals between the pictures can be judged by the progress of the sound waves.The stability of the oscillating process is demonstrated by the fact that these pictures, taken millions of cycles apart, can be considered to represent a single cycle. The pictures show that the oscillations, which are small near the base of the jet, build up as they

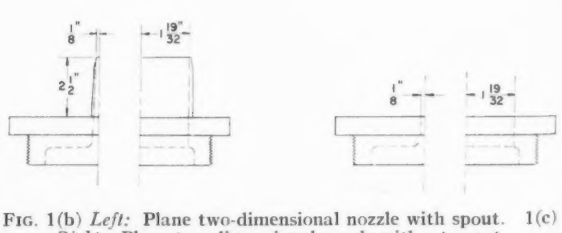

FIG. 1(b) *Left:* Plane two-dimensional nozzle with spout. 1(c) *Right:* Plane two-dimensional nozzle without spout.

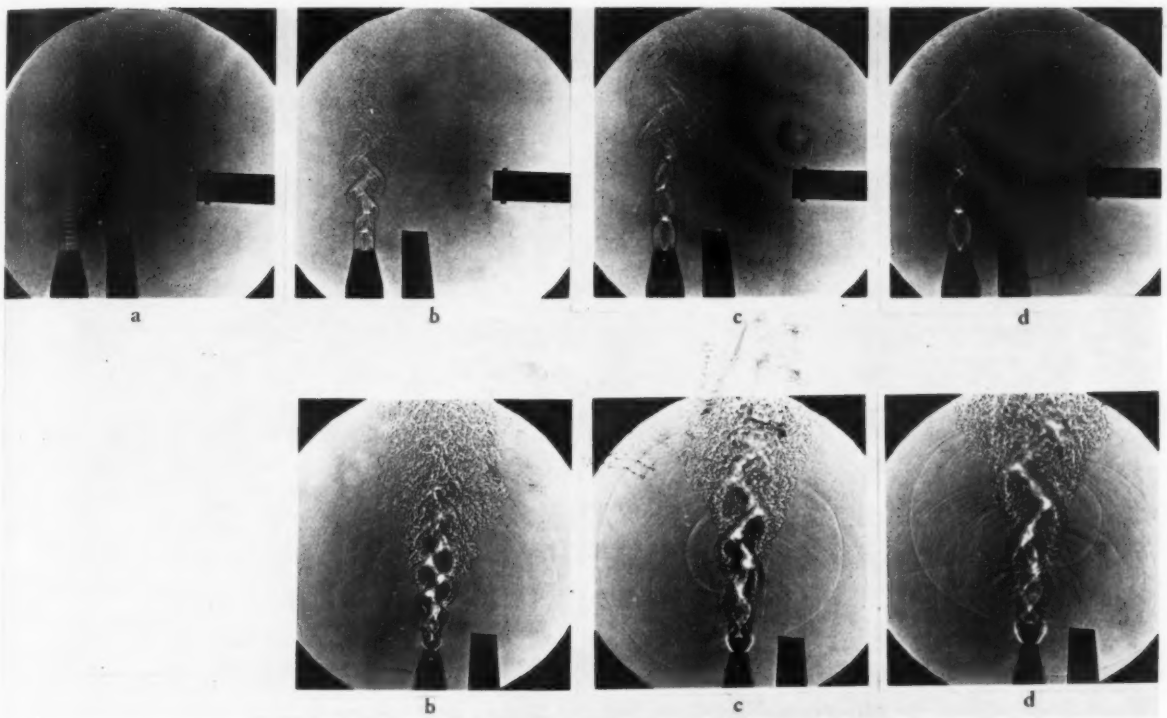

FIG. 2. Shadowgraphs of jet at various P_0. *Top:* film located 5 in. from jet; *bottom:* film located 4 ft. from jet. (a) P_0 = 30 psia; (b) P_0 = 39 psia; (c) P_0 54 psia; (d) P_0 64 psia.

travel out along the jet. After the third cell vortex tails appear which are left behind in an alternating manner. A new sound wave seems to originate when the jet returns to and contacts this vortex tail. These observations are interesting but offer no real explanation of the origin of the sound waves at this point.

Some quantitative observations also can be made from these pictures. The size of the shock-wave cells was measured and the results from these and similar pictures are shown in Fig. 4 as a function of stagnation pressure. The wavelength of the sound waves, the wavelengths of the jet oscillations, and the location of the apparent source of the sound waves can all be determined. At some pressures, it was possible to locate the source of both the major and minor wave system, and both of these are shown in Fig. 4. These results compare favorably with similar measurements on both the cell size and sound wavelength.[1] It should be pointed out now, and it will be shown in greater detail later, that the oscillations do not grow uniformly stronger with stagnation pressure but reach a peak, fall off, and then rise to a new peak. Between these peak regions, the frequency can be somewhat confused. The wavelengths may go in steps with increasing stagnation pressures, as indicated in Fig. 4. The pictures chosen to be presented are those at the peaks of the oscillations, since they are the most interesting.

If the sound wavelength, the jet oscillation wavelength, and the distance to the source of the sound are all nondimensionalized by the shock-cell size, the results shown in Fig. 5 are found. It would appear that all these quantities have the same dependence on the stagnation pressure, and all are related to each other by constants.

Microphone Studies

A more complete analysis of the frequency and amplitude of the sound waves as a function of stagnation pressure was obtained by analyzing the output of the microphone when located beside the jet in the position shown in Figs. 2(a) and 3(a). The results are shown in Figs. 6(a) and 6(b). The frequency decreases continuously as the stagnation pressure increases, and the amplitude has several peaks which suggest that the curve be broken into separate regions. These experiments were made in two different ways. As observed in the shadowgraphs (Fig. 2), there are sound waves reflected from the base flange entering the sound field around the jet. One set of measurements was taken with this configuration, and one with a sound-deadening material placed on the base flange so that the reflected waves were eliminated. The general frequency–stagnation pressure curve is substantially unaffected by this change but there are definite changes in the locations of the peak amplitudes. The frequency jumps that seem to take place between the regions of peak amplitude are decreased and almost eliminated with the use of the sound-absorb-

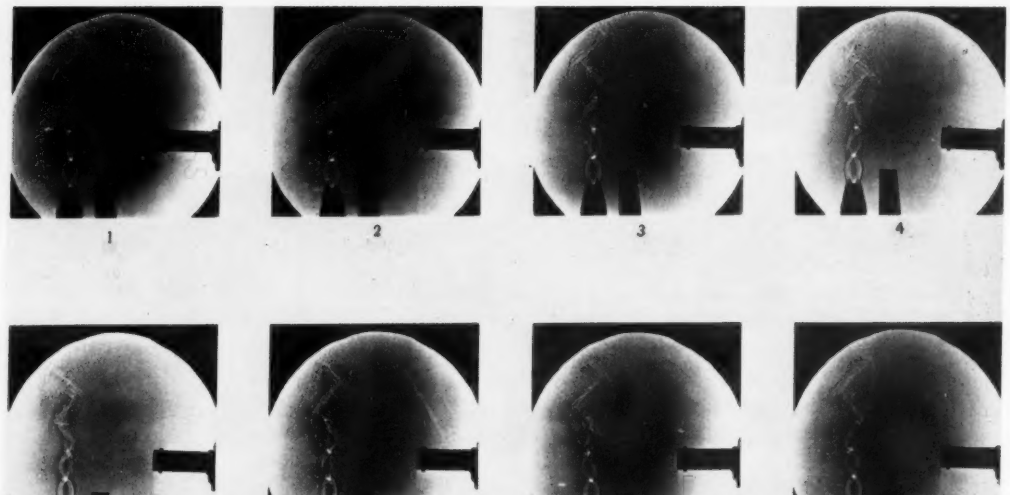

FIG. 3(a). Shadowgraphs of jet at 64 psia. Series show chronological history of jet oscillations. Read from left to right. Film located 5 in. from jet.

ing material. The frequency measured without sound-absorbing material on the flange sometimes showed an overlap when the frequency jump occurred. It is believed that this effect is caused by the oscillation being unstable and switching between the two modes. Pictures of the jet taken in these regions suggest this explanation, but complete proof is not available. Pictures of the jet both with and without the sound-absorbing material on the flange show the same results as the microphone records. These results suggest that the jet oscillations are sensitive to the external sound waves in the vicinity of the jet.

The direction of the sound radiation was also studied by means of the microphone. The shadowgraphs of the jet show a very prominent set of sound waves radiating from the jet in a circular shape. The microphone was mounted in a quadrant with the center located at the source of this sound-wave system, and measurements of wave forms were taken at various angular positions. Photographs of the wave forms as shown on an oscillograph are presented in Fig. 7. The angular positions are measured from the jet axis with 0° indicating the upstream direction. As the microphone approaches the downstream direction (140

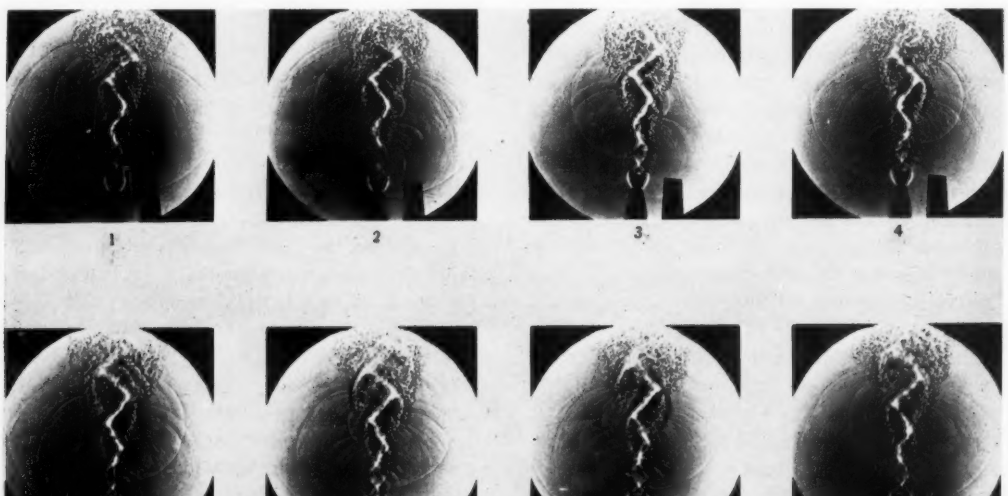

FIG. 3(b). Shadowgraphs of jet at 64 psia. Series show chronological history of jet oscillations. Read from left to right. Film located 4 ft from jet.

and 160°) the picture becomes more fuzzy, indicating the increase in background noise field and possible direct jet impingement. The 10° and 160° positions indicate an approximately sinusoidal variation at the fundamental frequency, corresponding to the wavelengths of the principal wave system. The 90° position shows another sinusoidal wave picture but at double the frequency of the fundamental system. The other pictures show the intermediate steps in changing from one system to the other.

These results, while not suggested by the shadowgraphs, are consistent with results presented in reference 1. The explanation suggested in reference 1 is that the interference of the sound waves from a series of sources located along the jet causes this effect. If the additional source, which is visible in some of the shadowgraphs, is considered, it can be determined that its location and phase are such that sound waves from

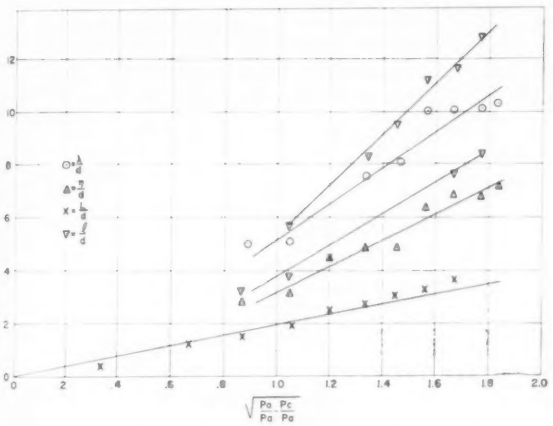

FIG. 4. Jet- and sound-field parameters nondimensionalized by jet width at various P_0.

the two sources reinforce each other in the 0° and 180° directions and interfere in the 90° direction. In the 90° direction the second harmonic of each source will reinforce and cause the double-frequency response observed. The amplitude shown at the 90° position gives a measure of the combined second harmonic component of these waves. The sound waves from these various sources would have to be of about the same strength to cause this complete interference of the first harmonic. This conclusion is inconsistent with the relative strength shown on the shadowgraphs.

Effect of Sound Waves Impinging on the Base of the Jet

References 1 and 2 suggest that the sound waves in the external field act upon the jet near its base to cause disturbances which are amplified by the jet and which, in turn, cause new sound waves. The sensitivity of low-speed laminar jets to sound waves has been well established.[3] The mechanism suggested in references 1 and 2 is a feedback mechanism. The effects observed in these experiments due to change of the sound reflection condition on the base flange lend support to these ideas. It follows from this reasoning that the jet could be stabilized if this feedback loop were broken.

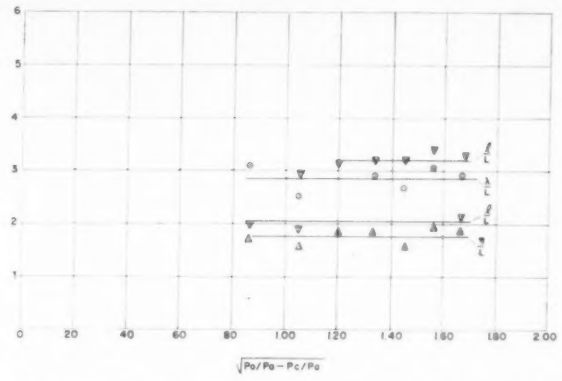

FIG. 5. Jet- and sound-field parameters nondimensionalized by shock cell at various P_0.

The method that was used to break the loop was a sound-deadening and reflecting baffle alongside the jet between the source of the sound and the jet base (Fig. 8). This mechanism provides a means of adjusting the vertical position of the two baffle plates and the size of the slit between them. Experiments were run in which the baffle plates served as reflecting surfaces and, when covered with soft material, as absorbing surfaces. The purpose of these baffles is to prevent the sound waves from propagating from their source to the base of the jet but not to interfere with the jet-flow field. While these two requirements are incompatible, it does appear possible to effectively block the returning sound waves without extending the baffles into the high-velocity part of the jet. There is some interference with the external flow field induced by the jet, but this interference is probably not very important. By use of these baffles, it was possible to stabilize the jet oscillations. Typical pictures with and without the baffles are shown in Fig. 9. Fig. 9(a) shows the jet oscillations without the baffles. Definite oscillations take place beginning at the end of the third cell. In Fig. 9(b) the baffles are used with a piece of sound-

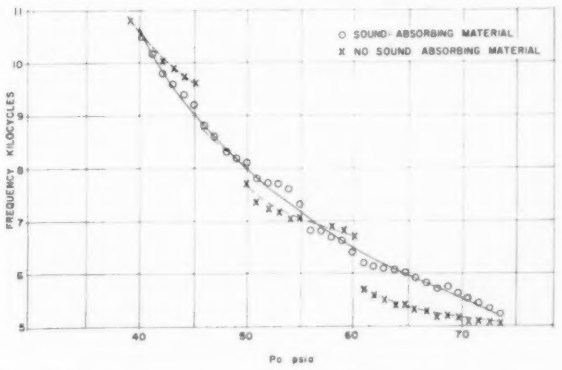

FIG. 6(a) Frequency of jet-sound field with and without sound-absorbing material on base flange, as a function of P_0.

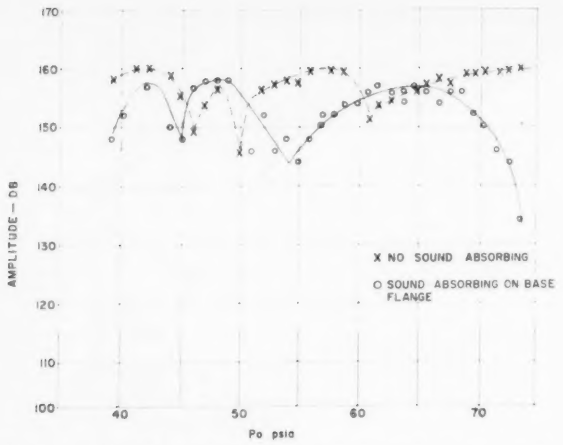

FIG. 6(b). Amplitude of jet-sound field with and without sound-absorbing material on base flange as a function of P_0.

absorbing material about $\frac{1}{2}$ in. thick and 1 in. high on each side of the jet, the metal on the top surface of the baffle being bare. The shadow of the fringes of the sound-absorbing material as blown up by the jet can be seen in the picture. With this baffle arrangement, the jet is stabilized so that there is almost no detectable oscillations, even over an extended field of vision. The two figures are presented so that the jet nozzle is in the same position in each picture.

Several configurations with the baffles were tried with different use of sound-absorbing material. The jet was stabilized by several of these arrangements. The simplest arrangement was obtained by using the flat slit nozzle and attaching sound-absorbing material on the face. The sound-absorbing material was cut back so that it could interfere very little with the jet flow. This configuration was very successful in stabilizing the jet and eliminating the characteristic screech. The flow with this configuration, both with and without the absorbing material, is shown in Figs. 10(a) and 10(b). This small change had an amazing effect. This arrangement appears to be an effective practical means for prevention of jet oscillations of this type.

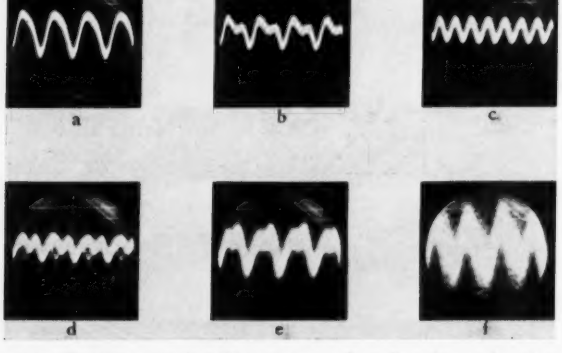

FIG. 7. Pictures of oscilloscope trace for microphone placed at different positions rotating about source of principal sound waves. $P_0 = 64$ psia. Angles measured from jet-axis upsteam direction: (a) 10°; (b) 60°; (c) 90°; (d) 120°; (e) 140°; (f) 160°.

While the stabilization of the jet caused almost complete elimination of the characteristic screech frequency, it does not affect the background roar of the jet. The measurements of the overall jet noise show that it is reduced by only about 3 db out of 100 db, however, the tone changes from the characteristic screech to a roar.

Since the feedback loop had been successfully broken by the use of the baffles, an attempt was made to provide a substitute means of excitation. For this purpose, a 40-watt speaker was located so as to cause sound waves to impinge on the base of the jet (Fig. 8). The speaker could not exactly reproduce the sound waves cut off by the baffles, but it was the best arrangement that could be made simply. Tests were run with the speaker driven at a given frequency and a microphone located above the baffle. The output of the microphone was connected to a frequency analyzer tuned to the oscillator frequency. The output of the analyzer was then recorded as a function of jet stagnation pressure. The results at three different oscillator frequencies are shown in Fig. 11. At about 42 psia stagnation pressure the microphone output peaks at all frequencies, but there is little effect of the speaker. At higher pressures, there is another noise peak that is very much affected by the speaker output. The stagnation pressures and frequencies at which this peak occurs are roughly those shown in Table 1. The last column shows the stagnation pressures at which natural vibrations at the three frequencies were ob-

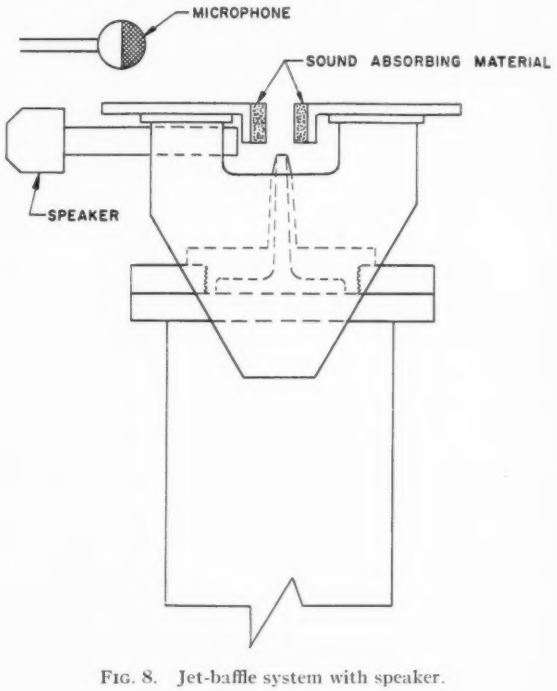

FIG. 8. Jet-baffle system with speaker.

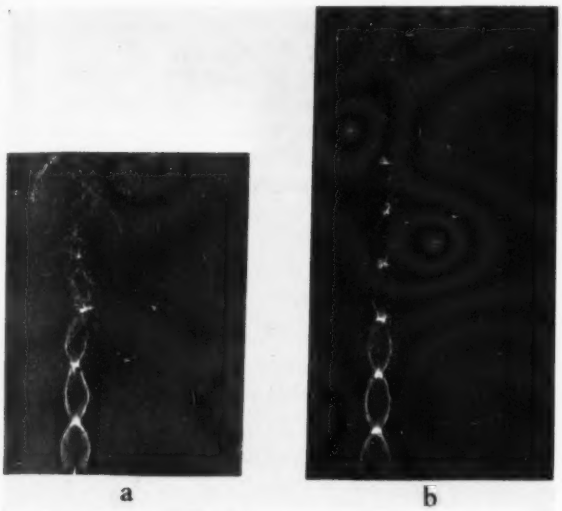

FIG. 9. Shadowgraph of two-dimensional nozzle at $P_0 = 48$ psia: (a) without baffles; (b) with baffles.

served, taken from Fig. 6. There is a fair correspondence between the last two columns, showing that the jet amplifies the sound at particular frequencies corresponding roughly to the frequencies observed for the jet screech.

Discussion

In references 1 and 2, the suggestion is made that the frequency-determining mechanism may involve the tuning of the feedback system. It is then shown that $(l/\lambda) + (l/\eta) = \text{const.} + \text{integer}$, and this result is cited as a proof of the feedback mechanism. The present results are in agreement with this timing mechanism. In Fig. 5, it was shown that all the quantities l, λ, η were related to L, the shock-cell size, by constants. The quantity l, which in some pictures was found to have multiple values, seems to be given by the formula $l/L = \text{const.} + (0 \text{ or } 1)$. From this relation to the shock-cell size, it is obvious that $(l/\lambda) + (l/\eta) = \text{const.}$ for either value of l/L. The fact that this sum differs by an integer when l/L changes by 1 is the result of the fact that $L/\lambda + L/\eta \backsimeq 1$. Until the mechanism that determines the location of the sound source can be determined, it is not obvious whether these results are proof of the feedback tuning mechanism or merely a result of some other mechanism that relates all these characteristic dimensions to the shock cell size.

Analyses have been made of the natural frequencies of vibration of incompressible jets, and these have been checked with experiment.[4] The relations give the wavelength of jet oscillations as a function of the size of the jet and the Strouhal number. If the method of reference 4 is applied to the present experiments, the jet wavelength as a function of stagnation pressure is found as shown in Fig. 12. The calculated wave lengths compare favorably with those measured, suggesting strongly that this mechanism of jet instability is important in the jet screech problem. The application of this incompressible theory to a case of compressible flow is clearly incorrect. The Mach number must have importance in the case of compressible flow, which is not indicated by the incompressible theory, yet the velocity itself must be of some importance since it is needed in forming the Strouhal number. Since the experiments were all run at an approximately constant speed of sound, the distinction between Mach number and velocity cannot be determined empirically.

TABLE 1

Frequency, cps	Stagnation pressure at peak noise, psia	Stagnation pressure for natural vibration without baffles, psia
6,000	65	64
7,250	59.5	56.5
8,000	58	51.5

Thus far, several empirical and theoretical relations have been considered which seem to be important. It is interesting to attempt to combine them. The relations which seem appropriate are as follows:

$$\eta = \eta(St, d)$$

or, for a compressible jet,

$$\eta = \eta(St, M, d) \tag{1}$$

$$(l/\eta) + (l/\lambda) = C_0 + \text{int.} \tag{2}$$

$$\lambda n = a \tag{3}$$

$$\eta = C_1 L, \quad \lambda = C_2 L, \quad l = (C_3 + \text{int.})L \tag{4}$$

$$L = L(M, d) \tag{5}$$

Since by (3) $n = a/\lambda$, and since, at a given M, a is characteristic of all the velocities, (1) becomes

$$\eta = \eta_1(\lambda, M, d)$$

and hence relation (2) can be written

$$l = l_1(\lambda, M, d, C_0 + \text{int.})$$

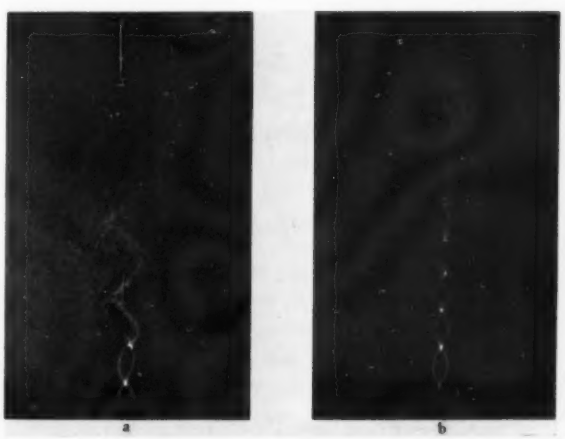

FIG. 10. Shadowgraph of two-dimensional nozzle, $P_0 = 54$ psia: (a) without sound-absorbing material on flange; (b) with sound-absorbing material on flange.

Combining relations (4) and (5) leads to similar results:

$$\eta = \eta_2(\lambda, M, d)$$

$$l = l_2(\lambda, M, d, C_3 + \text{int.})$$

At the stagnation pressures which give maximum oscillations, the values of η and l calculated as η_1, l_1 and η_2, l_2 must agree. Three maxima were observed in the range studied, so that agreement must occur at the three respective pressures. The principal wave systems all occur at the same value of the integers in relations (2) and (4), so that changes in these integers do not play a part in the tuning mechanism. One explanation of the jet behavior would be to assume that the tuning mechanism depends on the correspondence of these two functional relations for η and l. It should be noted that since the locations of the peak amplitudes change with the conditions at the base of the jet, these relations must be sensitive to the degree of excitation. Another point of view might suggest that since the functional relations agree at three points they are probably identical, and hence the tuning mechanism is not provided by the agreement of these relations.

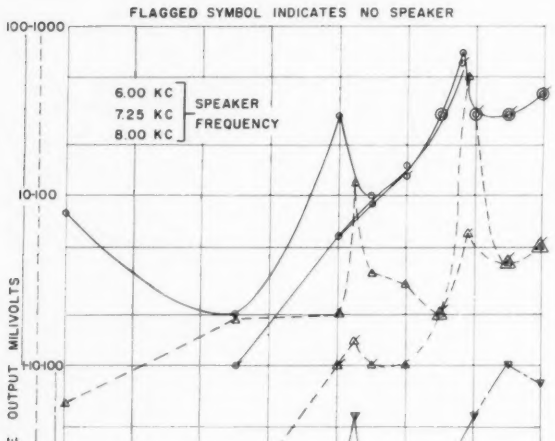

FIG. 11. Output of microphone placed above baffles, with speaker baffle arrangement in Fig. 8, as a function of P_0 and speaker frequency.

The five relations presented are based on different degrees of understanding, and not all are equally firmly established. The firmest are (3) and (5); (3) is almost trivial while (5) is firmly established at least for the inviscid core; (1) and (2) have a quasi-theoretical basis and have been checked empirically. Relation (4) is purely empirical and the basic mechanism involved is not understood; it might be merely a consequence of the other relations, but this seems very unlikely since the role of the shock waves would then be eliminated. Relation (4) must be connected with shock-wave effects, although the mechanism involved here is not clear.

Conclusions

(1) The oscillations of an overpressure plane two-dimensional sonic jet and the associated sound field are directly related to the size of the shock-wave cells.

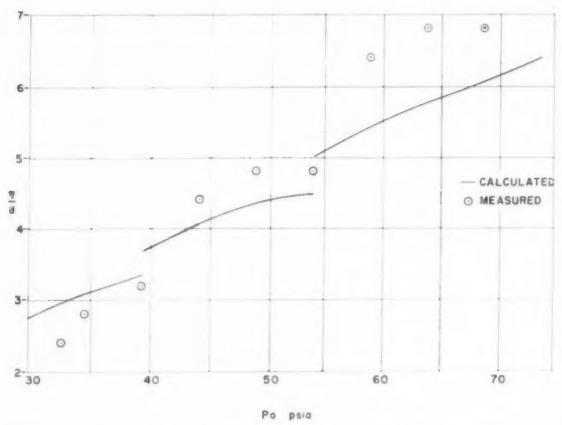

FIG. 12. Comparison of measured and predicted jet wavelengths at various P_0.

(2) Peak amplitudes of oscillation and sound occur at particular values of stagnation pressure.

(3) The interaction of the sound waves with the jet near the base are an important part of the instability. Shielding the base of the jet from the sound waves stabilizes the flow.

(4) The oscillations occur at frequencies of the order of the expected natural jet frequencies.

References

[1] Powell, A., *On the Noise Emanating from a Two-dimensional Jet Above the Critical Pressure*, The Aero. Quarterly, Vol. IV, Part II, pp. 103–122, February, 1953.

[2] Powell, A., *On the Mechanism of Choked Jet Noise*, Proc. Phys. Soc., Vol. B66, p. 1039, 1953.

[3] Brown, G. B., *Vortex Motion in Gaseous Jets and the Origin of Their Sensitivity to Sound*, Proc. Phys. Soc., Vol. 47, p. 703, 1935.

[4] Savic, P., *On Acoustically Effective Vortex Motion in Gaseous Jets*, Phil Mag., Vol. 32, p. 245, 1941.

Velocity and Range Considerations for the Attainment of Given Intercept Angles

WAYNE H. TEMPELMAN*

Convair-Astronautics, A Division of General Dynamics Corp.

Summary

Based on simplified two-body assumptions, a general analysis is presented for ballistic trajectories which result in a specified intercept angle at a given altitude. The minimum velocity required is derived starting with zero velocity and from a circular orbit. The range is obtained for initial intercepts at the specified altitude. The velocity requirements starting from a 150-nm circular orbit with final altitudes of 450,000 ft and 1,028 nm are presented in graphical form.

Symbols

a = constant defined in Eq. (4)
b = constant defined in Eq. (4)
e = eccentricity
r = radial distance from center of attracting body
R = dimensionless distance ratio, r_0/r_I
v = velocity
V = dimensionless velocity ratio, v/v_c
ΔV = velocity required starting from a circular orbit
α = dimensionless radial velocity, $V_0 \sin \gamma_0$
β = dimensionless horizontal velocity, $V_0 \cos \gamma_0$
γ = flight path angle with respect to the horizontal
δ = velocity (ΔV) angle with respect to the horizontal
θ = range central angle
λ_1 = Lagrange multiplier
ϕ = true anomaly

Superscripts

c = circular
d = downward
i = inward
I = intercept
o = outward
p = perigee
u = upward
0 = initial conditions

Introduction

THIS ARTICLE IS CONCERNED PRIMARILY with that class of trajectories which minimize the velocity required for a given intercept angle and altitude or, conversely, which maximize the intercept angle for a given velocity and altitude.

A particular application would be the return, with small guidance errors, of a data capsule from a satellite orbit. Analytical methods are developed in references 1 and 2 which define the maximum re-entry angle in terms of the heating and deceleration limits of the capsule during atmospheric descent. As the re-entry dispersion is generally minimized for maximized re-entry angle, the formulas herein presented would be useful in selecting optimum orbital ejection conditions for specified re-entry angles.

The usual assumption is made that the system consists of two bodies, one the attracting body considered as a point mass and the other the orbiting body with negligible mass as compared with that of the attracting body. The only force assumed to act is gravity, hence the influence of other bodies, the possible oblateness of the attracting body, and atmospheric effects are neglected.

Velocity Requirements

The velocity of a body in an orbit can be specified by a magnitude and a flight-path angle, which is taken herein as the angle with respect to the local horizon. If, at the initial point, the dimensionless velocity is represented by the components α (radial) and β (horizontal), the initial velocity required starting with zero velocity can be expressed as in Eqs. (1). The required velocity starting from a circular orbit ($\alpha = 0, \beta = 1$) is specified by Eqs. (2) (see Fig. 1).

$$V_0 = (\alpha^2 + \beta^2)^{1/2} \qquad \gamma_0 = \tan^{-1}(\alpha/\beta) \tag{1}$$

$$\Delta V = [\alpha^2 + (1 - \beta)^2]^{1/2} \quad \delta = \tan^{-1}[\alpha/(1 - \beta)] \tag{2}$$

The flight-path angle at the desired altitude will be referred to as the intercept angle (γ_I), and is derived from simplified two-body assumptions:

$$\gamma_I = \tan^{-1}[(-R^2\beta^2 + 2R - 2 + \alpha^2 + \beta^2)^{1/2}/(R\beta)] \tag{3}$$

where $R = r_0/r_I$ = (initial distance)/(intercept distance). Solving for the radial component of velocity,

$$\alpha = (a\beta^2 + b)^{1/2} \tag{4}$$

where

$$a = (R^2/\cos^2 \gamma_I) - 1$$

$$b = 2(1 - R)$$

Through use of Eqs. (1), (2), and (4), β can be expressed as a function of either γ_0 or δ:

$$\beta = [b/(\tan^2 \gamma_0 - a)]^{1/2} \tag{5}$$

$$\beta = \frac{\tan^2 \delta \pm [(a + b)\tan^2 \delta - ab]^{1/2}}{\tan^2 \delta - a} \tag{6}$$

Received May 3, 1960. Revised and received July 1, 1960.

* Research Engineer, Operations Analysis Group.

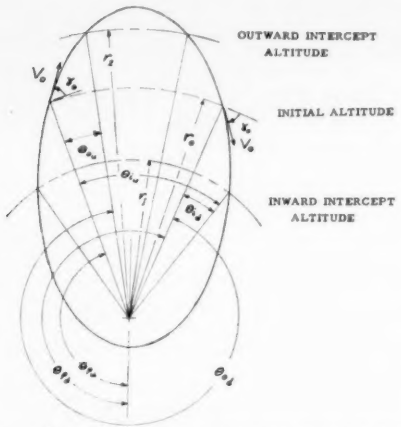

FIG. 1. Illustration of perigee and range angles.

The plus sign applies for $\delta > 90°$, the minus sign for $\delta < 90°$; and for $\delta = 90°$, $\beta = 1$.

Minimum Energy Requirements

On substituting Eq. (4) into Eq. (1) it becomes apparent that the velocity V_0 for a specified R and γ_I is minimum for the minimum permissible β. For outward intercepts ($R < 1$, $b > 0$), Eq. (5) is minimized for $\gamma_c = 90°$ ($\beta = 0$), and for inward intercepts ($R > 1$, $b < 0$) the value is $\gamma_0 = 0°$ ($\alpha = 0$). The corresponding velocities are found by combining Eqs. (1) and (4):

$$\left.\begin{aligned} R < 1: &\quad V_0 = b^{1/2} \\ R > 1: &\quad V_0 = (-b/a)^{1/2} \end{aligned}\right\} \tag{7}$$

Minimization of the required velocity (ΔV) starting from a circular orbit is accomplished by minimizing

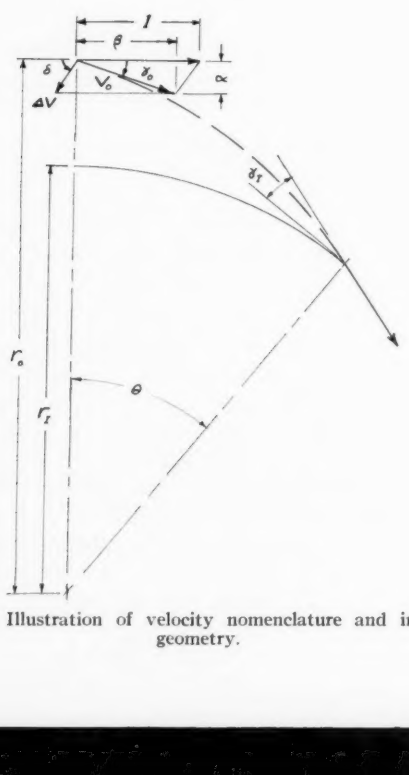

FIG. 2. Illustration of velocity nomenclature and intercept geometry.

Eq. (2) subject to the constraint on α, Eq. (4). With the use of Lagrange multipliers, the following three equations are obtained:

$$\left.\begin{aligned} 0 &= \alpha^2 - a\beta^2 - b \\ 0 &= \alpha/[\alpha^2 + (1-\beta)^2]^{1/2} + 2\lambda_1\alpha \\ 0 &= (1-\beta)/[\alpha^2 + (1-\beta)^2]^{1/2} + 2\lambda_1 a\beta \end{aligned}\right\} \tag{8}$$

By use of Eqs. (2) and the assumption $\alpha \neq 0$, the solution is obtained as

$$\left.\begin{aligned} \beta &= (\cos^2\gamma_I)/R^2 \\ \Delta V &= \{3 - 2R - [(\cos^2\gamma_I)/R^2]\}^{1/2} \\ \delta &= \cos^{-1}\{[\Delta V^2 - 2(1-R)]/\Delta V\} \end{aligned}\right\} \tag{9}$$

For $\alpha = 0$, the solution to Eq. (8) is given by Eq. (10), with ΔV and δ obtained from Eq. (2).

$$\left.\begin{aligned} \beta &= (-b/a)^{1/2} \\ \Delta V &= |1 - (-b/a)^{1/2}| \\ R > 1: \delta &= 0° \qquad R < 1: \delta = 180° \end{aligned}\right\} \tag{10}$$

The range of applicability of the solution for $\alpha \neq 0$ is determined by setting Eq. (4) equal to zero, which results in Eqs. (11):

$$\left.\begin{aligned} \beta &= [1 \pm (9 - 8R)^{1/2}]/2 \\ \gamma_{Ia,b} &= \cos^{-1}\{R([1 \pm (9-8R)^{1/2}]/2)^{1/2}\} \\ R > 1: &\quad \gamma_{Ia} < \gamma_I < \gamma_{Ib} \\ R < 1: &\quad \gamma_{Ia} < \gamma_I < 90° \end{aligned}\right\} \tag{11}$$

The solution minimizing V_0 [Eq. (7)] is equivalent to that minimizing ΔV [Eq. (10)] (since $\Delta V = 1 - V_0$ when $\alpha = \gamma = \delta = 0$), both for $R > 1.125$ and for $1 < R < 1.125$ when γ_I is outside the range given in Eq. (11) (see Fig. 3). The region where $\delta = 0°$ results in a minimum energy intercept originating from a circular orbit is shown in Fig. 4.

Range Considerations

The above analysis results in those velocity vectors which produce intercept at the specified intercept angle and altitude. Each velocity will result, in general, in intercepts at two different ranges depending on whether the velocity is applied upward or downward. This is due to the fact that the orbit intercepts a given radial distance in two places.

The intercept point is oriented relative to the initial point by the range angle $\ominus$ and to the perigee point by the true anomaly ϕ which, in turn, is oriented relative to the initial point by the perigee angle θ_p. There are two variables to consider in writing the range equations: (1) whether the desired intercept altitude is greater or smaller than r_0 and (2) the upward or downward application of velocity is used. Fig. 2 shows the four possibilities, from which the following ranges of angles are inferred for the cases restricted to initial intercept, the angles (measured from the last fictitious perigee passage in the rotational direction) being restricted to the principal values:

Outward Intercepts ($r_I > r_0$):

Upward application of velocity

$$0° < \theta_p < 180° \qquad 0° < \phi < 180°$$

$$\theta_{ou} = \phi - \theta_p$$

Downward application of velocity

$$180° < \theta_p < 360° \qquad 360° < \phi < 540°$$

$$\theta_{od} = \phi + \theta_p$$

Inward Intercepts ($r_I > r_0$):

Upward application of velocity

$$0° < \theta_p < 180° \qquad 180° < \phi < 360°$$

$$\theta_{iu} = 2\pi - \phi - \theta_p$$

Downward application of velocity

$$180° < \theta_p < 360° \qquad 180° < \phi < 360°$$

$$\theta_{id} = \theta_p - \phi$$

The true anomaly and perigee angles are given by

$$\left.\begin{aligned} \theta_p &= \cos^{-1}\,[(\beta^2 - 1)/e] \\ \phi &= \cos^{-1}\,[(\beta^2 R - 1)/e] \end{aligned}\right\} \qquad (12)$$

where $e = [\alpha^2\beta^2 + (\beta^2 - 1)^2]^{1/2}$.

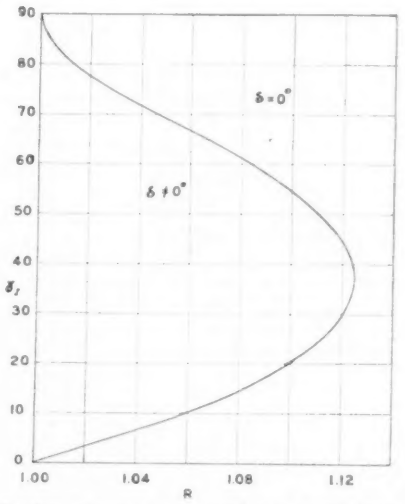

FIG. 3. Region where $\delta = 0$ results in a minimum energy intercept, $R > 1$.

The range equations can now be derived:

$$\left.\begin{aligned} \theta_{id} &= \cos^{-1}[(\beta^2 - 1)/e] - \cos^{-1}[(\beta^2 R - 1)/e] \\ \theta_{iu} &= 2\pi - \cos^{-1}[(\beta^2 - 1)/e] - \\ &\qquad \cos^{-1}[(\beta^2 R - 1)/e] \\ \theta_{od} &= \cos^{-1}[(\beta^2 R - 1)/e] + \cos^{-1}[(\beta^2 - 1)/e] \\ \theta_{ou} &= \cos^{-1}[(\beta^2 R - 1)/e] - \cos^{-1}[(\beta^2 - 1)/e] \end{aligned}\right\} \qquad (13)$$

It should be noted that the third range equation, for outward intercept with downward application of velocity, assumes an infinitesimally small attracting body. In actuality, the finiteness of the body would eliminate some of the trajectories.

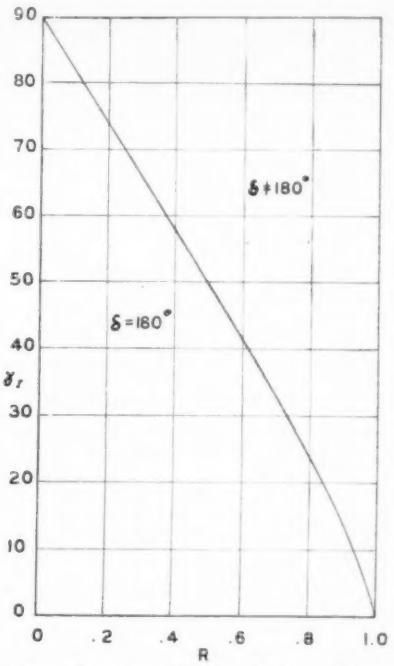

FIG. 4. Region where $\delta = 180°$ results in a minimum energy intercept, $R < 1$.

For inward intercepts ($R > 1$) the maximum applicable δ and the accompanying minimum range is obtained from the geometry for the limiting case of straight-line transfer with infinite velocity:

$$\left.\begin{aligned} \delta_{max} &= \cos^{-1}\,[(-\cos\gamma_I)/R] \\ \theta_{min} &= \cos^{-1}\,[(\cos\gamma_I)/R] - \gamma_I \end{aligned}\right\} \qquad (14)$$

The maximum range (maintaining the original orbital direction) occurs for an upward application of velocity of escape magnitude ($V_0 = 2^{1/2}$), which results in an orbit with eccentricity one. Equating the normal velocity components from Eqs. (4) and (1) yields the required velocity ΔV and the range:

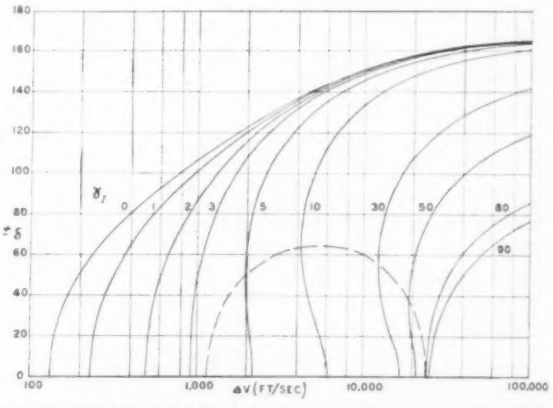

FIG. 5. Possible velocity vectors starting from a circular orbit for the attainment of given intercept angles for a descent from 150 nm to 450,000 ft.

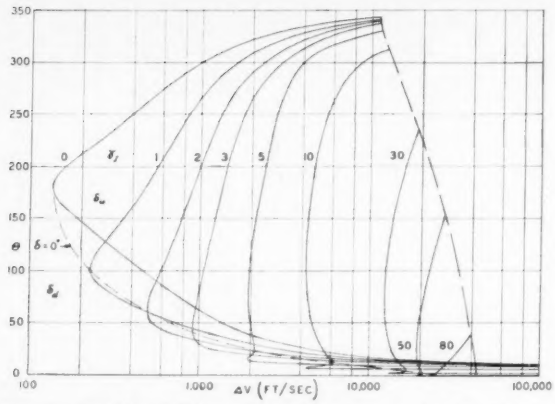

FIG. 6. Velocity requirements starting from a circular orbit for the attainment of a given range and intercept angle for a descent from 150 nm. to 450,000 ft.

$$\left.\begin{aligned} \beta &= (2/R)^{1/2} \cos \gamma_I \\ \Delta V &= [3 - 2(2/R)^{1/2} \cos \gamma_I]^{1/2} \\ \theta_{max} &= 2\pi - \cos^{-1} [(2/R)(\cos^2 \gamma_I) - 1] - \\ &\qquad \cos^{-1} (2 \cos^2 \gamma_I - 1) \end{aligned}\right\} \quad (15)$$

For outward intercepts ($R < 1$) there is a minimum δ (maintaining the original orbital direction) that corresponds to a vertical trajectory ($\gamma_0 = 90°$, $\beta = 0$) that just reaches the desired altitude. The required velocity V_0 is given by Eq. (7), and yields $\delta_{\min}$ and ΔV from Eqs. (2):

$$\left.\begin{aligned} \delta_{min} &= \tan^{-1}[2(R - 1)]^{1/2} \\ \Delta V &= (2R - 1)^{1/2} \end{aligned}\right\} \quad (16)$$

The maximum applicable angle δ and corresponding ranges for upward and downward application of velocity are determined from the geometry of a straight-line transfer:

$$\left.\begin{aligned} \delta_{max} &= \cos^{-1}[(-\cos \gamma_I)/R] \\ \theta_{u,d} &= \gamma_I \pm \cos^{-1}[(\cos \gamma_I)/R] \end{aligned}\right\} \quad (17)$$

where $\gamma_I > \cos^{-1} R$.

Figs. 5 to 8 show a typical example of both an outward and inward intercept. The dashed lines in Figs. 6 and 8 separate the upward from the downward applications of velocity for each γ_I curve, with the dashed lines in Figs. 5 and 7 representing the locus of minimum energy intercepts.

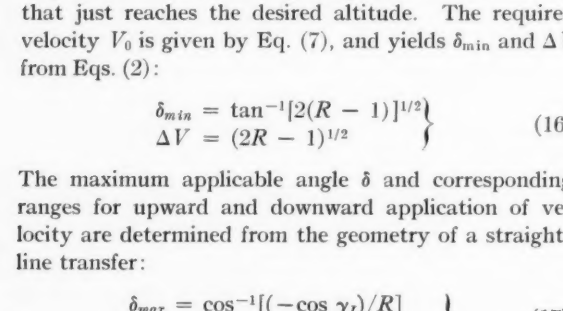

FIG. 7. Possible velocity vectors starting from a circular orbit for the attainment of given intercept angles for an ascent from 150 nm. to 1,028 nm.

Conclusions

(1) For inward intercepts with $R > 1.125$, the minimum energy-transfer trajectory starting with zero velocity or from a circular orbit is obtained by a horizontal application of velocity.

(2) For inward intercepts with $R < 1.125$, there are two ranges of intercept angles, one starting from zero degrees and the other ending at 90 degrees, where the first conclusion holds true. When the intercept angle lies between these two ranges, minimum energy transfers starting from a point with zero velocity are obtained with a horizontal application of velocity, whereas

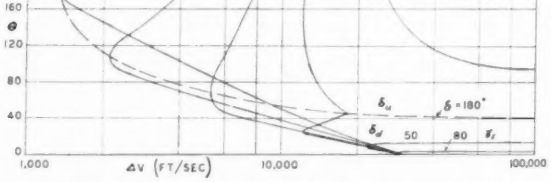

FIG. 8. Velocity requirements starting from a circular orbit for the attainment of a given range and intercept angle for an ascent from 150 nm. to 1,028 nm.

in starting from a circular orbit minimum energy transfers are obtained with a nonhorizontal application of velocity.

(3) For outward intercepts, minimum energy transfers starting with zero velocity are obtained by a vertical application of velocity, resulting in a range of zero degrees. Minimum energy transfers starting from a circular orbit are obtained by a horizontal forward application of velocity ($\delta = 180°$) for a limited range of intercept angles starting at zero degrees. Outside of this range the angle of velocity application decreases to some angle less than 90 degrees.

(4) Inward intercepts for a given γ_I result in a limited range coverage, range angles near zero degrees and near 360 degrees, being excluded.

(5) Outward intercepts, for a range of intercept angles starting at zero degrees, allow complete coverage

(*Continued on page 701*)

Aerodynamic Noise in Supersonic Wind Tunnels†

JOHN LAUFER*

California Institute of Technology

Summary

Hot-wire measurements in the free stream of a supersonic wind tunnel were made in the Mach number range of 1.6 to 5.0. It is shown that the mass-flow fluctuations increase very rapidly with increasing Mach number. If the fluctuation field is assumed to consist of sound waves—an assumption that is consistent with the measurements—the sound intensity is approximately proportional to M^4, within the range of the experiments. Furthermore, the orientation of the field is found to be different from the Mach line direction; it corresponds to a sound-source velocity of approximately one-half the free-stream velocity for the higher Mach numbers. It is shown that the turbulent boundary layer along the nozzle and the tunnel walls is responsible for this sound field.

Symbols

a	= sound velocity
e	= voltage across hot wire
Δe_T	= sensitivity coefficient for total temperature
Δe_m	= sensitivity coefficient for mass flow
m	= mass flow
M	= Mach number
p	= pressure
r	= $\Delta e_m/\Delta e_T$
R	= correlation coefficient
Re/in.	= Reynolds number per in. based on free-stream conditions
T	= static temperature
T_T	= total temperature
u	= velocity in the mean flow direction
u_n'	= particle velocity normal to the wave front
$\bar{u}_s$	= source velocity
α	= $\left(1 + \frac{\gamma - 1}{2} M^2\right)^{-1}$
β	= $\alpha(\gamma - 1)M^2$
γ	= ratio of specific heats
δ^*	= boundary-layer displacement thickness
θ	= angle between the normal to the wave front and the direction of flow
ρ	= density
$(\ )'$	= instantaneous values
$\overline{(\ )}$	= mean values
$\widetilde{(\ )}$	= root-mean-square values

Received June 20, 1960.

† This paper presents the results of one phase of research carried out at the Jet Propulsion Laboratory, California Institute of Technology, under joint sponsorship of the Department of the Army, Ordnance Corps (under Contract No. DA-04-495-Ord 18), and the Department of the Air Force.

* Chief, Gas Dynamics Section, Jet Propulsion Lab.

The author wishes to acknowledge the help of Dr. T. Vrebalovich, who made many of the measurements, and Dr. A. Kistler, who contributed valuable suggestions.

Introduction

IT IS WELL KNOWN that in a low-speed wind tunnel certain types of experiments are strongly affected by the turbulence level of the free stream. The classical example is the drag measurement of a sphere. Prandtl-Wieselsberger[1] pointed out that the difference in drag values obtained in various wind tunnels is due to turbulence in the free stream. Later, Taylor[2] obtained a parameter correlating the measurements. Dryden and co-workers[3] carried out systematic experiments and substantiated Taylor's theoretical work. When a better understanding of turbulence produced behind grids had been gained, effective methods were devised to reduce the turbulence level in the free stream.[4]

In all the preceding cases the disturbances were predominantly velocity fluctuations having vorticity. Since no cooling systems were required, very few temperature fluctuations were present in the stream. Furthermore, disturbances due to noise could be minimized by proper design of the propeller and its shaft.

It soon became apparent that in supersonic wind tunnels the fluctuations differed in source and nature from those experienced in low-speed tunnels. In 1954, the author noted[5] that large velocity fluctuations in the supply section do not influence the transition Reynolds number in the free stream at high Mach numbers. He suggested, as a possibility, that sound-type disturbances originating from the turbulent shear layer on the tunnel walls might be present in the free stream. Later, in 1956, some wind-tunnel measurements at the NACA Lewis Laboratory indicated that very large fluctuations are present in an $M = 3$ flow.‡ The most comprehensive treatment of the subject is given by Morkovin,[6, 7] who discusses all the possible sources of disturbances in a supersonic wind tunnel, points out the difficulties of measuring these fluctuations, and gives an approximate value for the turbulence level encountered in the wind tunnel used in his investigations. The present investigation was undertaken in connection with experiments relating to the stability problem of the supersonic laminar boundary layer. From experience obtained in low-speed work, it was known that the detection of the unstable Tollmien-Schlichting oscillations is difficult, if not impossible, when the free-stream disturbance level is high. For

‡ Private communication from J. C. Evvard, Lewis Laboratory, Cleveland, Ohio.

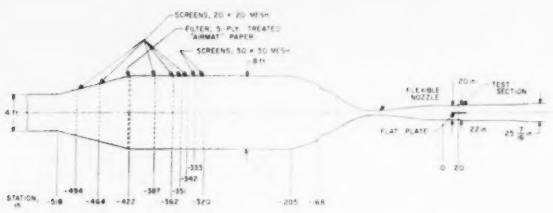

FIG. 1. Schematic diagram of the tunnel.

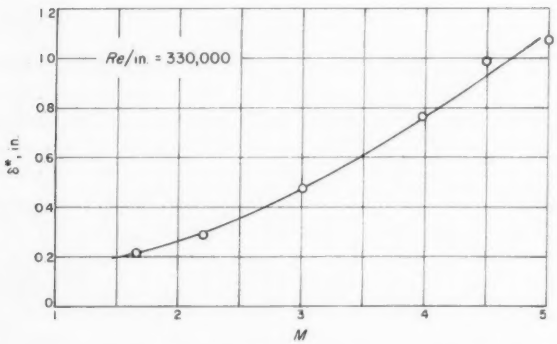

FIG. 2. Variation with Mach number of boundary-layer thickness on the tunnel wall.

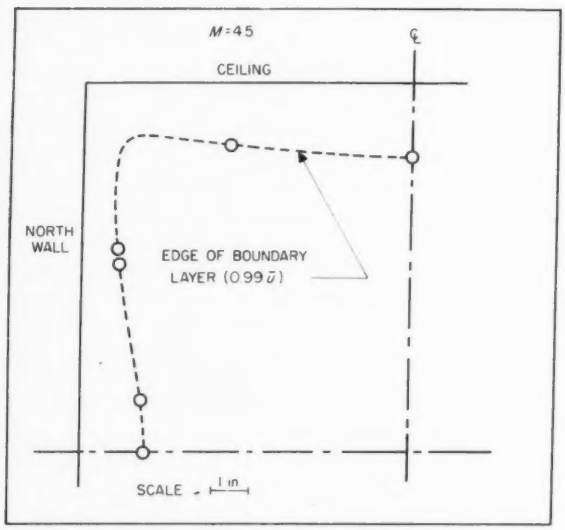

FIG. 3. Boundary-layer thickness distribution in a tunnel cross section.

this reason, considerable time and effort were spent to study the fluctuations in the free stream and to find means of reducing their amplitude.

Equipment

Wind Tunnel

Most of the experiments were carried out in the Jet Propulsion Laboratory 18 × 20-in. supersonic wind tunnel. The peak Mach number of the tunnel is 5. Dimensions and details of the supply section, nozzle, and test section are shown in Fig. 1. Screens 1 and 2 in the cone section are used to prevent separation. The air filter is a commercially available Airmat paper filter† with a drag of about 50 to 100 times the dynamic pressure. The first four damping screens are 20 mesh with 0.016-in. diameter steel wires; the last two screens are 30 mesh with 0.003-in. diameter wires. In the supply section all corners are faired.

The flexible-nozzle walls are of the continuous third-derivative design.[8] The mean pressure variation in the working section is less than 2% for the entire Mach number range. Details of the mean flow distribution at various Mach numbers are given in reference 9. The boundary layers on the tunnel walls at the throat and downstream from the throat are turbulent under all flow conditions except when otherwise stated. Fig. 2 gives boundary-layer displacement thicknesses measured on the center of the upper flexible wall as a function of Mach number. The approximate shape of the thickness distribution around the circumference of the tunnel test section is shown in Fig. 3.

The turbulence level in the supply section was found to be due to velocity fluctuations only, no temperature fluctuation being detected. The turbulence level was 1 per cent for all Reynolds numbers and Mach numbers, except at $M \geqslant 4.5$, where $\tilde{u}/\bar{u} = 0.5$ percent.

Hot-Wire Probe

All the hot wires employed in the experiments were made of 90 per cent platinum and 10 per cent rhodium with diameters of 0.00005 or 0.0001 in. and corresponding nominal lengths of 0.015 or 0.020 in. They were mounted on a probe as shown in Fig. 4. The main body of the probe was hollow and diamond-shaped with a 5-degree wedge attached. A thin razor blade 0.060 in. wide and 0.004 in. thick was soldered to this wedge. The razor blade was coated with an electrically insulating varnish; two jeweler's broaches were glued to the blade, and a final coat of varnish was baked over the surface. The broaches extended 0.050 in. in front of the thin, razor-sharp leading edge and were spaced either 0.015 or 0.020 in. apart. Lead wires from the broaches were fastened to the rear of the wedge and passed through the center of the diamond-shaped piece to the gold-plated pins which plugged into a vertical traverse mechanism (Fig. 5). With this mechanism the hot wire could be placed close to the upper wall of the tunnel in order to protect the wire from the rough flow conditions which obtain during the starting of the wind tunnel. With this traverse, the wire could also be placed at any vertical position in the tunnel.

Hot-Wire Amplifier

It is more difficult to meet the design requirements of the hot-wire equipment used for fluctuation measurements in supersonic flows than in low-speed flows.

† Manufactured by American Air-Filter Co., Louisville, Ky.

Much higher frequencies are expected in supersonic flows, and an amplifier with a frequency response of several hundred kilocycles is therefore needed. Low-noise input circuitry is especially critical in such an amplifier because of the greater frequency bandwidth and lower level of the fluctuations expected. The commercially available hot-wire set* satisfies these requirements and has been used throughout the present experiment.

Experimental Results

Early Experiments

It is well known that the transition Reynolds number on a model placed in a wind tunnel is sensitive to the turbulence level of the tunnel free stream. This fact has been utilized by the author[5] to obtain some qualitative concept of how the free-stream turbulence level changes as the tunnel Mach number increases. Of course, any conclusion arrived at from this relatively crude method has to be weighed very carefully, since the stability of the boundary layer is also a function of the Mach number. However, although the available theoretical calculations[10] indicated that in the low supersonic range the boundary layer becomes more stable as the free-stream Mach number increases, the experiments indicated a sharp decrease in the value of the transition Reynolds number. Thus, it was tentatively concluded that the turbulence level of a supersonic tunnel increases with increasing Mach number. And it was further concluded that the turbulence is not due to fluctuations originating in the supply section, since a tenfold increase in the velocity fluctuation there did not affect the transition Reynolds number of the model at $M > 2.5$. The velocity-fluctuation increases did, however, decrease the transition Reynolds number appreciably at lower Mach numbers.

Hot-Wire Measurements

To gain a better understanding of the free-stream fluctuations, a more direct method of measurement is required. Thus far, the most successful is the hot-wire technique, with which the magnitudes of certain types of fluctuations can be obtained. The main difficulty with this technique is that these fluctuations represent an algebraic combination of fluctuations of several basic physical quantities, and, with the exception of some special cases, it is not possible to calculate the magnitude of the fluctuation of each basic quantity separately. Specifically, the hot wire in a supersonic stream responds to both mass-flow and total-temperature fluctuations, and the instantaneous voltage across the wire may be expressed[11]

$$e' = \Delta e_T(T_T'/\bar{T}_T) - \Delta e_m(m'/\bar{m}) \qquad (1)$$

where

$$T_T'/T_T = \alpha(T'/\bar{T}) + \beta(u'/\bar{u})$$

* Model 50B, manufactured by Shapiro and Edwards, South Pasadena, Calif.

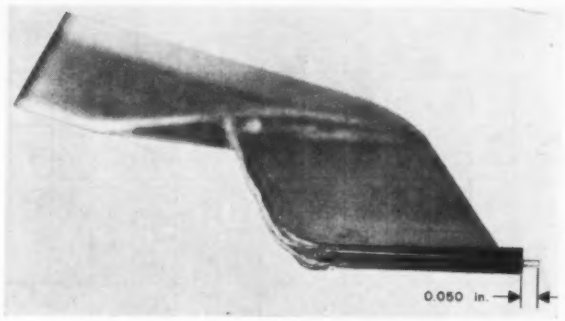

FIG. 4. Hot-wire probe.

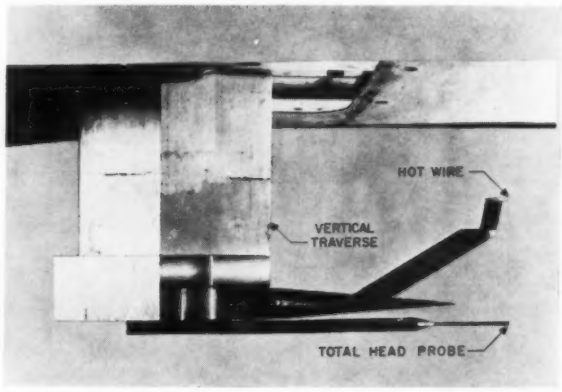

FIG. 5. Hot wire and total head probe.

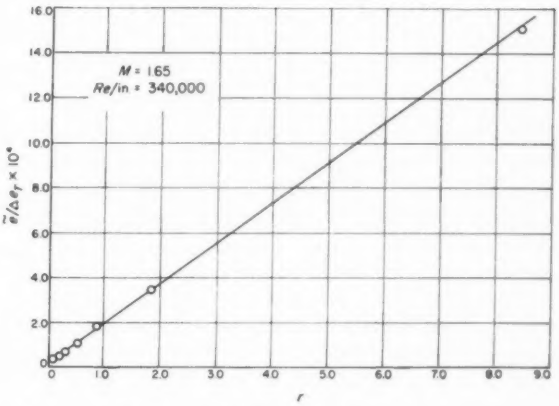

FIG. 6. Mode diagram for $M = 1.6$.

and $$m'/\bar{m} = (u'/\bar{u}) + (\rho'/\bar{\rho})$$

and Δe_m and Δe_T are sensitivity coefficients that are determined by mean flow conditions and the mean temperature of the hot wire. The measured mean-square value of the voltage may be written in the form

$$\frac{\overline{e'^2}}{\Delta e_T^2} = \frac{\overline{T_T'^2}}{\bar{T}_T^2} - 2rR_{mT}\frac{\overline{\tilde{m}\tilde{T}_T}}{\bar{m}\bar{T}_T} + r^2\frac{\overline{m'^2}}{\bar{m}^2} \qquad (2)$$

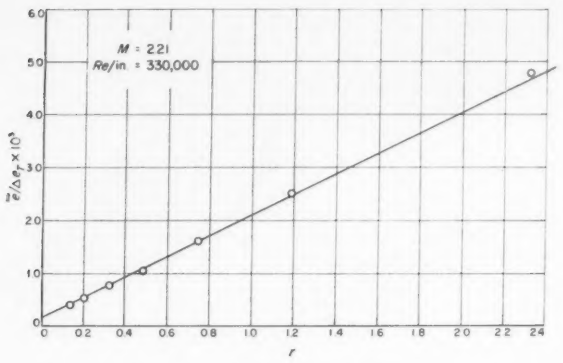

FIG. 7. Mode diagram for $M = 2.2$.

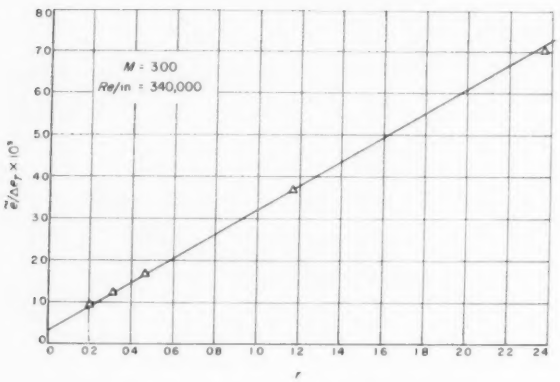

FIG. 8. Mode diagram for $M = 3.0$.

where $$r = \Delta e_m/\Delta e_T$$

and $$R_{mT} = \overline{m'T'_T}/\tilde{m}\tilde{T}_T$$

If under a given flow condition $\overline{e'^2}$ is measured for three different values of r (i.e., at three different mean wire temperatures), the values of $\tilde{T}_T$, $\tilde{m}$, and R_{mT} may be calculated. In practice, the measurements are carried out at more than three wire temperatures, and from plots of $\tilde{e}/\Delta e_T$ vs. r the values of the three unknowns may be obtained more accurately by a fairing technique. Figs. 6 through 10 show some typical results obtained in the 18 × 20-in. wind tunnel. The calculated mass-flow fluctuations are plotted in Fig. 11. Their large magnitudes at the high Mach numbers are quite startling: they are approximately 50 times higher than those measured in a low-turbulence, low-speed wind tunnel.

One remarkable feature of these fluctuations is that without exception the correlation coefficient R_{mT} is found to be approximately -1 (the mode diagrams in Figs. 6–10 are always straight lines within the accuracy of the measurements)—that is to say, the mass-flow and total-temperature fluctuations exhibit a high degree of correlation. This is a strong restrictive condition. Thus, the fluctuating field in the free stream must be of a very special kind. Unfortunately, from the hot-wire data alone it is not possible to obtain any more definitive information. What can be done, however, is to postulate a certain simple type of fluctuation field and to determine whether the calculated hot-wire response (mode diagram) is consistent with the measured response. It is clear that the field cannot be due to pure velocity fluctuations associated with vorticity. In this case,

$$m'/\bar{m} = u'/\bar{u}$$

and $$T_T'/\bar{T}_T = \beta u'/\bar{u}$$

Consequently,

$$R_{mT} = \overline{m'T_T'}/\bar{m}\tilde{T}_T = \overline{u'^2}/\overline{u'^2} = +1$$

This expression, in contrast with the results, corresponds to mode diagrams having straight lines with negative slopes.

Assuming pure temperature fluctuations that are not associated with pressure changes, i.e., entropy fluctuations, then

$$\frac{m'}{\bar{m}} = -\frac{T'}{\bar{T}} \qquad \frac{T_T'}{\bar{T}_T} = \alpha\frac{T'}{\bar{T}}$$

since $$\frac{T'}{\bar{T}} = -\frac{\rho}{\bar{\rho}'} \qquad \frac{u'}{\bar{u}} = 0$$

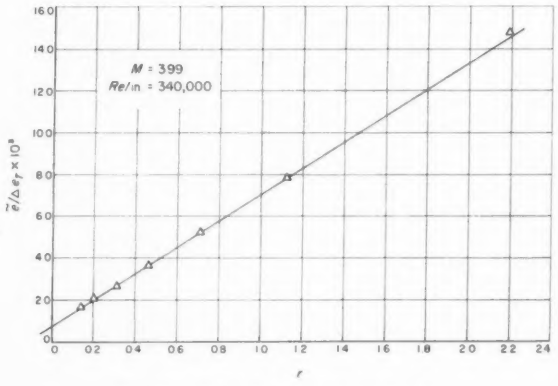

FIG. 9. Mode diagram for $M = 4.0$.

This gives the proper sign for the correlation coefficient R_{mT}. However, rewriting the hot-wire equation in terms of the r.m.s. temperature fluctuations

$$\tilde{e}/\Delta e_T = (\alpha + r)\tilde{T}/\bar{T}$$

gives $r = -\alpha$ for $\tilde{e}/\Delta e_T = 0$. This condition is not satisfied by the measurements.

As a matter of fact, the existence of these two types of fluctuations or their combinations can be ruled out within the framework of the linear theory[12] using simple physical arguments. Neither in the nozzle nor in the working section does the tunnel free stream contain turbulent shear fields or shock waves. Therefore, since both vorticity and entropy fluctuations are

convected along streamlines, they could only exist in the working section through convection from the supply section. However, as noted earlier, the temperature (or entropy) fluctuations are undetectable here; thus, they must be negligibly small in the working section also. Since the per cent of velocity fluctuations associated with vorticity in the supply section is greatly diminished (to less than 0.01 per cent) through the nozzle because of the large ratio (40 at $M = 1.6$ and 1,500 at $M = 5.0$) of mean velocities in the working and supply sections (see the calculations of Tucker in reference 13), they cannot be the source of the high fluctuation level measured in the working section.

The only other simple fluctuating field[12] is a pure sound field in which the isentropic relation between the fluctuating quantities holds. Thus,

$$\frac{p'}{\bar{p}} = \gamma \frac{\rho'}{\bar{\rho}} = \frac{\gamma}{\gamma - 1} \frac{T'}{\bar{T}}$$

and

$$\frac{m'}{\bar{m}} = \frac{u'}{\bar{u}} + \frac{1}{\gamma} \frac{p'}{\bar{p}} \qquad \frac{T_T'}{\bar{T}_T} = \alpha(\gamma - 1)\left(\frac{p'}{\gamma \bar{p}} + M^2 \frac{u'}{\bar{u}}\right)$$

The hot-wire equation now becomes

$$e' = \alpha(\gamma - 1)\left(\frac{p'}{\gamma \bar{p}} + M^2 \frac{u'}{\bar{u}}\right) \Delta e_T - \left(\frac{p'}{\gamma \bar{p}} + \frac{u'}{\bar{u}}\right) \Delta e_m \tag{3}$$

or

$$\frac{e'}{\Delta e_T} = (\beta - r) \frac{u'}{\bar{u}} + [\alpha(\gamma - 1) - r] \frac{p'}{\gamma \bar{p}}$$

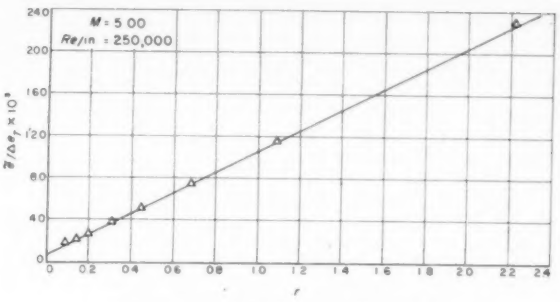

FIG. 10. Mode diagram for $M = 5.0$.

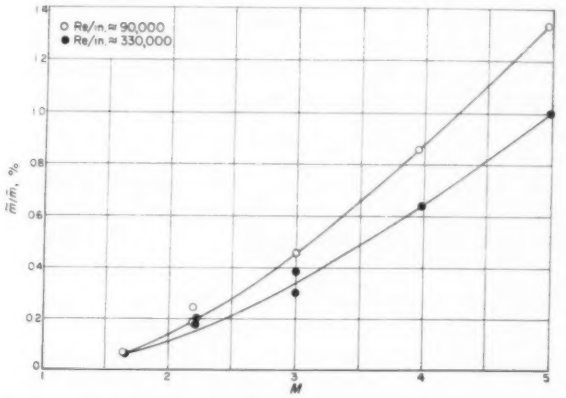

FIG. 11. Variation of mass-flow fluctuations with tunnel Mach number.

The mean-square voltage is

$$\frac{\overline{e'^2}}{\Delta e_T^2} = (\beta - r)^2 \frac{\overline{u'^2}}{\bar{u}^2} + 2(\beta - r)[\alpha(\gamma - 1) - r] R_{up} \frac{\tilde{u}\tilde{p}}{\bar{u}\bar{p}} + [\alpha(\gamma - 1) - r]^2 \frac{\overline{p'^2}}{\gamma^2 \bar{p}^2}$$

It is not difficult to show algebraically that the condition $R_{mT} = -1$ corresponds to $R_{up} = -1$; accordingly, the final result is

$$\frac{\tilde{e}}{\Delta e_T} = (\beta - r) \frac{\tilde{u}}{\bar{u}} - [\alpha(\gamma - 1) - r] \frac{\tilde{p}}{\gamma \bar{p}} = \alpha(\gamma - 1)\left(M^2 \frac{\tilde{u}}{\bar{u}} - \frac{\tilde{p}}{\gamma \bar{p}}\right) + \left(\frac{\tilde{p}}{\gamma \bar{p}} - \frac{\tilde{u}}{\bar{u}}\right) r \tag{4}$$

The assumption of a pure sound field with waves moving against the mean stream ($R_{up} = -1$) can thus be made consistent with the measurements. Using the mode diagrams obtained from the measurements, it is now possible to calculate separately all the fluctuating quantities present in the free stream. Fig. 12 shows the r.m.s. pressure fluctuations (made dimensionless by the dynamic pressure) as a function of the free-stream Mach number. It is to be noted that the mean pressure level of the tunnel (that is, the value of the Re/in.) influences the free-stream fluctuation amplitudes.

Providing that the preceding interpretation of the measurements is correct, further information can be extracted from the hot-wire data. It can be shown that the sound has a preferred orientation which is not in the direction of the characteristics; in other words, the measured pressure variations or at least their major portion are not caused by fluctuating Mach waves. Since the average wavelength of the field can be estimated to be of the order of an inch or less, it is safe to assume that the measurements are made in the far field of the sound source, and the waves may be assumed to be plane.

For a plane wave, the relation between u_n', the particle velocity normal to the wave front, and p' may be written

$$\frac{|u_n'|}{\bar{u}} = \frac{1}{M} \frac{p'}{\gamma \bar{p}}$$

However, it should be remembered that the hot wire is sensitive only to velocity variations in the direction of the mean flow such that

$$u' = |u_n'| \cos \theta$$

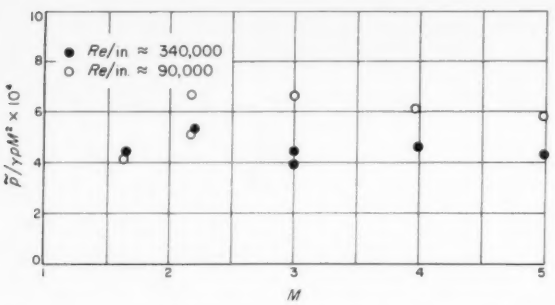

FIG. 12. Variation of pressure fluctuations with tunnel Mach number.

where θ is the angle between the normal to the wave front and the direction of the mean flow. Therefore,

$$u'/\bar{u} = (1/M)(p'/\gamma\bar{p}) \cos\theta \qquad (5)$$

For a Mach wave, $\cos\theta = -1/M$, and the r.m.s. pressure fluctuation due to a fluctuating Mach wave is given (see also reference 11)

$$\tilde{p}/\gamma\bar{p} = M^2(\tilde{u}/\bar{u}) \qquad (6)$$

Examining Eq. (4),

$$\tilde{e}/\Delta e_T = [(M^2 - 1)/M^2](\tilde{p}/\gamma\bar{p})r$$

Thus, in the mode diagram the straight line goes through the origin. This, however, is not the case for the present measurements.

In order to determine whether the accuracy of the measurements is sufficiently high to rule out the existence of fluctuating Mach waves in the free stream, the following experiment was performed. A tape 0.004 in. thick was placed across one of the nozzle walls of the wind tunnel at such a position that the weak shock wave originating from the tape crossed the hot wire. The shocklet was, of course, fluctuating because of the presence of a turbulent boundary layer on the nozzle wall. If the velocity and pressure due to these fluctuations are designated by u_2' and p_2', then, by Eq. (6),

$$p_2'/\gamma\bar{p} = M^2(u_2'/\bar{u})$$

Furthermore, it is easily shown that in the resulting mode diagram the intercept at $r = 0$ should have the same value as measured in the clean tunnel without the fluctuating shocklet. That is, writing e_{12} for the sum $e_1 + e_2$,

$$\left[\frac{\tilde{e}_{12}}{\Delta e_T}\right]_{r=0} = \alpha(\gamma - 1)\left(M^2\frac{\tilde{u}_1}{\bar{u}} - \frac{\tilde{p}_1}{\bar{p}}\right) \equiv \left(\frac{\tilde{e}_1}{\Delta e_T}\right)_{r=0}$$

where the subscript 1 corresponds to the clean tunnel condition.

The mode diagram in Fig. 13 shows that at $r = 0$ the value of $\tilde{e}/\Delta e_T$ did not change with the shocklet present.

This experiment supports the reliability of the hot-wire technique and indicates that sound fluctuations

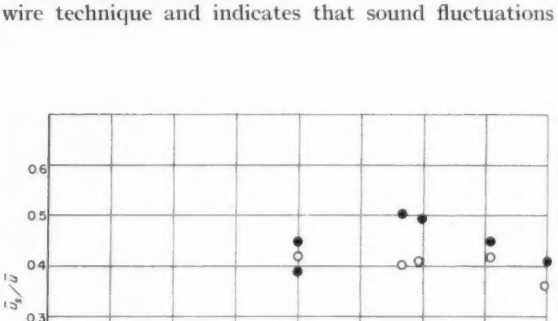

FIG. 14. Variation of source velocity with tunnel Mach number.

the orientation of which is not in the direction of the characteristics are indeed present, which means that the source of this field cannot be fixed but must be moving with respect to the tunnel reference.

Using Eq. (5), and remembering that $R_{up} = -1$, it is possible now to calculate the most probable orientation of the waves and, in turn, to obtain a mean propagation velocity of the sound source u_s. Since

$$(\bar{u} - \bar{u}_s)/a = -1/(\cos\theta)$$

$$\frac{\bar{u}_s}{\bar{u}} = 1 + \frac{1}{M\cos\theta} = 1 - \frac{\tilde{p}/\gamma\bar{p}}{M^2\tilde{u}/\bar{u}}$$

Fig. 14 represents this ratio measured at various free-stream Mach numbers. No values are shown at lower Mach numbers; here the determination of $\bar{u}_s/\bar{u}$ becomes less accurate because of the relatively lower amplitudes of the fluctuations. It should be mentioned here that the computed value of $\bar{u}_s$ is rather sensitive to the assumption that *all* the sound fluctuations are emitted from the same source. If, for instance, some Mach-wave fluctuations are also present—a condition

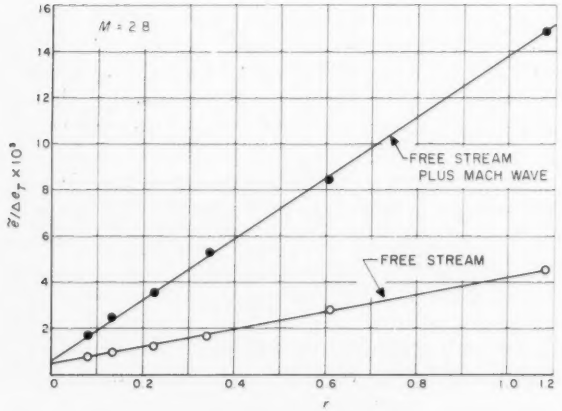

FIG. 13. Mode diagram for a fluctuating Mach wave superimposed on free-stream fluctuations.

that cannot be completely ruled out, especially in the low Mach number flows—the computed value of $\tilde{u}_s$ would increase.* The points in Fig. 14 thus represent a lower limit for the propagation velocities.

Discussion

The preceding interpretation of the hot-wire measurements shows the fluctuating field existing in the wind tunnel to be a sound field the intensity of which increases rapidly as the tunnel Mach number is increased. (Incidentally, the intensity was found to be uniform across the tunnel—less than 1 per cent variation—especially for the higher Mach number flows: as the flow Mach number decreased, the extent of the uniform field decreased toward the center position of the tunnel.) Furthermore, the field is not isotropic, but has a preferred direction. From this direction the source velocity was computed and was found to be between 0.4 and 0.5 times the free-stream velocity.

The question then arises as to what mechanism can produce such a fluctuation field. It has already been shown that the field does not originate from the supply section, where the sound fluctuations are negligibly small. Mechanical vibrations are also ruled out, since the frequencies encountered are very high. It is proposed, therefore, that the reason for this intense sound field is the presence of turbulent boundary layers along the tunnel walls: the fluctuations are identified with the aerodynamic noise produced by the turbulent boundary layers on the walls. In the following discussions arguments and evidences will be described which support this contention.

(*a*) It may be argued that if the boundary layers on the tunnel walls are indeed responsible for the fluctuations picked up by the hot wire, and if the hot wire is "protected" from the tunnel walls by an appropriately placed shield, a reduced voltage fluctuation should appear across the wire. The following experiment was therefore performed. A flat plate was placed on the center line of the tunnel spanning the working section from wall to wall. A hot wire was moved in the free stream over the plate in such a way that it could traverse ahead of the plate leading edge and behind the leading-edge shock wave. In the latter position the wire was shielded by the plate from the radiation coming from the boundary layer on the bottom wall. Of course, it was still exposed to the reflected field of that layer and to the direct field of the layers on three other walls. Nevertheless, Fig. 15 clearly shows the mean-square voltage fluctuation across the wire (which is roughly proportional to $\tilde{p}^2/\bar{p}^2$) decreased by about 20 per cent. (The wire sensitivity change was negligible ahead of and behind the shock.) The large peak in Fig. 15 corresponds to the position at which the wire crossed the leading-edge shock. Ahead of that position, $\tilde{e}^2$ corresponds to the free-stream fluctuation level; behind it, the reduced values of $\tilde{e}^2$ indicate the shielding effect of the plate.

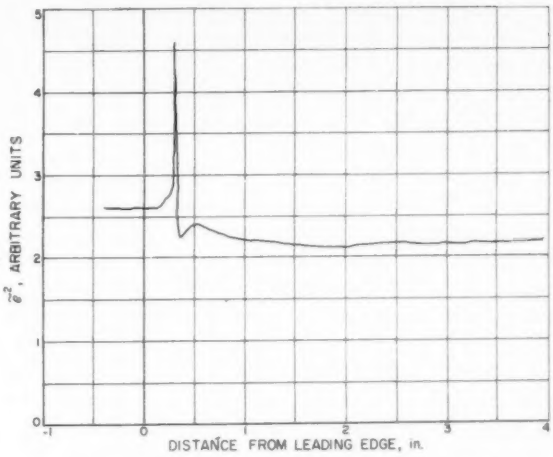

FIG 15. Free-stream fluctuations with a "shield."

(*b*) Adopting the suggestion of Liepmann[14] that the sound field due to a turbulent boundary layer may be considered the result of the displacement thickness fluctuation of the layer, it is expected that the sound intensity increases with increasing mean boundary-layer thickness. Indeed, the experiments show that for a constant Mach number flow with an increase in Reynolds number per inch of the tunnel, which corresponds to thinning of the wall boundary layers, the sound-field intensity decreases (Fig. 12).

(*c*) The recent experimental work of Willmarth[15] has indicated that the pressure fluctuations on the wall due to a turbulent boundary layer have a characteristic propagation velocity which is $0.8\bar{u}$ and is constant with Mach number in the range of the experiments (up to $M = 0.67$). Although the connection between the wall and free-stream pressure fluctuations produced by a turbulent layer is not understood as yet, it is clear that they must be interrelated. Considering Willmarth's results, it is not surprising, therefore, that in the present work it is possible to identify a source velocity which is different from the free-stream Mach number.

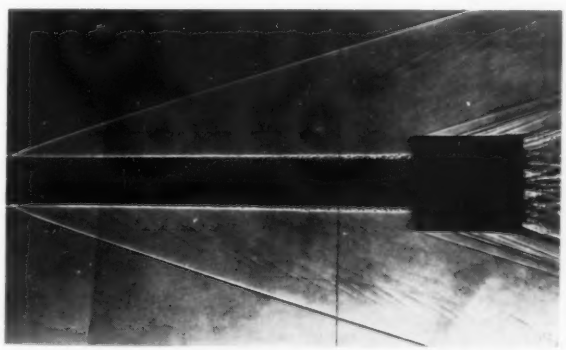

FIG 16. Shadowgraph of model in free flight.

* The author is grateful to Dr. M. V. Morkovin who pointed out this to him.

(*d*) Schlieren photographs obtained in a wind tunnel cannot reveal the pressure radiation field in the free stream because of the presence of turbulent boundary layers on the tunnel windows. However, some schlieren photographs taken in free flight[16] do reveal that it is possible to recognize an average orientation of the sound field emanating from the turbulent boundary layer which does not coincide with that of the Mach lines (Fig. 16).* As a matter of fact, from a rough estimate of sound-field orientation, a source speed is obtained which is about half the free-stream velocity and is in agreement with the present findings.

(*e*) Finally, it was possible to operate the wind tunnel at pressures low enough (Re/in. = 26,000; M = 4.5) that the boundary layers on the four walls in the test section were observed to be laminar. Under these conditions, the mass-flow fluctuations decreased by a factor of 10 (to about 0.11 per cent). The mode diagram indicated furthermore that these fluctuations were primarily temperature disturbances in the flow. This experiment thus proved definitely that the source of the large free-stream turbulence is indeed the turbulent wall boundary layers.

Conclusions

Hot-wire measurements made in the working section of a supersonic wind tunnel showed that the amplitudes of the mass-flow fluctuations increase very rapidly as the flow Mach number is increased. They further indicated that the fluctuation field is of a very special kind: one in which the mass-flow and total-temperature fluctuations show a high degree of correlation.

These measurements are interpreted to be the result of a sound field which is proportional in intensity to M^4, within the range of the experiments, and in which the sound waves have a preferred orientation. A source velocity can be calculated which was found to be approximately one half the free-stream velocity at the higher Mach numbers.

Finally, it is proposed and proved that the sound field is produced by the turbulent boundary layers on the tunnel walls.

The nature of the free-stream turbulence described here is believed to be characteristic of all supersonic wind tunnels that have turbulent boundary layers on the walls and good flow conditions in the nozzle and supply section. Some measurements were carried out, for example, in a smaller (12 × 12-in.) tunnel with similar results.

The presence of the sound field in the wind tunnel may be utilized to great advantage in the study of the aerodynamic noise produced by supersonic turbulent boundary layers. Thus far such work has not been done experimentally.

On the other hand, the presence of the sound field handicaps any experimental work on stability and transition problems which arise at high Mach numbers. On the basis of the present results, any measurements of transition Reynolds number obtained in wind tunnels with turbulent wall boundary layers should be accepted with great reserve.

* Fig. 16 originally appeared as Fig. 4c of NACA Technical Note 4235 (*Observations of Turbulent-Burst Geometry and Growth in Supersonic Flow* by C. S. James). The author is grateful to the National Aeronautics and Space Administration for permission to republish it here. It is to be noted in this figure that the wavelets near and along the leading-edge shock are due to turbulent spots and are to be disregarded; instead, reference should be made to the fine wave structure in the vicinity of the turbulent boundary layers.

References

[1] Wieselsberger, C., *Der Luftwiderstand von Kugeln*, Zeitschrift für Flugtechnik und Motorluftschiffahrt, Vol. 5, p. 140, 1914.

[2] Taylor, G. I., *Statistical Theory of Turbulence—V*, Proc. Roy. Soc. (London), Series A, Vol. 156, pp. 307–317, 1936.

[3] Dryden, H. L., Schubauer, G. B., Mock, W. C., Jr., and Skramstad, H. K., *Measurements of Intensity and Scale of Wind-Tunnel Turbulence and Their Relation to the Critical Reynolds Number of Spheres*, NACA TR 581, 1937.

[4] Schubauer, G. B., Spangenberg, W. G., and Klebanoff, P. S., *Aerodynamic Characteristics of Damping Screens*, NACA TN 2001, January, 1950.

[5] Laufer, J., *Factors Affecting Transition Reynolds Number of Models in Supersonic Wind Tunnels*, Journal of the Aeronautical Sciences, Vol. 21, No. 7, July, 1954.

[6] Morkovin, M. V., *On Transition Experiments at Moderate Supersonic Speeds*, Journal of the Aeronautical Sciences, Vol. 24, No. 7, pp. 480–486, 1957.

[7] Morkovin, M. V., *On Supersonic Wind Tunnels with Low Free-Stream Disturbances*, Air Force Office of Scientific Research, TN 56-540, November, 1956.

[8] Riise, N., *Flexible-Plate Nozzle Design for Two-Dimensional Supersonic Wind Tunnels*, Jet Propulsion Laboratory, Report No. 20-74, Pasadena, California, June, 1954.

[9] Steinbacher, R. J., *Calibration of a Continuous Third-Derivative Nozzle in the 20-Inch Supersonic Wind Tunnel*, SWT 20-C21, Jet Propulsion Laboratory, Pasadena, California.

[10] Lees, L., *Instability of Laminar Flow and Transition to Turbulence*, Consolidated Vultee, Report ZA-7-006, San Diego, Calif.

[11] Kovasznay, L. S. G., *The Hot-Wire Anemometer in Supersonic Flow*, Journal of the Aeronautical Sciences, Vol. 17, No. 9, pp. 565–572, 1950.

[12] Kovasznay, L. S. G., *Turbulence in Supersonic Flow*, Journal of the Aeronautical Sciences, Vol. 20, No. 10, pp. 657–675, 1953.

[13] Tucker, M., *Combined Effects of Damping Screens and Stream Convergence on Turbulence*, NACA TN 2878, January, 1953.

[14] Liepmann, H. W., *On the Acoustic Radiation from Boundary Layers and Jets*, paper presented at 23rd IAS Meeting, January 24–28, 1955.

[15] Willmarth, W. W., *Space-Time Correlations and Spectra of the Wall Pressure in a Turbulent Boundary Layer*, GALCIT report submitted to NACA, February, 1958.

[16] James, C. S., *Observations of Turbulent-Burst Geometry and Growth in Supersonic Flow*, NACA TN 4235, April, 1958.

✦ ✦ ✦

Transfer From an Arbitrary Initial Flight Condition to a Point Target

HARVEY L. ROTH*
Bell Aerosystems Company

Summary

In Part I of this paper is developed a noniterative method for obtaining the minimum impulse necessary to reach a stationary point target from an initial flight condition where the target need not be in the original plane of motion. The degenerate cases of minimum energy trajectories and departure from a circular orbit are given special attention. In Part II are obtained several sets of partial derivatives essential to an evaluation of range and/or flight-time errors at target. Special consideration is given to the singular points at which the Jacobian determinant associated with the transformation from one set of derivatives to another vanishes. Although the two parts constitute separate problems, both are needed for an overall evaluation of particular missions.

PART I

Minimization of Fuel Required to Reach a Point Target From Any Initial Flight Condition

(A) *Preliminary Remarks*

It is important to find the most economical manner in which to move a vehicle from one point to another. This paper considers the single-impulse transfer from an arbitrary initial flight condition to a specified point destination. In the first part, the minimum impulse transfer is obtained. In Part II the pertinent error derivatives and their singularities are discussed. The entire analysis deals with motion in an inverse-square force field.

(B) *The Minimum-Energy Trajectory*

It is well known that a spherical body sets up a gravitational field where the force F (per unit mass) is of the following form (reference 1, pp. 95–97):

$$F = F(r) = K/r^2 \tag{1}$$

where K = constant for a given sphere and r is the geocentric radius or distance from the center of the sphere. It is further known that a vehicle under the influence of only the above force will move along a conic section, i.e., a curve described (reference 1, pp. 227–229; reference 2, pp. 1A1–1A7, etc.) by the following equation:

$$r_i = \frac{\rho}{1 - e\cos\theta_i}; \qquad r_f = \frac{\rho}{1 - e\cos\theta_f} \tag{2}$$

where ρ is the semi-latus rectum, e is the eccentricity, and θ is the angle between the major axis and the geocentric radius vector. Since $\rho, e > 0$, $r = r_{max}$ when $\theta = 0°$.

If V_i denotes the vehicle speed at the point i, it can be shown that[2]

$$\left.\begin{aligned} \rho &= r_i\beta_i\cos^2\gamma_i \\ e &= \sqrt{1 - \beta_i(2 - \beta_i)\cos^2\gamma_i} \end{aligned}\right\} \tag{3}$$

where $\beta_i = V_i^2 r_i/\lambda$; $\lambda = gr^2 = g_0 r_0^2$ = const.; g = acceleration due to gravity at the surface of the sphere; and γ = the angle between the velocity vector and the local horizontal plane.† If the projection of the velocity $\mathbf{V}_i$ on the radius vector points away from the center of the sphere, γ is positive; otherwise γ is negative (see Fig. 1).

The range R from point i to point f is defined as the length of the projection on the sphere's surface of that portion of the trajectory between i and f. If the radius of the sphere is denoted by r_0, then $R = r_0(\theta_f - \theta_i)$.

The range angle θ_R is defined by the following expression:

$$\theta_R = R/r_0 = \theta_f - \theta_i \tag{4}$$

and therefore:

$$\begin{aligned} \cos\theta_f &= \cos(\theta_i + \theta_R) \\ &= \cos\theta_i\cos\theta_R - \sin\theta_i\sin\theta_R \end{aligned} \tag{5}$$

Combining Eqs. (2), (3), and (4) yields the following result:

† The local horizontal plane at a point i is the plane perpendicular to r_i.

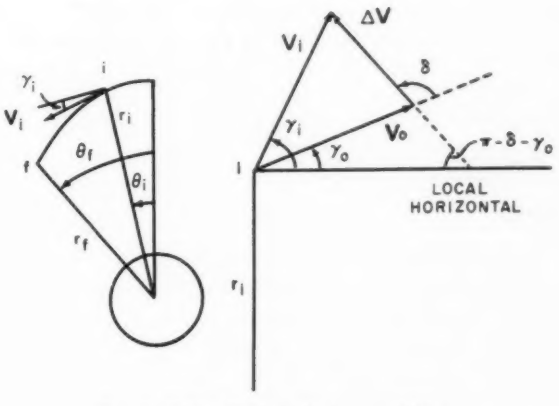

FIG. 1. (*left*). Basic trajectory variables.
FIG. 2. (*right*). Two-dimensional velocity vector diagram.

Received May 3, 1960. Revised and received July 2, 1960.
* Aerophysics Group.

$$\left.\begin{aligned} V_i^2 &= \frac{\lambda(1-\cos\theta_R)}{\eta\cos\gamma_i[r_i\cos\gamma_i + r_f\sin\gamma_i\sin\theta_R - r_f\cos\gamma_i\cos\theta_R]} \\ &= \frac{\lambda(1-\cos\theta_R)}{\eta\cos\gamma_i[r_i\cos\gamma_i - r_f\cos(\theta_R+\gamma_i)]} \\ \text{or } \beta_i &= \frac{1-\cos\theta_R}{\cos\gamma_i[\eta\cos\gamma_i - \cos(\theta_R+\gamma_i)]} \end{aligned}\right\} \tag{6}$$

where β_i is defined in Eq. (3) and $\eta = r_i/r_f$.

The minimum speed at point i necessary to move a vehicle from point i to point f through a specified angle θ_R (or range R) is found by solving either of the following equations for γ_i:

$$dV_i^2/d\gamma_i = V_i\,dV_i/d\gamma_i = 0,$$

or equivalently

$$d\beta_i/d\gamma_i = 0 \tag{7}$$

where, in general, $V_i \neq 0$.

From Eqs. (6) and (7) it follows that the minimum velocity is applied at an angle γ_m given by the following expression:

$$\tan\gamma_m = -\frac{\eta-\cos\theta_R}{\sin\theta_R} \pm \sqrt{\left(\frac{\eta-\cos\theta_R}{\sin\theta_R}\right)^2 + 1} \tag{8}$$

An examination of derivatives of V_i of various orders with respect to γ_i shows that $V_i \to \infty$ when $d^nV_i/d\gamma_i^n \to \infty$ for any n. It is further seen that all the derivatives of V_i exist and are finite at all other values of γ_i.

However, not all solutions to Eq. (8) need represent physically realizable situations.

From Eq. (6) it is seen that the points at which $V_i \to \infty$ are given by:

$$\gamma_i = \pm 90° \qquad \text{and} \qquad \gamma_i = \arctan\left(\frac{\cos\theta_R - \eta}{\sin\theta_R}\right) \tag{9}$$

The physically impossible situation $V_i^2 < 0$ occurs for $\tan\gamma_i < (\cos\theta_R - \eta)/(\sin\theta_R)$.

It further follows from Eq. (6) that the plot of V_i^2 versus γ_i does not go through $V_i^2 = 0$. Therefore if a V_i, γ_i combination exists for the r_i, r_f, θ_R combination in question, then a minimum V_i also exists whose value is determined by solving Eq. (8).

Since the energy E (per unit mass) associated with a trajectory is given by

$$E = \frac{V_i^2}{2} - \frac{\lambda}{r_i} = \frac{V_f^2}{2} - \frac{\lambda}{r_f} = \text{const.}$$

where r_i is specified, minimizing V_i minimizes the energy—i.e., the trajectory chosen above is, in fact, the minimum-energy trajectory.

(C) *The In-Plane Transfer From Flight Condition to Point*

Consider a vehicle having a velocity of magnitude V_0 at an angle γ_0. It is desired to change impulsively the magnitude and direction of this velocity by adding an increment ΔV at an angle δ to the original velocity. The vector $\Delta\mathbf{V}$ is related to $\mathbf{V}_0$ and the resulting velocity $\mathbf{V}_i$ by the following equation (see Fig. 2):

$$(\Delta V)^2 = V_i^2 + V_0^2 - 2V_0V_i\cos(\gamma_i - \gamma_0) \tag{10}$$

$$\sin\delta = (V_i/\Delta V)\sin(\gamma_i - \gamma_0) = \sqrt{\beta_i/\Delta\beta}\,\sin(\gamma_i - \gamma_0)$$

$$\cos\delta = (1/\Delta V)[V_i\cos(\gamma_i - \gamma_0) - V_0] = \sqrt{\beta_i/\Delta\beta}\,\cos(\gamma_i - \gamma_0) - \sqrt{\beta_0/\Delta\beta} \tag{11}$$

where

$$\Delta\beta = (\Delta V)^2 r_i/\lambda$$

If a vehicle has a velocity $\mathbf{V}_0$ at the point i, then there is a nondenumerable set of values for the $\Delta\mathbf{V}$ necessary to move the vehicle to a point f in the original plane of motion. Substituting Eq. (6) into Eq. (10) gives ΔV as a function of γ_i as follows:

$$(\Delta V)^2 = \frac{\lambda(1-\cos\theta_R)}{\eta\cos\gamma_i[r_i\cos\gamma_i - r_f\cos(\theta_R+\gamma_i)]} + V_0^2 - 2V_0\cos(\gamma_i-\gamma_0)\sqrt{\frac{\lambda(1-\cos\theta_R)}{\eta\cos\gamma_i[r_i\cos\gamma_i - r_f\cos(\theta_R+\gamma_i)]}}$$

or

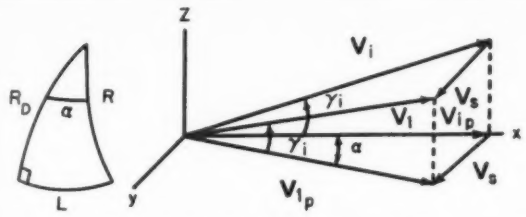

FIG. 3. (*left*). Spherical range triangle.
FIG. 4. (*right*). Three-dimensional velocity vector diagram.

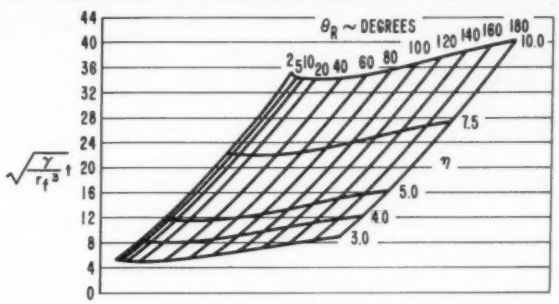

FIG. 8. Carpet of "dimensionless flight time" $\sqrt{\lambda/r_f^3}\,t$ vs. η and θ_R for a circular orbit.

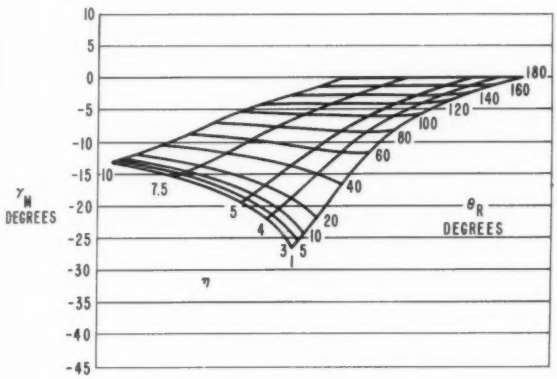

FIG. 5. Carpet of γ_m vs. η and θ_R for a circular orbit.

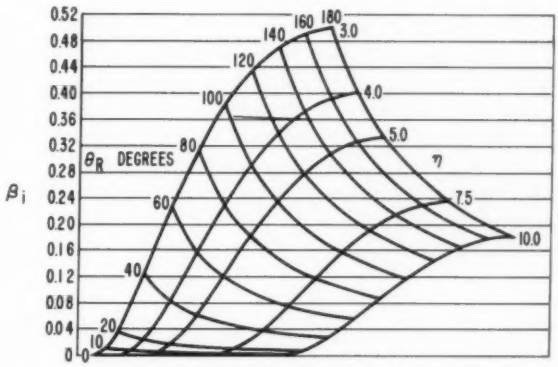

FIG. 9. Carpet of β_i vs. η and θ_R for a circular orbit.

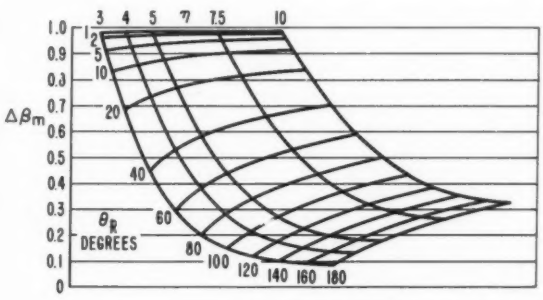

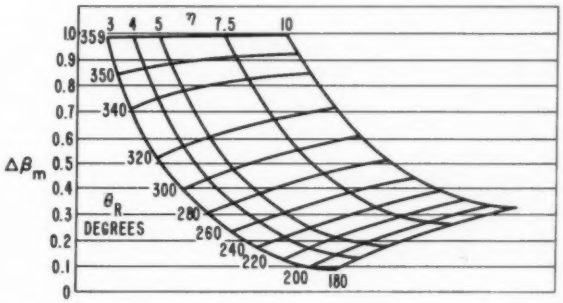

FIG. 6. (*left:* Part I; *right:* Part II). Carpet of minimum $\Delta\beta$ vs. η and θ_R for a circular orbit.

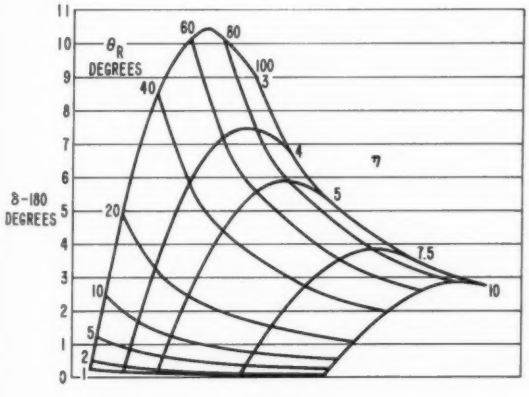

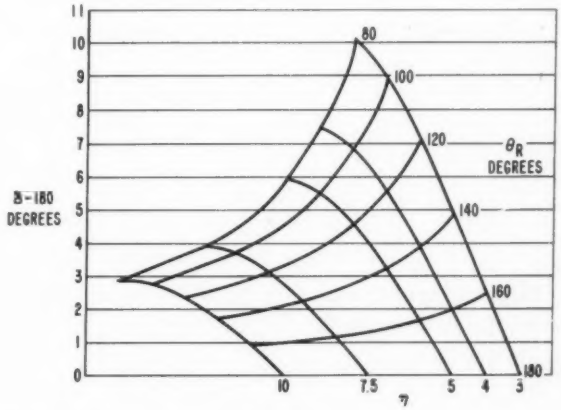

FIG. 7 (*left:* Part I; *right:* Part II). Carpet of δ vs. η and θ_R for a circular orbit.

$$\Delta\beta = \frac{1 - \cos\theta_R}{\cos\gamma_i[\eta\cos\gamma_i - \cos(\theta_R + \gamma_i)]} + \beta_0 - 2\cos(\gamma_i - \gamma_0)\sqrt{\frac{\beta_0(1 - \cos\theta_R)}{\cos\gamma_i[\eta\cos\gamma_i - \cos(\theta_R + \gamma_i)]}} \tag{12}$$

As before, the minimum ΔV is found by setting $d(\Delta V)^2/d\gamma_i = 0$ [see the discussion following Eq. (8)]. Furthermore, it is shown in reference 3 that minimizing ΔV results in minimizing the fuel expenditure when ΔV is added impulsively.

(D) *The General Three-Dimensional Problem*

In general, an initial velocity $\mathbf{V}_0$ will be specified along with the in-plane range R_D and the lateral range L. If $\theta_D \equiv R_D/r_0$, $\theta_L \equiv L/r_0$, where r_0 is the radius of the reference sphere, it then follows from spherical trigonometry that the total range R is given by the following expression:

$$\cos\theta_R = \cos(R/r_0) = \cos\theta_D\cos\theta_L \tag{13}$$

The angle α between the initial plane (the plane of $\mathbf{V}_0$) and the final plane (the plane of R) is given by (see Fig. 3):

$$\cot\alpha = \sin\theta_R\cot\theta_L \tag{14}$$

It is further noted that the range R can be achieved by obtaining range R in the $\mathbf{V}_0$ plane and then rotating the vector $\mathbf{V}_i$ such that its magnitude and angle with the local horizontal is unchanged. This is achieved by rotating the horizontal projection of $\mathbf{V}_i$ through an angle α (see Fig. 4).

In summary, the method is as follows. The proper V_i, γ_i, r_i, r_f combination is used in order to obtain a range R in the plane of $\mathbf{V}_i$. The plane of $\mathbf{V}_i$ is then rotated through an angle α by adding a velocity $\mathbf{V}_s$ to $\mathbf{V}_i$ in such a manner that the resultant velocity $\mathbf{V}_1$ has the same magnitude and γ as $\mathbf{V}_i$. Since $|\mathbf{V}_i|\sin\gamma_i = |\mathbf{V}_1|\sin\gamma_i = V_i\sin\gamma_i$, it follows that both ends of the vector $\mathbf{V}_s$ are equidistant from the horizontal plane—i.e., $\mathbf{V}_s$ is in the horizontal plane.

From simple trigonometric considerations, the magnitude of $\mathbf{V}_s$ is given by the following expression:

$$V_s = 2V_i\cos\gamma_i\sin(\alpha/2) \tag{15}$$

The total velocity increment $\Delta\mathbf{V}_T$ is the vector sum of $\Delta\mathbf{V}$ [see Eq. (10) and the preceding remarks] and $\mathbf{V}_s$, where, from the previous discussion, $\mathbf{V}_s$ lies in the local horizontal plane and $\Delta\mathbf{V}$ lies in the local vertical plane containing the vector $\mathbf{V}_0$.

Consider the following reference system. Let the x-axis be the intersection of the local horizontal and local vertical planes containing $\mathbf{V}_i$; the y-axis is the perpendicular to the x-axis in the horizontal plane (i.e., the perpendicular to the local vertical plane) and the z-axis is a line perpendicular to the above two axes (or the perpendicular to the local horizontal plane).

From the previous discussion, the x, y, z components of $\mathbf{V}_s$ and $\Delta\mathbf{V}$ are as follows (see Figs. 2 and 4):

$$\left.\begin{aligned} &\Delta V_x = \Delta V\cos(\pi - \delta - \gamma_0),\ \Delta V_y \equiv 0, \qquad \Delta V_z = \Delta V\sin(\pi - \delta - \gamma_0) \\ &V_{sx} = V_s\cos\frac{\pi - a}{2}, \qquad V_{sy} = V_s\sin\frac{\pi - \alpha}{2}, \qquad V_{sz} \equiv 0 \end{aligned}\right\} \tag{16}$$

The magnitude of the total velocity increment $\Delta\mathbf{V}_T$ is therefore given by the following expression:

$$\begin{aligned}(\Delta V_T)^2 = (V_{sx} + \Delta V_x)^2 + (\Delta V_z)^2 + (V_{sy})^2 = [V_s\sin(\alpha/2) + \Delta V\cos(\pi - \delta - \gamma_0)]^2 + \\ [\Delta V\sin(\pi - \delta - \gamma_0)]^2 + [V_s\cos(\alpha/2)]^2 = (\Delta V)^2 + V_s^2 + 2V_s\,\Delta V\sin(\alpha/2)\cos(\pi - \delta - \gamma_0)\end{aligned} \tag{17}$$

Substituting Eqs. (10), (11), and (15) into Eq. (17) yields the following result:

$$\left.\begin{aligned}(\Delta V_T)^2 &= V_0^2 + V_i^2 - 2V_0V_i\cos(\gamma_i - \gamma_0) + 4V_i^2\cos^2\gamma_i\sin^2(\alpha/2) + \\ &\qquad 4V_i\cos\gamma_i\sin^2(\alpha/2)[\Delta V\cos(\pi - \delta - \gamma_0)] \\ &= V_0^2 + V_i^2 - 2V_0V_i\cos(\gamma_i - \gamma_0) + 4V_i^2\cos^2\gamma_i\sin^2(\alpha/2) + \\ &\qquad 4V_i\cos\gamma_i\sin^2(\alpha/2)(V_0\cos\gamma_0 - V_i\cos\gamma_i) \\ &= V_0^2 + V_i^2 - 2V_0V_i(\cos\gamma_0\cos\alpha\cos\gamma_i + \sin\gamma_0\sin\gamma_i) \\ &\qquad \text{or } \Delta\beta_T = \beta_0 + \beta_i - 2\sqrt{\beta_0\beta_i}\,(\cos\gamma_0\cos\alpha\cos\gamma_i + \sin\gamma_0\sin\gamma_i)\end{aligned}\right\} \tag{18}$$

Substituting the value of V_i from Eq. (6) and setting $d(\Delta V_T)^2/d\gamma_i = 0$ gives the following equation for γ_m, the value of γ_i corresponding to the minimum ΔV_T:

$$\begin{aligned}\frac{2(\eta - \cos\theta_R)\tan\gamma_m - \sin\theta_R(1 - \tan^2\gamma_m)}{+\sqrt{\eta - \cos\theta_R + \sin\theta_R\tan\gamma_m}} \\ = +\sqrt{\beta_0/(1 - \cos\theta_R)}[2\sin\gamma_0(\eta - \cos\theta_R) - \cos\gamma_0\sin\theta_R\cos\alpha + \sin\gamma_0\sin\theta_R\tan\gamma_m]\end{aligned} \tag{19}$$

Squaring both sides of Eq. (19) yields the following equation in γ_m:

$$A_1 \tan^4 \gamma_m + A_2 \tan^3 \gamma_m + A_3 \tan^2 \gamma_m + A_4 \tan \gamma_m + A_5 = 0 \tag{20}$$

where

$$A_1 = \sin^2 \theta_R \qquad A_2 = [4(\eta - \cos \theta_R) - D \sin^2 \gamma_0 \sin^2 \theta_R] \sin \theta_R$$
$$A_3 = 4(\eta - \cos \theta_R)^2 - 2 \sin^2 \theta_R - D \sin \gamma_0 \sin^2 \theta_R[5 \sin \gamma_0(\eta - \cos \theta_R) - 2 \cos \gamma_0 \sin \theta_R \cos \alpha]$$
$$A_4 = D \sin \theta_R[\cos \gamma_0 \sin \theta_R \cos \alpha - 2 \sin \gamma_0(\eta - \cos \theta_R)][4 \sin \gamma_0(\eta - \cos \theta_R) - \cos \gamma_0 \sin \theta_R \cos \alpha] - 4 \sin \theta_R(\eta - \cos \theta_R)$$
$$A_5 = \sin^2 \theta_R - D(\eta - \cos \theta_R)[2 \sin \gamma_0(\eta - \cos \theta_R) - \cos \gamma_0 \sin \theta_R \cos \alpha]^2 \qquad D = \beta_0/(1 - \cos \theta_R)$$

Eq. (20) may be solved for $\tan \gamma_m$ in closed form. The method of solution, discovered by Ferrari, may be found in any standard text on the theory of equations (see, for example, reference 4, pp. 94–96). As in the previous sections, a study of the zeros and infinities of ΔV_T and the continuity of the derivatives of ΔV_T with respect to γ_f establishes that one of the solutions of Eq. (19) gives the minimum ΔV_T. [See the discussion following Eq. (8).]

The in-plane minimum (discussed in the previous section) is easily obtained by setting $\alpha = 0$. In general, the minimum ΔV_T (or $\Delta\beta_T$) is obtained by substituting the γ_m obtained into Eq. (18). The corresponding value of δ is found from Eqs. (10) and (11).

If time of transfer t is important, it might be desirable to use Eq. (18) to plot ΔV_T versus γ_f while a plot of transit time versus γ_f may be obtained from the following equations [see Eq. (3); references 2, 5, etc.]:

$$\sin \theta_f = -\beta_f \cos^2 \gamma_f \frac{\tan \gamma_f}{e} \qquad \cos \theta_f = \frac{1 - \beta_f \cos^2 \gamma_f}{e}$$

$$\frac{\sqrt{\lambda}}{r_f^{3/2}} t = \sqrt{\eta \beta_f} \frac{\cos \gamma_f}{2 - \beta_f} \left\{ \frac{e \sin (\theta_f + \theta_R)}{1 - e \cos (\theta_f + \theta_R)} - \frac{e \sin \theta_f}{1 - e \cos \theta_f} + \frac{2}{\sqrt{1 - e^2}} \left[\arctan \left(\sqrt{\frac{1 + e}{1 - e}} \tan \frac{\theta_f + \theta_R}{2} \right) - \arctan \left(\sqrt{\frac{1 + e}{1 - e}} \tan \frac{\theta_f}{2} \right) \right] \right\} \tag{21}$$

From geometric considerations and from the conservation of angular momentum, the impact variables may be found from the following equations:

$$\tan \gamma_f = \frac{-e \sin (\theta_f + \theta_R)}{1 - e \cos (\theta_f + \theta_R)} \qquad \beta_f = \frac{\eta \beta_f \cos^2 \gamma_f}{\cos^2 \gamma_f} \tag{22}$$

Although the above technique considers only the case of firing when $r = r_f$, the results may readily be modified to investigate the merits of firing at a later point in the original orbit. The values of ρ_0, e_0, and θ_0 corresponding to the given values of β_0, γ_0, and r_f are obtained from Eqs. (3) and (21), respectively. However, $\theta_\tau = \theta_0 + \theta_D$ where θ_τ is the in-plane range angle from apogee. Therefore, other points along the initial trajectory can be investigated by arbitrarily choosing various reference angles θ_0'. The corresponding value of $\theta_D' = |\theta_0' - \theta_\tau|$. Eq. (2) and the law of conservation of energy

$$E = \frac{(V_0')^2}{2} - \frac{\lambda}{r_f'} = \frac{V_0^2}{2} - \frac{\lambda}{r_f} = \text{const.}$$

can then be used to obtain new values of V_0 and γ_0. The lateral range L obviously remains constant. The above technique can then be utilized for various values of θ_0' and an appropriate firing point can be obtained.

(E) *Transfer From a Circular Orbit to a Point in the Orbital Plane*

An interesting special case of the analysis of the previous section is the transfer from a circular orbit to a point in the plane of the circular orbit. For this case, Eqs. (11), (12), (19), and (20), reduce, respectively, to:

$$\left.\begin{aligned} &\sin \delta = \sqrt{\beta_f/\Delta\beta} \sin \gamma_m; \qquad \cos \delta = \sqrt{1/\Delta\beta}[\sqrt{\beta_f} \cos \gamma_m - 1] \\ &\Delta\beta = \frac{1 - \cos \theta_R}{\cos \gamma_m[\eta \cos \gamma_m - \cos (\theta_R + \gamma_m)]} + 1 - 2 \cos \gamma_m \sqrt{\frac{1 - \cos \theta_R}{\cos \gamma_m[\eta \cos \gamma_m - \cos (\theta_R + \gamma_m)]}} \\ &\frac{2(\eta - \cos \theta_R) \tan \gamma_m - \sin \theta_R(1 - \tan^2 \gamma_m)}{+ \sqrt{\eta - \cos \theta_R + \sin \theta_R \tan \gamma_m}} = -\sqrt{1 + \cos \theta_R} \\ &A_1 \tan^4 \gamma_m + A_2 \tan^3 \gamma_m + A_3 \tan^2 \gamma_m + A_4 \tan \gamma_m + A_5 = 0 \end{aligned}\right\} \tag{23}$$

where $A_1 = \sin^2 \theta_R \qquad A_2 = 4 \sin \theta_R(\eta - \cos \theta_R)$

$$A_3 = 4(\eta - \cos\theta_R)^2 - 2\sin^2\theta_R \qquad A_4 = -\sin\theta_R[4(\eta - \cos\theta_R) + \sin\theta_R(1 + \cos\theta_R)]$$

$$A_5 = \sin^2\theta_R\left[1 - \frac{\eta - \cos\theta_R}{1 - \cos\theta_R}\right]$$

It is noted that γ_m, $\Delta\beta$ minimum, δ, $(\sqrt{\lambda}/r_f^{3/2})t$, β_i, β_f, and γ_f are all functions of only η and θ_R. Therefore the solution to the problem of the present section can be summarized in graphical form. Figs. 5 through 11 are carpets of the above variables versus η and θ_R. All the carpets exhibit values for $\theta_R \leq 180°$, and Fig. 6 is extended to values of $\theta_R > 180°$ in order to illustrate that the minimum value of $\Delta\beta_m$ apparently occurs for $\theta_R = 180°$, i.e., for a Hohmann transfer.

PART II

The Error Derivatives

(A) *The In-Plane Problem*

In the previous sections a method was developed for obtaining all V_i, γ_i combinations for a given total range R where r_i and r_f are fixed [see Eq. (6)]. Since r_i, r_f, and R are specified, and V_i is a function of γ_i, the error derivatives

$$\frac{\partial R}{\partial r_i}, \frac{\partial R}{\partial V_i}, \frac{\partial R}{\partial \gamma_i}, \frac{\partial t}{\partial r_i}, \frac{\partial t}{\partial V_i}, \text{ and } \frac{\partial t}{\partial \gamma_i}$$

[where t is given by Eq. (21)] can also be obtained as functions of γ_i alone.

Let F denote a general function of V_i, r_i, r_f, and γ_i (which may be taken to be either R or t). The resulting error derivatives $\partial F/\partial r_i$, $\partial F/\partial V_i$, and $\partial F/\partial\gamma_i$ (r_f is treated as a constant throughout Part II) are assumed to be known (see reference 6 for the method of evaluating $\partial R/\partial V_i$, $\partial t/\partial V_i$, etc.).

Since the velocity increment $\Delta\mathbf{V}_T$ and not the resulting velocity $\mathbf{V}_i$ is supplied by the vehicle's propulsive system, a transformation of variables from V_i, r_i, γ_i to ΔV_T, $\bar{r}_i$, α, δ will be performed. This transformation will give the error derivatives with respect to the controlled variables.

Consider first the in-plane case. The transformation from V_i, r_i, γ_i to ΔV, $\bar{r}_i$, δ is given by Eqs. (10), (11), and the following equation:

$$\bar{r}_i = r_i \tag{24}$$

For a given initial orbit, $V_0 = f(r_i)$, $\gamma_0 = g(r_i)$, $dV_0/dr_i = f'$, $d\gamma_0/dr_i = g'$. It therefore follows that:

$$\left.\begin{aligned}
&\frac{\partial\Delta V}{\partial V_i} = \frac{V_i - V_0\cos(\gamma_i - \gamma_0)}{\Delta V} \qquad \frac{\partial\delta}{\partial V_i} = \frac{V_i\sin^2(\gamma_i - \gamma_0)}{(\Delta V)^2\sin\delta\cos\delta}\left[1 - \frac{V_i\{V_i - V_0\cos(\gamma_i - \gamma_0)\}}{(\Delta V)^2}\right]\\
&\frac{\partial\bar{r}_i}{\partial V_i} \equiv \frac{\partial\bar{r}_i}{\partial\delta} \equiv 0 \qquad \frac{\partial\Delta V}{\partial\gamma_i} = \frac{V_iV_0\sin(\gamma_i - \gamma_0)}{\Delta V}\\
&\frac{\partial\delta}{\partial\gamma_i} = \frac{V_i^2\sin(\gamma_i - \gamma_0)}{(\Delta V)^2\sin\delta\cos\delta}\left[\cos(\gamma_i - \gamma_0) - \frac{V_iV_0\sin^2(\gamma_i - \gamma_0)}{(\Delta V)^2}\right]\\
&\frac{\partial\Delta V}{\partial r_i} = \frac{[V_0 - V_i\cos(\gamma_i - \gamma_0)]f' - V_iV_0\sin(\gamma_i - \gamma_0)g'}{\Delta V}\\
&\frac{\partial\delta}{\partial r_i} = \frac{V_i\sin(\gamma_i - \gamma_0)}{(\Delta V)^2\sin\delta\cos\delta}\left[\frac{\{V_i\cos(\gamma_i - \gamma_0) - V_0\}\sin(\gamma_i - \gamma_0)f'}{(\Delta V)^2} + V_i\left\{\cos(\gamma_i - \gamma_0) + \frac{V_0\sin^2(\gamma_i - \gamma_0)}{(\Delta V)^2}\right\}g'\right]\\
&\partial\bar{r}_i/\partial r_i = d\bar{r}_i/dr_i = 1
\end{aligned}\right\} \tag{25}$$

Since

$$d\Delta V = (\partial\Delta V/\partial V_i)\,dV_i + (\partial\Delta V/\partial\gamma_i)\,d\gamma_i + (\partial\Delta V/\partial r_i)\,dr_i$$

$$d\delta = (\partial\delta/\partial V_i)\,dV_i + (\partial\delta/\partial\gamma_i)\,d\gamma_i + (\partial\delta/\partial r_i)\,dr_i, \text{ etc.}$$

it follows that

$$\frac{\partial F}{\partial q_i} = \frac{\partial F}{\partial\Delta V}\frac{\partial\Delta V}{\partial q_i} + \frac{\partial F}{\partial\delta}\frac{\partial\delta}{\partial q_i} + \frac{\partial F}{\partial\bar{r}_i}\frac{\partial\bar{r}_i}{\partial q_i} \tag{26}$$

where $q_i = V_i$, γ_i or r_i. The three equations in (26) can be solved for $\partial F/\partial\Delta V$, $\partial F/\partial\delta$ and $\partial F/\partial\bar{r}_i$ to yield the following expressions:

$$\left.\begin{aligned} \frac{\partial F}{\partial \Delta V} &= \frac{\begin{vmatrix} \frac{\partial F}{\partial V_t} & \frac{\partial \delta}{\partial V_t} \\ \frac{\partial F}{\partial \gamma_t} & \frac{\partial \delta}{\partial \gamma_t} \end{vmatrix}}{D} \qquad \frac{\partial F}{\partial \delta} = \frac{\begin{vmatrix} \frac{\partial \Delta V}{\partial V_t} & \frac{\partial F}{\partial V_t} \\ \frac{\partial \Delta V}{\partial \gamma_t} & \frac{\partial F}{\partial \gamma_t} \end{vmatrix}}{D} \\ \frac{\partial F}{\partial \bar{r}_t} &\equiv \left.\frac{\partial F}{\partial r_t}\right|_{\substack{\Delta V = \text{const.} \\ \delta = \text{const.}}} = \frac{\partial F}{\partial r_t} - \frac{\partial F}{\partial \Delta V}\frac{\partial \Delta V}{\partial r_t} - \frac{\partial F}{\partial \delta}\frac{\partial \delta}{\partial r_t} \end{aligned}\right\} \tag{27}$$

where $\dfrac{\partial F}{\partial r_t} = \left.\dfrac{\partial F}{\partial r_t}\right|_{\substack{V_t = \text{const.} \\ \gamma_t = \text{const.}}}$ and $D = \left|\dfrac{\partial(\Delta V, \delta, \bar{r}_t)}{\partial(V_t, \gamma_t, r_t)}\right|$

is the Jacobian determinant associated with the transformation in question.

From Eq. (25) and the elementary properties of determinants (reference 7, pp. 300–306, and reference 8, pp. 22–26) it is seen that the above determinant D is equal to the Jacobian determinant associated with the transformation from V_t, γ_t to $\Delta V, \delta$. Its value is given by the following expression:

$$D = \left|\frac{\partial(\Delta V, \delta, \bar{r}_t)}{\partial(V_t, \gamma_t, r_t)}\right| = \left|\frac{\partial(\Delta V, \delta)}{\partial(V_t, \gamma_t)}\right| = \begin{vmatrix} \frac{\partial \Delta V}{\partial V_t} & \frac{\partial \delta}{\partial V_t} \\ \frac{\partial \Delta V}{\partial \gamma_t} & \frac{\partial \delta}{\partial \gamma_t} \end{vmatrix}$$

$$= \frac{V_t^2 \sin(\gamma_t - \gamma_0)}{(\Delta V)^3 \sin\delta\cos\delta}\left[V_t\cos(\gamma_t - \gamma_0) - V_0\right] = \frac{V_t^2 \sin(\gamma_t - \gamma_0)}{\Delta V \sin\delta} \tag{28}$$

Evidently [see Eq. (27)] singular points occur when the Jacobian determinant $D = 0$ or ∞ as is well known from transformation theory (see references 9, 10, etc.). From Eq. (28), if ΔV and V_t are assumed finite, singular points occur only when

$$\Delta V = 0, \; V_t = 0, \; \gamma_t = \gamma_0 \qquad \text{or} \qquad \delta = 0^\circ \quad \text{or} \quad 180^\circ$$

(*B*) *The General Problem*

A similar analysis will now be presented for the general three-dimensional case where, as before, $V_0 = f(r_t)$, $\gamma_0 = g(r_t)$. From Eq. (15),

$$\partial F/\partial V_s = (\partial F/\partial V_t)(\partial V_t/\partial V_s), \; \partial F/\partial\alpha = (\partial F/\partial V_t)(\partial V_t/\partial\alpha) \tag{29}$$

where $\partial V_t/\partial V_s = [2\cos\gamma_t \sin(\alpha/2)]^{-1}$

and $$\partial V_t/\partial\alpha = -(V_s/4)\sec\gamma_t \operatorname{ctn}(\alpha/2)\csc(\alpha/2) = (V_t/2)\operatorname{ctn}(\alpha/2)$$

Similarly:

$$\frac{\partial F}{\partial \tilde{\gamma}_t} = \left.\frac{\partial F}{\partial \gamma_t}\right|_{\substack{V_s = \text{const.} \\ \alpha = \text{const.}}} = \frac{\partial F}{\partial \gamma_t} + \frac{\partial F}{\partial V_t}\frac{\partial V_t}{\partial_t \gamma} = \frac{\partial F}{\partial_t \gamma} + \frac{V_s}{2}\csc\frac{\alpha}{2}\tan\gamma_t\sec\gamma_t\frac{\partial F}{\partial V_t}$$

$$= \frac{\partial F}{\partial \gamma_t} + V_t\tan\gamma_t\frac{\partial F}{\partial V_t} \tag{30}$$

In a manner analagous to that of the previous section, the derivatives $\partial F/\partial V_s$, $\partial F/\partial\alpha$, $\partial F/\partial\tilde{\gamma}_t$, $\partial F/\partial r_t$ are transformed into $\partial F/\partial\Delta V_T$, $\partial F/\partial\bar{\alpha}$, $\partial F/\partial\delta$, $\partial F/\partial\bar{r}_t$, where $\bar{\alpha} = \alpha$ and $\bar{r}_t = r_t$.
It is easily shown that:

$$\left.\begin{aligned} \frac{\partial F}{\partial \Delta V_T} &= \frac{\begin{vmatrix} \frac{\partial F}{\partial V_s} & \frac{\partial \delta}{\partial V_s} \\ \frac{\partial F}{\partial \tilde{\gamma}_t} & \frac{\partial \delta}{\partial \tilde{\gamma}_t} \end{vmatrix}}{J}; \qquad \frac{\partial F}{\partial \delta} = \frac{\begin{vmatrix} \frac{\partial \Delta V_T}{\partial V_s} & \frac{\partial F}{\partial V_s} \\ \frac{\partial \Delta V_T}{\partial \tilde{\gamma}_t} & \frac{\partial F}{\partial \tilde{\gamma}_t} \end{vmatrix}}{J} \\ \frac{\partial F}{\partial \bar{\alpha}} &= \frac{\partial F}{\partial \alpha} - \frac{\partial F}{\partial \Delta V_T}\frac{\partial \Delta V_T}{\partial \alpha} - \frac{\partial F}{\partial \delta}\frac{\partial \delta}{\partial \alpha}, \qquad \frac{\partial F}{\partial \bar{r}_t} = \frac{\partial F}{\partial r_t} - \frac{\partial F}{\partial \Delta V_T}\frac{\partial \Delta V_T}{\partial r_t} - \frac{\partial F}{\partial \delta}\frac{\partial \delta}{\partial r_t} \end{aligned}\right\} \tag{31}$$

where $$J = \begin{vmatrix} \dfrac{\partial \Delta V_T}{\partial V_s} & \dfrac{\partial \delta}{\partial V_s} \\ \dfrac{\partial \Delta V_T}{\partial \tilde{\gamma}_i} & \dfrac{\partial \delta}{\partial \tilde{\gamma}_i} \end{vmatrix}$$

The coefficients can be evaluated with the aid of Eqs. (10), (11), (15) and (18). They are given by the following expressions:

$$\left.\begin{aligned}
\frac{\partial \Delta V_T}{\partial V_s} &= \frac{V_i \sec \gamma_i - V_0(\tan \gamma_i \sin \gamma_0 + \cos \gamma_0 \cos \alpha)}{2\Delta V_T} \csc \frac{\alpha}{2} \\
\frac{\partial \Delta V_T}{\partial \tilde{\gamma}_i} &= \frac{V_i(V_i \tan \gamma_i - V_0 \sec \gamma_i \sin \gamma_0)}{\Delta V_T} \\
\frac{\partial \Delta V_T}{\partial \alpha} &= \frac{1}{2\Delta V_T}\left[V_i V_0 \operatorname{ctn} \frac{\alpha}{2}\left\{\cos(\gamma_i - \gamma_0) + 2\cos\gamma_i \cos\gamma_0 \sin^2\frac{\alpha}{2}\right\} - V_i^2 \operatorname{ctn}\frac{\alpha}{2}\right] \\
\frac{\partial \Delta V_T}{\partial r_i} &= \frac{1}{\Delta V_T}\left[\{V_0 - V_i(\cos\gamma_i \cos\gamma_0 \cos\alpha + \sin\gamma_i \sin\gamma_0)\}f' + \right. \\
&\qquad \left. V_i V_0(\cos\gamma_i \sin\gamma_0 \cos\alpha - \sin\gamma_i \cos\gamma_0)g'\right] \\
\frac{\partial \delta}{\partial V_s} &= \frac{V_i V_0 \sin^2(\gamma_i - \gamma_0)\sec\gamma_i}{2(\Delta V)^4 \sin\delta\cos\delta}[V_0 - V_i\cos(\gamma_i - \gamma_0)]\csc\frac{\alpha}{2} = -\frac{V_i V_0 \sin^2(\gamma_i - \gamma_0)\sec\gamma_i}{2(\Delta V)^3 \sin\delta}\csc\frac{\alpha}{2} \\
\frac{\partial \delta}{\partial \tilde{\gamma}_i} &= \frac{V_i^2 \sin(\gamma_i - \gamma_0)}{(\Delta V)^2 \sin\delta\cos\delta}\left[\cos(\gamma_i - \gamma_0) + \frac{V_0 \sin(\gamma_i - \gamma_0)}{(\Delta V)^2} \times \right. \\
&\qquad \left. \{V_0 \tan\gamma_i - V_i \sin(\gamma_i - \gamma_c) - V_i \tan\gamma_i \cos(\gamma_i - \gamma_0)\}\right] \\
\frac{\partial \delta}{\partial \alpha} &= \frac{V_i^2 V_0 \sin^2(\gamma_i - \gamma_0)}{2(\Delta V)^4 \sin\delta\cos\delta}[V_i\cos(\gamma_i - \gamma_0) - V_0]\operatorname{ctn}\frac{\alpha}{2} = +\frac{V_i^2 V_0 \sin^2(\gamma_i - \gamma_0)}{2(\Delta V)^4 \sin\delta}\operatorname{ctn}\frac{\alpha}{2} \\
\frac{\partial \delta}{\partial r_i} &= \frac{V_i^2 \sin(\gamma_i - \gamma_0)g'}{(\Delta V)^2 \sin\delta\cos\delta}\left[\frac{V_i V_0}{(\Delta V)^2}\sin^2(\gamma_i - \gamma_0) - \cos(\gamma_i - \gamma_0)\right] - \\
&\qquad \frac{V_i^2 \sin^2(\gamma_i - \gamma_0)f'[V_0 - V_i\cos(\gamma_i - \gamma_0)]}{(\Delta V)^4 \sin\delta\cos\delta} \\
&\partial\bar{\alpha}/\partial V_s \equiv \partial\bar{\alpha}/\partial\tilde{\gamma}_i \equiv \partial\bar{\alpha}/\partial r_i \equiv 0; \qquad \partial\bar{\alpha}/\partial\alpha = d\bar{\alpha}/d\alpha = 1 \\
&\partial\bar{r}_i/\partial V_s \equiv \partial\bar{r}_i/\partial\tilde{\gamma}_i \equiv \partial\bar{r}_i/\partial\alpha \equiv 0; \qquad \partial\bar{r}_i/\partial r_i = d\bar{r}_i/dr_i = 1
\end{aligned}\right\} \quad (32)$$

The Jacobian determinant associated with the transformation in question is given by the following expression (see reference 9, pp. 142–146):

$$J = \begin{vmatrix} \dfrac{\partial \Delta V_T}{\partial V_s} & \dfrac{\partial \delta}{\partial V_s} & \dfrac{\partial \bar{\alpha}}{\partial V_s} & \dfrac{\partial \bar{r}_i}{\partial V_s} \\ \dfrac{\partial \Delta V_T}{\partial \tilde{\gamma}_i} & \dfrac{\partial \delta}{\partial \tilde{\gamma}_i} & \dfrac{\partial \bar{\alpha}}{\partial \tilde{\gamma}_i} & \dfrac{\partial \bar{r}_i}{\partial \tilde{\gamma}_i} \\ \dfrac{\partial \Delta V_T}{\partial \alpha} & \dfrac{\partial \delta}{\partial \alpha} & \dfrac{\partial \bar{\alpha}}{\partial \alpha} & \dfrac{\partial \bar{r}_i}{\partial \alpha} \\ \dfrac{\partial \Delta V_T}{\partial r_i} & \dfrac{\partial \delta}{\partial r_i} & \dfrac{\partial \bar{\alpha}}{\partial r_i} & \dfrac{\partial \bar{r}_i}{\partial r_i} \end{vmatrix} = \begin{vmatrix} \dfrac{\partial \Delta V_T}{\partial V_s} & \dfrac{\partial \delta}{\partial V_s} & 0 & 0 \\ \dfrac{\partial \Delta V_T}{\partial \tilde{\gamma}_i} & \dfrac{\partial \delta}{\partial \tilde{\gamma}_i} & 0 & 0 \\ \dfrac{\partial \Delta V_T}{\partial \alpha} & \dfrac{\partial \delta}{\partial \alpha} & 1 & 0 \\ \dfrac{\partial \Delta V_T}{\partial r_i} & \dfrac{\partial \delta}{\partial r_i} & 0 & 1 \end{vmatrix} = \begin{vmatrix} \dfrac{\partial \Delta V_T}{\partial V_s} & \dfrac{\partial \delta}{\partial V_s} \\ \dfrac{\partial \Delta V_T}{\partial \tilde{\gamma}_i} & \dfrac{\partial \delta}{\partial \tilde{\gamma}_i} \end{vmatrix} \quad (33)$$

i.e., the Jacobian determinant associated with the transformation

$$\{V_s, \tilde{\gamma}_i, \alpha, r_i\} \rightarrow \{\Delta V_T, \delta, \bar{\alpha}, \bar{r}_i\}$$

is equal to the Jacobian determinant associated with the transformation

$$\{V_s, \tilde{\gamma}_i\} \rightarrow \{\Delta V_T, \delta\}$$

A comparison of Eqs. (31) and (33) shows that the method employed above breaks down at the singular points $J = 0$ and $J = \infty$.

The method of extending the above analysis to obtain either $\partial R_D/\partial V_s$, $\partial L/\partial V_s$, etc., [see Eq. (13)] or the derivatives of R, R_D, or L with respect to another

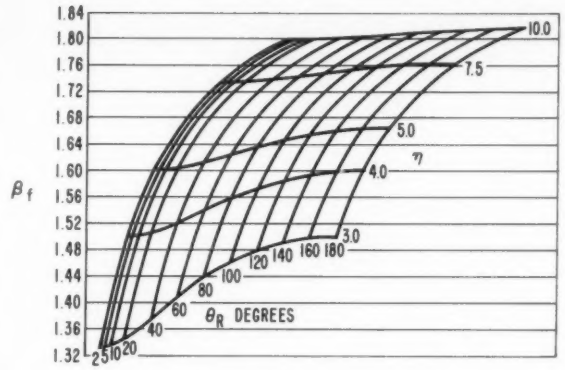

FIG. 10. Carpet of β_f vs. η and θ_R for a circular orbit.

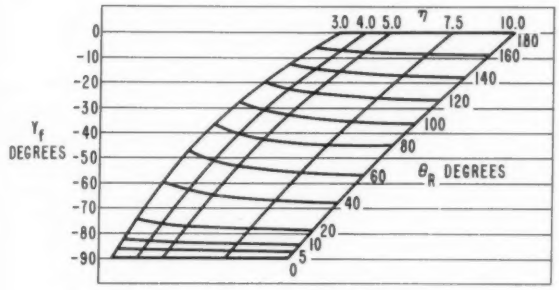

FIG. 11. Carpet of γ_f vs. η and θ_R for a circular orbit.

set of variables is straightforward. Furthermore, it is difficult to anticipate which variables will be important in a given problem. Any extensions of the above theory will therefore be left to the reader.

FINAL REMARKS

In Part I a method was developed for obtaining the minimum impulse (which results in the minimum fuel expenditure) necessary to move a vehicle from an initial flight condition to a stationary point target. The method requires the solution of a single quartic equation. Other possible modes of transfer may also be investigated by the methods developed in Part I. In each case the corresponding values of flight time and impact variables (final flight-path angle and velocity) are obtained.

Part II dealt with the evaluation of the error derivatives corresponding to any chosen transfer orbit. The resulting error derivatives are of importance in correlating initial instrumentation errors with miss distances at the target. For a given design problem a trade-off between permissible fuel expenditure, flight time, allowable errors, etc., would have to be made with the use of the results of both of the above sections.

References

[1] Becker, R. A., *Introduction to Theoretical Mechanics*, McGraw-Hill Book Company, Inc., New York, 1954.

[2] Adler, A. A., *Introduction to Trajectory Mechanics*, Bell Aircraft Research Note 101, September, 1957.

[3] Lawden, D. F., *Orbital Transfer via Tangential Ellipses*, J. British Interplanetary Soc., Vol. 11, November, 1956.

[4] Uspensky, V. J., *Theory of Equations*, 1st Ed., McGraw-Hill Book Company, Inc., New York, 1948.

[5] Ramsey, A. S., *Dynamics* (Part II), Cambridge University Press, 1957.

[6] Roth, H. L., *Equations and Charts for the Evaluation of the Error Derivatives and Time of Flight of a Ballistic Vehicle*, Bell Aircraft Research Note 108, October, 1959.

[7] Birkhoff, G. and MacLaine, S., *A Survey of Modern Algebra*, Revised Ed., Macmillan Company, New York, 1954.

[8] Bocher, M., *Introduction to Higher Algebra*, Macmillan Company, New York, 1957.

[9] Courant, R., *Differential and Integral Calculus*, Vol. II, Interscience Publishers, Inc., New York, 1947.

[10] Fine, H. B., *Calculus*, Macmillan Company, New York, 1950.

✦ ✦ ✦

Velocity and Range Considerations

Continued from page 684

(assuming an infinitesimally small attracting body). For a range of intercept angles extending to 90 degrees, there is a range of range angles which cannot be attained.

References

[1] Chapman, D. R., *An Approximate Method for Studying Entry Into Planetary Atmospheres*, NACA TN4276, May, 1958.

[2] Lees, L., Hartwig, F. W., and Cohen, C. B., *Use of Aerodynamic Lift During Re-entry into the Earth's Atmosphere*, J. Am. Rocket Soc., Sept., 1959.

Change of Address

It is important that the Institute be notified of changes in address 30 days in advance of publishing date to ensure receipt of every issue of the JOURNAL and AERO/SPACE ENGINEERING. Notices should be sent directly to:

Institute of the Aerospace Sciences, Inc.
2 East 64th Street, New York 22, N.Y.

A Theory of Ring-Stiffened Cylinders†

R. J. DUFFIN*
Duke University

(1) Introduction

RING-STIFFENED cylinders are of widespread use in present-day engineering practice. For example, the fuselage of an airplane is essentially a thin-walled cylinder reinforced with uniformly spaced rings. The body of a rocket may be characterized in the same way. Thus the following problem is of importance in the design of such structures. *What are the distributed stresses when a concentrated load is applied to a ring?* This paper shows how to obtain ordinary differential equations which determine these distributed stresses.

The first attempt at the solution of the stress problem was based on the assumption that the fuselage system could be treated as a simple beam. For example, see the paper of J. A. Wise.[1] Experiment showed, however, that such a beam analysis must be rather far from the truth. A more accurate analysis was given by Wignot, Combs, and Ensrud.[2] They took account of the interaction between the ring and the cylindrical shell and obtained a differential equation. Unfortunately, their analysis is not complete. This was pointed out by Kuhn, Duberg, and Griffith[3] in a paper comparing theory and experiment.

A significant advance was made by N. J. Hoff and coworkers at Brooklyn Polytechnic Institute.[4, 5, 6] The method of Hoff is to express the stress in the cylinder and in the ring as Fourier series in the angle. Then the total strain energy is calculated as a function of the Fourier coefficients. According to the variational principle of Castigliano the equilibrium state is determined by minimizing the strain energy. This minimization process leads Hoff to an infinite set of simultaneous linear equations for the Fourier coefficients. Fortunately it proves possible to solve these equations by a step-by-step process. The stresses are then found by summing a sufficient number of terms of the Fourier series. The Hoff analysis is found to give good agreement with experiment.[5]

In a previous note the writer followed the basic assumptions of the Hoff treatment, but Fourier series were not employed.[7] Instead, classical methods of the calculus of variations were used to obtain the Euler differential equation. The Euler equation is an eighth order ordinary differential equation with constant coefficients.** The independent variable is the angle, and the dependent variable is the bending moment in the ring. The Fourier series method is then seen to be merely a special way of solving the Euler differential equation.

An advantage of the differential equation approach to the problem is greater flexibility; thus there is no difficulty in taking into account a stiffening ring having variable cross section. The only difference in this case is that one of the coefficients of the differential equation becomes variable rather than constant. The solution of the differential equation can then be obtained by use of digital or analog computers.

In Hoff's treatment it is supposed that the applied forces lie in the plane of the ring. In a recent report, J. Adachi was concerned with the stress problem of the ring-stiffened cylinder when the applied forces are perpendicular to the plane of the ring.[8] Adachi idealized the problem by supposing that it was sufficient to consider an end-stiffened flat sheet. He indicates the desirability of having a theory avoiding this idealization.

In this paper a general approach is developed which permits the applied force to have an arbitrary direction. Also the assumptions on the properties of the ring are relaxed. Thus in the Hoff treatment only flexure in the plane of the ring was taken into account. It was assumed that the ring was perfectly flexible perpendicular to its plane. In the present theory account is taken of flexure perpendicular to the plane and torsion as well as flexure in the plane.

The theory is again based on Castigliano's principle. The strain energy is taken to consist of five separate terms resulting from shear stress τ in the cylinder, normal stress σ parallel to the axis of the cylinder, bending moment L perpendicular to the plane of the ring, torsional moment M of the ring, and bending moment N in the plane of the ring. The Euler equations resulting may be written as two ordinary differential equations of the seventh order relating the moments M and N.

(2) A Cantilever Beam

In order to be definite, this paper treats the specific problem of a cantilever beam. The beam consists of a

Received June 6, 1960. Revised and received October 24, 1960.

† Prepared under Contract No. DA-31-124-ORD-10, Office of Ordnance Research, U.S. Army, September 9, 1959.

* Professor, Department of Mathematics, Carnegie Institute of Technology.

The writer is indebted to George J. Detko of the Army Ballistic Missile Agency for suggesting this investigation.

** The referee has pointed out that this eighth order differential equation had previously been derived by George E. Griffith in NACA Technical Note 2512, October 1951, "Stresses in a Two-Bay Noncircular Cylinder Under Transverse Loads." It is of interest to note that Griffith does not use variational methods in his derivation.

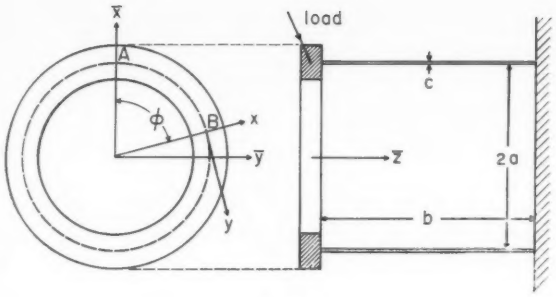

FIG. 1.

thin, cylindrical shell of radius a, length b, and thickness c. A reinforcing ring is attached to one end of the cylinder, and the other end of the cylinder is built into a wall, as shown in Fig. 1. The center of the ring is taken as the origin of coordinates $\bar{x}$, $\bar{y}$, $\bar{z}$. The $\bar{z}$ axis is taken along the axis of the cylinder. A concentrated load is applied to the top of the ring at point A on the positive $\bar{x}$ axis. The $\bar{x}$, $\bar{y}$, and $\bar{z}$ components of the load force will be denoted by X_1, Y_1, Z_1. The concentrated load also has a couple, and the $\bar{x}$, $\bar{y}$, and $\bar{z}$ components of this couple are denoted by L_1, M_1, and N_1.

The angle ϕ measures rotation in the positive direction about the $\bar{z}$ axis. The initial side of the angle is taken to be the positive $\bar{x}$ axis. The terminal side of the angle ϕ intersects the centroidal circle of the ring at B. The point B is taken as origin of a rotated coordinate system x, y, z. The x axis is along the terminal side of the angle ϕ. The z axis is parallel to the $\bar{z}$ axis.

The entire ring will now be thought of as a free body. Then the conditions for equilibrium are expressed by the following six equations:

$$aX_1 = +\int_0^{2\pi} T \sin\phi \, d\phi \tag{1a}$$

$$aY_1 = -\int_0^{2\pi} T \cos\phi \, d\phi \tag{1b}$$

$$aZ_1 = -\int_0^{2\pi} S \, d\phi \tag{1c}$$

$$L_1 = -\int_0^{2\pi} S \sin\phi \, d\phi \tag{2a}$$

$$M_1 = -\int_0^{2\pi} S(1 - \cos\phi) \, d\phi \tag{2b}$$

$$N_1 = -\int_0^{2\pi} T(1 - \cos\phi) \, d\phi \tag{2c}$$

Here S/a^2 is the force on unit length of the ring acting in the z direction. Likewise T/a^2 is the force on unit length of the ring acting in the y direction. Of course S results from a normal stress σ_z in the cylinder, and T results from a shearing stress τ in the cylinder. S and T have been defined to have dimensions of moment of force in order to simplify the writing of some of the equations to follow.

There will also be a force R/a^2 on unit length of the ring acting in the x direction. Following Hoff we assume that R is negligible for thin cylinders, so R is omitted in Eqs. (1) and (2).

In order to avoid unessential complications, the following three minor restrictions are made: (a) The principal axes of inertia of the ring are to coincide with the x and z axes. However, the ring does not have to have a rectangular cross section as shown in Fig. 1. (b) The line of action of the force S is to go through the centroidal circle. This will be true if the radius of the centroidal circle of the ring is the same as the radius of the cylinder. (c) The line of action of T is tangent to the centroidal circle. This will be sensibly true if the z thickness of the ring is small compared to its radius.

(3) Stress in the Ring

To consider flexural and torsional stress in the ring, it is useful to regard the portion AB of the ring subtended by the angle ϕ as a free body. Such a free body is diagrammed in Fig. 2. Acting on the cut at B there will be forces X, Y, Z in the x, y, z directions, and there will be couples L, M, N in the x, y, z directions. Of course L is the bending moment perpendicular to the plane of the ring, M is the torsional moment, and N is the bending moment in the plane of the ring. These quantities are functions of the angle ϕ. For $\phi = 0+$, we designate these quantities as X_0, Y_0, Z_0, L_0, M_0, N_0. Taking moments at the point B in the x, y, z directions yields the following three equations of equilibrium:

$$L = L_0 \cos\phi + M_0 \sin\phi - aZ_0 \sin\phi + \int_0^{\phi} S \sin\theta \, d\xi \tag{3}$$

$$M = M_0 \cos\phi - L_0 \sin\phi + aZ_0(1 - \cos\phi) - \int_0^{\phi} S(1 - \cos\theta) \, d\xi \tag{4}$$

$$N = N_0 + aX_0 \sin\phi + aY_0(1 - \cos\phi) - \int_0^{\phi} T(1 - \cos\theta) \, d\xi \tag{5}$$

Here $\theta = \phi - \xi$

It is desirable to write relations (3), (4), and (5) as differential equations rather than integral equations. To do this the following derivative formulas will be employed:

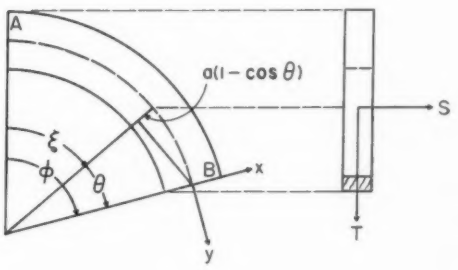

FIG. 2.

$$F = \int_0^\phi S(1 - \cos\theta)\, d\xi, \quad F' = \int_0^\phi S \sin\theta\, d\xi$$

$$F'' = \int_0^\phi S\cos\theta\, d\xi, \quad F''' = S - \int_0^\phi S\sin\theta\, d\xi$$

$$F''' + F = S$$

Here, of course, the superscripts denote differentiation with respect to ϕ. It is thereby seen that (3), (4), and (5) are equivalent to the following three differential equations:

$$L = -M' \tag{6}$$

$$M''' + M' = -S \tag{7}$$

$$N''' + N' = -T \tag{8}$$

To apply Castigliano's principle, it is required to have an expression for the strain energy U_r of the ring as a function of the stresses in the ring. According to hypothesis (a) the principal axes of the cross section at B are the x and z axes. Let I_x and I_z be the moments of inertia of the cross section at B about the x and z axes. Then according to Love (reference 9, § 255, § 258), in the "ordinary approximate theory" the strain energy is given by

$$U_r = \int_0^{2\pi} (lL^2 + mM^2 + nN^2)\, d\phi \tag{9}$$

If E is Young's modulus and G the shear modulus, then l, m, and n are given as

$$l = a/2EI_x, \quad m = a/2GI_t', \quad n = a/2EI_z$$

Here I_t is the torsional constant of the cross section B. For example, if B is circular, then $I_x = I_z = I_t/2$.

If the principal axes of the cross section are not parallel to the x and z axes, the expression for U_r will contain a term of the form LN. This generalization will not be treated here. It is also to be noted that Eq. (9) assumes that energy due to longitudinal strain and transverse shear are negligible. Presumably it would be possible to take account of these in the strain energy, but it is believed that the "ordinary approximate theory" is sufficiently accurate for most technical applications.

(4) Displacement of the Ring

The method of this paper is essentially concerned with stress and not with strain. However, the theory would be somewhat incomplete without relations for the strains and the displacements. This section will give formulas for the displacements of the ring, assuming that the stresses L, M, N are known. If only the stresses are of concern, this section may be omitted.

As usual, let u, v, w be the displacements in the x, y, z directions. Let β be the angle of twist in the y direction. Then the stress-strain relations corresponding to the stresses L, M, and N are

$$L/EI_x = w''/a^2 - \beta/a \tag{10}$$

$$M/GI_t = \beta'/a + w'/a^2 \tag{11}$$

$$N/EI_z = -u''/a^2 - u/a^2 \tag{12}$$

To verify any one of these equations, it is noted that if the second term on the right vanishes, the equation is clearly satisfied. In this case the equation has the same form as for a straight beam. The correctness of the second term on the right can be checked by noting that, if the ring is given a rigid displacement, the right side of the equation vanishes.

It is supposed that M and N are known. Then u is determined by solving the differential Eq. (12). Elimination of β between Eqs. (10) and (11) gives

$$w''' + w' = -a^2M''/EI_x + a^2M/GI_t$$

This equation determines w. Then β may be obtained directly from Eq. (10). The displacement v is determined by the equation

$$v' = -u \tag{13}$$

This equation merely states that the ring is treated as being inextensible.

The above treatment of the deflection of a ring is essentially that given in a paper by H. B. Tabakman.[10] In that paper Tabakman solves Eqs. (10) and (11) in various simple cases of interest.

(5) Stress in the Cylinder

Following Love (reference 9, § 343), the so-called "extensional solution" of a thin cylinder is determined by the equilibrium equations:

$$\sigma_y = ap/c \tag{14}$$

$$(\partial\sigma_y/\partial y) + (\partial\tau/\partial z) = 0 \tag{15}$$

$$(\partial\sigma_z/\partial z) + (\partial\tau/\partial y) = 0 \tag{16}$$

Here σ_y and σ_z are the normal stresses in the y and z directions, τ is the shear stress, and p is the internal pressure in the x direction. These equilibrium equations may be readily derived by considering a unit area of the cylinder as shown in Fig. 3. It is assumed that inextensional forces resulting from flexure of the shell are inappreciable and can be neglected.

In the present problem the only external forces on the cylinder are at the two ends. In particular the pressure p is zero. It follows from Eq. (14) that $\sigma_y = 0$. It then follows from Eq. (15) that τ is independent of z. In other words, $\tau = \tau(\phi)$. Making use of this last relation, Eq. (16) can be integrated to obtain

$$\sigma_z = -\tau' z/a + \rho(\phi) \tag{17}$$

Here ρ is a function only of ϕ.

Recalling the definitions of S and T and hypotheses (b) and (c), it is seen that the following boundary conditions must hold.

$$S = c\rho/a^2, \quad T = c\tau/a^2 \tag{18}$$

It was assumed above that there was no radial force transmitted from the cylinder to the ring—that is,

$R = 0$. This assumption is seen to fit in with the "extensional solution" stress state of the cylinder because the extensional solution cannot transmit force perpendicular to the surface.

The strain energy of a unit area of the cylinder is given by

$$U_1 = [(\sigma_z^2/2E) + (\sigma_y^2/2E) + (\tau^2/2G)]c \quad (19)$$

Here E is Young's modulus for the cylinder and G is the shear modulus. In the special case treated here, the term in σ_y vanishes. A discussion of the strain energy will be found in Love (reference 9, § 328).

Substituting the expression for σ_z given by Eq. (17) into relation (19) gives

$$U_1 = \frac{c(\tau')^2 z^2}{2a^2E} - \frac{c\tau'\rho z}{aE} + \frac{c\rho^2}{2E} + \frac{c\tau^2}{2G}$$

The total energy of the cylinder is given by

$$U_c = \int_0^{2\pi} a d\phi \int_0^b U_1 dz$$

Carrying out the integration with respect to z gives

$$U_c = \int_0^{2\pi} [hT^2 + i(T')^2 - 2jT'S + kS^2] d\phi \quad (20)$$

Here h, i, j, and k are constants, defined as

$$h = b/2Gc,\ i = b^3/6Eca^2,\ j = b^2/4Eca,\ k = b/2Ec$$

(6) Displacement of the Cylinder

As was mentioned above, this paper is primarily concerned with stress rather than with strain. For the sake of completeness this section treats the strains and displacements in the cylinder. If only the stresses are of concern, this section may be omitted. However, consideration of the strains leads to a better understanding of the problem.

Now u, v, w will denote displacements of a point on the cylinder in the x, y, z directions. Let ϵ_y and ϵ_z denote the normal strains in the y and z direction. Let γ denote the shear. Then the stress-strain relations are:

$$E\epsilon_y = \sigma_y - \nu\sigma_z \quad (21)$$

$$E\epsilon_z = \sigma_z - \nu\sigma_y \quad (22)$$

$$G\gamma = \tau \quad (23)$$

Here ν is Poisson's ratio. In the special case considered here, $\sigma_y = 0$. The strains are defined in terms of the displacements by the following relations (reference 9, § 334):

$$\epsilon_y = (1/a)(\partial v/\partial\phi) + (u/a) \quad (24)$$

$$\epsilon_z = \partial w/\partial z \quad (25)$$

$$\gamma = (\partial v/\partial z) + (1/a)(\partial w/\partial\phi) \quad (26)$$

Eqs. (24), (25), and (26) will now be integrated to obtain u, v, and w. From Eqs. (17), (22), and (25) it results that

$$E(\partial w/\partial z) = -(\tau' z/a) + \rho(\phi)$$

Integration of this equation gives

$$w = -(\tau' z^2/2aE) + (\rho z/E) + \zeta(\phi) \quad (27)$$

Here ζ is a function only of ϕ. This relation and Eq. (23) are substituted in Eq. (26) and then integrated. This yields

$$v = \frac{\tau'' z^3}{6a^2E} - \frac{\rho' z^2}{2aE} - \frac{\zeta' z}{a} + \frac{\tau z}{G} + \eta(\phi) \quad (28)$$

Relation (28) together with relations (21) and (17) are substituted in Eq. (24) to obtain the following expression for u:

$$u = -\frac{\tau''' z^3}{6a^2E} + \frac{\rho'' z^2}{2aE} + \frac{\zeta'' z}{a} - \frac{\tau' z}{G} - \eta' + \frac{\nu\tau' z}{E} - \frac{a\nu\rho}{E} \quad (29)$$

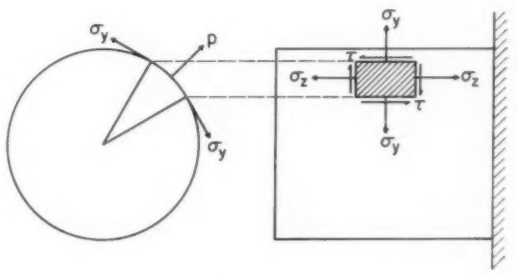

FIG. 3.

If relations (29), (28), and (27) for u, v, and w are studied, it will be discovered that all the boundary conditions at both ends of the cylinder cannot be satisfied. For example, Eqs. (13) and (24) are in conflict. This difficulty is seen to arise from relations (21) and (22), causing ϵ_y and ϵ_z to be proportional rather than independent. To explain such a paradoxical result Love introduces the "edge-effect" (reference 9, § 339). By "edge-effect" is meant that the flexural strains cannot be considered as small in the immediate neighborhood of the boundary circles of the cylinder. Since the flexural strains have been neglected in the above treatment, it cannot be expected that all boundary conditions are compatible.

The expressions derived for u, v, and w are not without some significance. They do give a measure of the displacement in the cylinder away from the boundary circles.

The boundary conditions on stress are assumed to hold rigorously. That is, Eq. (18) applies where the ring and cylinder meet. If there were another ring attached to the other end of the cylinder, a similar boundary condition would apply there.

(7) The Variational Principle of Castigliano

The principle of Castigliano may be formulated in this way: *A linear elastic system is in equilibrium under the action of prescribed external forces. Then the strain energy of the system is a minimum with respect to a variation of internal forces. The varied forces must be in virtual equilibrium.* By "virtual equilibrium" is meant that the varied forces must balance, but the varied forces do not have to be compatible with the stress-strain relationships. An analysis of this variational principle is given in references 6 and 11, p. 272. The latter reference may be consulted for techniques in the calculus of variations which are now to be employed.

Let U be the total elastic energy of the system. Adding relations (9) and (20) for U_r and U_c gives

$$U = \int_0^{2\pi} [hT^2 + i(T')^2 - 2jT'S + kS^2 + lL^2 + mM^2 + nN^2]d\phi \quad (30)$$

To apply Castigliano's principle we vary X_0, Y_0, Z_0, L_0, M_0, N_0, S, and T. Then virtual equilibrium will be maintained if we assume relations (1) and (2) for external forces and relations (3), (4), and (5) for the internal forces. These are subsidiary conditions to be imposed on the variation. The variation of U may be written

$$2^{-1}\delta U = \int_0^{2\pi} [(hT - iT'' + jS')\delta T + (-jT' + kS)\delta S + lL\delta L + mM\delta M + nN\delta N]d\phi \quad (31)$$

Here the following integration by parts has been employed:

$$\int_0^{2\pi} (iT' - jS)\delta T'd\phi = \int_0^{2\pi} (-iT'' + jS')\delta T d\phi + (iT' - jS)\delta T \Big|_0^{2\pi}$$

The second term on the right here is an end-point relation. This is recognized as a natural boundary condition and may be set equal to zero.

To analyze the above natural boundary condition it is first necessary to note an imposed boundary condition resulting from the continuity of shear stress τ. In particular this means that $\tau(0) = \tau(2\pi)$. It is convenient here and in what follows to employ the shorthand notation

$$\Delta\tau = \tau(2\pi) - \tau(0)$$

Thus the boundary condition imposed by continuity may be written as $\Delta\tau = 0$ or $\Delta T = 0$. Inspecting the natural boundary condition now shows that it may be written in the form

$$\Delta(iT' - jS) = 0 \quad (32)$$

Consider a variation in which only N_0, X_0, and Y_0 are varied. Then it results from Eq. (31) that

$$0 = \int_0^{2\pi} nN[\delta N_0 + a \sin\phi\delta X_c + a(1 - \cos\phi)\delta Y_0]d\phi$$

Since the three variations are independent, the following three conditions must hold:

$$\int_0^{2\pi} nNd\phi = 0 \quad (33)$$

$$\int_0^{2\pi} nN \sin\phi\, d\phi = 0 \quad (34)$$

$$\int_0^{2\pi} nN \cos\phi\, d\phi = 0 \quad (35)$$

Similarly, varying Z_0, L_0, and M_0 yields the following three conditions:

$$\int_0^{2\pi} [-lL \sin\phi + mM(1 - \cos\phi)]d\phi = 0 \quad (36)$$

$$\int_0^{2\pi} [lL \cos\phi - mM \sin\phi]d\phi = 0 \quad (37)$$

$$\int_0^{2\pi} [lL \sin\phi + mM \cos\phi]d\phi = 0 \quad (38)$$

Next we consider a variation when only T is varied. The value of δN is determined by the subsidiary condition (5). Thus

$$\delta N = -\int_0^{2\pi} \delta T(1 - \cos\theta)d\xi$$

This expression is substituted in Eq. (31), and the following identity is employed:

$$-\int_0^{2\pi} nN\delta N d\xi = \int_0^{2\pi} nN \int_0^{\xi} \delta T(1 - \cos\theta)d\phi d\xi = \int_0^{2\pi} \delta T \int_\phi^{2\pi} nN(1 - \cos\theta)d\xi d\phi$$

Setting the coefficient of δT equal to zero gives the following Euler equation:

$$hT - iT'' + jS' = \int_\phi^{2\pi} nN(1 - \cos\theta)d\xi + \lambda_1 \quad (39)$$

Here λ_1 is a function of the form

$$\lambda_1 = a_1 + b_1 \cos\phi + c_1 \sin\phi$$

The constants a_1, b_1, and c_1 are Lagrange multipliers resulting from the subsidiary conditions (1a), (1b), and (2c). These conditions may be written

$$\int_0^{2\pi} \delta T \sin\phi d\phi = \int_0^{2\pi} \delta T \cos\phi d\phi = \int_0^{2\pi} \delta T(1 - \cos\phi)d\phi = 0$$

Finally we consider a variation when only S is varied. The integral of δM is transformed in the same way as the integral of δN was transformed above. For δL the following identity is employed:

$$-\int_0^{2\pi} lL\delta L d\xi = \int_0^{2\pi} lL \int_0^{\xi} \delta S \sin\theta \, d\phi = \int_0^{2\pi} \delta S \int_\phi^{2\pi} lL \sin\theta \, d\xi$$

Setting the coefficient of δS equal to zero in (31) gives

$$-jT' + kS = \int_\phi^{2\pi} [lL \sin\theta + mM(1 - \cos\theta)]d\xi + \lambda_2 \quad (40)$$

Here λ_2 is a Lagrange function of the same form as λ_1, but resulting from the subsidiary conditions (1c), (2a), and (2b).

It is convenient to introduce the following linear combination of relations (39) and (40):

$$KS' - JT = \int_0^{2\pi} [lL \cos\theta + mM \sin\theta - \bar{n}N(1 - \cos\theta)]d\xi + \lambda_3 \quad (41)$$

Here K, J, and $\bar{n}$ are defined as

$$K = k - j^2/i, \quad J = jh/i, \quad \bar{n} = jn/i$$

The function λ_3 has the same form as λ_1. The solution of the problem is now determined by the integrodifferential Eqs. (40) and (41).

(8) The Differential Equations

In general it is more desirable to work with differential equations than with integrodifferential equations. Also it is desirable to use as few dependent variables as possible. To carry out such simplifications let $-\zeta$ and $-\eta$ denote the left sides of Eqs. (40) and (41). Thus

$$\zeta = jT' - kS \quad (42)$$

$$\eta = -KS' + JT \quad (43)$$

Then successive differentiations of Eq. (40) yield

$$\zeta = \int_0^{\phi} [lL \sin\theta + mM(1 - \cos\theta)] \, d\xi + \lambda_4$$

$$\zeta' = \int_0^{\phi} [lL \cos\theta + mM \sin\theta]d\xi + \lambda_4'$$

$$\zeta'' = \int_0^{\phi} [-lL \sin\theta + mM \cos\theta]d\xi + \lambda_4'' + lL$$

Similarly, successive differentiations of Eq. (41) yield

$$\eta = \int_0^{\phi} [lL \cos\theta + mM \sin\theta - \bar{n}N(1 - \cos\theta)]d\xi + \lambda_5$$

$$\eta' = \int_0^{\phi} [-lL \sin\theta + mM \cos\theta - \bar{n}N \sin\theta]d\xi + \lambda_5' + lL$$

$$\eta'' = \int_0^{\phi} [-lL \cos\theta - mM \sin\theta - \bar{n}N \cos\theta]d\xi + \lambda_5'' + (lL)' + mM$$

In the above relations λ_4 and λ_5 are of the same form as λ_1. The following combination of derivatives is seen to eliminate the integrals:

$$\zeta''' + \zeta' = (lL)' + mM \quad (44a)$$

$$\eta''' + \eta' = (lL)'' + (mM)' - \bar{n}N \quad (45a)$$

To achieve greater generality l, m, and n are here treated as functions of ϕ. Of course they are assumed to be differentiable and periodic. Making use of Eqs. (42) and (43) yields the differential equations

$$-j(T^{(4)} + T^{(2)}) + k(S^{(3)} + S^{(1)}) + (lL)' + mM = 0 \quad (44b)$$

$$K(S^{(4)} + S^{(2)}) - J(T^{(3)} + T^{(1)}) + (lL)'' + (mM)' - \bar{n}N = 0 \quad (45b)$$

To reduce the number of variables, S and T are eliminated from Eqs. (44) and (45) by use of Eqs. (7) and (8). This gives the following pair of differential equations which determine the solution of the problem:

$$j(N^{(7)} + 2N^{(5)} + N^{(3)}) - k(M^{(6)} + 2M^{(4)} + M^{(2)}) - (lM')' + mM = 0 \quad (46)$$

$$-K(M^{(7)} + 2M^{(5)} + M^{(3)}) + J(N^{(6)} + 2N^{(4)} + N^{(2)}) - (lM')'' + (mM)' - \bar{n}N = 0 \quad (47)$$

In this formulation of the problem only the variables pertaining to the ring appear.

(9) The Boundary Conditions

The basic Eqs. (46) and (47) are of the seventh order. It is seen that they are equivalent to fourteen first-order equations; therefore there must be fourteen boundary conditions. To take count it is noted that Eqs. (1) and (2) give six boundary conditions; relationships (33) through (38) yield six more; and the continuity condition, $\Delta T = 0$, and the natural boundary condition, (32), bring the total to fourteen. The first twelve of these conditions are integral conditions rather than end-point conditions.

It is desirable to express all of the boundary conditions in the conventional end-point form. To carry this out, it is seen from Eqs. (3) and (2a) that

$$\Delta L = -\int_0^{2\pi} S \sin\xi \, d\xi = L_1$$

Making use of Eq. (6) gives

$$\Delta M' = -L_1 \quad (48)$$

Similar considerations show that the boundary conditions (2b) and (2c) are transformed into

$$\Delta M = M_1 \quad (49)$$

$$\Delta N = N_1 \quad (50)$$

It is seen from Eqs. (5) and (1a) that

$$\Delta N' = \int_0^{2\pi} T \sin\xi \, d\xi = aX_1$$

Thus Eqs. (1a), (1b), and (1c) become

$$\Delta N' = aX_1 \tag{51}$$

$$\Delta N'' = aY_1 \tag{52}$$

$$\Delta M'' = aZ_1 - M_1 \tag{53}$$

From the integral formula for ζ and from boundary condition (36), it is seen that $\Delta\zeta = 0$. From the integral formula for ζ' and from boundary condition (37), it is seen that $\Delta\zeta' = 0$. Similarly, from the integral formula for η together with boundary conditions (37), (33), and (35), it is seen that $\Delta\eta = 0$. From Eq. (43) it is seen that $\Delta S' = 0$, because $\Delta\eta$ and ΔT both vanish. Eliminating T' between Eq. (42) and the natural boundary condition (32), it is seen that $\Delta S = 0$ because $\Delta\zeta = 0$. Because $\Delta\zeta' = 0$, it follows that $\Delta T'' = 0$. These results are summarized in the five relations

$$\Delta T = \Delta T' = \Delta T'' = \Delta S = \Delta S' = 0 \tag{54}$$

From the integral relationship for ζ'' it follows that

$$\Delta\zeta'' = l\Delta L = lL_1$$

Here boundary conditions (38) and (48) have been employed. In a similar fashion the integral relationships for η' and η'' yield

$$\Delta\eta' = l\Delta L = lL_1$$

$$\Delta\eta'' = m\Delta M + \Delta(lL)' = m\Delta M + l\Delta L' + l'\Delta L$$

$$\Delta\eta'' = (m + l)M_1 - laZ_1 + l'L_1$$

All fourteen boundary conditions are now expressed as end-point conditions. However, for the sake of simplicity it is desirable to eliminate the intermediate variables ζ and η and to express the last three conditions in terms of S and T. Thus, since $\Delta\eta' = -K\Delta S''$, it follows that

$$\Delta S'' = -lL_1/K \tag{55}$$

Since $\Delta\zeta'' = j\Delta T''' - k\Delta S''$, it follows that

$$\Delta T''' = (K - k)lL_1/Kj \tag{56}$$

Since $\Delta T'' = 0$, it follows that $\Delta\eta'' = -K\Delta S'''$, hence

$$\Delta S''' = [-(m + l)M_1 + laZ_1 - l'L_1]/K \tag{57}$$

The boundary conditions are now expressed by the end-point relations (48) to (57), inclusive.

For certain degenerate cases to be treated in the next section, it is necessary to give two other relations resulting from the boundary conditions. From relation (44a) it follows that

$$\Delta\zeta''' = -\Delta\zeta' + m\Delta M + l\Delta L' + l'\Delta L$$

Substitution of the boundary expressions already obtained yields

$$\Delta\zeta''' = (m + l)M_1 - laZ_1 + l'L_1$$

Since $\Delta\zeta^{(3)} = j\Delta T^{(4)} - k\Delta S^{(3)}$, it results that

$$\Delta T^{(4)} = [-(m + l)M_1 + laZ_1 - l'L_1] \times (k - K)/Kj \tag{58}$$

Likewise it follows from Eq. (45a) that

$$\Delta\eta''' = -\Delta\eta' + l\Delta L'' + 2l'\Delta L' + l''\Delta L + m\Delta M' + m'\Delta M - \hat{n}\Delta N$$

Substituting the boundary expressions obtained above gives

$$\Delta\eta''' = (-2l - m + l'')L_1 + (m + 2l')M_1 - 2l'aZ_1 - \hat{n}N_1$$

Since $\Delta\eta^{(3)} = K\Delta S^{(4)} + J\Delta T^{(3)}$, it results that

$$K\Delta S^{(4)} = [J(K - k)l/Kj + 2l + m - l'']L_1 - (m + 2l')M_1 + 2l'aZ_1 + \hat{n}N_1 \tag{59}$$

Of course relations (58) and (59) impose no further conditions on the system. They are merely alternative expressions for two of the boundary conditions.

(10) Four Special Cases

In many practical situations some of the terms in the strain energy will be inappreciable compared with others. This will result in reducing the number of variables and thereby simplifying the problem. These simplified problems could be treated afresh, patterning the procedure after the general case just given. It is easier, however, to specialize the general solution which has already been obtained. This will now be done in four special cases of some importance.

The first case corresponds to the problem treated by Hoff. It is assumed that the ring is perfectly flexible in a direction perpendicular to its plane. Thus there may be no normal stress in the cylinder where it meets the ring. So $S = 0$ characterizes this case. It is seen that the variation of T again gives Eq. (39). Differentiating Eq. (39) three times yields the differential equation

$$-i(T^{(5)} + T^{(3)}) + k(T^{(3)} + T^{(1)}) + nN = 0$$

Eliminating T by means of relation (8) gives the following differential equation for the bending moment in the ring

$$i(N^{(8)} + 2N^{(6)} + N^{(4)}) - k(N^{(6)} + 2N^{(4)} + N^{(2)}) + nN = 0 \tag{60}$$

Three boundary conditions are given by Eqs. (50), (51), and (52). Thus

$$\Delta N = N_1, \quad \Delta N' = aX_1, \quad \Delta N'' = aY_1 \tag{61}$$

Only forces perpendicular to the axis of a cylinder are considered. Similarly, only couples are applied parallel to the axis of the cylinder. Thus $Z_1 = L_1 = M_1 = 0$. The boundary conditions are obtained from Eqs. (54), (56), and (58); thus

$$\Delta T = \Delta T' = \Delta T'' = \Delta T^{(3)} = \Delta T^{(4)} = 0 \tag{62}$$

Together, Eqs. (61) and (62) account for eight boundary conditions for the differential equation (60) of the eighth order.

The second case goes to the opposite extreme. Thus it is now supposed that the ring is rigid perpendicular to its plane. More precisely this case is characterized by taking $l = m = 0$. This means that there is no strain energy resulting from flexure in the z direction or torsion in the y direction. Let $\psi = K\zeta' - k\eta = jKT'' - kJT$.

It follows from Eqs. (44a) and (45a) that $\psi''' + \psi' = k\bar{n}N$. Then T is eliminated from this relation by means of Eq. (8), resulting in the eighth order differential equation

$$-jK(N^{(8)} + 2N^{(6)} + N^{(4)}) + kJ(N^{(6)} + 2N^{(4)} + N^{(2)}) - k\bar{n}N = 0 \quad (63)$$

The boundary conditions are the same as before—that is, (61) and (62). However, relation (62) now follows because l and m are zero. It is not necessary to assume that Z_1, L_1, and M_1 are zero.

The third case to be considered concerns a ring which is flexible in its own plane. The applied force is considered to be parallel to the z axis. This case is characterized by the relation $N = 0$. Thus Eq. (46) becomes

$$k(M^{(6)} + 2M^{(4)} + M^{(2)}) + (lM')' - mM = 0 \quad (64)$$

Boundary conditions (48), (49), and (53) apply. Thus

$$\Delta M = M_1, \quad \Delta M' = -L_1, \quad \Delta M'' = aZ_1 - M_1 \quad (65)$$

Boundary conditions (54) and (55) give

$$\Delta S = 0, \quad \Delta S' = 0, \quad \Delta S'' = -lL_1/K \quad (66)$$

Thus Eqs. (65) and (66) are six boundary conditions for the sixth order differential equation on the torsional moment.

The fourth case is the opposite extreme to the third case. Thus it is now supposed that the ring is rigid in its plane. This case can be characterized by the relation $n = 0$. Let

$$Q = J\zeta - j\eta' = jKS'' - kJS$$

Making use of (44a) and (45a) gives

$$Q''' + Q' = -j(lL)''' - j(mM)'' + J(lL)' + JmM$$

Eliminating S by means of relation (7) yields the following eighth order differential equation on the torsional moment

$$-jK(M^{(8)} + 2M^{(6)} + M^{(4)}) + kJ(M^{(6)} + 2M^{(4)} + M^{(2)}) = j(lM')''' - j(mM)'' - J(lM')' + JmM \quad (67)$$

The boundary conditions include (65) and (66) and the two further conditions (57) and (59).

(11) Further Generalizations

(A) The stress distribution resulting from a concentrated load applied at the angle ϕ_0 is, of course, obtained by rotating the standard solution just found through the angle ϕ_0. More generally the stress distribution corresponding to a system of concentrated loads is obtained by superimposing such rotated solutions.

(B) The differential equations corresponding to a distributed load are given by similar methods. Moreover, the standard solution obtained here serves as a Green's function for the continuous loading problem.

(C) The differential equations for a cylinder with several reinforcing rings are obtained in essentially the same way. It is seen that a system of equations results involving three moments L_i, M_i, and N_i for each ring and two stress variables S_i and T_i for each section of the cylinder.

(D) The cylindrical shell does not need to be isotropic. Hoff made use of this notion to incorporate the effect of stringers—that is, longitudinal stiffening rods. Likewise the treatment applies if the cylinder is corrugated, as in the problem studied by Adachi.[8]

(E) It is permissible to have the parameters vary with the angle ϕ. The above treatment applies directly, without change, for a ring of variable cross section because it has not been assumed that the coefficients l, m, and n are constant. Moreover, the treatment could be modified to take into account a cylinder whose thickness varies with the angle ϕ.

(F) A similar theory could be developed for cylinders which are not circular, such as elliptic cylinders.

References

[1] Wise, J. A., *Analysis of Circular Rings for Monocoque Fuselages*, Journal of the Aeronautical Sciences, Vol. 6, pp. 460–463, 1939.

[2] Wignot, J. E., Combs, H., and Ensrud, A. F., *Analysis of Circular Shell-Supported Frames*, NACA TN 929, 1944.

[3] Kuhn, P., Duberg, N. E., and Griffith, G. E., *The Effect of Concentrated Loads on Flexible Rings in Circular Shells*, NACA Wartime Report L-66, 1945.

[4] Hoff, N. J., *Stresses in a Reinforced Monocoque Cylinder Under Concentrated Symmetric Transverse Loads*, Jour. Appl. Mech., Vol. 11, pp A235–A239, 1944.

[5] Hoff, N. J., Salerno, V. L., Leibowitz, Harold, Boley, Bruno A., and Nardo, Sebastian V., *Concentrated Load Effects in Reinforced Monocoque Structures* (Reissner Anniversary Volume), pp. 277–332; Edwards, Ann Arbor, Mich., 1949.

[6] Hoff, N. J., *The Analysis of Structures, Based on the Minimal Principles and the Principle of Virtual Displacements;* John Wiley & Sons, Inc., New York, 1956.

[7] Duffin, R. J., *Differential Equations for the Stress in Cylinders With Reinforcing Rings*, Duke University TR No. 3, Contract No. DA-31-ORD-10, Office of Ordnance Research, Jan. 22, 1959.

[8] Adachi, J., *Stress Distribution in an End-Stiffened Corrugated Sheet Under Concentrated Longitudinal End Load*, Watertown Arsenal Laboratories Report TR 893/204, April 1, 1958.

[9] Love, A. E. H., *A Treatise on the Mathematical Theory of Elasticity*, 4th Ed., Cambridge University Press, 1927.

[10] Tabakman, H. D., *Formulas and Charts for Calculating Deflection of Circular Rings Loaded Normal to Plane of Curvature*, Machine Design, pp. 167–172, Nov. 14, 1957.

[11] Courant, R., and Hilbert, D., *Methods of Mathematical Physics*, Vol. 1, Ch. IV; Interscience Publishers, Inc., New York, 1953.

Vortex Containment for the Gaseous-Fission Rocket†

JACK L. KERREBROCK* AND ROBERT V. MEGHREBLIAN**
California Institute of Technology

Summary

The nuclear rocket is potentially capable of much higher specific impulse than any chemically fueled rocket, because of the high energy content per unit mass of the fissionable material. While a part of this potential can be realized by use of a low molecular weight propellant heated by solid fuel plates, it seems clear that the full potential can be realized only if the fissionable material can be retained in gaseous form, and its fission energy transferred directly to the propellant.

The purpose of this paper is to consider the possibility of retaining the fissionable material, in gaseous form, in the pressure field of a vortex, while the low molecular weight propellant diffuses radially inward through it. A two-dimensional, laminar, vortex flow is studied, the propellant being introduced tangentially at the periphery and withdrawn at the center.

The mass-flow capacity of the vortex, per unit of vortex length, is found to be independent of the vortex diameter, so that a large number of small-diameter vortices filling a given volume will have a much larger mass-flow capacity than a single vortex of the same volume. At tangential Mach numbers of the order of unity in a mixture of hydrogen and plutonium, the mass-flow capacity is of the order of 0.01 pounds per second-foot.

If the vortex pressure gradient decreases monotonically outward, it is possible to maintain the heavy gas in a highly peaked distribution, away from both the center and the periphery of the vortex; however, for very high heating rates, or very large temperature ratios, the pressure gradient cannot decrease monotonically outward, and in this case the concentration of heavy gas near the periphery of the vortex will be high.

Insofar as the vortex-containment mechanism limits the gaseous nuclear rocket, its performance potential is very high. It may be that its performance will actually be limited by other factors, such as radiant heat transfer from the gas to solids, the difficulty of maintaining fissionable material in gaseous form, and the difficulty of generating vortices with the required low radial mass-flow rates and high tangential velocities. The potential of the gaseous fission rocket seems to warrant intensive study of these problems.

Introduction

THE NUCLEAR ROCKET, in which the fission reaction acts as a source of energy to heat the propellant, which is then expanded through a nozzle to produce thrust, is potentially capable of much higher specific impulse than is any chemically fueled rocket. This is because the energy content of the heated propellant per unit mass is not limited, as in the case of the chemical rocket, by the chemical energy content of the propellants. The energy content of the fissionable material per unit mass is in fact so high that it need not be used as propellant; its energy may be extracted and used to heat a separate propellant.

However, the problem of transferring the energy from the fissioning fuel to the propellant makes full realization of this great potential difficult. A portion of it can be realized by choosing a propellant with a very low molecular weight, so that even with the propellant temperature limited to the values obtainable with heat transfer from fissionable materials in solid form, the propellant enthalpy, and hence the specific impulse, is considerably above that attainable with chemical propellants. It seems likely that, with hydrogen as the propellant, values of specific impulse ranging from 800 seconds to perhaps 1,200 seconds may be obtained, depending on the pressure at which the hydrogen is heated.

It seems clear, though, that the full potential of the nuclear rocket can be realized only if the fissionable material is retained in gaseous form, and heat is transferred from it to the propellant without the interposition of any solid surface. Two methods are available for this energy transfer: radiation and direct molecular collisions. Of these, we shall consider only the latter. To effect the direct transfer of the kinetic energy of the fission fragments to the propellant by molecular collisions, the fissionable material and propellant must be in intimate gaseous mixture within a nuclear reactor in which a chain reaction can be supported. It is readily demonstrated that the requirement for nuclear criticality, together with the desire for large amounts of heat addition to the gaseous propellant, dictate rather high concentrations of fissionable material in the gas mixture. If this mixture is then simply exhausted through a nozzle, the loss of fissionable material is prohibitive from the standpoint of cost. Thus, it is essential that the fissionable material be retained within the reactor, while the propellant flows through it.

The purpose of this paper is to consider the possibility of containing the fissionable material within a vortex flow. The strong radial pressure gradients which can be generated in vortices are capable of producing appreciable diffusion of a light propellant gas, such as hydrogen, through a heavy gas, such as plutonium. Thus, it seems possible that a distribution of fissionable gas may be held in a vortex while the lighter propellant gas diffuses radially inward through it, absorbing the fission energy. One possible imple-

Received May 20, 1960.

† This paper is based largely upon the analysis and results of reference 1, which was declassified December 21, 1959.

* Senior Research Fellow, Daniel and Florence Guggenheim Jet Propulsion Center.

** Chief of the Physical Sciences Division, Jet Propulsion Laboratory.

mentation of this concept is shown schematically in Fig. 1. The propellant gas, and enough fissionable gas to make up losses, would be introduced with a high tangential velocity at the periphery of the vortex tube, through a series of jets distributed over its surface. The propellant would then diffuse radially inward, through the distribution of fissionable gas, and leave the tube axially near its center.

For the purposes of analysis, this flow will be idealized to a two-dimensional vortex flow, into which the fluid is introduced uniformly at the periphery with a tangential velocity, and from which it is withdrawn at some radius near the center, as by a cylindrical sink at that radius. No attempt will be made to treat the three-dimensional flow near the axis; it is felt that this flow is not of crucial importance to the containment mechanism. A question does arise as to the proper boundary conditions to be applied at the inner and outer radii of the two-dimensional flow; this question will be discussed in some detail.

The flow will be assumed to be laminar. It may seem that this assumption is rather extreme, because the Reynolds number of the flow, based on the high tangential velocity and the tube diameter, must be large, and the resulting turbulent mixing would tend to invalidate the laminar calculation. However, the nature of turbulent vortex flows is not well understood, particularly when the fluid is compressible, so that conclusions based on turbulent mixing processes for radically different flows (e.g., pipe flow) may be completely erroneous. The point of view which is taken here is that the validity of the laminar diffusion calculation can best be judged by direct comparison with experiment.

Fission-fragment heating of the propellant is assumed to occur locally at the point of fission—i.e., the range of the fission fragments is assumed small compared to the radius of the vortex. At one hundred atmospheres pressure and 2,000°K., the range of fission fragments in hydrogen is about 0.7 cm.,[2] however, half of their energy is deposited in the first 0.2 cm., hence, at this pressure and temperature, the vortex radius must be one centimeter or larger. An additional assumption, that the heating rate is proportional to the concentration of fissionable material, implies that the neutron flux within the vortex is constant. It will be assumed that the mole fraction of fissionable gas in the mixture is small. This assumption simplifies the analysis considerably, and because of the much larger mass of the fissionable atoms compared to that of the propellant atoms, is valid even when the density of fissionable material is considerably greater than that of the propellant.

Finally, the vortex flow will be assumed inviscid, so that the tangential velocity is inversely proportional to the radius. The justification for this is that the radial-inflow Reynolds number is sufficiently large for the interesting cases that viscous effects are in fact small, except near the solid outer boundaries of the vortex. Boundary-layer-like flows with high rates of shear will exist on such surfaces, and the resultant torque may make the attainment of vortices with sufficiently high tangential velocities difficult; however, this problem will not be considered here.

In the present paper, we shall be concerned with the process of diffusion of the propellant through the heavy gas, with heat addition. No detailed consideration will be given to the many other problems, such as radiant heat transfer and nuclear criticality; which must clearly be of great importance for a gaseous reactor.

Nevertheless, some estimates of the performance of gaseous nuclear rockets, as limited by the vortex containment, will be given. It must be recognized that these estimates cannot reflect the ultimate potential of the gaseous nuclear rocket with vortex containment. They can only serve to indicate the limits imposed by the containment scheme itself.

Formulation of the Diffusion Problem

For a complete description of the two-component gas mixture, two new variables must be added to the usual fluid dynamic set. These may be taken as the

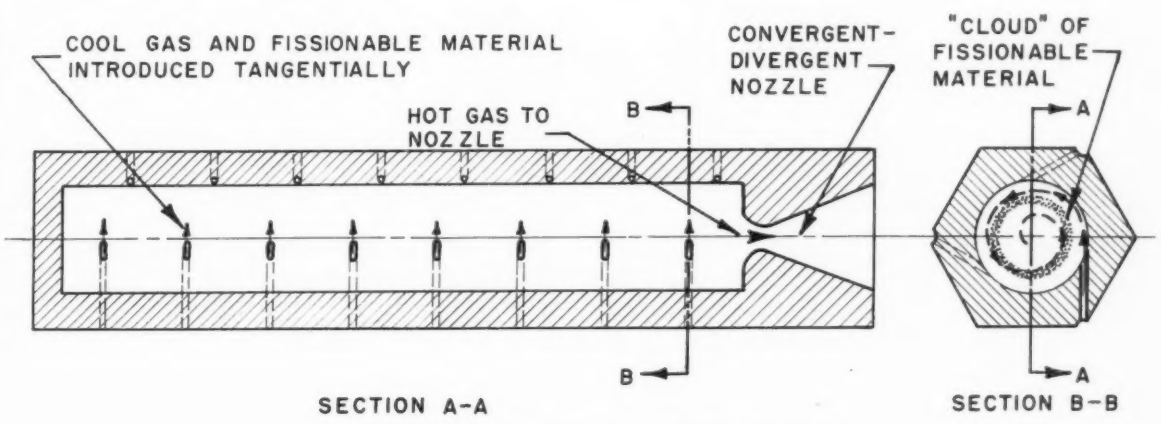

FIG. 1. Specialization of the vortex tube for rocket propulsion.

density and velocity of one species, say the heavy gas, in which case the continuity equation for the heavy gas and the relation connecting its diffusion velocity to the pressure and concentration gradients complete the set of governing equations.

In the two-dimensional vortex flow, the continuity equation for the mixture is quite simple. If u is the radial gas velocity, ρ the density, and r the radius, then

$$\rho u r = (\mathfrak{M}_1 + \mathfrak{M}_2)/2\pi \tag{1}$$

where $\mathfrak{M}_1$ and $\mathfrak{M}_2$ are the constant mass flows of the light and heavy gases, respectively, per unit of vortex length. Similarly, since the two gases do not react chemically, the heavy gas satisfies the continuity equation

$$\rho_2(u + u_2)r = \mathfrak{M}_2/2\pi \tag{2}$$

where u_2 is the diffusion velocity of the heavy gas.

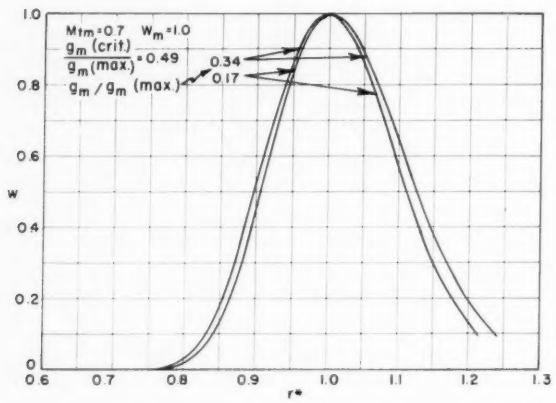

FIG. 2. Variation of density ratio, w, with dimensionless radius, r^*, for g_m less than g_m (crit).

The Diffusion Equation

Neglecting thermal diffusion, the diffusion velocity is related to the concentration and pressure gradients by:[3]

$$u_2\left(\frac{\rho}{\rho - \rho_2}\right) = -D_{12}\left\{\frac{n}{n - n_2}\frac{d\log(n_2/n)}{dr} + \frac{n(m_1 - m_2)}{\rho}\frac{d\log p}{dr}\right\} \tag{3}$$

where n is the total gas concentration, p the total gas pressure, m_1 and m_2 the respective molar masses, and D_{12} is the binary diffusion coefficient. Now by using Eq. (2) to eliminate u_2, Eq. (3) may be put in the form

$$\left(\frac{\mathfrak{M}_2}{\mathfrak{M}_1 + \mathfrak{M}_2} - \frac{\rho_2}{\rho}\right) = \frac{-2\pi r\rho_1 D_{12}}{\mathfrak{M}_1 + \mathfrak{M}_2}\left(\frac{\rho_2}{\rho}\right)\times \left\{\frac{n}{n - n_2}\frac{d\log(n_2/n)}{dr} + \frac{n(m_1 - m_2)}{\rho}\frac{d\log p}{dr}\right\} \tag{4}$$

It is convenient to rewrite this expression in terms of the ratio of fissionable material and propellant densities, $w = \rho_2/\rho_1$. As was mentioned previously, it will be assumed that $n_2/n \ll 1$, however, because $m_2 \gg m_1$, it does not follow that $w \ll 1$. In terms of w, the diffusion equation then becomes

$$\left(\frac{\mathfrak{M}_2}{\mathfrak{M}_1 + \mathfrak{M}_2} - \frac{w}{1 + w}\right) = \frac{-2\pi r\rho_1 D_{12}}{\mathfrak{M}_1 + \mathfrak{M}_2}\left(\frac{w}{1 + w}\right)\times \left\{\frac{d\log w}{dr} - \frac{(m_2/m_1 - 1)}{1 + w}\frac{d\log p}{dr}\right\} \tag{5}$$

It will become clear later that $\mathfrak{M}_2/\mathfrak{M}_1$ is determined by the value of w at the boundary where the flow leaves the vortex (in this case, the inner boundary). Thus, $\mathfrak{M}_2/\mathfrak{M}$, is a characteristic value of the diffusion equation. The magnitude of this characteristic value influences the behavior of w where it is of the order of $\mathfrak{M}_2/\mathfrak{M}_1$; where $w \gg \mathfrak{M}_2/\mathfrak{M}_1$, the behavior is controlled by the factor $2\pi r\rho_1 D_{12}/(\mathfrak{M}_1 + \mathfrak{M}_2)$, and by the behavior of the pressure gradient.

The radial flow velocity must be of the order of the diffusion velocity, and it is readily verified that it is therefore small compared to the tangential velocity. In this case, the radial momentum equation becomes simply

$$dp/dr = \rho v^2/r$$

where v is the tangential velocity; using the fact that $n_2 \ll n_1$, this may be written:

$$(d\log p)/(d\log r) = (1 + w)v^2/RT \tag{6}$$

where R is the gas constant for the light gas. Substituting this result into Eq. (5) and multiplying through by $(1 + w)/w$ yields

$$1 - \left(\frac{1 + w}{w}\right)\left(\frac{\mathfrak{M}_2}{\mathfrak{M}_1 + \mathfrak{M}_2}\right) = \frac{2\pi\rho_1 D_{12}}{\mathfrak{M}_1 + \mathfrak{M}_2}\left[\frac{d\log w}{d\log r} - \left(\frac{m_2}{m_1} - 1\right)\frac{v^2}{RT}\right] \tag{7}$$

The most important features of the vortex containment mechanism can be seen quite readily from Eq. (7). Suppose first that there is no radial flow, so that $\mathfrak{M}_1 = \mathfrak{M}_2 = 0$; then the quantity in square brackets must be zero, and we have

$$\log w = \left(\frac{m_2}{m_1} - 1\right)\int\left(\frac{v^2}{RT}\right)\frac{dr}{r} + \text{constant}$$

Thus, w increases monotonically with r for $m_2/m_1 > 1$. This is of course the equilibrium distribution for a given variation of v and T with r.

Next, suppose that $\mathfrak{M}_1$ and $\mathfrak{M}_2$ each have some negative value, but that $|\mathfrak{M}_2| \ll |\mathfrak{M}_1|$; then, except where w is very small, the left side of Eq. (7) is unity, and except for the variation of the quantity $2\pi\rho_1 D_{12}/(\mathfrak{M}_1 + \mathfrak{M}_2)$, the sum of the two terms in brackets must be a negative constant. Thus, initially as $\mathfrak{M}_1$ decreases from zero, dw/dr must decrease. If $\mathfrak{M}_1$ is made sufficiently negative, dw/dr can be made zero at any given

value of r. Now, for such a value of $\mathfrak{M}_1$, if v^2/RT decreases monotonically with increasing r, dw/dr will be positive for r less than the point at which dw/dr is zero, and negative for r larger than this value. Thus, a simple maximum is produced.

The position of this maximum may be obtained by solving Eq. (7) with $dw\ dr = 0$. If $M_{tm} = v/(\gamma RT)^{1/2}$ is the tangential Mach number at the point of the maximum, and other quantities evaluated at the maximum are similarly denoted by subscript m, then

$$\gamma M_{tm}^2 = \frac{-1}{(m_2/m_1) - 1}\left(\frac{\mathfrak{M}_1 + \mathfrak{M}_2}{2\pi\rho_1 D_{12}}\right)_m \times \left[1 - \left(\frac{1 + w_m}{w_m}\right)\left(\frac{\mathfrak{M}_2}{\mathfrak{M}_1 + \mathfrak{M}_2}\right)\right] \quad (8)$$

Eq. (8) contains one of the most important pieces of information to be derived from the analysis, namely, that the radial mass flow permitted by the diffusion process is independent of the diameter of the vortex, and in fact depends only on $\mathfrak{M}_2/\mathfrak{M}_1$, γ, M_{tm}^2 and the product $(\rho_1 D_{12})_m$ evaluated at the maximum point of w, since for the cases of interest $\mathfrak{M}_2/(\mathfrak{M}_1 + \mathfrak{M}_2) \ll w_m/(1 + w_m)$. For a given pair of gases, $(\rho_1 D_{12})_m$ depends only on T_m. The most important fact is that the mass flow rate per unit of vortex length is independent of the vortex radius. Physically, this is a result of the fact that for a fixed Mach number, the pressure gradient is inversely proportional to the vortex radius, and the resulting diffusion velocity is therefore also inversely proportional to the radius of the vortex. But the mass flow rate per unit of vortex length is proportional to the product of the radial velocity (which is essentially the diffusion velocity) and the vortex radius, and hence is constant.

Finally, if v^2/RT is not monotonic but first decreases and then increases with increasing r, w can have both a maximum and a minimum. It will be demonstrated that this situation can occur with heat addition in a free vortex. There will then be two positions in the vortex where $dw/dr = 0$. In a free vortex, where $v \propto 1/r$, there will be a level of heat addition below which only a simple maximum will exist because T does not vary rapidly enough to overcome the variation of v. This value will be termed the critical rate of heat addition. There will also be a larger rate of heat addition above which no maximum of w can exist, because (v^2/RT) increases monotonically with increasing r. This value will be termed the maximum rate of heat addition. Both of these values are of course dependent on $2\pi\rho_1 D_{12}/(\mathfrak{M}_1 + \mathfrak{M}_2)$, $\mathfrak{M}_2/\mathfrak{M}_1$, m_2/m_1, and M_{tm}.

The Energy Equation

To make these relationships quantitative, we must consider the energy equation, since it describes the behavior of T. The viscous dissipation will be neglected, as it is quite negligible in a flow with large heat addition. The equation in terms of the enthalpy h is then[3]

$$\rho u\frac{dh}{dr} = u\frac{dp}{dr} - \frac{1}{r}\frac{d}{dr}(rq) + g \quad (9)$$

where $q = \lambda(dT/dr) + (C_{p2} - C_{p1})\rho_2 u_2 T$, λ being the heat conductivity, and g is the volumetric rate of heat addition. In this case, g of course represents the heating by fission fragments.

The heating rate is proportional to the concentration, n_2, of fissionable material, to its fission cross section, σ_f, and to the neutron flux, ϕ. If the local energy release per fission is Q, then $g = Q\sigma_f\phi\eta_2$. In the present work, it will be assumed that σ_f and ϕ are independent of r. Q is a constant for practical purposes, so the heating rate is simply proportional to n_2. h is the enthalpy of the gas mixture, and under the assumption that $n_2 \ll n$, it can be written as $h = C_{p1}T/(1 + w)$. The specific heat of the light gas will be taken constant, although this is a very crude assumption for diatomic gases at the temperatures which are

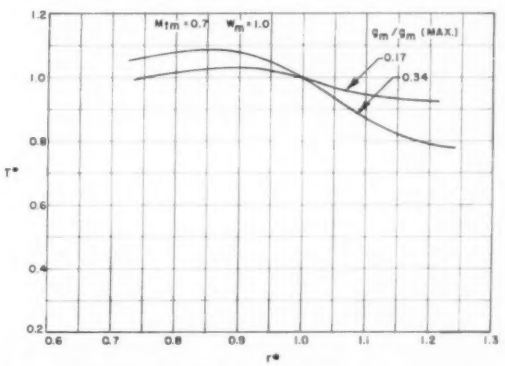

FIG. 3. Variation of dimensionless temperature, T^*, with dimensionless radius, r^*, for g_m less than g_m (crit).

of interest for the gaseous fission rocket. We make the assumption in order that the calculations shall not depend explicitly on the temperature and pressure level, as they would if the exact relationship between h and T were included. With the expression previously given for dp/dr, Eq. (9) then becomes

$$\frac{d}{dr}\left(\frac{C_{p1}T}{1 + w}\right) = \frac{v^2}{r} - \frac{2\pi}{\mathfrak{M}_1 + \mathfrak{M}_2} \times \frac{d}{dr}\left[\lambda r\frac{dT}{dr} + (C_{p2} - C_{p1})r\rho_2 u_2 T\right] + Q\sigma_f\phi n_2/\rho u$$

From Eq. (2),

$$\rho_2 u_2 r = [(\mathfrak{M}_1 + \mathfrak{M}_2)/2\pi][\mathfrak{M}_2/(\mathfrak{M}_1 + \mathfrak{M}_2) + w/(1 + w)]$$

and from Eq. (1),

$$Q\sigma_f\phi n_2/\rho u = [2\pi Q\sigma_f\phi/m_2(\mathfrak{M}_1 + \mathfrak{M}_2)]r\rho_1 w$$

so that

$$\frac{d}{dr}\left(\frac{T}{1+w}\right)=\frac{v^2}{C_{p1}r}+\left(1-\frac{C_{p2}}{C_{p1}}\right)\times$$
$$\frac{d}{dr}\left[\left(\frac{\mathfrak{M}_2}{\mathfrak{M}_1+\mathfrak{M}_2}-\frac{w}{1+w}\right)T\right]-\frac{2\pi}{\mathfrak{M}_1+\mathfrak{M}_2}\times$$
$$\frac{d}{dr}\left(\frac{\lambda}{C_{p1}}\,r\,\frac{dT}{dr}\right)+\frac{2\pi Q\sigma_f\,\phi}{m_2C_{p1}(\mathfrak{M}_1+\mathfrak{M}_2)}\,r\rho_1 w \quad (10)$$

It will be helpful to consider the relative magnitudes of the heat transfer by conduction and diffusion. Assuming that rdT/dr and T are of the same order, the ratio of the conductive and diffusive heat transfer rates is $[2\pi\lambda/C_{p1}(\mathfrak{M}_1+\mathfrak{M}_2)]/[w/(1+w)]$, at points where $w \gg \mathfrak{M}_2/\mathfrak{M}_1$. Now according to Euchen's formula,[3] the heat conductivity, viscosity, and specific heat are related by $\lambda = (9\gamma-5)\mu C_v/4$, so that the ratio becomes

$$\frac{9\gamma-5}{4\gamma}\left(\frac{1+w}{w}\right)\left(\frac{2\pi\mu}{\mathfrak{M}_1+\mathfrak{M}_2}\right) \quad (11)$$

It will become clear later that w must be of the order of unity or greater over most of the vortex to provide sufficient fissionable material for nuclear criticality, so that the factor $(1+w)/w$ is of order unity. The factor $(\mathfrak{M}_1+\mathfrak{M}_2)/2\pi\mu$ is the radial Reynolds number of the flow; for the situations of interest it is of the order of 100. Thus, conduction can be neglected compared to diffusive energy transport, except where $r(dT/dr) \gg T$.

Neglecting the conduction term, carrying out the indicated differentiation, and eliminating dw/dr with Eq. (7), we find the following expression for $(d\log T)\div(d\log r)$:

$$\frac{d\log T}{d\log r}=\frac{\dfrac{1+w}{w}\left[(\gamma-1)M^2+\dfrac{2\pi Q\sigma_f\,\phi r^2\rho_1 w}{m_2C_{p1}(\mathfrak{M}_1+\mathfrak{M}_2)T}\right]+\dfrac{C_{p2}}{C_{p1}}\left(\dfrac{1}{1+w}\right)\left\{\dfrac{\mathfrak{M}_1+\mathfrak{M}_2}{2\pi\rho_1D_{12}}\left[1-\left(\dfrac{1+w}{w}\right)\left(\dfrac{\mathfrak{M}_2}{\mathfrak{M}_1+\mathfrak{M}_2}\right)\right]+\left(\dfrac{m_2}{m_1}-1\right)\gamma M^2\right\}}{\dfrac{1}{w}+\left(1-\dfrac{C_{p2}}{C_{p1}}\right)\left[1-\left(\dfrac{1+w}{w}\right)\left(\dfrac{\mathfrak{M}_2}{\mathfrak{M}_1+\mathfrak{M}_2}\right)\right]} \quad (12)$$

From Eq. (7), the accompanying expression for $(d\log w/d\log r)$ is

$$\frac{d\log w}{d\log r}=\left(\frac{\mathfrak{M}_1+\mathfrak{M}_2}{2\pi\rho_1D_{12}}\right)\left[1-\left(\frac{1+w}{w}\right)\left(\frac{\mathfrak{M}_2}{\mathfrak{M}_1+\mathfrak{M}_2}\right)\right]+\left(\frac{m_2}{m_1}-1\right)\gamma M^2 \quad (13)$$

and from Eq. (6),

$$(d\log p)/(d\log r)=\gamma M^2(1+w) \quad (14)$$

With the proper boundary conditions, and the relation $\rho_1 = p/RT$, these three first-order nonlinear equations may be solved for T, w, and p, if v is given as a function of r. As was mentioned in the introduction, it will be assumed in the present work that $v \propto 1/r$, i.e., that the flow is inviscid.

Only those solutions yielding a maximum of w within the vortex will be considered. For heating rates below the critical heating rate, such solutions offer the possibility of containing the fissionable material within the vortex, away from the outer wall. For heating rates above the critical value, the value of w at the outer boundary of the vortex will be higher, in contrast.

To facilitate the numerical integration, it is desirable to rewrite the equations in terms of dimensionless variables. A particularly convenient set of variables is obtained by dividing each of the variables by its value at the radius, r_m, where w is a maximum. Such variables will be denoted by an asterisk—e.g., $r^* = r/r_m$, $T^* = T/T_m$. It is also convenient to introduce a dimensionless heating rate g_m, evaluated at r_m, as

$$g_m = -[2\pi Q\sigma_f\,\phi r_m{}^2n_{2m}]/[C_{p1}(\mathfrak{M}_1+\mathfrak{M}_2)T_m] \quad (15)$$

Through Eq. (8), $(\mathfrak{M}_1+\mathfrak{M}_2)/2\pi\rho_1 D_{12}$ may be related to M_{tm}, w_m, and $\mathfrak{M}_2/(\mathfrak{M}_1+\mathfrak{M}_2)$, provided the dependence of D_{12} on the state of the gas mixture is specified. For the present purposes, the simple result for D_{12} based on hard-sphere collisions, namely,

$$D_{12} = (3/8nd_{12}{}^2)[(m_1+m_2)kT/2\pi m_1m_2]^{1/2} \quad (16)$$

is adequate. k is Boltzmann's constant and d_{12} is the effective collision diameter. Thus, $D_{12}/(D_{12})m = T^{*3/2}/p^*$, and

$$\frac{\mathfrak{M}_1+\mathfrak{M}_2}{2\pi\rho_1D_{12}}=\left(\frac{\mathfrak{M}_1+\mathfrak{M}_2}{2\pi\rho_1D_{12}}\right)_m T^{*-1/2}=-\frac{\gamma M_{tm}{}^2[(m_2/m_1)-1]T^{*-1/2}}{1-\left(\dfrac{1+w_m}{w_m}\right)\left(\dfrac{\mathfrak{M}_2}{\mathfrak{M}_1+\mathfrak{M}_2}\right)} \quad (17)$$

With these relations, Eq. (12) becomes

$$\frac{d \log T^*}{d \log r^*} = \frac{\dfrac{1+w}{w}\left[\dfrac{(\gamma-1)M_{tm}^2}{r^{*2}T^*} - gm\dfrac{r^{*2}p^*w}{T^{*2}w_m}\right]}{\dfrac{1}{w} + \left(1 - \dfrac{C_{p2}}{C_{p1}}\right)\left[1 - \left(\dfrac{1+w}{w}\right)\left(\dfrac{\mathfrak{M}_2}{\mathfrak{M}_1 + \mathfrak{M}_2}\right)\right]} + \frac{\dfrac{\gamma M_{tm}^2[(m_2/m_1) - 1](C_{p2}/C_{p1})}{(1+w)T^{*1/2}}\left[\dfrac{1}{r^{*2}T^{*1/2}} - \dfrac{1 - \left(\dfrac{1+w}{w}\right)\left(\dfrac{\mathfrak{M}_2}{\mathfrak{M}_1 + \mathfrak{M}_2}\right)}{1 - \left(\dfrac{1+w_m}{w_m}\right)\left(\dfrac{\mathfrak{M}_2}{\mathfrak{M}_1 + \mathfrak{M}_2}\right)}\right]}{\dfrac{1}{w} + \left(1 - \dfrac{C_{p2}}{C_{p1}}\right)\left[1 - \left(\dfrac{1+w}{w}\right)\left(\dfrac{\mathfrak{M}_2}{\mathfrak{M}_1 + \mathfrak{M}_2}\right)\right]} \tag{18}$$

Similarly, Eq. (13) is

$$\frac{d \log w}{d \log r^*} = \frac{\gamma M_{tm}^2[(m_2/m_1) - 1]}{T^{*1/2}}\left[\frac{1}{r^*T^{*1/2}} - \frac{1 - \left(\dfrac{1+w}{w}\right)\left(\dfrac{\mathfrak{M}_2}{\mathfrak{M}_1 + \mathfrak{M}_2}\right)}{1 - \left(\dfrac{1+w_m}{w_m}\right)\left(\dfrac{\mathfrak{M}_2}{\mathfrak{M}_1 + \mathfrak{M}_2}\right)}\right] \tag{19}$$

and Eq. (14) reduces to

$$(d \log p^*)/(d \log r^*) = \gamma M_{tm}^2(1+w)/r^{*2}T^* \tag{20}$$

Boundary Conditions

The system of three first-order differential equations, (18), (19), and (20), allows one boundary condition to be satisfied on each of the three variables w, T^*, and p^*. In addition, the quantity $\mathfrak{M}_2/(\mathfrak{M}_1 + \mathfrak{M}_2)$ is a characteristic value of the diffusion equation, as will be demonstrated. It is of course clear that by neglecting conduction in the energy equation Eq. (18) is reduced from a second-order equation to a first-order equation; this reduces the number of applicable boundary conditions to one. In a vortex such as is sketched in Fig. 1, the boundary condition on T at the vortex tube surface, namely, that the gas temperature equals the surface temperature, is lost. Similarly, by neglecting the radial acceleration in the radial momentum equation, Eq. (20) is reduced to a first-order equation. If the pressure is specified at any radius in a tube such that in Fig. 1, Eq. (20) appears to determine the pressure everywhere else. Actually, the three-dimensional flow near the axis of such a tube would be an important factor in determining the pressure level in the tube.

The situation is perhaps not so clear in the case of the diffusion equation. If, for example, the vortex is assumed to be bounded at its inner and outer radii by porous cylinders, it may appear that the value of the density ratio, w, in the vortex just adjacent to the surface of each of the porous cylinders should equal the value of w in the gas mixture flowing through the porous cylinder. However, this is only true if the direction of gas flow is from the vortex to the porous surface, i.e., if the boundary is an outflow boundary. At such a boundary, the mass flow rate of each species is proportional to its concentration. The inner boundary of the present vortex flow is such a boundary; if the radius of this inner boundary is r_c, and the corresponding value of w is w_c, then it is clear that the quantity $\mathfrak{M}_2/(\mathfrak{M}_1 + \mathfrak{M}_2)$, which is the ratio of heavy gas mass flow to total mass flow, is simply

$$\mathfrak{M}_2/(\mathfrak{M}_1 + \mathfrak{M}_2) = w_c/(1 + w_c) \tag{21}$$

Thus, the characteristic value of the diffusion equation is determined at the inner boundary.

In contrast, all that is required at the outer, or inflow, boundary is that the gas flowing into the vortex have the same w as that leaving, namely, w_c. It is neither necessary nor in general possible for the value of w in the vortex adjacent to the inflow boundary to equal w_c. The transition from one value of w to the other at the inflow boundary occurs by a mixing process, and results in an increase of the entropy of the gas mixture. This entropy increase due to mixing is offset by the separative effect in the vortex, so that the entropies of mixing of the inlet and outlet flows are equal.

For the present calculations, the boundary conditions will be applied at $r^* = 1$, and are simply

$$T^*(1) = 1, \quad p^*(1) = 1, \quad w(1) = w_m \tag{22}$$

where w_m is the maximum value of w. For given values of g_m, w_c, w_m, M_{tm}, m_2/m_1, C_{p2}/C_{p1}, and γ, the solution can then be obtained by forward integration. The inner radius of the vortex is then defined as that radius at which w is equal to w_c.

The last statement implies that the fluid leaves the vortex at the radius r_c, as though there were a cylindrical sink there. This condition would be approximated by a porous cylinder of radius r_c. The three-dimensional flow near the axis of a tube such as that sketched in Fig. 1 would act as a sink distributed over the portion of the tube volume within the radius of the exit nozzle. For a precise evaluation of the loss of fissionable material from the vortex, a treatment of this

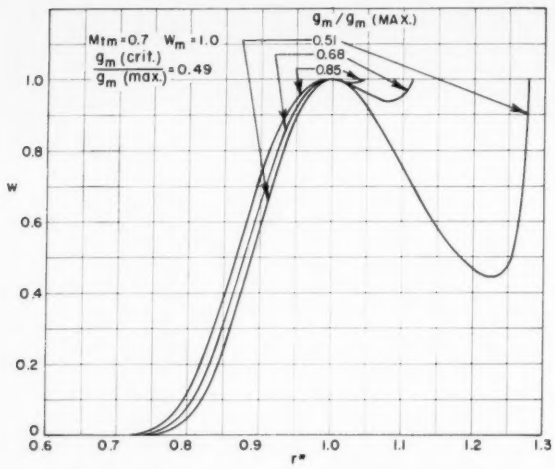

FIG. 4. Variation of density ratio, w, with dimensionless radius, r^*, for g_m greater than g_m (crit).

distributed sink would be essential; for the present purpose, w_c will be taken to be very small (10^{-4}), and the fluid will be assumed to leave the vortex at r_c. This gives a very conservative estimate of the loss rate.

Finally, it should be noted that for $w_c/w_m \ll 1$, the character of the solutions for T^*, p^*, and w is independent of the magnitude of w_c [see Eq. (19)].

The Critical and Maximum Heating Rates

The maximum heating rate has been defined as the highest heating rate for which w has a maximum within the vortex. Equivalently, $g_{m(max)}$ is the largest value of g_m for which w has a maximum at $r^* = 1$; that is, the largest value of g_m for which d^2w/dr^{*2} is negative at $r^* = 1$. From Eq. (19),

$$\left(\frac{d^2w}{dr^{*2}}\right)_{r^*=1} = -\gamma M_{tm}^2 \left(\frac{m_2}{m_1} - 1\right) \times w_m[2 + (1/2)(dT^*/dr^*)_{r^*=1}]$$

so that for $g_{m(max)}$, $(dT^*/dr^*)_{r^*=1} = -4$. Now from Eq. (18),

$$\left(\frac{dT^*}{dr^*}\right)_{r^*=1} = \frac{\dfrac{1 + w_m}{w_m}[(\gamma - 1)M_{tm}^2 - g_m]}{\dfrac{1}{w_m} + \left(1 - \dfrac{C_{p2}}{C_{p1}}\right)\left[\dfrac{1 - (w_c/w_m)}{1 + w_c}\right]} \quad (23)$$

whence

$$g_{m(max)} = (\gamma - 1)M_{tm}^2 + 4\left[\frac{1}{w_m} + \left(1 - \frac{C_{p2}}{C_{p1}}\right)\left(\frac{1 - (w_c/w_m)}{1 + w_c}\right)\right]\left(\frac{w_m}{1 + w_m}\right) \quad (24)$$

and for $w_c \ll 1$ and $w_c \ll w_m$, this is

$$g_{m(max)} = 4 + (\gamma - 1)M_{tm}^2$$

The critical heating rate has been defined as the smallest heating rate for which $dw/dr^* = 0$ for some $r^* > 1$. From Eq. (19), for $w_c \ll w_m$, dw/dr^* is zero if $T^* = 1/r^{*4}$; however, since T^* can be obtained only from integration of the differential equations, the value of $g_{m(crit)}$ cannot readily be obtained analytically. The values of $g_{m(crit)}/g_{m(max)}$ obtained from the solutions of the equations will be given later.

Solution of the Diffusion Problem

Solutions of a system of equations equivalent to Eqs. (18), (19), and (20) with boundary conditions (22) were given in reference 1. These were obtained by forward integration of the equations, from $r^* = 1$ to both smaller and larger r^*. The parameters which characterize the gas mixture, and which occur explicitly in Eqs. (18), (19), and (20), were chosen to be representative of hydrogen and plutonium gas. Specifically, $m_2/m_1 = 119.5$, $C_{p2}/C_{p1} = 0.008$, and $\gamma = 1.31$ were chosen. The exit density ratio, w_c, was taken as 0.0001.

The remaining parameters are then g_m, which measures the heating rate; M_{tm}, which measures the strength of the vortex; and w_m, which is a measure of the density ratio of heavy gas contained in the vortex. While the specification of w_c effectively determines the inner boundary of the vortex, the value of r^* corresponding to the outer boundary is arbitrary. The numerical solutions must, however, be terminated for some r^* greater than unity. In the calculations reported in reference 1, they were terminated when the density ratio w reached $w_m/10$ for $g_m < g_{m(crit)}$, and when w reached w_m, for $g_m > g_{m(crit)}$.

*Solutions for w and T**

Solutions for w and T^*, for two subcritical values of the heating parameter, are shown in Figs. 2 and 3. The heating rates are 0.17 $g_{m(max)}$ and 0.34 $g_{m(max)}$. For the chosen values of $M_{tm} = 0.7$ and $w_m = 1.0$, $g_{m(crit)}/g_{m(max)} = 0.49$. In this range of $g_m/g_{m(max)}$, the w profile is rather insensitive to g_m, even though a considerable amount of heating takes place. If g_m were zero, T^* would decrease quite rapidly with decreasing r^*, because of the expansion in the pressure gradient pro-

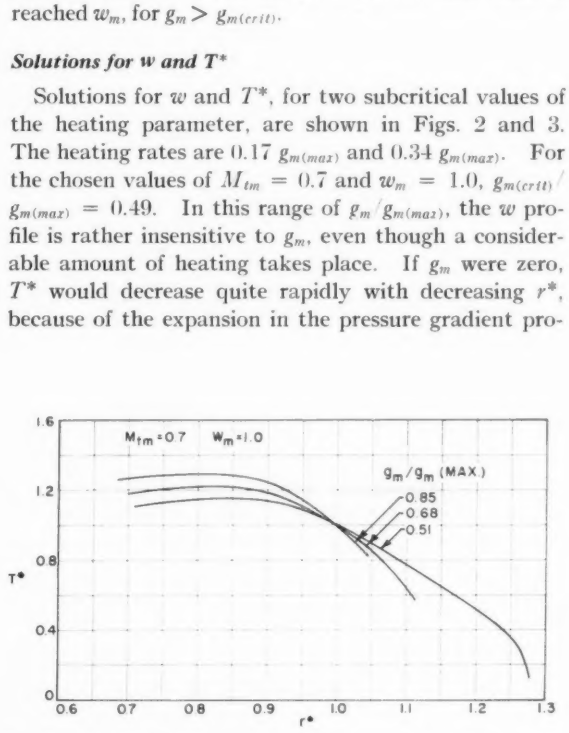

FIG. 5. Variation of dimensionless temperature, T^*, with dimensionless radius r^*; for g_m greater than g_m (crit).

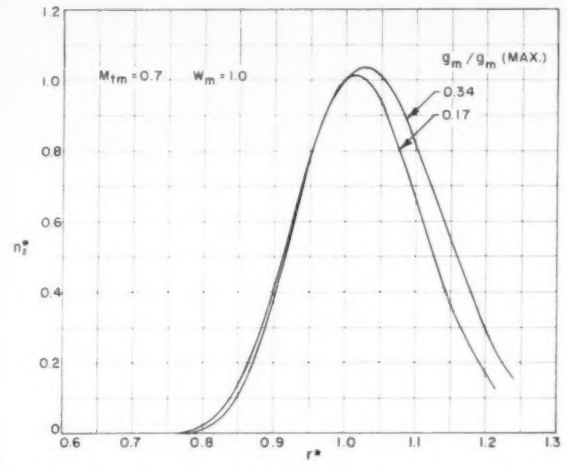

FIG. 6. Variation of dimensionless fuel concentration, n_2^*, with dimensionless radius, r^*, for g_m less than g_m (crit.)

duced by the vortex. It follows that for sufficiently large r^*, T^* would increase with r^*. In Figs. 2 and 3, the solutions are carried out approximately to the value of r^* at which $dT^*/dr^* = 0$.

As g_m increases, dT^*/dr^* increases until the critical value, $g_{m(crit)}$, is reached. The solutions then change character to that shown in Figs. 4 and 5. The essential differences are that w has a second stationary point for some $r^* > 1$, and that dT^*/dr^* becomes increasingly negative with increasing r^*, instead of eventually becoming positive, as in Fig. 3. The behavior appears to be singular, with w approaching infinity and T^* approaching zero as r^* approaches some value. Thus, in principle, very large temperature ratios, from the outside of the vortex to the inside, can be obtained with sufficiently large heating rates.

However, the irregular behavior of w and T^* implies very large concentrations of heavy gas in the outer portions of the vortex tube. This is illustrated in Figs. 6 and 7, which give the profiles of n_2^* corresponding to the w and T^* profiles of Figs. 2 and 3, and 4 and 5, respectively. For the subcritical heating rates, the profiles of n_2^* and w are at least qualitatively similar; however, for the supercritical heating rates, n_2^* becomes very large in the outer portions of the tube. This is, of course, principally a reflection of the fact that the gas density is much larger in the outer portions because of the large temperature change.

Values of $g_{m(crit)}/g_{m(max)}$ obtained from a series of integrations are summarized in Table 1.

The sharpness of the peak in the w distribution increases rapidly with increasing M_{tm}, as shown in Fig. 8 for three cases having $g_m/g_{m(crit)} \approx 1.02$. Thus, as the Mach number increases, the amount of heavy gas which is retained in the vortex, for a fixed value of w_m, is reduced. On the other hand, increasing M_{tm} increases the mass flow capacity of the vortex, as may be seen from Eq. (8).

TABLE 1

Critical Heating Rates

M_{tm}	$w_m = 0.2$	$w_m = 0.5$	$w_m = 1.0$	$w_m = 4.0$
0.5	0.455	0.450	0.441	0.410
0.7	0.505	0.499	0.487	0.434
1.0	0.580	0.574	0.557	0.470

In contrast to the strong dependence of the profiles of w on M_{tm}, their dependence on w_m is quite weak. w/w_m is shown in Fig. 9 for three values of w_m, and for $g_m/g_{m(crit)} \approx 1.02$, as before. This insensitivity of w/w_m to w_m may be understood from a careful examination of Eqs. (18) and (19). If we consider only the range of w where $w/(1 + w) \gg \mathfrak{M}_2/(\mathfrak{M}_1 + \mathfrak{M}_2)$, they reduce approximately to:

$$\frac{d \log T^*}{d \log r^*} = \gamma M_{tm}^2 \left(\frac{m_2}{m_1} - 1\right) \frac{C_{p2}}{C_{p1}} \frac{w}{(1+w)^2} \left(\frac{1}{r^{*2} T^{*1/2}} - 1\right) + \frac{(\gamma - 1) M_{tm}^2}{r^{*2} T^*} - g_m \frac{r^{*2} p^*}{T^{*2}} \left(\frac{w}{w_m}\right)$$

and

$$\frac{d \log w}{d \log r^*} = \frac{\gamma M_{tm}^2}{T^{*1/2}} \left(\frac{m_2}{m_1} - 1\right)\left(\frac{1}{r^{*2} T^{*1/2}} - 1\right)$$

In the energy equation, the first term represents the energy transport by diffusion, and this term depends directly on the magnitude of w; however, it is zero at two points (the maximum and minimum of w) on the curves of Fig. 9, so it seems reasonable that it is fairly small over most of the vortex. Of the other two terms, the last depends on w/w_m, and not on w_m itself. Thus, it may be said that the profiles of w/w_m are similar for different values of w_m because the diffusive energy transport is comparatively unimportant.

Performance Parameters

In addition to the three parameters determining the solutions, namely, M_{tm}, w_m, and g_m, the value of r^* cor-

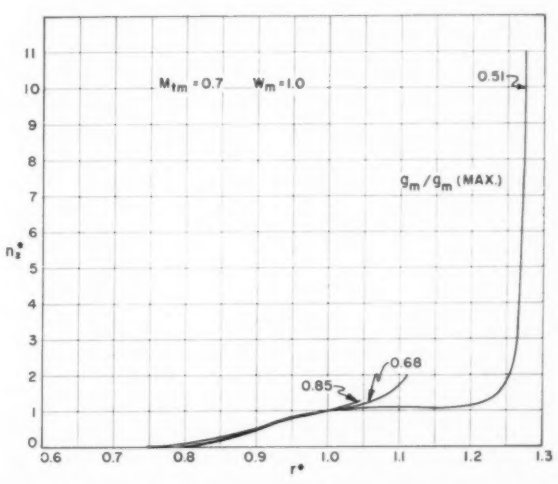

FIG. 7. Variation of dimensionless fuel concentration, n_2^*, with dimensionless radius, r^*, for g_m greater than g_m (crit).

responding to the periphery of the vortex must be specified in describing an actual vortex. For given values of M_{tm}, w_m, and g_m, the pressure and temperature ratios across the vortex, for example, depend on the value of r_p^*. In order to reduce the number of parameters by one, a rather arbitrary choice of r_p^* will therefore be made. For the cases with subcritical heating rates, r_p^* will be taken as that value of r^* greater than unity for which $w/w_m = 0.1$. For the supercritical cases r_p^* will be taken as the value of r^* greater than unity for which $w = w_m$.

With these choices, there is then, for given values of w_m and M_{tm}, a definite relationship between the temperature ratio across the vortex, T_c/T_p, and the heating parameter. This relationship is shown in Fig. 10 for $M_{tm} = 0.7$. It will be noted that the characteristics are markedly different for the subcritical and supercritical solutions. As the heating parameter is increased, the temperature ratio, T_c/T_p, increases continuously until $g_{m(crit)}$ is reached. At this point, the profile of w switches from the type shown in Fig. 2 to that shown in Fig. 4, and the temperature ratio becomes very large. As g_m is increased beyond $g_{m(crit)}$, T_c/T_p decreases again, because with the above choice for the outer radius, r_p^* decreases with increasing g_m. For $g_m/g_{m(max)} = 1$, the outer boundary of the vortex is at the maximum of w, i.e., at $r^* = 1$. Because of the sensitivity of the profiles in the neighborhood of $g_{m(crit)}$, it was rather difficult to establish the exact end points of the subcritical characteristics; hence, these end points are labeled approximate. For $M_{tm} = 0.7$, the maximum values of T_c/T_p which can be obtained with a simple maximum of w vary from about 3.0 for $w_m = 0.2$ to 2.5 for $w_m = 4.0$. Values for other Mach numbers are given in Table 2.

It is convenient to relate other performance parameters to the temperature ratio, w_m, and M_{tm}. The pressure ratio from the inner to the outer boundary is shown in Fig. 11 for $M_{tm} = 0.7$. As w_m increases, the pressure drop through the vortex increases also. This increase may be regarded as due to the increased resistance to flow offered by the more dense distribution of heavy gas as w_m increases.

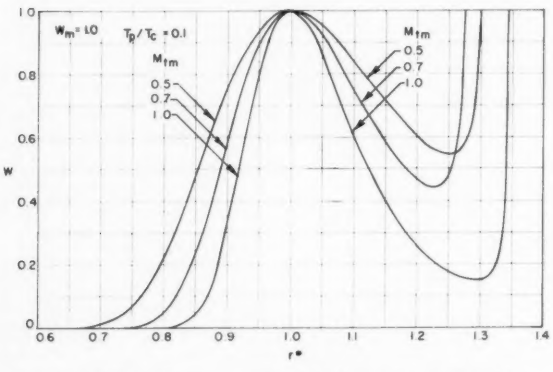

FIG. 8. Effect of the tangential Mach number at the point of maximum density ratio, M_{tm}, on the variation of the density ratio, w, with dimensionless radius, r^*.

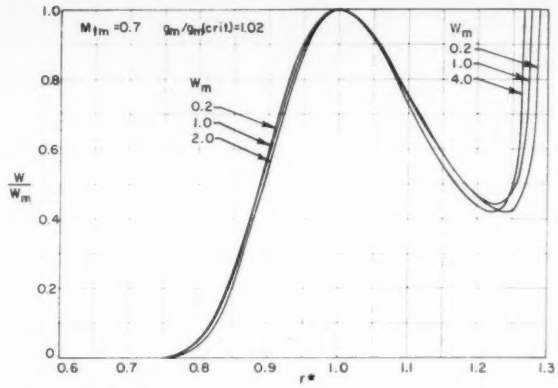

FIG. 9. Effect of the maximum density ratio, w_m, on the variation of the density ratio, w, with the dimensionless radius, r^*.

The Mach number of the vortex at its periphery, M_{tp}, is related to M_{tm} by

$$M_{tp} = M_{tm}/r_p^* T_p^{*1/2} \tag{25}$$

Since w/w_m and T^* were found to be independent of w_m for given M_{tm}, it is not surprising that, as a function of T_c/T_p, M_{tp} depends only on M_{tm}. This dependence is shown in Fig. 12, from which it is clear that rather high values of M_{tp} are required when T_p/T_c is small. This is due simply to the very rapid decrease of T_p^* with increasing r^* for these cases; however, it is important to note that the mass flow capacity of the vortex depends on M_{tm} [Eq. (8)], and that as T_p/T_c (or T_p^*) decreases, it will become more difficult to obtain satisfactorily high values of M_{tm}.

From Eq. (8), the mass flow capacity of the vortex per unit length, $\mathfrak{M}_1$, is related to M_{tm} and the diffusion coefficient. Using Eq. (16), the relation may be written as

$$\mathfrak{M}_1 = \frac{3[2\pi k m_1(1 + m_1/m_2)]^{1/2}}{8\, d_{12}^2} \left(\frac{m_2}{m_1} - 1\right) \times \frac{\gamma T_p^{1/2}}{[1 - (w_c/w_m)]} \Psi \tag{26}$$

where $\Psi = M_{tm}^2/T_p^{*1/2}$. Since T_p^* is independent of w_m, so is Ψ; its dependence on M_{tm} and T_p/T_c is shown in Fig. 13. It is clear that for given values of T_p and M_{tm}, $\mathfrak{M}_1$ increases with increasing T_c/T_p; however, if M_{tp} is held fixed, Ψ decreases with increasing T_c/T_p, as indicated by the lines of constant M_{tp} included in Fig. 13.

The radius r_c of the inner boundary of the vortex effectively determines the maximum possible length-to-diameter ratio of a vortex such as that in Fig. 1, since

TABLE 2

Maximum of T_c/T_p for Subcritical Solutions		
M_{tm}	w_m 0.2–1.0	$w_m = 4.0$
0.5	4.2	3.8
0.7	3.0	2.5
1.0	2.9	2.4

all of the mass flow must leave the vortex axially near its center, and the radius of the exit nozzle must be less than r_c. Thus, the ratio r_c/r_p is an important performance parameter. Its dependence on M_{tm}, w_m, and T_c/T_p is shown in Fig. 14. In contrast to M_{tp} and Ψ, r_c/r_p is dependent to some extent on w_m. This is because the profile of w depends on the magnitude of w itself, and not w/w_m alone, near r_c, where $w \approx w_c$. All the values or r_c/r_p are near 0.5 or larger, so that for the range of M_{tm} covered in Fig. 14, the heavy gas is essentially confined to the outer half of the vortex radius.

It is convenient to refer the heating parameter to the conditions in the vortex at its periphery. Thus,

$$g_p = -\frac{2\pi Q\sigma_f \phi n_{2p} r_p^2}{\mathfrak{M}_1(1 + w_c)C_{p1}T_p} = g_m(n_{2p}{}^* r_p{}^{*2}/T_p{}^*) \quad (27)$$

is a direct measure of the rate of enthalpy increase in the outer portion of the vortex, and if it is given as a function of T_c/T_p, w_m, and M_{tm}, it permits the calculation of the neutron flux, ϕ, required to give any specified temperature ratio. The dependence of g_p on w_m and T_c/T_p for $M_{tm} = 0.7$ is shown in Fig. 15. It increases rapidly as T_c/T_p increases, as would be expected. The large difference between the supercritical and subcritical cases for a given T_c/T_p is due simply to the fact that $w_p/w_m = 1$ for the former and $w_p/w_m = 0.1$ for the latter. If the values of g_p for the subcritical case are multiplied by 10, they very nearly fall on the curve for the supercritical case, in the range of T_c/T_p where the two overlap.

Finally, to complete the description of the vortex from the nuclear standpoint, we need some measure of the total amount of fissionable gas and of propellant gas in it. We may define a mean propellant density by

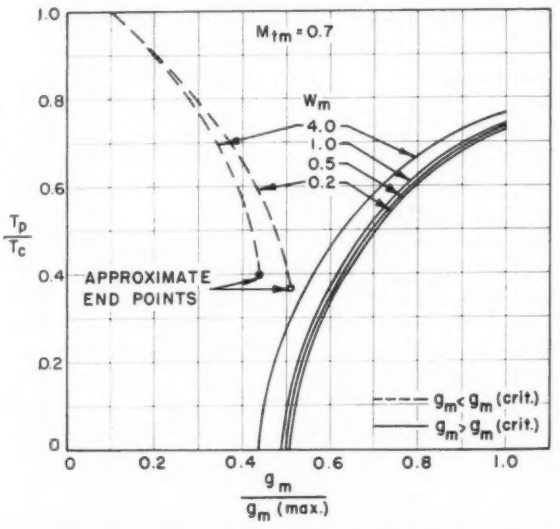

FIG. 10. Dependence of the overall temperature ratio, T_p/T_c on the ratio of the heating parameter g_m to its maximum permissible value; for $M_{tm} = 0.7$.

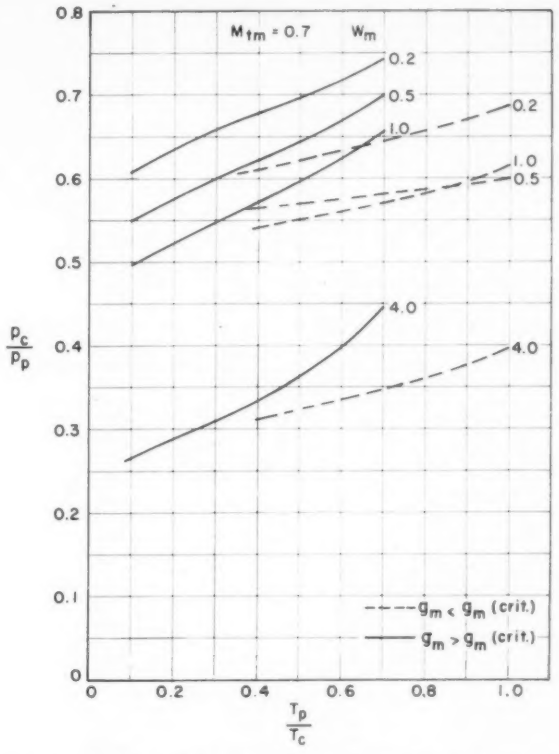

FIG. 11. Dependence of the overall pressure ratio, p_c/p_p, on the overall temperature ratio, T_p/T_c; for $M_{tm} = 0.7$.

$$\frac{\bar{\rho}_1}{\rho_{1p}} = \frac{\rho_{1c}{}^* r_c{}^{*2} + 2\int_{r_c{}^*}^{r_p{}^*} \rho_1{}^* r^* dr^*}{\rho_{1p}{}^* r_p{}^{*2}} \quad (28)$$

if we assume $\rho_1{}^*$ is constant at $\rho_{1c}{}^*$ for $r^* < r_c{}^*$. Similarly, if we define a mean density ratio, $\bar{w}$, by

$$\frac{\bar{w}}{w_m} = 2\,\frac{\rho_{1p}}{\bar{\rho}_1}\,\frac{T_p{}^*}{p_p{}^* r_p{}^{*2}}\int_{r_c{}^*}^{r_p{}^*} n_2{}^* r^* dr^* \quad (29)$$

then the average density of the fissionable gas is $\rho_2{}^* = \bar{w}(\bar{\rho}_1/\rho_{1p})\rho_{1p}$. $\bar{\rho}_1/\rho_{1p}$ and $\bar{w}/w_m$ are given in Figs. 16 and 17 for $M_{tm} = 0.7$. We see that $\bar{w}/\bar{w}_m$ is largest for the supercritical cases, because $w = w_m$ both at $r^* = 1$ and at $r^* = r_p{}^*$; and that it has a maximum, because w deviates more from w_m in the outer portions of the vortex as T_p/T_c decreases. $\bar{\rho}_1/\rho_{1p}$ increases monotonically with T_p/T_c, simply because of the influence of the temperature on the density. There is also some influence of w_m, which arises from the variation of the pressure drop with w_m.

Performance and Criticality Estimates

The significance of the results obtained from the preceding analysis of the heating separation process may perhaps be better revealed if incorporated into the performance analysis of a gaseous vortex reactor for rocket propulsion. In the present section the characteristic performance parameters of the rocket are

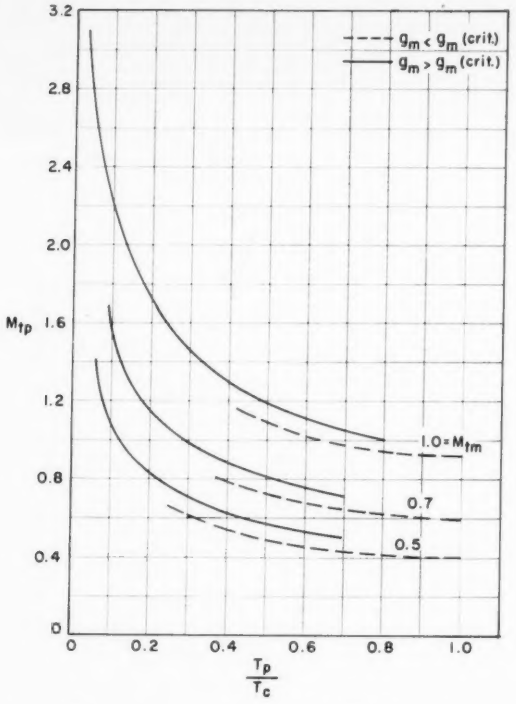

FIG. 12. Dependence of the tangential Mach number at the periphery, M_{tp}, on the overall temperature ratio, T_p/T_c.

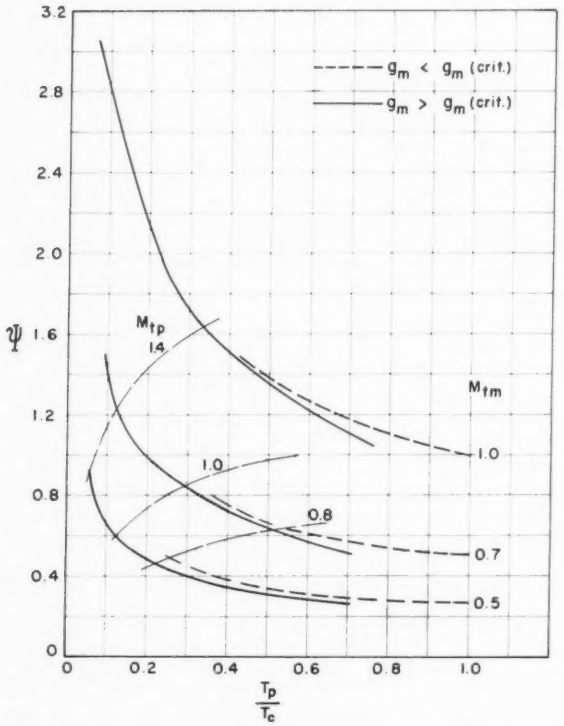

FIG. 13. Dependence of the relative mass flow capacity, Ψ, on the overall temperature ratio, T_p/T_c.

calculated in terms of the parameters derived from the separation analysis and from the nuclear configuration. To be definitive, such an analysis would have to include an optimization of the entire system for some mission, and this would imply a detailed study of many aspects of the vehicle configuration, as well as those of the power plant. The intent of the present analysis, however, is much more modest; it is simply to provide a physical feeling for the several parameters which characterize the performance of the vortex tube as applied to rocket propulsion.

To this end, the requirements imposed on the reactor system by the overall energy balance, and by criticality, will be estimated. The weight, thrust-to-weight ratio, neutron flux, and various other parameters will then be given for some representative examples.

It is assumed in these computations that the reactor core consists of a cylindrical bundle of vortex tubes such as that shown in Fig. 1, the diameter being equal to the length l of an individual tube. Both graphite and beryllium oxide will be considered as moderators. In those cases where the temperature ratio T_c/T_p is such that heat must be added to the propellant, by fissionable material, before it enters the vortex tubes, it will be assumed that the fissionable material not contained in the tubes is uniformly dispersed in the moderator. Some reduction in overall size and weight should be obtainable by concentrating this solid fuel in as small a volume as possible, but this refinement will not be considered here.

Energy Balance

Although most of the fission power generated in the vortex tubes appears directly as an increase in the enthalpy of the gas mixture, there will always be some fraction ζ carried by radiation which penetrates the gas and is deposited directly in the surrounding solid regions of the reactor. The radiation mechanism is both thermal and nuclear (gamma rays and neutrons); therefore, in general ζ will depend on the properties of the gas and the nuclear characteristics of the reactor.

In the special case that the propellant gas is the only available heat sink, the propellant must be passed first through the solid regions of the engine to remove the energy deposition represented by ζ, and thence into the vortex tubes for further heating. Consider now a system in which some of the fissionable material is contained in solid fuel plates so that a fraction f of the fission reactions occur in the solid regions. If P is the total power generated in this system, h_c the enthalpy per unit mass of propellant corresponding to the temperature in the vortex core, and $\dot{m}$ the mass flow rate of propellant, then $P = \dot{m}\, h_c$. The total power deposited in the solid regions P_s is then

$$P_s = fP + \zeta P_c = [f + \zeta(1 - f)]P$$

where $P_c = (1 - f)P$, the fission power released directly into the gas mixture in the cavity. Further, if h_p is the enthalpy corresponding to the maximum tempera-

ture in the solid, then for the present case $P_s = \dot{m}h_p$, and we obtain

$$h_c/h_p = 1/[f + \zeta(1 - f)] \qquad (30)$$

Now, the specific impulse I for a rocket engine with a completely expanded nozzle is simply $g^2I^2/2 = h$, where g is the gravitational constant. Thus, the ratio given in Eq. (30) is the square root of the corresponding specific impulses. The significance of this result may be appreciated if one thinks of the quantity I_p as the maximum possible specific impulse attainable in a solid-fuel (temperature-limited) reactor. Then I_c/I_p would be the performance gain to be realized in incorporating some gas-phase fission heating. Fig. 18 shows this ratio as a function of f for the case $\zeta = 0.1$. Evidently, with an all gas-phase reactor ($f = 0$), it is possible to achieve specific impulses about three times as large as with an all solid-fuel nuclear engine.

If the restriction that all heat must be transferred to the propellant is removed by providing radiators for rejection of heat from the solid parts of the reactor, h_c/h_p can, at least in principle, be larger than the value given by Eq. (30). However, if an appreciable fraction of the total power is radiated, the radiator weight will be so large that the thrust-to-weight ratio will necessarily be much less than unity. This is not necessarily a disadvantage for space propulsion applications.

Criticality

Estimates of the critical size of the reactor have been obtained from two-group, two-region calculations for a completely reflected cylinder. The calculations were done on a digital computer using a two-group, two-region code, and a reflector savings program.*

The reactor core was taken to be a homogeneous mixture of moderator, plutonium and hydrogen. The proportions of the latter two were determined from the separation analysis. Fast fission was neglected and the resonance escape probability was taken as unity.

The thickness of the beryllium reflector for each reactor and the void fraction β of the core were selected to minimize the combined core and reflector weight. The calculations made by Lafyatis and Nelson indicated that $\beta = 0.6$ would be near optimum for most configurations of interest.

The fission cross section of plutonium has a marked resonance at a neutron energy of 0.3 electron volts, which coincides with the mean thermal neutron energy (Maxwell distribution) for a temperature of 2,330°K. Thus, the neutron temperature has an important effect on the critical mass for the systems considered here. It was assumed that the neutron temperature was equal to the moderator temperature, which in turn was taken equal to T_p.

Rocket Engine Performance

For the present purpose, the performance of the vortex tube reactor may be characterized by the specific impulse, the total thrust, and the ratio of thrust to reactor (core plus reflector) weight.

The specific impulse is determined from the total energy content H_c of the propellant gas at the vortex "core" condition. In the present system, the total energy is given by the enthalpy per unit mass of gas, h_c, plus the kinetic energy due to the tangential velocity v_c of the propellant at the core radius r_c. Thus,

* The calculations were made by P. G. Lafyatis and M. L. Nelson of the Oak Ridge National Laboratory, USAEC.

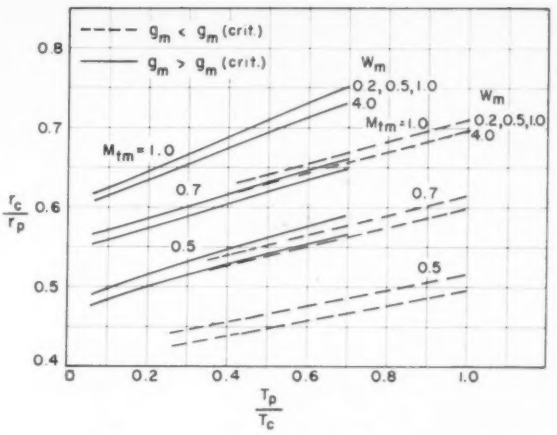

FIG. 14. Dependence of the ratio of exit radius to tube radius on the overall temperature ratio, T_p/T_c.

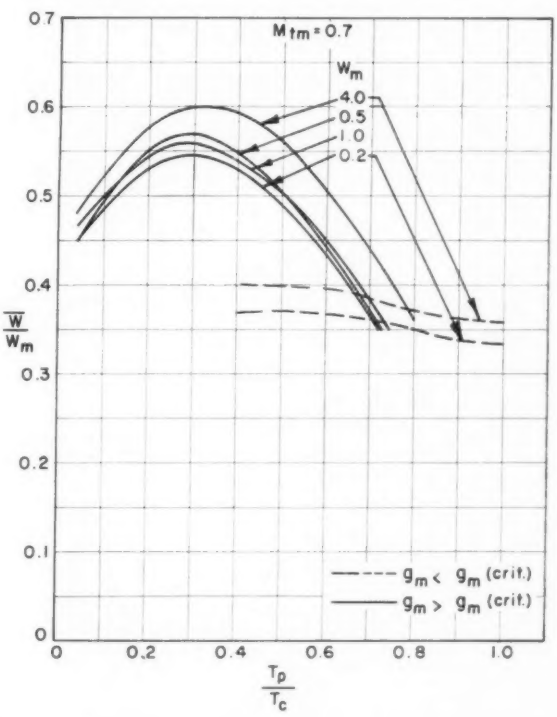

FIG. 15. Dependence of the ratio of average to maximum density on the overall temperature ratio, T_p/T_c, for $M_{tm} = 0.7$.

$$H_c = h_c + (v_c^2/2) \tag{31}$$

If we use the fact that the tangential velocity in the vortex is inversely proportional to the radius, then we can relate v_c to v_p, the tangential velocity at the tube periphery, thus:

$$v_c^2 = \gamma_c R_c T_p M_{tp}^2 (r_p/r_c)^2$$

where γ_c, R_c refer to the core conditions; and Eq. (31) may be written

$$H_c = h_c \left[1 + \frac{\gamma - 1}{2} M_{tp}^2 \left(\frac{r_p}{r_c}\right)^2 \left(\frac{T_p}{T_c}\right) \right] \tag{32}$$

where we have used $h_c = C_{pc} T_c$. For the systems to be considered here, the second term in Eq. (32) is in the order of 0.2 and will be neglected in these computations. This means that we are underestimating the energy available to the gas and will therefore obtain a slightly conservative estimate of engine performance.

The total thrust F from the assembly of vortex tubes in the reactor is

$$F = Nl\mathfrak{M}_1 c \tag{33}$$

where l is the length of the tubes, N the number of tubes, $\mathfrak{M}_1$ is the mass flow rate per unit length of tube, and c is the rocket exhaust velocity, where $c^2/2 = h_c$. Now, the product $\mathfrak{M}_1 l$ is related to the nozzle throat radius r_t by

$$\mathfrak{M}_1 l = \pi r_t^2 \rho_t a_t \tag{34}$$

where ρ_t is the propellant gas density and a_t the velocity of sound at the throat. These are related to the core conditions by

$$\rho_t = \rho_{1c} \left(\frac{2}{\gamma + 1} \right)^{1/(\gamma-1)}$$

and

$$a_t^2 = 2 \left(\frac{\gamma - 1}{\gamma + 1} \right) h_c$$

Thus, Eq. (34) may be written

$$\mathfrak{M}_1 l = \pi r_p^2 \rho_{1c} [(\gamma - 1) h_c]^{1/2} \times \left(\frac{2}{\gamma + 1} \right)^{(\gamma+1)/2(\gamma-1)} \left(\frac{r_c}{r_p}\right)^2 \left(\frac{r_t}{r_c}\right)^2 \tag{35}$$

Substitution into the thrust equation yields

$$F = (\pi/4) \beta l^2 \gamma p_c \left(\frac{2}{\gamma - 1} \right)^{1/2} \times \left(\frac{2}{\gamma + 1} \right)^{(\gamma+1)/2(\gamma-1)} \left(\frac{r_c}{r_p}\right)^2 \left(\frac{r_t}{r_c}\right)^2 \tag{36}$$

where we have used the relation $\rho_{1c} = \gamma p_c/(\gamma - 1) h_c$ and introduced the expression for the reactor core volume $\pi r_p^2 Nl/\beta$, which is $\pi l^3/4$ for a square cylinder, to eliminate N. The quantity r_t/r_c is the ratio of nozzle throat radius to the radius at which $w \to w_c$ in the vortex tube. Note that $0 < r_t/r_c < 1$. It can be seen from Eq. (36) that the thrust of this system is actually limited by the size of the area which can be provided at the back face of the reactor for the exhaust nozzles, without allowing the fissionable material to be blown out. This area is $\pi \beta l^2 (r_c/r_p)^2/4$. The thrust is also proportional to the pressure p_c, but independent of the "core" temperature T_c. The ratio r_c/r_p is of course

TABLE 3

Numerical Examples of Vortex Tube Reactors*

Parameter	Case Number 1	2	3	4	5	6
T_c/T_p	1.56	1.56	1.56	4.05	4.05	4.05
w_m	0.5	1.0	4.0	0.5	1.0	4.0
M_{tp}	1.0	1.0	1.0	1.0	1.0	1.0
T_c, °R.	7,020	7,020	7,020	10,000	10,000	10,000
T_p, °R.	4,500	4,500	4,500	2,470	2,470	2,470
p_c, atm.	100	100	100	100	100	100
p_p, atm.	213	231	498	171	188	338
r_c/r_p	0.66	0.66	0.65	0.59	0.59	0.58
$\bar{w}/\omega_m$	0.34	0.35	0.36	0.56	0.56	0.54
g_p	0.96	0.96	1.50	56	56	81
$\mathfrak{M}_1$, lb./sec. ft.	0.0198	0.0198	0.0198	0.0121	0.0121	0.0121
I, sec.	1,196	1,196	1,196	1,426	1,426	1,426
n_{2g}, cm.^{3}	0.40×10^{18}	0.85×10^{18}	5.2×10^{18}	0.49×10^{18}	1.01×10^{18}	5.12×10^{18}
l, ft.	15.4 (14.0)	10.2 (8.5)	3.8 (4.1)	16.8 (16.7)	11.7 (10.1)	4.5 (4.5)
$F/(r_t/r_c)^2$, lb.	15.3×10^6 (12.6×10^6)	6.7×10^6 (4.65×10^6)	0.90×10^6 (1.02×10^6)	14.6×10^6 (14.3×10^6)	7.02×10^6 (5.25×10^6)	1.01×10^6 (1.01×10^6)
Weight, lb.	180,000 (120,000)	75,000 (35,000)	10,000 (5,300)	230,000 (180,000)	100,000 (55,000)	15,000 (6,700)
$[F/(r_t/r_c)^2]$/weight	85 (98)	89 (133)	90 (192)	64 (80)	70 (94)	67 (150)
$N/(r_t/r_c)^2$	55,400 (50,400)	36,700 (30,600)	13,300 (14,300)	66,200 (65,800)	46,100 (39,800)	17,100 (17,100)
$\phi/(r_t/r_c)^2$, neutrons/cm.^{2}-sec.	0.78×10^{18} (0.85×10^{18})	0.53×10^{18} (0.64×10^{18})	0.26×10^{18} (0.24×10^{18})	1.6×10^{18} (1.6×10^{18})	1.0×10^{18} (1.2×10^{18})	0.54×10^{18} (0.54×10^{18})
$r_p(r_t/r_c)$, in.	0.305 (0.291)	0.248 (0.226)	0.154 (0.159)	0.304 (0.303)	0.253 (0.236)	0.160 (0.160)

* Performance parameters based on $\beta = 0.6$, $\gamma = 1.31$, $Q = 7.36 \times 10^{-12}$ cal./fission, $C_{p1} = 3.54$ cal./gm.-°K., and $\sigma_f = 975$ barns for $T_p = 2{,}470$°R., and $C_{p1} = 5.25$ cal./gm.-°K. and $\sigma_f = 810$ barns for $T_p = 4{,}500$°R.

determined by the diffusion process in the tubes. It depends principally upon M_{tm}, increasing as M_{tm} increases.

Eq. (36) contains the factor $(r_t/r_c)^2$, which may have any value from zero to unity. Thus, for a given set of vortex tube parameters and critical reactor size, the thrust may have any value from zero to that given by Eq. (36) for $r_t/r_c = 1$. As this ratio increases, the number of tubes in the reactor increases, each tube decreasing in diameter. This may be seen by equating Eqs. (33) and (36) and solving for N. Then, using $h_c \approx C_{pc}T_c$, we obtain

$$N = \frac{\pi\beta l p_c \gamma^{1/2}}{4\mathfrak{M}_1(RT_c)^{1/2}} \left(\frac{2}{\gamma+1}\right)^{\frac{\gamma+1}{2(\gamma-1)}} \left(\frac{r_c}{r_p}\right)^2 \left(\frac{r_t}{r_c}\right)^2 \quad (37)$$

For a given set of vortex tube parameters, $\mathfrak{M}_1$ and r_c/r_p are fixed. Then, for fixed p_c and T_c, the number of tubes is proportional to $(r_t/r_c)^2$.

The average neutron flux required to give the heat release rates implied by these performance parameters may be determined from Eq. (27), which gives

$$\phi = g_p \frac{(1+w_c)C_{p1}T_p}{2n_{2p}\sigma_f Q}\left(\frac{\mathfrak{M}_1}{\pi r_p^2}\right)$$

where $h_p = C_{p1}T_p$. The last factor above may be eliminated by applying Eq. (35). If we note also that

$$n_{2p} = w_p\rho_{1p}/m_2 = w_p(p_c/m_2RT_c)(p_p/p_c)(T_c/T_p)$$

then the expression for ϕ may be written

$$\phi = \frac{g_p(1+w_c)m_2C_{p1}T_c(\gamma RT_c)^{1/2}}{2w_p l\sigma_f Q} \times \left(\frac{T_p}{T_c}\right)^2 \left(\frac{2}{\gamma+1}\right)^{\frac{\gamma+1}{2(\gamma-1)}} \left(\frac{p_c}{p_p}\right)\left(\frac{r_c}{r_p}\right)^2 \left(\frac{r_t}{r_c}\right)^2 \quad (38)$$

g_p increases with increasing T_c/T_p (Fig. 15), and C_{p1} also increases with increasing T_c, so that ϕ will increase quite rapidly with increasing T_c.

Numerical Examples

It was mentioned previously that the enthalpy ratio h_c/h_p (or the temperature ratio T_c/T_p) is the most important parameter in determining the characteristics of the vortex tube. On the other hand, the fissionable material concentration determines the overall size and weight of the reactor. Accordingly, examples have been selected with two representative values of T_c/T_p, and three values of w_m. The pressure at the vortex core has been taken as 100 atmospheres for all cases, so that w_m is nearly a direct measure of the fuel concentration in the gas phase.

Cases 1, 2, and 3 have $T_c/T_p = 1.56$. This temperature ratio corresponds to about half the heat being added to the propellant by solid fuel elements, and half by the vortex tubes. The temperature leaving the solid reactor, T_p, has been set at the upper limit for graphite fuel elements, namely, 4,500°R.; hence the chamber temperature, T_c, is 7,020°R. This is of the same order as the chamber temperature for contemporary chemical rocket motors—e.g., liquid O_2 and JP-4 give $T_c \approx 6{,}300$°R.

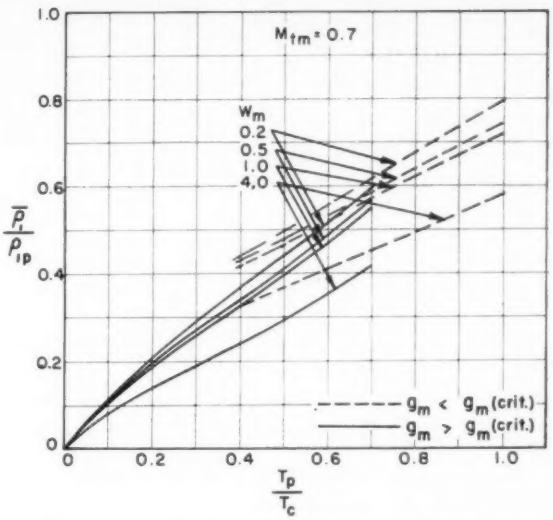

FIG. 16. Dependence of the ratio of average to peripheral propellant densities on the overall temperature ratio, T_p/T_c; for $M_{tm} = 0.7$.

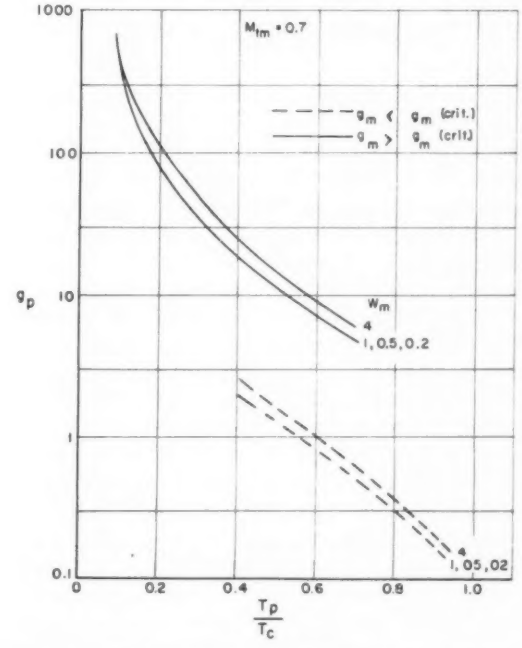

FIG. 17. Dependence of the heating parameter, g_p, on the overall temperature ratio, T_p/T_c; for $M_{tm} = 0.7$.

Cases 4, 5, and 6 have the largest values of T_c/T_p possible for $T_c = 10{,}000$°R. They represent systems with chamber temperatures considerably higher than the best obtainable with chemical rockets. At the same time, the temperatures entering the vortex tubes are considerably below the limits for graphite or the refrac-

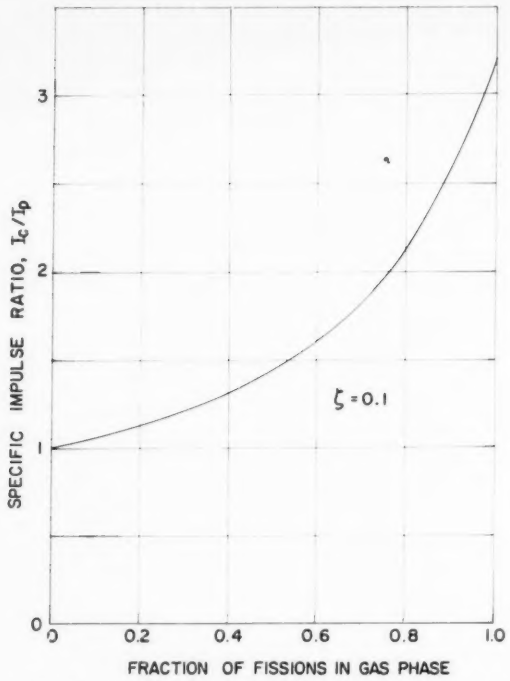

FIG. 18. Specific impulse ratio, I_c/I_p, as function of gas-phase fission heating.

tory metals. These systems have all fissionable material in the gas phase.

Some characteristics of these reactors are shown in Table 3. The values for beryllium-oxide-moderated reactors are shown in parentheses. The first few quantities listed are characteristic of the vortex tube itself, and hence are independent of the moderator used.

Although the reactor weights (core plus reflector) are very high for fuel concentrations of the order of 0.5×10^{18} cm.$^{-3}$, they are quite reasonable if the concentration can be increased to about 5.0×10^{18} cm.$^{-3}$ These higher fuel concentrations imply high pumping pressures, however. For Case 3, p_p is 498 atmospheres, or 7,320 psi. The pumping pressure must be taken as about twice this figure, to allow for the pressure drops in the inlet nozzles and solid reactor. It should be noted that the increase in average fuel concentration, $\bar{n}_2$, by a factor of 10 from Case 1 to Case 3 requires only a little more than doubling of the pumping pressure. This increase is due to the higher pressure drop caused by increasing w_m. To achieve the same concentration increase by raising the general pressure level with constant w_m, it would be necessary to increase the pumping pressure tenfold, to about 4,000 atmospheres. The beryllium-oxide-moderated reactors are in all cases lighter than the corresponding graphite-moderated reactors. This is due to the decreased neutron-slowing-down length and decreased diffusion length in beryllium oxide as compared to graphite.

Although the reactor weights are rather high, the thrust-to-weight ratios are also quite high if r_t/r_c is near unity. It may, however, be more realistic to take r_t/r_c a little less than unity, to allow for three-dimensional flow effects in the long, thin, vortex tubes. If r_t/r_c is taken as 0.5, for example, the beryllium-oxide-moderated reactor described in Case 3 has a thrust of 255,000 lbs., and a thrust-to-weight ratio of 48. The latter figure is somewhat lower than that for a chemical system; however, the specific impulse is at least twice that of the best chemical rockets. In order to give this performance the reactor would contain 950 vortex tubes, each 0.32 in. in diameter. The average neutron flux would be 5.2×10^{16} neutrons/sec.-cm.^{2}

It seems from comparison of Cases 3 and 6, for example, that as T_c is increased, the critical size and weight of the reactor increase. This effect is due to a lower average fuel concentration in the higher temperature reactor. The gas-phase fuel concentrations, $\bar{n}_{2g}$, are about the same in the two cases, but the lower-temperature reactor contains considerable solid fuel.

Concluding Remarks

In conclusion, it seems worth while to summarize the more important results of the analysis. One of these is that the mass flow capacity per unit length of the vortex tube, as limited by the rate of diffusion of propellant through the fissionable gas, is independent of the tube diameter. Thus, even though the mass flow per unit of tube length is only of the order of 0.01 pounds per second per foot, the mass flow capacity per unit volume of an assembly of small-diameter tubes can be quite large.

A second important conclusion is that containment of the fissionable material within the vortex, away from its outer boundary, is possible only if the pressure gradient decreases monotonically with increasing radius. As a corollary of this, there is a critical heating rate above which such containment is impossible.

Insofar as the vortex containment mechanism limits the performance of the gaseous nuclear rocket, the performance capability is very high. It may well be that the performance will actually be limited by other factors, such as radiant heat transfer from the gas to solids, the difficulty of maintaining fissionable material in gaseous form at the required concentrations and temperatures, and the difficulty of generating vortices with the required low radial mass-flow rates and high tangential velocities. The potential of the gaseous fission rocket seems to warrant intensive study of these problems.

References

[1] Kerrebrock, J. L., and Meghreblian, R. V., *An Analysis of Vortex Tubes for Combined Gas-Phase Fission Heating and Separation of the Fissionable Material*, Oak Ridge National Laboratory Memorandum CF 57-11-3, November 1, 1957. Classification AEC-C86, declassified December 21, 1959.

[2] Evans, R. D., *The Atomic Nucleus*, McGraw-Hill Book Co., Inc., 1955.

[3] Chapman, S., and Cowling, T. G., *The Mathematical Theory of Non-Uniform Gases*, Cambridge University Press, 1958.

Torsional Analysis of Thin-Walled Shells With Many Closely Spaced Spar Webs

DAVID W. FOX* AND ROBERT M. RIVELLO**
The Johns Hopkins University

Summary

The torsional shear flow distribution and rigidity of thin-walled cylinders with closely spaced internal spar webs is investigated. The spar webs are assumed to be so numerous that the spar material may be regarded as a continuous shear-resisting medium. The differential equation and boundary conditions which must be satisfied by the shear flow are derived from the Bredt theory of torsion. This differential equation is solved explicitly for those cases in which the shell cross section is given by a parallelogram, trapezoid, triangle, or double wedge. The results are related to the corresponding rigidities and shear flows given for the same section by the Bredt theory in which the internal spar material is neglected.

Symbols

A	=	area
G	=	shear modulus of elasticity
J	=	torsion constant
T	=	torque
a, b, c d, e	=	cross-sectional dimensions
h	=	height
k	=	core solidity defined by Eq. (6)
n	=	number of cells
q	=	shear flow
s	=	arc length
t	=	thickness
x, y	=	Cartesian coordinates
α	=	angle between section face and x axis
θ	=	angle of twist per unit length
τ	=	shear stress

Subscripts

i	—	refers to ith cell
t	—	top
b	—	bottom

Introduction

THE CURRENT TREND toward increased unit loading and decreased thickness of aerodynamic surfaces has resulted in the use of structures having relatively heavy skins supported by a large number of internal webs that stabilize the skin and resist shear and torsional loads. For this type of structure, known as multispar or multicell construction, the torsion may be analyzed, when warping is not restrained, by the well-known Bredt theory.[1] When both the shear flow and the angle of twist are desired this procedure requires the solution of a system of simultaneous linear algebraic equations equal in size to the number of cells plus one. When the number of cells is large and exact solution of the simultaneous equations becomes tedious, approximate methods of solution involving less labor become desirable. In this direction, methods of successive approximation and iteration[2–4] have been used. The process of idealizing the structure by lumping several webs together in order to reduce the number of equations to a more manageable size seems less desirable. On the other hand, if the number of webs is quite large, another approach suggests itself, the concept of a continuous shear-supporting spar web medium. In this idealization, which is the subject of this paper, the simultaneous equations are approximated by a linear second-order differential equation with end conditions. In this note the boundary value problems are solved explicitly for the differential equations that arise from the consideration of cross sections in the shape of a parallelogram, trapezoid, triangle, or double wedge. These results, which apply to sections often used in supersonic airfoils, should be useful for design studies in which the work involved in solving a large system of simultaneous equations is not justified or when the number of cells is so large that solution of the system of equations is not feasible. An example of the latter case occurs in the consideration of some forms of sandwich box-beam construction.[5]

The theory presented here was given in less complete form in reference 6 and has been extended to the calculation of shear flows due to a shearing force and to the location of the shear center.[7]

A recent note by Niedenfuhr[8] treats the problem of torsion of a uniform rectangular section with any number of equally spaced identical cells by the techniques of linear difference equations with constant coefficients.

In contrast to this paper, in which it is assumed that the continuous shear-supporting web medium possesses shear rigidity in one direction only, Seide[9] and Cheng[10] have treated the case of a rectangular cross-section sandwich with a nonisotropic core and McComb[11] studied rectangular, triangular, and diamond cross sections with an isotropic core reinforcement.

Theory

We consider a cylindrical structure with the cross

Received June 30, 1960.

* Research Assistant Professor, Institute for Fluid Dynamics and Applied Mathematics, University of Maryland, College Park, Md., and Consultant, Applied Physics Laboratory, The Johns Hopkins University, Silver Spring, Md.

** Associate Professor of Aeronautical Engineering, University of Maryland, College Park, Md., and Consultant, Applied Physics Laboratory, The Johns Hopkins University, Silver Spring, Md.

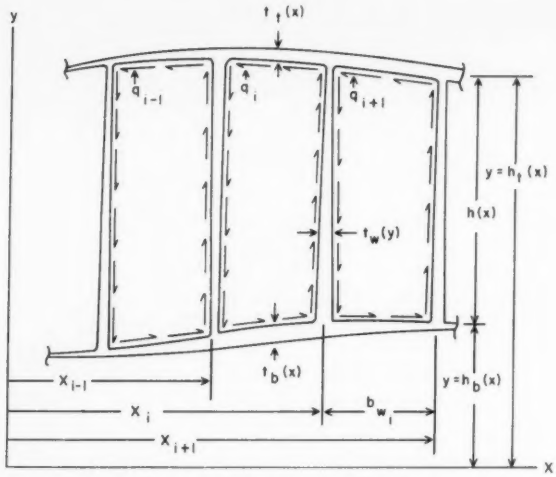

FIG. 1. Segment of multicell structure.

section divided into a number of cells by vertical internal webs. We assume that all walls of the cross section are thin and that warping is unrestrained so that Bredt's theory of torsion applies.

For such a structure the ith cell together with the two adjacent cells is shown in Fig. 1. In terms of the shear flows, the angle of twist per unit length is determined by the Bredt equation[1] which in the usual notation is given by

$$2A_i\theta = \int_{C_i} (q/Gt)\, ds \tag{1}$$

Writing out the integral and the expression for A_i in Eq. (1) gives

$$(q_i - q_{i-1}) \int_{h_b(x_{i-1})}^{h_t(x_{i-1})} \frac{dy}{t_w(y)} - (q_{i+1} - q_i) \times \int_{h_b(x_i)}^{h_t(x_i)} \frac{dy}{t_w(y)} + q_i \int_{x_{i-1}}^{x_i} \left\{ \frac{1}{t_t(x)} \left[1 + \left(\frac{dh_t}{dx} \right)^2 \right]^{1/2} + \frac{1}{t_b(x)} \left[1 + \left(\frac{dh_b}{dx} \right)^2 \right]^{1/2} \right\} dx = 2G\theta \int_{x_{i-1}}^{x_i} h(x)\, dx \tag{2}$$

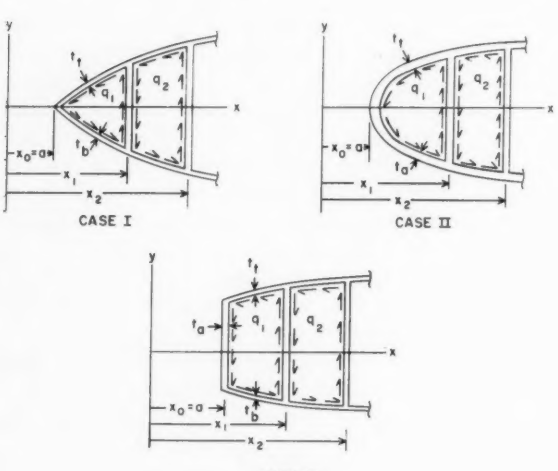

FIG. 2. Geometry of end closures.

in which h is defined by $h(x) = h_t(x) - h_b(x)$, the subscripts t and b referring to the top and bottom surfaces, respectively. Here we have assumed G to be a constant throughout the structure. If G is not the same everywhere, Eq. (2) still holds if the G occurring there and in later equations is interpreted as a reference shear modulus G_{ref} and the t's are interpreted to be equivalent thicknesses defined by

$$t_{equiv} = t(G/G_{ref})$$

Assuming that h_t, h_b, t_t, and t_b are smooth enough, the mean value theorem for integrals may be applied to Eq. (2) to yield

$$(q_i - q_{i-1}) \frac{h(x_{i-1})}{\bar{t}_w(x_{i-1})} - (q_{i+1} - q_{i-1}) \frac{h(x_i)}{\bar{t}_w(x_i)} + \beta(\bar{x}) q_i (x_i - x_{i-1}) = 2G\theta h(\bar{x})(x_i - x_{i-1}) \tag{3}$$

where $\bar{x}$ satisfies $x_{i-1} \leq \bar{x} \leq x_i$, $\bar{t}_w(x_i)$ is the effective thickness of the cell wall at x_i defined by the relation

$$\frac{1}{\bar{t}_w(x_i)} = \frac{1}{h(x_i)} \int_{h_b(x_i)}^{h_t(x_i)} \frac{dy}{t_w(y)} \tag{4}$$

and $\beta(x)$ is given by

$$\beta(x) = \frac{1}{t_t(x)} \left[1 + \left(\frac{dh_t}{dx} \right)^2 \right]^{1/2} + \frac{1}{t_b(x)} \left[1 + \left(\frac{dh_b}{dx} \right)^2 \right]^{1/2} \tag{5}$$

Define $k(x_i)$ by the relation

$$k(x_i) = \bar{t}_w(x_i)/(x_{i+1} - x_i) = \bar{t}_w(x_i)/b_{w_i} \tag{6}$$

By use of this definition Eq. (3) can be put into the suggestive form

$$\frac{(q_{i+1} - q_i)\, h(x_i)}{(x_{i+1} - x_i)\, k(x_i)} - \frac{(q_i - q_{i-1})\, h(x_{i-1})}{(x_i - x_{i-1})\, k(x_{i-1})} - \beta(\bar{x}) q_i = -2G\theta h(\bar{x}) \tag{7}$$

which is a formal difference approximation to the second-order linear differential equation

$$\frac{d}{dx} \left(\frac{h(x)}{k(x)} \frac{dq}{dx} \right) - \beta(x) q = -2G\theta h(x) \tag{8}$$

The boundary conditions that are appropriate with Eq. (8) arise from the consideration of the Bredt equations for the end cells, and consequently they depend on the manner in which the section is closed. Three typical cases are shown in Fig. 2.

If the section is closed by a sharp edge as shown in Case I of Fig. 2, the appropriate equation for the first cell, obtained in the same manner as Eq. (7), is given by

$$\left(\frac{q_2 - q_1}{x_2 - x_1} \right) \left(\frac{h(x_1) - h(x_0)}{x_1 - x_0} \right) - k(x_1) \beta(\bar{x}) q_1 = -2G\theta h(\bar{x}) k(x_1) \tag{9}$$

This may be regarded as a formal difference approximation to the differential boundary condition

$$\left[\frac{dq}{dx} \frac{dh}{dx} - k\beta q \right]_{x = a^+} = 0 \tag{10}$$

The notation a^+ means the limit from the right of a, and similarly a^- means the limit from the left of a.

If the section is closed by a rounded edge as in Case II, then the first cell equation may be written

$$\left(\frac{q_2 - q_1}{x_2 - x_1}\right) - q_1\beta(\bar{x})k(x_1)\left(\frac{x_1 - x_0}{h(x_1)}\right) = -2G\theta k(x_1)\left(\frac{x_1 - x_0}{h(x_1)}\right) \quad (11)$$

and the corresponding boundary condition for Eq. (8) is given by

$$\left[\frac{dq}{dx} - qk\left(\frac{1}{t_t}\frac{h_t}{h} + \frac{1}{t_b}\frac{h_b}{h}\right)\right]_{x=a^+} = 0 \quad (12)$$

In Case III the closure is accomplished by a web of thickness t_a. Here the equation for the first cell may be written

$$\left(\frac{q_2 - q_1}{x_2 - x_1}\right)h(x_1) - k(x_1)q_1\left[\frac{h(x_a)}{\bar{l}(x_0)} + \beta(\bar{x})(x_1 - x_0)\right] = -2G\theta h(\bar{x})k(x_1)(x_1 - x_0) \quad (13)$$

and the appropriate boundary condition for Eq. (8) is

$$\left[\frac{dq}{dx} - \frac{k}{l_a}q\right]_{x=a^+} = 0 \quad (14)$$

Similarly, the boundary conditions for sharp-edge, rounded-edge, and web closures at the right-hand side of the cross section are found to be

$$\left[\frac{dq}{dx}\frac{dh}{dx} + k\beta q\right]_{x=c^-} = 0 \quad (15)$$

$$\left[\frac{dq}{dx} + qk\left(\frac{1}{t_t}\frac{h_t}{h} + \frac{1}{t_b}\frac{h_b}{h}\right)\right]_{x=c^-} = 0 \quad (16)$$

and

$$\left[\frac{dq}{dx} + \frac{k}{t_c}q\right]_{x=c^-} = 0 \quad (17)$$

Whenever the section is interrupted by a thick web or a change in construction which reflects itself in a discontinuity in the coefficients of Eq. (8), it is necessary to have two conditions in order to join the values of q which hold to the right and to the left. If there is a web of thickness t_d at $x = d$, then the appropriate conditions arise from the limiting forms of the equations which hold for the cells adjacent to the web. They are

$$\frac{1}{k}\frac{dq}{dx}\bigg|_{x=d^+} = \frac{q(d^+) - q(d^-)}{t_d} \quad (18)$$

and

$$\frac{1}{k}\frac{dq}{dx}\bigg|_{x=d^-} = \frac{q(d^+) - q(d^-)}{t_d} \quad (19)$$

If there occurs at $x = e$ a discontinuity in construction with no thick web, then the shear flow q and $(h/k)(dq/dx)$ must be continuous. The matching conditions are thus

$$q\big|_{x=e^+} = q\big|_{x=e^-} \qquad \frac{h}{k}\frac{dq}{dx}\bigg|_{x=e^+} = \frac{h}{k}\frac{dq}{dx}\bigg|_{x=e^-} \quad (20)$$

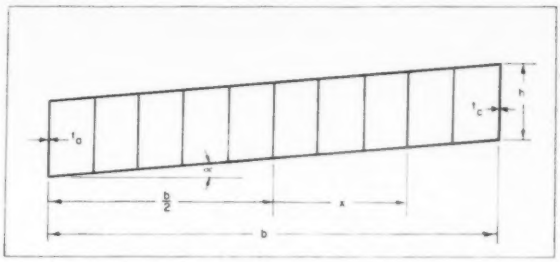

FIG. 3. Parallelogram cross-section.

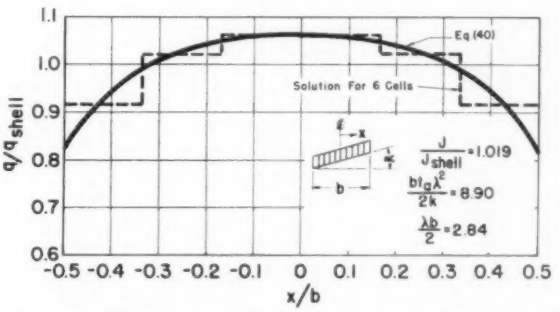

FIG. 4. Shear flow distribution for typical parallelogram cross section with identical end webs.

In the case in which the section is symmetrical about a vertical centerline (supposedly at $x = s$), we need consider only half of the section with the symmetric boundary condition

$$\frac{dq}{dx}\bigg|_{x=s} = 0 \quad (21)$$

The shear stress τ applied by the faces to the spar web medium is given by

$$\tau = dq/dx \quad (22)$$

and an approximation to the web shear flow in the finite case is obtained by multiplying this stress by the web spacing b_w.

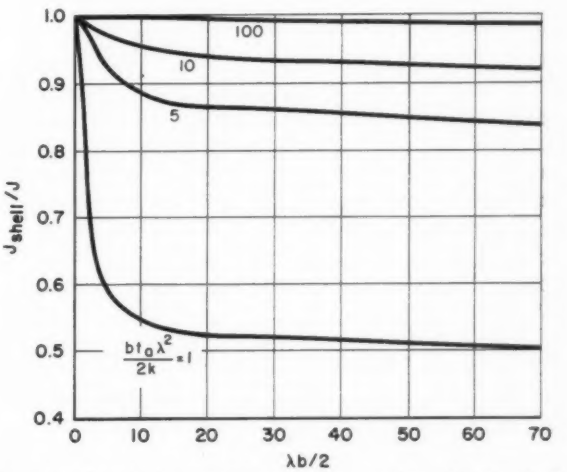

FIG. 5. J_{shell}/J for parallelogram cross section with identical end webs.

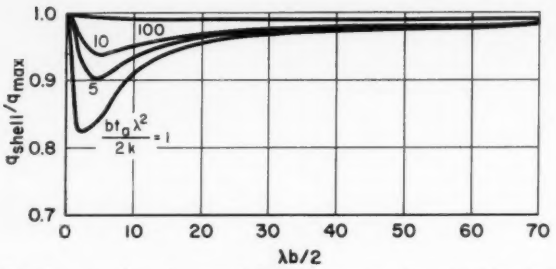

FIG. 6. q_{shell}/q_{max} for parallelogram cross section with identical end webs.

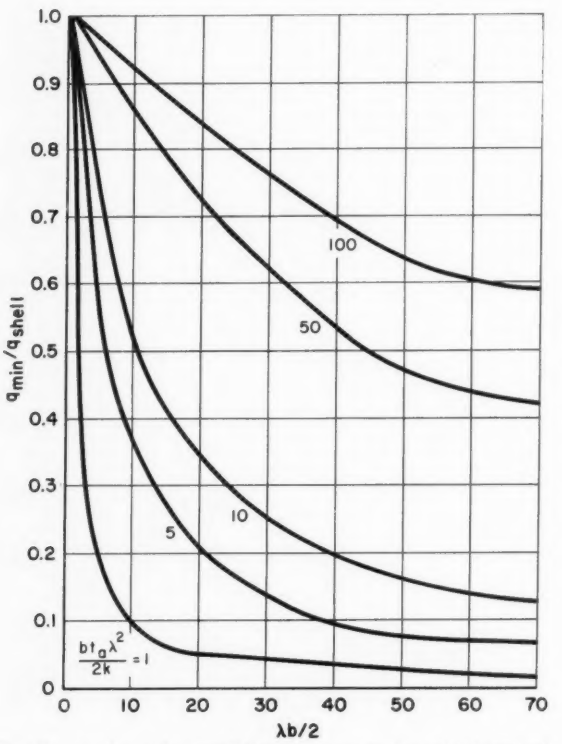

FIG. 7. q_{min}/q_{shell} for parallelogram cross section with identical end webs.

The differential equation (8) and an appropriate pair of boundary conditions form a self-adjoint system for which the existence of a unique solution can be guaranteed under reasonable restrictions on the coefficients of the differential equation (8). Such a solution gives an approximate solution to the interior cell equations and the end cell equations which arise from the Bredt theory, provided that $k(x)$ is chosen to be a smooth function that takes the values $k(x_i)$ defined by Eq. (6) at the points x_i. The function $k(x)$ accounts for the variation in spacing and effective thickness of the vertical webs and is, in fact, an expression for the solidity of the core of the idealized structure.

Altogether, the differential equation (8) with its boundary conditions defines an idealized model of the given structure in which the shape defined by h_t and h_b and the face thicknesses t_t and t_b is preserved, but in which the discrete internal webs are replaced by a continuous shear-supporting core.

It is clear that the solution of the Bredt equations (1) and that of the corresponding boundary value problem will depend linearly on the prescribed angle of twist per unit length. Since the torque rather than the angle of twist is usually given, the torque may be related to the angle of twist by the second Bredt relationship[1]

$$T = 2\sum_{i=1}^{n} A_i q_i \tag{23}$$

where the summation extends over all cells. For our idealized structure, the limiting form

$$T = 2\int qh\,dx \tag{24}$$

is used; here the integral is taken over the entire width of the cross section. In either case the torsion constant J is defined by the relationship

$$J = T/G\theta \tag{25}$$

It is not easy as a rule to obtain explicit solutions of Eq. (8) with appropriate boundary conditions; however, simple solutions can be found when h_t and h_b are linear in x, k is constant, and where t_t and t_b are constant but not necessarily equal. The simplest and most important cases in which k is constant arise from equally spaced webs of constant thickness. Within these restrictions, solutions for structures having cross sections in the shapes of parallelograms, trapezoids, triangles, and double wedges are given in the following. The usefulness of these solutions is increased by the frequent occurrence of such cross sections in supersonic airfoils.

For thin airfoils with sharp or web-closed edges described by the boundary conditions for Cases I or III of Fig. 2, the terms $(dh_t/dx)^2$ and $(dh_b/dx)^2$ will be small compared to unity. If, in addition, the top and bottom skin thicknesses are constant, β becomes nearly constant and approximately equal to $(t_t + t_b)/t_t t_b$.

Applications

In this section we will assume that the quantities t_t, t_b, and k are constants and that h_t and h_b are, at most, linear functions of x.

(1) *Parallelogram Cross Section*

When the cross section is a parallelogram, h is constant and h_t and h_b are linear with slope $\tan\alpha$ (see Fig. 3). Accordingly, Eq. (8) may be put into the especially simple form

$$(d^2q/dx^2) - \lambda^2 q = -2G\theta k \tag{26}$$

in which λ is given by

$$\lambda = \left[\frac{k(t_t + t_b)}{ht_t t_b \cos\alpha}\right]^{1/2} \tag{27}$$

The appropriate boundary conditions for end closures of thickness t_a and t_c at the ends $x = \pm b/2$ are given by Eqs. (14) and (17) so that

$$\left[\frac{dq}{dx} - \frac{k}{t_a} q\right]_{x=-b/2} = 0 \tag{28}$$

and

$$\left[\frac{dq}{dx} + \frac{k}{t_c} q\right]_{x=+b/2} = 0 \tag{29}$$

The solution of the system, given by Eqs. (26), (28), and (29), is

$$q = 2kG\theta\lambda^{-2}(1 - C \sinh \lambda x - D \cosh \lambda x) \tag{30}$$

in which C and D are expressed by

$$C = \frac{\lambda(t_a - t_c) \sinh (\lambda b/2)}{k[1 + (\lambda^2 t_a t_c/k^2)] \sinh \lambda b + \lambda(t_a + t_c) \cosh \lambda b} \tag{31}$$

and

$$D = \frac{\lambda(t_a + t_c) \cosh (\lambda b/2) + 2k \sinh (\lambda b/2)}{k[1 + (\lambda^2 t_a t_c/k^2)] \sinh \lambda b + \lambda(t_a + t_c) \cosh \lambda b} \tag{32}$$

Application of formulas (24) and (25) to the right-hand side of Eq. (30) yields the torsion constant in the form

$$J = 4hk\lambda^{-2}[b - 2D\lambda^{-1} \sinh (\lambda b/2)] \tag{33}$$

and the expression for the shear flow, given in terms of the torque, yields

$$q = 2Tk \lambda^{-2} J^{-1} (1 - C \sinh \lambda x - D \cosh \lambda x) \tag{34}$$

In the special case where $t_a = t_c$, the expressions are somewhat simpler. Corresponding to Eqs. (30), (33), and (34), we have

$$q = 2kG\theta\lambda^{-2} \left(1 - \frac{\cosh \lambda x}{\cosh (\lambda b/2) + (\lambda t_a/k) \sinh (\lambda b/2)}\right) \tag{35}$$

$$J = 4khb\lambda^{-2} \left(\frac{(\lambda b/2) \coth (\lambda b/2) + (bt_a\lambda^2/2k) - 1}{(\lambda b/2) \coth (\lambda b/2) + (bt_a\lambda^2/2k)}\right) \tag{36}$$

and

$$q = \frac{T}{2bh} \left(\frac{(\lambda b/2) \coth (\lambda b/2) + (bt_a\lambda^2/2k) - (\lambda b/2)(\sinh \lambda b/2)^{-1} \cosh \lambda x}{(\lambda b/2) \coth (\lambda b/2) + (bt_a\lambda^2/2k) - 1}\right) \tag{37}$$

It is interesting to compare the results in this simple case with those obtained from the Bredt theory when the internal webs are completely neglected. In the latter case, which we shall designate as the shell case, the results are

$$q_{shell} = T/2bh \tag{38}$$

and

$$J_{shell} = \frac{4(bh)^2}{(b/\cos \alpha)[(1/t_t) + (1/t_b)] + (2h/t_a)} \tag{39}$$

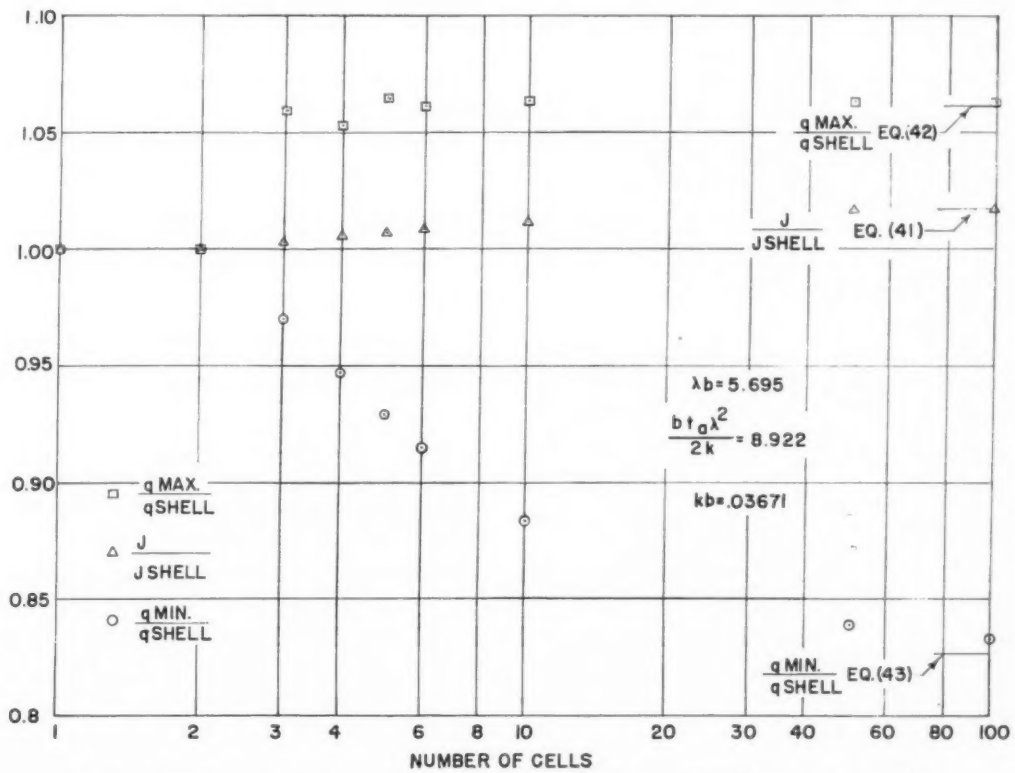

FIG. 8. Comparison of finite number of cells to theory for a typical parallelogram, cross section.

so that the ratios of corresponding quantities are given by

$$\frac{q}{q_{\text{shell}}} = \frac{(\lambda b/2)\coth(\lambda b/2) + (bt_a\lambda^2/2k) - (\lambda b/2)[\cosh \lambda x/\sinh(\lambda b/2)]}{(\lambda b/2)\coth(\lambda b/2) + (bt_a\lambda^2/2k) - 1} \tag{40}$$

and

$$\frac{J}{J_{\text{shell}}} = \left(1 + \frac{2k}{bt_a\lambda^2}\right)\frac{(\lambda b/2)\coth(\lambda b/2) + (bt_a\lambda^2/2k) - 1}{(\lambda b/2)\coth(\lambda b/2) + (bt_a\lambda^2/2k)} \tag{41}$$

Examination of the expression for q shows that the maximum shear flow occurs at the center and that the minimum ocurs at the ends. These values are given by

$$\frac{q_{max}}{q_{\text{shell}}} = \frac{(\lambda b/2)\tanh(\lambda b/4) + (bt_a\lambda^2/2k)}{(\lambda b/2)\coth(\lambda b/2) + (bt_a\lambda^2/2k) - 1} \tag{42}$$

and

$$\frac{q_{min}}{q_{\text{shell}}} = \frac{(bt_a\lambda^2/2k)}{(\lambda b/2)\coth(\lambda b/2) + (bt_a\lambda^2/2k) - 1} \tag{43}$$

A graph of a typical shear flow distribution obtained from Eq. (40) is given in Fig. 4. Similarly, Figs. 5, 6, and 7 give graphs of the functions in Eqs. (41), (42), and (43) for a range of values of the parameters which encompasses most practical cases. It may be observed that except for very small values of $bt_a\lambda^2/2k$ which do not ordinarily occur in practice, the values of the maximum shear flow and torsion constant are affected little by the interior structure. For the minimum shear flow this is not the case.

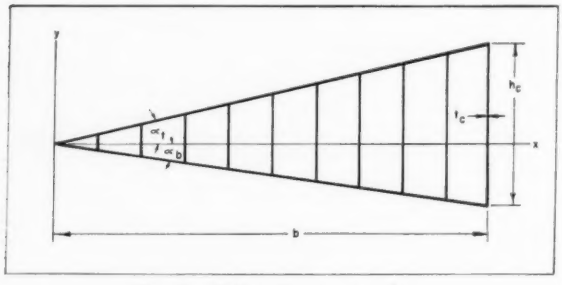

FIG. 9. Triangular cross section.

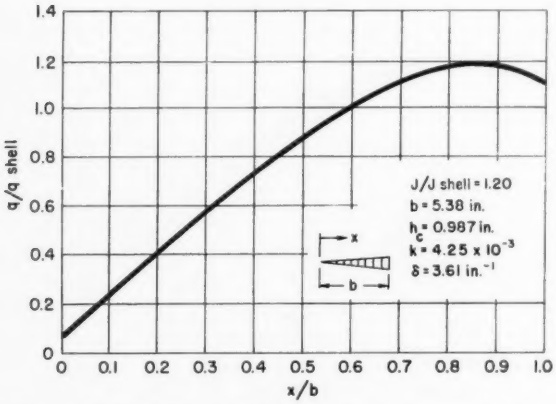

FIG. 10. Shear flow distribution for typical triangular cross section.

A comparison of the solutions for sections having a finite number of cells with the continuous solution obtained from Eqs. (41), (42), and (43) is shown in Fig. 8. In the results given there for typical section parameters, the web thickness t_w is decreased as the number of cells is increased so that k remains constant. It is evident that as the number of cells increases the ratios q_{max}/q_{shell} and J/J_{shell} approach those of the continuous solution rapidly, while the approach of q_{min}/q_{shell} is slower. The figure also indicates the degree of approximation that may be expected when sections with a large number of cells are approximated by lumping webs together instead of replacing them by a continuous spar web medium.

The shear flow distribution for a 6-cell section is compared with the distribution obtained from Eq. (40) in Fig. 4.

(2) *Triangular Cross Section*

In the triangular section it is convenient to choose the origin as vertex (see Fig. 9) and to designate the height of the section at the thick end by h_c. The height of the section is given by

$$h = h_c(x/b) \tag{44}$$

The top and bottom faces make angles α_t and α_b with the x axis. For this cross section, Eq. (8) may be put in the form

$$(d/dx)[x(dq/dx)] - \delta q = -2kG\theta x \tag{45}$$

in which δ is given by

$$\delta = \frac{kb}{h_c}\frac{t_t\cos\alpha_t + t_b\cos\alpha_b}{t_t t_b\cos\alpha_t\cos\alpha_b} \tag{46}$$

The applicable boundary conditions are given by Eqs. (9) and (17), respectively (by putting $a = 0$, $c = b$). For these, Eq. (45) has the solution

$$q = G\theta[(2k/\delta^2)(1 + \delta x) - CI_0(2\sqrt{\delta x})] \tag{47}$$

In this equation and those which follow $I\nu$ and $K\nu$ are modified Bessel functions of the first and second kind, respectively, and of order ν (see reference 12).

$$C = \frac{(2k/\delta)(1 + kb/t_c + k/t_c\delta)}{(k/t_c)I_0(2\sqrt{\delta b}) + \sqrt{\delta}\,b\,I_1(2\sqrt{\delta b})} \tag{48}$$

Application of Eqs. (24) and (25) to the expression given by Eq. (47) yields the following expression for the torsion constant:

$$J = (2h_c/\delta)\{(kb/\delta)(1 + 2\delta b/3) - C[\sqrt{\delta b}\,I_1(2\sqrt{\delta b}) - I_2(2\sqrt{\delta b})]\} \tag{49}$$

A typical shear flow distribution for a triangular section is shown in Fig. 10; it has been normalized by dividing it by the shear flow obtained when the interior material is neglected. As may be seen from this figure substantial errors in shear flow result from neglecting the interior. The core increases the torsional rigidity by 20 percent.

(3) *Double-Wedge Cross Section*

The differential equation (45) applies to each side of a double-wedge section symmetrical about a vertical axis provided the coordinates are those shown in Fig.

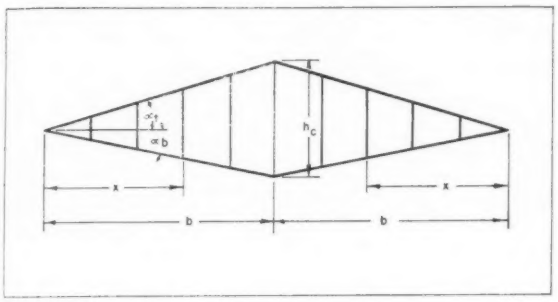

FIG. 11. Double-wedge cross section.

11. Since the section is symmetrical, the boundary condition at $x = b$ is that given by Eq. (21), and, as usual, Eq. (10) holds at $x = 0$.

The solution for each half of the wedge has the same form as that for the triangle—i.e., Eq. (47)—but here the constant C has the value

$$C = 2k\sqrt{\delta b}/[\delta^2 I_1(2\sqrt{\delta b})] \tag{50}$$

The torsional constant, obtained in the usual way, is found to be

$$J = (4h_c/\delta)\{(kb/\delta)(1 + 2\delta b/3) - 2k\sqrt{\delta b}/[\delta^2 I_1(2\sqrt{\delta b})] \times [\sqrt{\delta b}\, I_1(2\sqrt{\delta b}) - I_2(2\sqrt{\delta b})]\} \tag{51}$$

The solution given here is not limited strictly to physically symmetric double wedges, but in fact applies to any double wedge which can be put into mathematically symmetrical form.

Fig. 12 shows the distribution of q/q_{shell} for a typical double wedge made up of two triangles, each with the same section properties as that to which Fig. 10 applies. The result applies whether or not a thick central web is present. It is to be noted that here the torsion constant is increased by 27 percent due to the presence of the interior web material.

(4) *Trapezoidal Cross Section*

For trapezoidal cross sections the differential equation has the form given in Eq. (45) provided that the origin is chosen to be at the projected vertex of the section (Fig. 13). The appropriate boundary conditions are expressed by Eqs. (14) and (17). From these q is obtained in the form

$$q = 2kG\theta[(1/\delta^2)(1 + \delta x) - CI_0(2\sqrt{\delta x}) - DK_0(2\sqrt{\delta x})] \tag{52}$$

where C and D are given by

$$C = \frac{u(a)r(c) - u(c)r(a)}{p(a)r(c) - p(c)r(a)} \qquad D = \frac{u(c)p(a) - u(a)p(c)}{p(a)r(c) - r(a)p(c)} \tag{53}$$

in which we have put

$$\left.\begin{aligned} p(x) &= \gamma(x)I_0(2\sqrt{\delta x}) + \sqrt{\delta/x}\,xI_1(2\sqrt{\delta x}) \\ r(x) &= \gamma(x)K_0(2\sqrt{\delta x}) - \sqrt{\delta/x}\,K_1(2\sqrt{\delta x}) \\ u(x) &= (1/\delta^2)[\delta + \gamma(x) + \delta x\gamma(x)] \end{aligned}\right\} \tag{54}$$

$$\text{and} \quad \gamma(x) = \begin{cases} -k/t_a, & x = a \\ +k/t_c, & x = c \end{cases} \tag{55}$$

The torsional rigidity found from Eqs. (24) and (25) is

$$J = (2kh_c/c\delta^2)[v(c) - v(a)] \tag{56}$$

where

$$v(x) = x^2 + (2\delta/3)x^3 - 2\delta x\{C[\sqrt{\delta x}I_1(2\sqrt{\delta x}) - I_2(2\sqrt{\delta x})] - D[\sqrt{\delta x}K_1(2\sqrt{\delta x}) + K_2(2\sqrt{\delta x})]\} \tag{57}$$

The shear flow is given in terms of the torque T by

$$q = (2kT/J)[(1/\delta^2)(1 + \delta x) - CI_0(2\sqrt{\delta x}) - DK_0(2\sqrt{\delta x})] \tag{58}$$

(*Continued on page 752*)

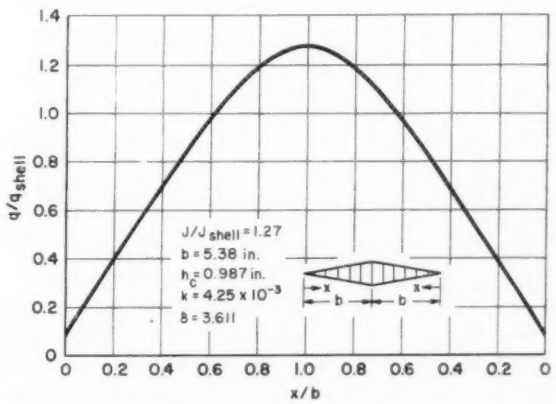

FIG. 12. Shear flow distribution for typical double wedge.

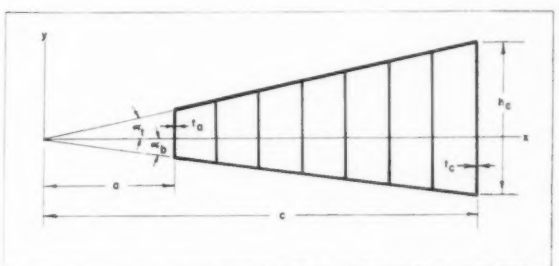

FIG. 13. Trapezoidal cross section.

Frequency-Response Functions of Orthotropic Sandwich Plates†

M. P. BIENIEK* AND A. M. FREUDENTHAL*

Columbia University

Summary

A method is presented for the determination of the frequency-response functions of the components of deformation and of stress in orthotropic sandwich plates. It applies to the case of simply supported rectangular plates, loaded by pressure normal to their planes. The analysis takes into account the transverse shear deformation of the core and the material damping of the core and of the facings. The results are presented in the form of expressions suitable for numerical evaluation. An example illustrates the application of this theory.

Introduction

IN ORDER TO PREDICT the behavior of a structural element subject to the action of random loading (for instance, random noise), it is necessary to determine the frequency-response functions of various quantities such as the components of deformation, the components of stress, etc. This paper deals with the frequency-response functions for a rectangular sandwich plate. The loading is assumed in the form of a normal pressure, uniformly distributed over the surface of the plate and random in time. The frequency-response function of any quantity S (deformation, stress) is the function $\bar{S}(i\omega)$, such that the quantity S corresponding to the loading $q = 1e^{i\omega t}$ is represented in the form

$$S = S(t) = \bar{S}(i\omega)e^{i\omega t} \tag{1}$$

The dimensions of the plate and the coordinate system are shown in Fig. 1. The analysis takes into account the effect of transverse shear deformation of the core. The thickness of the facings is assumed to be small in comparison to the thickness of the core.

The basic theory of such plates has been developed in two papers by R. D. Mindlin[1, 2] in which the detailed discussion of the assumptions is presented.

The materials of the core and of the facings are assumed to be orthotropic. The elastic constants of the core E_{xz}, E_{yy}, E_{xy}, G_z, G_y, G_z are defined by the stress-strain relations

$$\left.\begin{aligned} \sigma_{yz} &= 2G_x\epsilon_{yz}, \quad \sigma_{zz} = 2G_y\epsilon_{zz}, \quad \sigma_{xy} = 2G_z\epsilon_{xy} \\ \sigma_{xx} &= E_{xz}\epsilon_{zz} + E_{xy}\epsilon_{yy}, \quad \sigma_{yy} = E_{yy}\epsilon_{yy} + E_{xy}\epsilon_{zz} \end{aligned}\right\} \tag{2}$$

and the elastic constants of the facings E'_{zz}, E'_{yy}, E'_{xy}, G'_z by the relations

$$\left.\begin{aligned} \sigma'_{xy} &= 2G'_z\epsilon_{xy}, \qquad \sigma'_{zz} = E'_{zz}\epsilon'_{zz} + E'_{xy}\epsilon'_{yy}, \\ &\qquad\qquad \sigma'_{yy} = E'_{yy}\epsilon'_{yy} + E'_{xy}\epsilon'_{zz} \end{aligned}\right\} \tag{3}$$

The transverse shear deformations of the facings are neglected. If the materials of the core and of the facings are isotropic, then

$$G_x = G_y = G_z = G = E/2(1 + \nu)$$
$$E_{zz} = E_{yy} = E/(1 - \nu^2), \quad E_{xy} = E\nu/(1 - \nu^2)$$

with similar equalities for the constants of the facings.

The effect of damping is introduced by the use of the complex moduli of elasticity (reference 3, p. 276)

$$\begin{aligned} \bar{G}_x &= G_x(1 + i\mu_x), & \bar{G}_y &= G_y(1 + i\mu_y) \\ \bar{G}_z &= G_z(1 + i\mu_z), & \bar{E}_{zx} &= E_{zz}(1 + i\eta_{zz}) \\ \bar{E}_{yy} &= E_{yy}(1 + i\eta_{yy}), & \bar{E}_{xy} &= E_{xy}(1 + i\eta_{xy}) \end{aligned} \tag{4}$$

The coefficients μ_x, μ_y, μ_z are 2π times the specific damping $\Delta W_d/W_p$, where ΔW_d is the energy dissipated during one cycle in shear, and W_p is maximum shear strain energy. The coefficients η are related in a similar way to the dissipated and the strain energies in the cyclic tension-compression tests. In general, $\mu_x, \ldots, \eta_{xy}$ depend on the frequencies and amplitudes of cyclic stresses or deformations. In first approximation, it is assumed that the damping is frequency-independent. This assumption is in fair agreement with experimental results for various materials. It is also assumed that damping is independent of amplitude of applied stress. This assumption is less justified by the experimental evidence, since the damping of real materials usually increases with increasing amplitudes. However, without this assumption nonlinear equations of the problem would be obtained. A proper selection of constant coefficients $\mu_x, \ldots, \eta_{xy}$, for an expected (not too wide) stress and strain range, may provide sufficient accuracy of the results of the analysis. The coefficients of damping and the complex moduli of elasticity of the facings will be denoted by μ'_z, η'_{zx}, η'_{yy}, η'_{xy} and $\bar{G}'_z$, $\bar{E}'_{xx}$, $\bar{E}'_{yy}$, $\bar{E}'_{xy}$, respectively.

Basic Equations

The equations of motion of an elastic, orthotropic, sandwich plate are derived in reference 2, in the form

$$\frac{\partial M_x}{\partial x} + \frac{\partial M_{xy}}{\partial y} - Q_x = I\frac{\partial^2\psi_x}{\partial t^2}$$

Received May 16, 1960. Revised and received October 6, 1960.

† This research was supported by the United States Air Force under Contract AF-33-616-7042 monitored by the Materials Laboratory, Wright Air Development Center, Wright-Patterson Air Force Base, Ohio.

* Visiting Associate Professor and Professor of Civil Engineering, respectively.

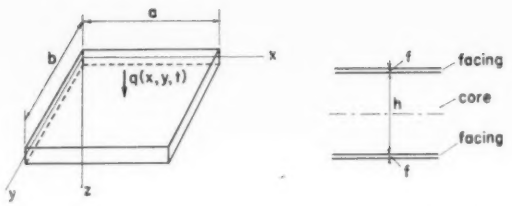

FIG. 1. Coordinate system and dimensions of plate.

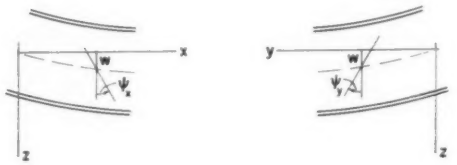

FIG. 2. Components of deformation w, ψ_x, ψ_y.

$$\frac{\partial M_{xy}}{\partial x} + \frac{\partial M_y}{\partial y} - Q_y = I\frac{\partial^2 \psi_y}{\partial t^2}$$
$$\frac{\partial Q_x}{\partial x} + \frac{\partial Q_y}{\partial y} + q = M\frac{\partial^2 w}{\partial t^2} \qquad (5)$$

where M_x, M_y, M_{xy} are bending and torsional moments, respectively; Q_x, Q_y are transverse shear forces; w, ψ_x, ψ_y are the components of deformation of the plate as shown in Fig. 2; q is the loading perpendicular to the plane of the plate; I is the moment of inertia of the mass of the plate with respect to its middle plane; M is the mass of the plate. The internal forces $M_x, \ldots,$ Q_y are taken per unit length of the cross section, the loading q, moment I and mass M per unit area of the plate.

If the densities of the core and the facings are ρ and ρ', respectively, then

$$\left.\begin{aligned} M &= \rho h + 2\rho' f \\ I &= \rho h^3/12 + \rho' f h^2/2 \end{aligned}\right\} \qquad (6)$$

where h is the thickness of the core and f is the thickness of one facing.

The relations between the internal forces $M_x, \ldots,$ Q_y and the components of deformation w, ψ_x, ψ_y, as derived in reference 2, are

$$\left.\begin{aligned} Q_x &= K_x[\psi_x + (\partial w/\partial x)] \\ Q_y &= K_y[\psi_y + (\partial w/\partial y)] \\ M_x &= D_x(\partial\psi_x/\partial x) + D_{xy}(\partial\psi_y/\partial y) \\ M_y &= D_y(\partial\psi_y/\partial y) + D_{xy}(\partial\psi_x/\partial x) \\ M_{xy} &= H_{xy}[(\partial\psi_y/\partial x) + (\partial\psi_x/\partial y)] \end{aligned}\right\} \qquad (7)$$

where

$$\left.\begin{aligned} K_x &= \kappa^2 G_x h, \qquad K_y = \kappa^2 G_y h \\ D_x &= E_{xx}h^3/12 + E'_{xx}h^2 f/2 \\ D_y &= E_{yy}h^3/12 + E'_{yy}h^2 f/2 \\ D_{xy} &= E_{xy}h^3/12 + E'_{xy}h^2 f/2 \\ H_{xy} &= G_z h^2/12 + G'_z h^2 f/2 \end{aligned}\right\} \qquad (8)$$

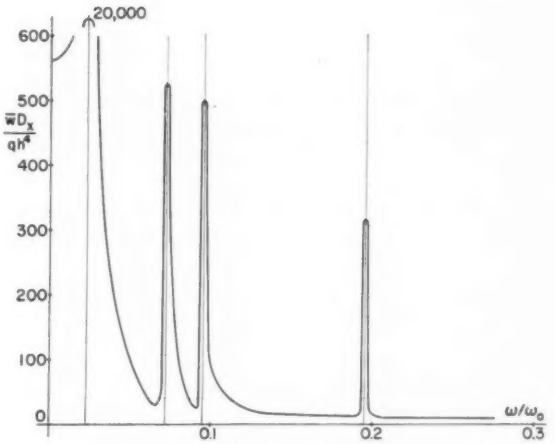

FIG. 3. Deflection, $\bar{w}$, as a function of frequency, ω.

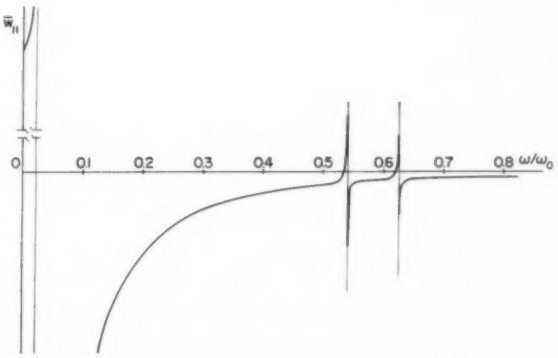

FIG. 4. Deflection $\bar{w}_{11}$ ($m = 1$, $n = 1$) as a function of frequency ω/ω_0 (plate without damping).

The equations (5), (7), and (8) are also valid for plates with damping if the moduli $E_{xx}, \ldots, G_z$ are replaced by the complex moduli $\bar{E}_{xx}, \ldots, \bar{G}_z$, E'_{xx}, $\ldots$, $\bar{G}'_z$. As it follows from reference 2, the coefficient κ for sandwich plates is very close to 1, and therefore it will be neglected in further considerations.

Substituting the expressions (7) into Eqs. (5), the following three equations for the components of deformation are obtained:

$$\left.\begin{aligned} &\bar{D}_x\frac{\partial^2\psi_x}{\partial x^2} + \bar{D}_{xy}\frac{\partial^2\psi_y}{\partial x\partial y} + \bar{H}_{xy}\frac{\partial^2\psi_y}{\partial x\partial y} + \bar{H}_{xy}\frac{\partial^2\psi_x}{\partial y^2} - \bar{K}_x\left(\psi_x + \frac{\partial w}{\partial x}\right) = I\frac{\partial^2\psi_x}{\partial t^2} \\ &\bar{D}_y\frac{\partial^2\psi_y}{\partial y^2} + \bar{D}_{xy}\frac{\partial^2\psi_x}{\partial x\partial y} + \bar{H}_{xy}\frac{\partial^2\psi_x}{\partial x\partial y} + \bar{H}_{xy}\frac{\partial^2\psi_y}{\partial x^2} - \bar{K}_y\left(\psi_y + \frac{\partial w}{\partial y}\right) = I\frac{\partial^2\psi_y}{\partial t^2} \\ &\bar{K}_x\frac{\partial\psi_x}{\partial x} + \bar{K}_y\frac{\partial\psi_y}{\partial y} + \bar{K}_x\frac{\partial^2 w}{\partial x^2} + \bar{K}_y\frac{\partial^2 w}{\partial y^2} + q = M\frac{\partial^2 w}{\partial t^2} \end{aligned}\right\} \qquad (9)$$

The coefficients $\bar{D}_x, \ldots, \bar{K}_y$ are now complex, as they contain the complex moduli of elasticity in the form (4). Eqs. (9) determine a unique solution if on the boundary one quantity of each of the pairs

$$(M_i, \psi_i), \quad (M_{ij}, \psi_j), \quad (Q_i, w); \qquad i = x, y, \quad j = x, y$$

are given. For the simply supported plate, the following boundary conditions will be assumed:

$$\left.\begin{array}{llll} \text{for} & x = 0,a, & M_x = 0, & \psi_y = 0, \quad w = 0 \\ \text{for} & y = 0,b, & M_y = 0, & \psi_x = 0, \quad w = 0 \end{array}\right\} \tag{10}$$

Determination of Dynamic Response

In order to determine the response of the plate to a loading random in time and with known space distribution $\bar{q}(x, y)$ it is necessary to determine first the response of the plate to the loading

$$q(x, y, t) = \bar{q}(x, y)e^{i\omega t} \tag{11}$$

Employing Fourier-series expansion, the loading $q(x, y, t)$ may be represented in the form

$$q(x, y, t) = \sum_{m=1}^{m=\infty} \sum_{n=1}^{n=\infty} Q_{mn} \sin \alpha_m x \sin \beta_n y \, e^{i\omega t} \tag{12}$$

where

$$\begin{array}{llll} \alpha_m = m\pi/a & , & \beta_n = n\pi/b \\ m = 1, 2, 3, \ldots, & & n = 1, 2, 3, \ldots \end{array}$$

with the coefficients Q_{mn} properly determined for each particular type of loading $\bar{q}(x, y)$. If the loading is in the form of the unit pressure uniformly distributed over the plate, i.e., $\bar{q}(x, y) = \text{const.} = 1$, then

$$Q_{mn} = 16/mn\pi^2; \qquad m = 1, 3, 5, \ldots, \quad n = 1, 3, 5 \ldots \tag{13}$$

The solutions for ψ_x, ψ_y, w are assumed in the forms

$$\left.\begin{array}{rcl} \psi_x &=& \sum_m \sum_n \Psi_{xmn} \cos \alpha_m x \sin \beta_n y \, e^{i\omega t} = \bar{\psi}_x e^{i\omega t} \\ \psi_y &=& \sum_m \sum_n \Omega_{ymn} \sin \alpha_m x \cos \beta_n y \, e^{i\omega t} = \bar{\psi}_y e^{i\omega t} \\ w &=& \sum_m \sum_n W_{mn} \sin \alpha_m x \sin \beta_n y e^{i\omega t} = \bar{w} e^{i\omega t} \end{array}\right\} \tag{14}$$

which satisfy the boundary conditions (10). Substituting (14) into Eqs. (9) the following system of linear algebraic equations is obtained for Ψ_{xmn}, Ω_{ymn}, W_{mn}:

$$\left.\begin{array}{l} (\bar{D}_x\alpha_m^2 + \bar{H}_{xy}\beta_n^2 + \bar{K}_x - I\omega^2)\Psi_{xmn} + (\bar{D}_{xy}\alpha_m\beta_n + \bar{H}_{xy}\alpha_m\beta_n)\Psi_{ymn} + \bar{K}_x\alpha_m W_{mn} = 0 \\ (\bar{D}_{xy}\alpha_m\beta_n + \bar{H}_{xy}\alpha_m\beta_n)\Psi_{xmn} + (\bar{D}_y\beta_n^2 + \bar{H}_{xy}\alpha_m^2 + \bar{K}_y - I\omega^2)\Psi_{ymn} + \bar{K}_y\beta_n W_{mn} = 0 \\ \bar{K}_x\alpha_m\Psi_{xmn} + \bar{K}_y\beta_n\Psi_{ymn} + (\bar{K}_x\alpha_m^2 + \bar{K}_y\beta_n^2 - M\omega^2)W_{mn} = Q_{mn} \end{array}\right\} \tag{15}$$

The coefficients of these equations are complex, and the solutions are, in general, also complex functions of ω or $i\omega$: $\Psi_{xmn}(i\omega)$, $\Psi_{ymn}(i\omega)$, $W_{mn}(i\omega)$. It is easy to check that the solution for W_{mn} is

$$W_{mn} = Q_{mn}\left[\frac{\mathcal{E}I\omega^2 + \mathcal{F}}{I^2\omega^4 + \mathcal{A}I\omega^2 + \mathcal{B}} + \mathcal{G} - M\omega^2\right]^{-1} \tag{16}$$

The functions Ψ_{xmn} and Ψ_{ymn} can be expressed in terms of W_{mn} in the following way:

$$\Psi_{xmn} = W_{mn}\frac{\bar{K}_x\alpha_m I\omega^2 + \mathcal{C}}{I^2\omega^4 + \mathcal{A}I\omega^2 + \mathcal{B}} \tag{17}$$

$$\Psi_{ymn} = W_{mn}\frac{\bar{K}_y\beta_n I\omega^2 + \mathcal{D}}{I^2\omega^4 + \mathcal{A}I\omega^2 + \mathcal{B}} \tag{18}$$

The notations in the expressions (16), (17), and (18) are:

$$\left.\begin{array}{rcl} \mathcal{A} &=& -(\bar{D}_x\alpha_m^2 + \bar{D}_y\beta_n^2 + \bar{H}_{xy}\alpha_m^2 + \bar{H}_{xy}\beta_n^2 + \bar{K}_x + \bar{K}_y) \\ \mathcal{B} &=& (\bar{D}_x\alpha_m^2 + \bar{H}_{xy}\beta_n^2 + \bar{K}_x)(\bar{D}_y\beta_n^2 + \bar{H}_{xy}\alpha_m^2 + \bar{K}_y) - (\bar{D}_{xy} + \bar{H}_{xy})^2\alpha_m^2\beta_n^2 \\ \mathcal{C} &=& -\bar{K}_x\alpha_m(\bar{D}_y\beta_n^2 + \bar{H}_{xy}\alpha_m^2 + \bar{K}_y) + \bar{K}_y\beta_n(\bar{D}_{xy}\alpha_m\beta_n + \bar{H}_{xy}\alpha_m\beta_n) \\ \mathcal{D} &=& -\bar{K}_y\beta_n(\bar{D}_x\alpha_m^2 + \bar{H}_{xy}\beta_n^2 + \bar{K}_x) + \bar{K}_x\alpha_m(\bar{D}_{xy}\alpha_m\beta_n + \bar{H}_{xy}\alpha_m\beta_n) \end{array}\right\} \tag{19}$$

$$\left.\begin{array}{rcl} \mathcal{E} &=& \bar{K}_x^2\alpha_m^2 + \bar{K}_y^2\beta_n^2 \\ \mathcal{F} &=& -\bar{H}_{xy}\bar{K}_x^2\alpha_m^4 - \bar{H}_{xy}\bar{K}_y^2\beta_n^4 + (-\bar{D}_y\bar{K}_x^2 + 2\bar{D}_{xy}\bar{K}_x\bar{K}_y + 2\bar{H}_{xy}\bar{K}_x\bar{K}_y + \bar{D}_x\bar{K}_y^2)\alpha_m^2\beta_n^2 - \\ & & \qquad \bar{K}_x^2\bar{K}_y\alpha_m^2 - \bar{K}_x\bar{K}_y^2\beta_n^2 \\ \mathcal{G} &=& \bar{K}_x\alpha_m^2 + \bar{K}_y\beta_x^2 \end{array}\right\} \tag{20}$$

If the frequency-response functions $\bar{\psi}_x = \bar{\psi}_x(i\omega)$, $\bar{\psi}_y = \bar{\psi}_y(i\omega)$, $\bar{w} = \bar{w}(i\omega)$ are known, the frequency-response function of any component of deformation or stress can be easily calculated.

Considering the stress σ_{xx} in the facing,

$$\sigma_{xx} = E'_{xx}\frac{h}{2}\frac{\partial \psi_x}{\partial x} + E'_{xy}\frac{h}{2}\frac{\partial \psi_y}{\partial y} \tag{21}$$

Consequently, the frequency-response function for σ_{xx} is

$$\bar{\sigma}_{xx}(i\omega) = -\bar{E}'_{xx}\frac{h}{2}\sum_m\sum_n \Psi_{xmn}\alpha_m \sin \alpha_m x \sin \beta_n y - \bar{E}'_{xy}\frac{h}{2}\sum_m\sum_n \Psi_{ymn}\beta_n \sin \alpha_m x \sin \beta_n y =$$

$$-\sum_m\sum_n\left[E'_{xx}(1 + i\eta'_{xx})\frac{h}{2}\Psi_{xmn}\alpha_m + E'_{xy}(1 + i\eta'_{xy})\frac{h}{2}\Psi_{ymn}\beta_n\right]\sin \alpha_m x \sin \beta_n y \tag{22}$$

and

$$\max \bar{\sigma}_{xx}(i\omega) = -\sum_m\sum_n\left[E'_{xx}(1 + i\eta'_{xx})\frac{h}{2}\Psi_{xmn}\alpha_m + E'_{xy}(1 + i\eta'_{xy})\frac{h}{2}\Psi_{ymn}\beta_n\right] \tag{23}$$

To determine the frequency-response function of the shear stress in the core $\bar{\sigma}_{xz}(i\omega)$, $(\sigma_{xz} = \bar{\sigma}_{xz}(i\omega)e^{i\omega t})$, it is necessary to start from the relation[2]:

$$\sigma_{xz} = G_x[\psi_x + (\partial w/\partial x)] \tag{24}$$

which implies

$$\bar{\sigma}_{xz}(i\omega) = G_x(1 + i\mu_x)\sum_m\sum_n(\Psi_{xmn} + W_{mn}\alpha_m)\cos \alpha_m x \sin \beta_n y \tag{25}$$

and

$$\max \bar{\sigma}_{xz}(i\omega) = G_x(1 + i\mu_x)\sum_m\sum_n(\Psi_{xmn} + W_{mn}\alpha_m) \tag{26}$$

Similarly

$$\bar{\sigma}_{yy}(i\omega) = -\sum_m\sum_n\left[E'_{yy}(1 + i\eta'_{yy})\frac{h}{2}\Psi_{ymn}\beta_n + E'_{xy}(1 + i\eta'_{xy})\frac{h}{2}\Psi_{xmn}\alpha_m\right]\sin \alpha_m x \sin \beta_n y \tag{27}$$

and

$$\bar{\sigma}_{yz}(i\omega) = G_y(1 + i\mu_y)\sum_m\sum_n(\Psi_{ymn} + W_{mn}\beta_n)\sin \alpha_m x \cos \beta_n y \tag{28}$$

Example

For the numerical evaluation of some of the above equations, a plate with the following dimensions has been assumed:

$$a = 20h,\ b = 16h,\ f = 0.05h$$

The elastic properties of the materials of the core and of the facings are described by the set of elastic constants

$$\begin{aligned} E_{xx} &= E_{yy} = E \\ E_{xy} &= E_{yx} = 0.3E \\ E'_{xx} &= E'_{yy} = E' = 50E \\ E'_{xy} &= E'_{yx} = 0.3E' \\ G_x &= G_y = G_z = 0.3846E \end{aligned}$$

The shear damping of only the core has been considered, with the damping coefficients

$$\mu_x = \mu_y = \mu_z = 0.1$$

Fig. 3 shows the response of this plate to a loading uniformly distributed on the surface and harmonically varying in time with the angular frequency ω. The absolute value of the dimensionless deflection $\bar{w}D_x/qh^4$ is given as a function of the dimensionless frequency ω/ω_0, where $\omega_0^2 = D_x/h^2I$. Some insight into the dynamic behavior of this plate may be obtained from Fig. 4, which represents the deflection $\bar{w}_{11}$ caused by the loading distributed sinusoidally over the surface and harmonic in time (in plotting the diagram, the effect of damping was neglected). As should be expected, three "resonant" frequencies result from the theory employed for this calculation. The classical plate theory would give only one of these frequencies.

Concluding Remarks

The expressions derived for the frequency-response functions of deformations and of stresses may be used to determine the behavior of a plate under normal pressure which is uniformly distributed over the surface of the plate and random in time. In particular, it is relatively easy to determine the power spectra of the components of deformation and of stresses for an arbitrary power spectrum of loading, even if this is not given in the form of a mathematical expression (it may be given, for instance, in the form of a diagram).

The material damping is considered in a manner which seems to be as exact as it can be without the use of nonlinear equations. The analysis neglects the inter-

(*Continued on page 752*)

Readers' Forum

BRIEF REPORTS of investigations in the aerospace sciences and discussions of papers published in the JOURNAL are presented in this special department. Entries must be restricted to a maximum of 1,300 words or the equivalent of one JOURNAL page including formulas and illustrations. Publication is completed as soon as possible after receipt of the material. The Editorial Committee does not hold itself responsible for the opinions expressed by the correspondents.

Contents

Magnetohydrodynamic Free-Convection Pipe Flow ..... KENNETH R. CRAMER 736

A Mass-Transfer Finite-Difference Formulation Employing Crocco Variables ..... J. P. MORAN AND P. B. SCOTT 737

Heat Transfer in the Incompressible Boundary Layer on a Flat Plate With Arbitrary Heat Flux ..... A. G. SMITH AND V. L. SHAH 738

Beam Column of Nonuniform Sections by Matrix Methods ..... H. SAUNDERS 740

Further Note on Airfoil Theory in Hydromagnetics ..... G. S. S. LUDFORD 741

Determination of Real-Gas Stagnation Temperature Based on Mass-Flow Consideration ..... FRANK L. CLARK AND CHARLES B. JOHNSON 742

Drag Reduction of an Airfoil by Injection of Sound Energy ..... PAUL K. CHANG 742

Comment on "Shear-Lag Solutions for Sheet-Stringer Panels by Means of a Hydrodynamic Analogy" ..... MARTIN GOLAND 743

Comments on "On the Rotational Motion of a Body Re-Entering the Atmosphere" ..... DUANE F. DUNLAP 744

Author's Reply ..... T. B. GARBER 744

A Note on the Compressible Turbulent Boundary Layer With Surface Mass Transfer ..... F. E. C. CULICK 745

The Epicyclic Analysis as Applied to Free-Flight Data ..... PETER J. MANTLE 747

Shock Propagation in Time Department Ducts ..... ROY GUNDERSEN 748

Stagnation-Point Heat Transfer in Equilibrium Dissociated Air With Variable Prandtl and Lewis Numbers ..... AEMER D. ANDERSON 749

Comparison of Flow-Direction Probes at Supersonic Speeds ..... FRANK W. BARRY 750

Magnetohydrodynamic Free-Convection Pipe Flow

Kenneth R. Cramer

Thermomechanics Laboratory, Aeronautical Research Laboratories, Air Force Research Division, Wright-Patterson Air Force Base, Ohio

December 2, 1960

IT HAS BEEN SHOWN[1] that transverse magnetic fields of practica strengths exert considerable influence on liquid-metal, free-convection, vertical, flat-plate and parallel-plate flow fields. The extent of influence was determined by the magnitude of a nondimensional parameter A which is the ratio of the Hartmann number to the fourth root of the Grashof number, and is a measure of the relative influence of the magnetic and buoyant forces. In this note the steady, fully developed, laminar, free-convection flow of a fluid of electrical conductivity σ_0 through a fully submerged, open-ended, constant-temperature, vertical pipe located in a transverse magnetic field of strength B_0 is analyzed in terms of the same parameter. The magnitude of its influence on the velocity and temperature profiles, the surface shear and heat transfer, and the volumetric flow rate is determined.

ANALYSIS

The magnetohydrodynamic, free-convection, pipe-flow, boundary-layer momentum and energy equations and their boundary conditions at the inner pipe radius a [Eqs. (1) to (3)] are transformed to the nondimensional equations (5) through (7) by the introduction of the new variables, Eq. (4), where N is the pipe temperature per foot and L is the pipe length.

$$\frac{d^2u}{dr^2} + \frac{1}{r}\frac{du}{dr} - \frac{\sigma_0 B_0^2}{\rho\nu}u = -\frac{g\beta(T - T_\infty)}{\nu} \tag{1}$$

$$(d^2T/dr^2) + (1/r)(dT/dr) = 0 \tag{2}$$

$$r = a : u = 0 \;\&\; T = T_a{}^\circ\mathrm{F} \tag{3}$$

$$\left.\begin{aligned} u &= (g\beta N)^{1/2}Lf(\eta), & \eta &= (g\beta N)^{1/4}\nu^{-1/2}r \\ a &= \nu^{1/2}(g\beta N)^{-1/4}, & \theta &= (T - T_\infty)/(T_w - T_\infty) \\ T_w - T_\infty &= NL, & A^2 &= \sigma_0 B_0^2/\rho(g\beta N)^{1/2} \end{aligned}\right\} \tag{4}$$

Contributors Please Note

Readers' Forum contributions that exceed the *Journal's* one-page limit will be returned to author for condensation and rewrite. Avoid inconvenience and delay by adhering to:

(1) Five, double-spaced, typewritten, manuscript pages ($8\frac{1}{2}$ by 11 in)., including wide margins, formulas, and headings, equal one printed page.

(2) For every illustration, deduct at least one-half or as much as one manuscript page, depending on the size of the illustration.

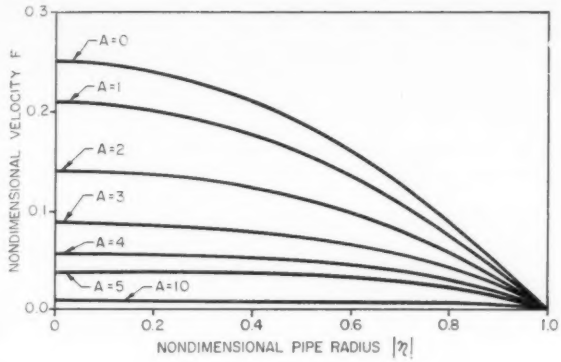

FIG. 1. Velocity profiles.

$$f'' + (1/\eta)f' - A^2 f = -\theta \tag{5}$$

$$\theta'' + (1/\eta)\theta' = 0 \tag{6}$$

$$\eta = 1 : f(1) = 0 \;\&\; \theta(1) = 1 \tag{7}$$

The solutions of Eqs. (5) and (6), where the velocity is in terms of modified Bessel functions of the first kind, are then

$$\theta = 1 \tag{8}$$

$$f = 1/A^2\{1 - [I_0(A\eta)]/[I_0(A)]\} \tag{9}$$

A separate solution, Eq. (10), is required for vanishing A since it appears in the denominator of Eq. (9).

$$f_{A=0} = \frac{1}{4}(1 - \eta^2) \tag{10}$$

The relations [Eq. (12)] for the volumetric flow rate Q are then obtained from Eq. (11) after substitution of the appropriate velocity functions:

$$Q = 2\pi \int_0^1 \eta f d\eta \tag{11}$$

$$\left.\begin{aligned} Q &= \pi/A^2\{1 - [2I_1(A)]/[AI_0(A)]\} \\ Q_{A=0} &= \pi/8 \end{aligned}\right\} \tag{12}$$

RESULTS

The solution of the energy equation is independent of the influence parameter; thus the temperature field is not altered by the magnetic field. In addition, no heat is transferred between the wall and fluid in the fully developed, steady-flow, constant-wall-temperature case.

Figs. (1) and (2) demonstrate the influence of the magnetic field on the velocity profile, surface shear, and flow rate. Increasing the influence parameter produces the expected flattening of the velocity profile and corresponding reduction of the surface shear and flow rate. Their asymptotic trend for large values of A demonstrates that flow separation and flow stoppage cannot be achieved, since the magnetic field exerts only a retarding force on the flow field.

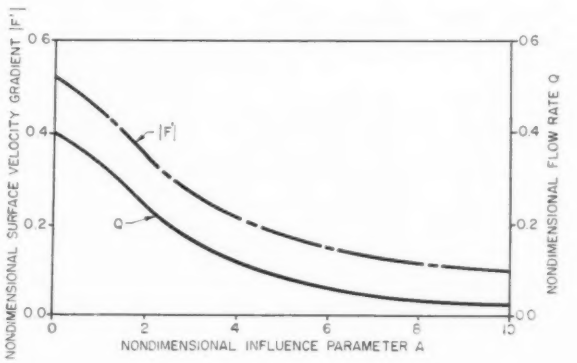

FIG. 2. Surface shear and flow rate.

Magnetic fields of practical strengths can exert considerable influence on free-convection pipe flows. For example, from the definition of A, a magnetic field of 10,000 gauss will produce an influence of A equal to ten on the flow of mercury through a 1-ft pipe with a wall temperature of 100°. Less than 1,000 gauss would be required to produce the same influence on liquid sodium and potassium flows.

REFERENCE

[1] Cramer, K. R., *Several Magnetohydrodynamic Free-Convection Solutions*, to be published.

A Mass-Transfer Finite-Difference Formulation Employing Crocco Variables*

J. P. Moran and P. B. Scott
Naval Supersonic Laboratory, Massachusetts Institute of Technology, Cambridge, Mass.
December 8, 1960

THE INJECTION of a foreign gas through a porous wall into the boundary layer is being studied as a possible means of cooling a high-speed vehicle. The complexity and nonlinearity of the describing equations makes it impossible to solve them exactly except for cases when certain restrictive boundary conditions apply. Here the laminar, binary, boundary-layer equations for the case of helium injection as derived by Baron[1] have been solved by a finite-difference scheme allowing for more general boundary conditions. This formulation employs the Crocco form of the equations using the same finite-difference approximations as Flügge-Lotz and Baxter.[2] The descriptive equations were programed for solution on an IBM-704 computer permitting wall temperature, injection rate, and external-flow properties to be varied with distance along the body. A finite-difference formulation of this type is not adequate when velocity overshoot exists—i.e., somewhere within the boundary layer the velocity exceeds its local external value—since the dependent variables have infinite derivatives at the point of maximum velocity and are double-valued in the vicinity of overshoot. For example, helium-injection boundary layers at moderate levels of injection are free from velocity overshoot only when the external pressure gradient is at most only slightly negative. This restriction therefore must be placed upon the external-velocity distribution in that case.

Solutions have been obtained for the problem of a porous plate having a solid leading edge, the downstream porous region having a mass-injection distribution varying inversely with the square root of distance from the tip. The numerical analysis carried out in the detailed report[3] gives reason to conclude that such solutions are a quite accurate representation of the exact solutions but for a small region immediately downstream of the solid edge. In Fig. 1 the variations of skin friction, heat transfer, and surface concentration are presented in normalized form against distance from the start of injection. The parameters employed are:

$$c_f\sqrt{Re},\ St_h\sqrt{Re},\ \text{and}\ c_{1w}$$

in which c_f = skin-friction coefficient, Re = Reynolds number based on stream properties and length from tip, St_h = Stanton number, and c_{1w} = mass concentration of helium at the surface. The distance is normalized with respect to solid-leading-edge

* This research was supported by the USAF under Contract AF49(638)-245 monitored by the Air Force Office of Scientific Research of the ARDC.

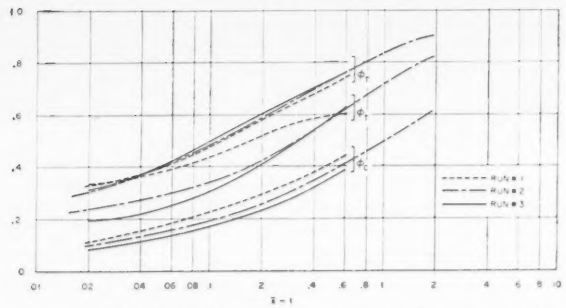

FIG. 1. Normalized skin friction, heat transfer, and surface concentration vs plate distance

length—i.e., $\bar{x} = x/L$. The normalized forms are:

$$\phi_\tau = \frac{(c_f\sqrt{Re})_{\bar{x}=1} - c_f\sqrt{Re}}{(c_f\sqrt{Re})_{\bar{x}=1} - (c_f\sqrt{Re})_{\bar{x}=\infty}}$$

$$\phi_T = \frac{(St_h\sqrt{Re})_{\bar{x}=1} - St_h\sqrt{Re}}{(St_h\sqrt{Re})_{\bar{x}=1} - (St_h\sqrt{Re})_{\bar{x}=\infty}}$$

$$\phi_c = \frac{c_{1w}}{(c_{1w})_{\bar{x}=\infty}}$$

The asymptotic values for the parameters were obtained from the similarity solutions of ref. 1. Boundary conditions for the solutions are given in the following table:

Run	$\frac{(\rho v)_w}{\rho^0 u^0}\sqrt{Re}$	M^0	$\frac{T_w}{T_{stream}}$	f_w for $L\to 0$ (ref. 1)
1	0.1083	0	0.8	−0.193
2	0.1597	0	0.8	−0.300
3	0.1986	0	0.8	−0.373

f_w is the injection parameter[1] and is related closely to

$$[(\rho v)_w]/(\rho^0 u^0)\sqrt{Re}$$

A solution for the boundary conditions of Run 3, but with the inclusion of an external Mach number of 3.25, was also obtained. The resulting wall concentration values were very close to those of Run 3. Shear and heat-transfer results were significantly different from Run 3 but are not presented here since exact asymptotic values are not known.

The curves are applicable to a solid-tipped cone after contracting the dimension $\bar{x}$ by the 1/3 power in accordance with Mangler's transformation. A cone of this type is useful in obtaining an experimental check for the similarity solutions of ref. 1 and others provided the solid tip is sufficiently small so that similarity is attained somewhere along the cone. The cone tip ideally should be porous, but structural limitations require that it be solid. The solution presented in Fig. 1 shows the rate of decay of the solid-leading-edge influence over a portion of the region of influence. The solutions were not carried to their asymptotes due to the prohibitive computer time required. However a combined application of the finite-difference program and Covert's approximations[4] as performed in the full report indicated that similarity profiles are approached along a cone within three solid-tip lengths downstream from the start of injection.

REFERENCES

[1] Baron, J. R., *The Binary Mixture Boundary Layer Associated With Mass Transfer Cooling at High Speeds*, Mass. Inst. of Technology, Naval Supersonic Lab., TR 160, (ASTIA AD 163-769), 1956.

[2] Flügge-Lotz, I., and Baxter, D. C., *The Solution of Compressible Laminar Boundary Layer Problems by a Finite Difference Method*, Part 2, *Further Discussion of the Method and Computation of Examples*, Stanford Univ., Div. of Eng. Mechanics, TR 110, 1957.

[3] Moran, J. P., and Scott, P. B., *A Mass Transfer Finite Difference Formulation Employing Crocco Variables*, Mass. Inst. of Tech., Naval Supersonic Lab., TR 433 (AFOSR TN-60-846), 1960.

[4] Covert, E. C., *Some Approximations to the Solutions to the Binary Boundary-Layer Problem*, Mass. Inst. of Tech., Naval Supersonic Lab., TR 390 (AFOSR TN-59-1091), 1959.

Heat Transfer in the Incompressible Boundary Layer on a Flat Plate With Arbitrary Heat Flux†

A. G. Smith* and V. L. Shah**
Department of Aircraft Propulsion, The College of Aeronautics, Cranfield, England
December 1960

SYMBOLS

x	=	distance from the leading edge
a	=	distance from the leading edge where heating starts
ξ	=	variable of integration
ρ	=	density of the fluid
C_p	=	specific heat
K	=	thermal conductivity
ν	=	kinematic viscosity
h	=	coefficient of heat transfer
U	=	velocity in the boundary layer
U_1	=	mainstream velocity
t	=	temperature in the boundary layer
t_1	=	mainstream temperature
t_w	=	wall temperature
δ	=	hydrodynamic boundary-layer thickness
Δ	=	thermal boundary-layer thickness
$\dot{q}_w''$	=	heat flux at the wall (quantity of heat per unit area and time)
m	=	slope of ramp heat input
C_f	=	friction factor
Pr	=	Prandtl number
Re	=	Reynolds number, U_1x/ν
Nu	=	Nusselt number, hx/K

RECENTLY Rubesin,[3] Eckert,[2] and Reynolds *et al.*[1] have derived analytical equations to find the heat-transfer coefficient on a flat plate for an arbitrary varying wall temperature. Following Klein and Tribus,[4] they have derived equations to find wall temperature for an arbitrary heat flux, from the heat-transfer equations for an arbitrary wall temperature.

Equations derived below directly from an integral energy equation are simple and still give results within 1.5 percent of those of Reynolds *et al.*[1] and Rubesin.[3]

Laminar Boundary Layer

For a step heat flux at $x = a$, such that $\dot{q}_w'' = 0$ for $x < a$ and $\dot{q}_w'' = b$ for $x > a$, the total energy at any section $x(x > a)$ is given by

$$\dot{q}_w''(x - a) = \rho U_1 C_p(t_w - t_1)\delta \int_0^\Delta \left(\frac{U}{U_1}\right)(1 - \theta)d(y/\delta) \quad (1)$$

For assumed cubic velocity and temperature profiles,

$$(U/U_1) = {}^3/_2(y/\delta) - {}^1/_2(y/\delta)^3 \quad (2)$$

$$\theta = (t - t_w)/(t_1 - t_w) = {}^3/_2(y/\Delta) - {}^1/_2(y/\Delta)^3 \quad (3)$$

Eq. (1) becomes

$$\dot{q}_w''(x - a) = \rho U_1 C_p(t_w - t_1)\delta\left[\frac{3}{20}\left(\frac{\Delta}{\delta}\right)^2 - \frac{3}{280}\left(\frac{\Delta}{\delta}\right)^4\right] \quad (4)$$

We are treating the case where the thermal boundary layer is thinner than the velocity boundary layer—that is, $(\Delta/\delta) < 1$. The second term in the right-hand expression of Eq. (4) is then small compared with the first, and can be neglected. The heat transfer at the wall is given by

$$\dot{q}_w'' = h(t_w - t_1) = -K\left(\frac{\partial t}{\partial y}\right)_{y=0} = \frac{3}{2}K\frac{(t_w - t_1)}{\Delta} \quad (5)$$

† This is a part of the research supported by U.S. Air Force under Contract No. AF 61(052)-267.

* Professor and Head of the Mechanical Engineering Department, University of Nottingham, Nottingham.
** Research Assistant.

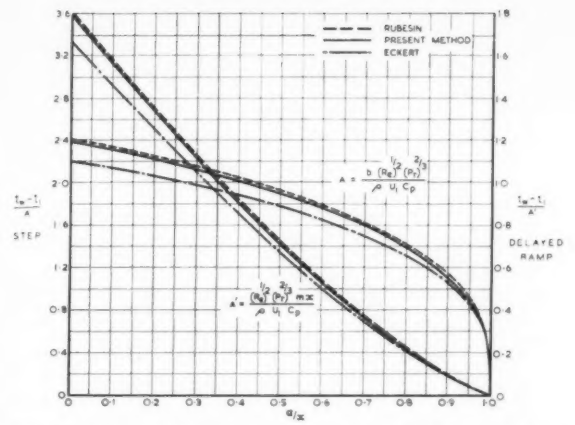

FIG. 1. Step and delayed-ramp heat input (laminar boundary layer).

For a laminar boundary layer, the velocity boundary-layer thickness is given by

$$\delta = 4.64x/\sqrt{Re} \tag{6}$$

Thus for a step heat flux, from Eqs. (4), (5), and (6),

$$(t_w - t_1) = \frac{2.395b(Re)^{2/3}(Pr)^{2/3}}{\rho U_1 C_p}\,[1 - (a/x)]^{1/3} \tag{7}$$

and

$$Nu_x/\sqrt{Re} = 0.418(Pr)^{1/3}[1 - (a/x)]^{-1/3} \tag{8}$$

Here b is the magnitude of the step heat flux. When compared to the similar equations of Eckert[2] and Rubesin,[3] it can be seen that Eq. (7) is relatively simple, for it does not contain the incomplete beta function. For any arbitrary heat flux, the wall temperature and the heat-transfer coefficient can be calculated by superimposing small steps. Thus for any arbitrary heat flux

$$(t_w - t_1) = \frac{2.395(Re)^{1/2}(Pr)^{2/3}}{\rho U_1 C_p}\int_0^x (1 - \xi/x)^{1/3}\frac{d\dot{q}_w''(\xi)}{d\xi}\,d\xi \tag{9}$$

and

$$\frac{Nu_x}{\sqrt{Re}} = \frac{0.418(Pr)^{1/3}\dot{q}_w''(x)}{\int_0^x (1 - \xi/x)^{1/3}[d\dot{q}_w''(\xi)/d\xi]d\xi} \tag{10}$$

It should be noted that the integral of Eqs. (9) and (10) must be taken in the Stieltjes sense. For a delayed-ramp heat input, when $\dot{q}_w'' = 0$ for $x < a$, and $\dot{q}_w'' = m(x - a)$ for $x > a$, Eqs. (9) and (10) give

$$(t_w - t_1) = \frac{1.797(Re)^{1/2}(Pr)^{2/3}mx}{\rho U_1 C_p}\,[1 - a/x]^{4/3} \tag{11}$$

and

$$Nu_x/\sqrt{Re} = 0.557(Pr)^{1/3}[1 - a/x]^{-1/3} \tag{12}$$

Turbulent Boundary Layer

For a step heat flux in the turbulent boundary layer, we assume velocity and temperature profiles

$$(U/U_1) = (y/\delta)^{1/7} \tag{13}$$

and

$$\theta = (t - t_w)/(t_1 - t_w) = (y/\Delta)^{1/7} \tag{14}$$

Then Eq. (1) becomes

$$\dot{q}_w''(x - a) = \rho U_1 C_p(t_w - t_1)\delta[(7/72)(\Delta/\delta)^{8/7}] \tag{15}$$

The heat-transfer momentum analogy derived by Reynolds *et al.*[1] for step heat flux is

$$St_x = \dot{q}_w''/[(t_w - t_1)\rho U_1 C_p] = (C_f/2)(\Delta/\delta)^{-1/7} \tag{16}$$

where the Prandtl-number dependence factor is applied afterward.

For a turbulent boundary layer

$$C_f/2 = 0.0296(Re)^{-0.2} \tag{17}$$

$$\delta/x = 0.37(Re)^{-0.2} \tag{18}$$

Thus for a step heat flux, from Eqs. (15) to (18),

$$(t_w - t_1) = \frac{32.95b}{\rho C_p U_1}(Re)^{0.2}(Pr)^{0.4}[1 - a/x]^{1/9} \tag{19}$$

and

$$Nu_x/(Re)^{0.8} = 0.03035(Pr)^{0.6}[1 - a/x]^{-1/9} \tag{20}$$

Here b is the magnitude of the step heat flux. A similar equation of Reynolds *et al.*[1] for a step heat flux also contains the incomplete beta function. For any arbitrary heat flux, the wall temperature and the heat-transfer coefficient are

$$(t_w - t_1) = \frac{32.95(Re)^{0.2}(Pr)^{0.4}}{\rho C_p U_1}\int_0^x (1 - \xi/x)^{1/9}\frac{d\dot{q}_w''(\xi)}{d\xi}\,d\xi \tag{21}$$

and

$$\frac{Nu_x}{(Re)^{0.8}} = \frac{0.03035(Pr)^{0.6}\dot{q}_w''(x)}{\int_0^x (1 - \xi/x)^{1/9}\dfrac{d\dot{q}_w''(\xi)}{d\xi}\,d\xi} \tag{22}$$

In Eqs. (21) and (22) the integral must be taken in the Stieltjes sense.

Results of the above equations are compared with those of Reynolds *et al.*,[1] Eckert,[2] and Rubesin,[3] for both turbulent and laminar boundary layers, and are plotted in Figs. 1 and 2. For the laminar case, the results of the above equations agree very well with those of Rubesin,[3] but not with those of Eckert.[2] The disagreement with Eckert is merely a numerical factor. Eckert's $(t_w - t_1)$ values are 8 percent lower than those of Eq. (7). For the turbulent case, the results agree within 1.5 percent of those of Reynolds *et al.*[1]

REFERENCES

[1] Reynolds, W. C., Kays, W. M., and Kline, S. J., *Heat Transfer in the Turbulent Incompressible Boundary Layer with Arbitrary Wall Temperature and Heat Flux*, NASA Memo. 12-3-58, Dec. 1958.

[2] Eckert, E. R. G., and Drake, R. M., *Heat and Mass Transfer*, McGraw-Hill Book Co., Inc., New York, 1959.

[3] Rubesin, M. W., *An Analytic Investigation of the Heat Transfer between a Fluid and a Flat Plate Parallel to the Direction of Flow having a Stepwise Discontinuous Surface Temperature*, M.S. Thesis, Univ. of California, Berkeley, 1945.

[4] Klein, J., and Tribus, M., "*Forced Convection from Non-isothermal Surfaces*," Univ. of Michigan, Eng. Res. Inst., Aug. 1952 (Contract AF 18(600)-51).

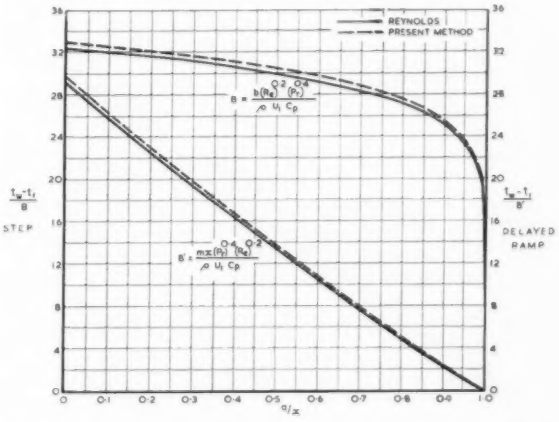

FIG. 2. Step and delayed-ramp heat input (turbulent boundary layer).

Beam Column of Nonuniform Sections by Matrix Methods

H. Saunders*
Missile and Space Vehicle Dept., General Electric Co., Philadelphia, Pa.
December 10, 1960

SUMMARY

An analytical solution of a beam column of nonuniform cross section was conducted and adapted to matrix form. Most of the available analyses consider a varying or uniform section but very few take into account abrupt changes. The matrix procedure as applied herein is called the "transfer-matrices" approach.[1]

NOMENCLATURE

$(EI)_i$	=	bending rigidity at station i
y_i	=	deflection at station i
P	=	axial force
M_i	=	moment at station i
Q_i	=	shear at station i
x	=	distance along beam
l_{i+1}	=	distance along beam between stations i and $i+1$
$\mathfrak{L}$	=	Laplace transform symbol
F_i	=	lumped static load at station

ANALYSIS

AN ELEMENT of a beam column with moments, shears, and axial forces acting upon it is illustrated in Fig. 1. The beam is divided into finite discrete stations with the static loads lumped at the stations. The differential equation for a typical ith section is

$$(EI)_{i+1}\frac{d^2y}{dx^2} = -P(y - y_i) + M_i + Q_i(x) \tag{1}$$

Simplifying, dividing by $(EI)_{i+1}$ and letting $\frac{P}{(EI)_{i+1}} = \bar{\alpha}_{i+1}^2$, one finds

$$\frac{d^2y}{dx^2} + \bar{\alpha}_{i+1}^2 y = \bar{\alpha}_{i+1}^2 y_i + \frac{M_i}{(EI)_{i+1}} + \frac{Qx}{(EI)_{i+1}} \tag{2}$$

Applying operational methods by taking the Laplace transform[2] of Eq. (2), then, one obtains

$$(s^2 + \bar{\alpha}_{i+1}^2)y(s) = sy(0) + y'(0) + \frac{\bar{\alpha}_{i+1}^2 y_i}{s} + \frac{M_i}{(EI)_{i+1}s} + \frac{Q_i}{s^2 EI_{iH}} \tag{3}$$

The initial condition are at $x = 0$, thus $y(0)$ and $y'(0)$ are actually y_i and y_i', respectively.

Dividing by $(s^2 + \bar{\alpha}_{i+1}^2)$ and taking the inverse,

$$y(x) = y_i + \frac{y_i' \sin \bar{\alpha}_{i+1}x}{\bar{\alpha}_{i+1}} + \frac{M_i(1 - \cos \bar{\alpha}_{i+1}x)}{\bar{\alpha}_{i+1}^2(EI)_{i+1}} + \frac{Q_i(\bar{\alpha}_{i+1}x - \sin \bar{\alpha}_{i+1}x)}{\bar{\alpha}_{i+1}^3(EI)_{i+1}} \tag{4}$$

Differentiating Eq. (4),

$$y'(x) = y_i' \cos \bar{\alpha}_{i+1}x + \frac{M_i \sin \bar{\alpha}_{i+1}x}{\bar{\alpha}_{i+1}(EI)_{i+1}} + \frac{Q_i(1 - \cos \bar{\alpha}_{i+1}x)}{\bar{\alpha}_{i+1}^2(EI)_{i+1}} \tag{5}$$

Differentiate Eq. (5) and divide by EI for the moment. Similarly, differentiate the moment equation and obtain the shear.

Now consider that $x = l_{i+1}$ and thus y, y', M and Q immediately to the right of station $i+1$ can be expressed in terms of the corresponding quantities at station i. The resulting deflections, slopes, moment and shear are expressed in matrix form:

$$|y|_{(i+1)^R} = |A_{i+1}|\,|y|_i \tag{6}$$

where

$$|y|_{i+1^R} = \begin{vmatrix} Q \\ M \\ y' \\ y \end{vmatrix}_{i+1^R} \quad \text{and} \quad |y|_i = \begin{vmatrix} Q \\ M \\ y' \\ y \end{vmatrix}_i$$

and A_{i+1} is the transfer matrix.[1]

$$A_{i+1} = \begin{vmatrix} \cos \bar{\alpha}_{i+1}l_{i+1} & -\bar{\alpha}_{i+1}\sin \bar{\alpha}_{i+1}l_{i+1} & -\bar{\alpha}_{i+1}^2(EI)_{i+1}\cos \bar{\alpha}_{i+1}l_{i+1} & 0 \\ \dfrac{\sin \bar{\alpha}_{i+1}l_{i+1}}{\bar{\alpha}_{i+1}} & \cos \bar{\alpha}_{i+1}l_{i+1} & -\bar{\alpha}_{i+1}(EI)_{i+1}\sin \bar{\alpha}_{i+1}l_{i+1} & 0 \\ \dfrac{1 - \cos \bar{\alpha}_{i+1}l_{i+1}}{\bar{\alpha}_{i+1}^2(EI)_{i+1}} & \dfrac{\sin \bar{\alpha}_{i+1}l_{i+1}}{\alpha_{i+1}(EI)_{i+1}} & \cos \bar{\alpha}_{i+1}l_{i+1} & 0 \\ \dfrac{\bar{\alpha}_{i+1}l_{i+1} - \sin \bar{\alpha}_{i+1}l_{i+1}}{\bar{\alpha}_{i+1}^3} & \dfrac{1 - \cos \bar{\alpha}_{i+1}l_{i+1}}{\bar{\alpha}_{i+1}^2(EI)_{i+1}} & \dfrac{-\sin \bar{\alpha}_{i+1}l_{i+1}}{\bar{\alpha}_{i+1}} & 0 \end{vmatrix} \tag{7}$$

The following relations can be written at station $i+1$ between $(i+1)^R$ and $(i+1)^L$

$$y_{i+1}{}^R = y_{(i+1)}{}^L \qquad M_{(i+1)}{}^R = M_{(i+1)}{}^L$$

$$y'_{(i+1)}{}^R = y'_{(i+1)}{}^L \qquad Q_{(i+1)}{}^R = Q_{(i+1)}{}^L + F_{i+1}$$

and similarly for stations $i+2$, $i+3 \ldots n$. Thus at station n, in terms of station 1,

$$\begin{vmatrix} Q \\ M \\ y' \\ y \end{vmatrix}_n = \begin{vmatrix} A_{11} & A_{12} & A_{13} & 0 \\ A_{21} & A_{22} & A_{23} & 0 \\ A_{31} & A_{32} & A_{33} & 0 \\ A_{41} & A_{43} & A_{43} & 1 \end{vmatrix} \begin{vmatrix} Q \\ M \\ y' \\ y \end{vmatrix}_1$$

For the various necessary conditions of the beam column:

(a) *Fixed ends:* $y_n = y_1 = y_n' = y_1' = 0$
Determine the critical load from $A_{31}A_{42} - A_{41}A_{32} = 0$.

(b) *Pin-ended:* $y_n = M_n = y_1 = M_1 = 0$
The critical load is $A_{21}A_{43} - A_{23}A_{41} = 0$.

(c) *Cantilever:* $y_n = y_n' = Q_1 = M_1 = 0$
Obtain the critical load from $A_{33} = 0$.

(d) *Clamped at station n and pinned at station 1:*

$$y_1 = M_1 = y_n = y_n' = 0$$

The critical load is obtained from $A_{31}A_{43} - A_{41}A_{33} = 0$.

(e) *Pinned at station n and clamped at station 1:*

$$y_n = m_n = y_1 = y_1' = 0$$

Determine the critical load from $A_{21}A_{42} - A_{22}A_{41} = 0$.

The simplest approach to the matrix solution is to assume

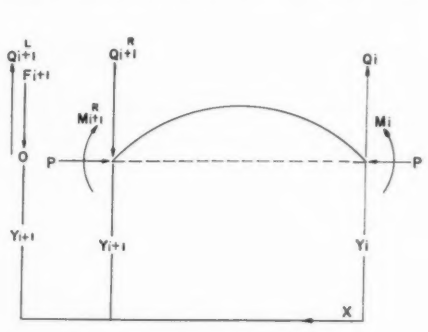

FIG. 1. Element of beam column.

* Engineer. Also, Lecturer, Dept. of Mechanical Engineering, Drexel Institute of Technology, Philadelphia.

α_{i+1}; then α_{i+2} can be selected from $\bar{a}_{i+1}{}^2 = \bar{a}_{i+2}{}^2[(EI)_{i+2}/(EI)_{i+1}]$.

REFERENCES

[1] Marguerre, K., *Vibration and Stability Problems of Beams Treated by Matrices*, J. Math. and Physics, Vol. 35, pp. 28–43, 1956.

[2] Thomsen, W. T., *Laplace Transformation*, pp. 3–5; Prentice Hall, Inc., Englewood Cliffs, N.J., 1950.

Further Note on Airfoil Theory in Hydromagnetics*

G. S. S. Ludford
Div. of Applied Mathematics,
Brown University, Providence, R.I.

December 19, 1960

THE PREVIOUS NOTE[1] was concerned with the lift loading on a thin airfoil moving at right angles to an applied magnetic field in a fluid of infinite electrical conductivity. The object of this sequel is to point out that the three basic integrals (I_1, I_2, I_3 below), which were there expressed in terms of hypergeometric functions, are in fact simple algebraic functions;† and to show that this leads to results comparable in simplicity to those in ordinary airfoil theory.

The airfoil has camber line $y = Y(x)$, $-b \leq x \leq b$, and moves in the negative x-direction with velocity U, the magnetic Mach number being $m = \tan \beta\pi$, $0 < \beta < 1/2$. The corresponding results in ordinary airfoil theory are obtained by setting $m = \infty$, $\beta = 1/2$ in the following.

First note that

$$I_1(x) = \int_{-b}^{b} \left(\frac{b+s}{b-s}\right)^{\beta} \frac{ds}{s-x} = \frac{\pi}{\sin \beta\pi}\left[1 - \cos \beta\pi \left(\frac{b+x}{b-x}\right)^{\beta}\right]$$

Thus the lift loading[1]

$$l_0(x) = \frac{2\sqrt{1+m^2}}{m}\,\rho U^2\left[\frac{\sin \beta\pi}{\pi}\left(\frac{b-x}{b+x}\right)^{\beta} I_1(x) + \cos \beta\pi\right]$$

on a flat plate at unit incidence $[Y'(x) = -1]$ becomes

$$l_0(x) = 2 \operatorname{cosec} \beta\pi\ \rho U^2[(b-x)/(b+x)]^{\beta}$$

The total lift on the plate is

$$L_0 = \int_{-b}^{b} l(x)dx = 4\beta\pi \operatorname{cosec}^2 \beta\pi \cdot \rho U^2 b$$

while the pitching moment about the center is

$$M_0 = -\int_{-b}^{b} xl(x)dx = 4\beta^2\pi \operatorname{cosec}^2 \beta\pi \cdot \rho U^2 b^2$$

The lift force acts at $x = -\beta b$—i.e., at the $\beta/2$-chord point forward of the center; it moves toward the center as m decreases—i.e., as the magnetic field becomes stronger.

The figure shows a graph of the lift coefficient $C_{L_0} = L_0/\rho U^2 b = 4\beta\pi \operatorname{cosec}^2 \beta\pi$ versus $1/m$. As m decreases from its value ∞ in the nonmagnetic case, C_{L_0} first decreases from $2\pi = 6.28$ to a minimum of 5.52 for $m = 2.33$ $(1/m = 0.429)$. It then increases, to 2π again for $m = 1$ and indefinitely thereafter as m tends to zero.

Secondly, note that

$$I_2(s) = \int_{-b}^{b} \left(\frac{b-x}{b+x}\right)^{\beta} \frac{dx}{s-x} = \frac{\pi}{\sin \beta\pi}\left[1 - \cos \beta\pi \left(\frac{b-s}{b+s}\right)^{\beta}\right]$$

$$I_3(s) = \int_{-b}^{b} x\left(\frac{b-x}{b+x}\right)^{\beta} \frac{dx}{s-x} = -\frac{\pi}{\sin \beta\pi}\left[2\beta b - s + \cos \beta\pi \left(\frac{b-s}{b+s}\right)^{\beta} s\right]$$

Thus the total lift and the pitching moment (about the center),[1]

$$L = -2\frac{\sqrt{1+m^2}}{m}\,\rho U^2\left\{\frac{\sin \beta\pi}{\pi}\int_{-b}^{b}\left(\frac{b+s}{b-s}\right)^{\beta} I_2(s)\,Y'(s)ds + \cos \beta\pi[Y'(b) - Y'(-b)]\right\}$$

and

$$M = 2\,\frac{\sqrt{1+m^2}}{m}\,\rho U^2\left[\frac{\sin \beta\pi}{\pi}\int_{-b}^{b}\left(\frac{b+s}{b-s}\right)^{\beta} I_3(s)\,Y'(s)ds + \cos \beta\pi \int_{-b}^{b} xY'(x)dx\right]$$

experienced by a general airfoil, become

$$L = -2 \operatorname{cosec} \beta\pi\ \rho U^2 \int_{-b}^{b}\left(\frac{b+s}{b-s}\right)^{\beta} Y'(s)ds = \lambda_1 L_0$$

and

$$M = -2 \operatorname{cosec} \beta\pi\ \rho U^2 \int_{-b}^{b}\left(\frac{b+s}{b-s}\right)^{\beta} (2\beta b - s)\,Y'(s)ds = \lambda_2 M_0$$

When the same airfoil is set at an angle of incidence α these values are augmented by αL_0 and αM_0 respectively. The moment about the $\beta/2$-chord point is then independent of α and this point is the focus[2] of the airfoil. For $\alpha = -\lambda_1$ there is no lift, while for $\alpha = -\lambda_2$ there is no moment about the center. Thus λ_1 and λ_2 define the first and second axes.[2] Expressions for them directly in terms of the shape of the camber line are obtained on integration by parts.

$$\lambda_1 = \frac{\sin \beta\pi}{\pi}\int_{-b}^{b} \frac{Y(s)ds}{(b-s)^{1+\beta}(b+s)^{1-\beta}}$$

$$\lambda_2 = \frac{\sin \beta\pi}{\pi}\int_{-b}^{b} \frac{(4\beta^2 - 1)b^2 - 2\beta bs + s^2}{2\beta^2 b^2} \times \frac{Y(s)ds}{(b-s)^{1+\beta}(b+s)^{1-\beta}}$$

We have used the fact that $Y(x)$ vanishes like $b - x$ at the trailing edge $x = b$.

In terms of the modified Glauert series,[1] given by

$$-U(\tan \theta/2)^{1-2\beta}\ \ Y'(b \cos \theta) = B_0 + \sum_{n=1}^{\infty} B_n \cos n\theta, \qquad x = b \cos \theta (0 \leq \theta \leq \pi)$$

they become

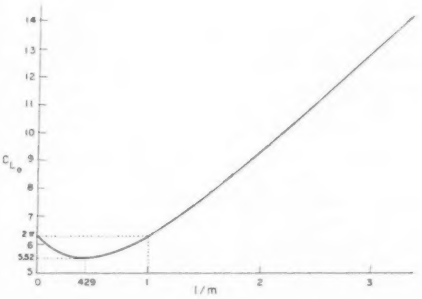

FIG. 1.

* This research has been supported by the Office of Naval Research, under Contract Nonr 562(07) with Brown University.

† This can be seen by transforming the argument of the hypergeometric functions to its reciprocal. As a by-product we obtain the complex velocity[1] $\partial\varphi/\partial x - i\partial\varphi/\partial y = iU\,[(z-b/z+b)^{\beta} - 1]$ for a flat plate at unit incidence.

$$\lambda_1 = (\sin \beta\pi/4\beta U)(2B_0 + B_1)$$

$$\lambda_2 = (\sin \beta\pi/8\beta^2 U)[2(4\beta - 1)B_0 + 2(2\beta - 1)B_1 - B_2]$$

These expressions contain only the first three Fourier coefficients, and the remaining coefficients therefore correspond to changes in the shape of the camber line which have no effect on the lift or moment. Of course the results given above may also be derived by means of the modified series, in the same way that Glauert used his original series.[3]

REFERENCES

[1] Ludford, G. S. S., *Note on Airfoil Theory in Hydromagnetics*, Journal of the Aerospace Sciences, Vol. 28, No. 6, pp. 511–512, June 1960.

[2] Milne-Thomson, L. M., *Theoretical Aerodynamics*, pp. 140–141; Macmillan & Co. Ltd., London, 1958.

[3] Glauert, H., *The Elements of Airfoil and Airscrew Theory*, pp. 87–90; Cambridge University Press, 1959.

Determination of Real-Gas Stagnation Temperature Based on Mass-Flow Consideration

Frank L. Clark and Charles B. Johnson*
Langley Research Center, NASA, Langley Field, Va.

December 21, 1960

ONE OF THE MAJOR PROBLEMS encountered in the operation of high-enthalpy test facilities is the determination of high stagnation temperatures ($T > 4{,}000°R$). Since these temperatures normally exceed the capabilities of available thermocouples, it is often necessary to resort to one of the various optical methods—such as pyrometry or the sodium-line reversal technique—for the determination of these temperatures. A method has been presented[1] whereby real-gas stagnation properties in a high-enthalpy system can be determined if the mass-flow rate through the system and the stagnation pressure are known. In the present analysis, this method was applied to determine stagnation temperature for stagnation pressures ranging from 100 to 1,000 atm. Nitrogen is considered to be the flow medium and the expansion of the gas from the stagnation chamber is assumed to be an isentropic and steady-state process. The maximum temperature dealt with (5,000°R) was low enough that the gas remained in an undissociated state; however, the method may be extended to other gases which may or may not be dissociated, provided the thermodynamic properties of the gas in the desired pressure and temperature range are known.

A one-dimensional analysis of the flow is used to evaluate the mass flow per unit area at the throat of a nozzle for various stagnation pressures and temperatures. The evaluation of mass flow per unit area at the throat of a nozzle is a trial-and-error procedure and was performed in the following manner. Starting with an assumed stagnation pressure and temperature, an initial value of stagnation entropy was obtained from published data.[2, 3] The flow in the system was expanded by reducing the stagnation temperature at a constant value of stagnation entropy. At each assumed temperature the values of pressure, density, and enthalpy were obtained from Ref. 2 or 3; the velocity at each point was calculated from the energy equation.

The result of the analysis is presented in Fig. 1, wherein mass flow per unit throat area is plotted against stagnation temperature. The dashed lines represent ideal-gas calculations. The spread between the ideal-gas and real-gas curves becomes larger as the stagnation pressure is increased. It may be seen from Fig. 1 that a significant error in stagnation temperature could result by using the ideal-gas relationship. For example, at a mass flow per unit throat area of 16,000 lb/ft²-sec and a stagnation pressure of 1,000 atm., the values of stagnation temperature as given by the two curves differ by approximately 600°.

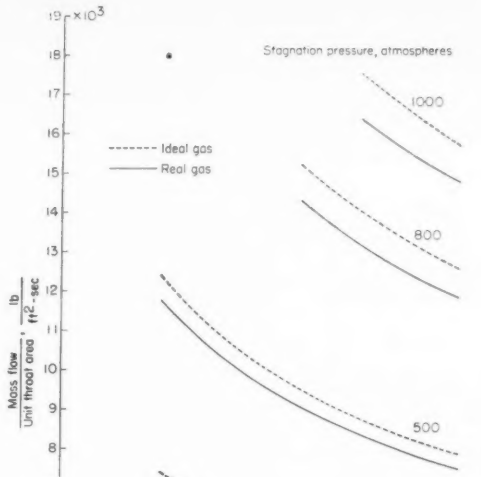

FIG. 1. Variation of mass flow per unit throat with stagnation temperature for various stagnation pressures.

REFERENCES

[1] Warren, W. R., *Determination of Air Stagnation Properties in a High-Enthalpy Test Facility*, Readers' Forum, Journal of the Aero/Space Sciences, Vol. 26, No. 12, pp. 835–836, Dec. 1959.

[2] Hilsenrath, J., Beckett, C. W., *et al.*, *Tables of Thermal Properties of Gases*, NBS Cir. 564, U. S. Dept. of Commerce, 1955.

[3] Hall, N. A., and Ibele, W. E., *Thermodynamic Properties of Air, Nitrogen, and Oxygen as Imperfect Gases*, Univ. of Minnesota, Eng. Exp. Station, Tech. Paper No. 85, Dec. 1951.

Drag Reduction of an Airfoil by Injection of Sound Energy

Paul K. Chang
Associate Professor, Dept. of Mechanical and Aeronautical Engineering, The Catholic University of America, Washington 17, D.C.

December 19, 1960

THIS PAPER presents preliminary results on the reduction of total drag of an airfoil by injecting sound energy into the free airstream. It was found that the maximum effect was assured when the sound energy was directed opposite to the free stream and it is shown that the drag can be reduced by more than 20 percent at zero angle of attack. At an angle of attack of 15°, the power saved by the drag reduction is 19 times as great as the power input required to generate the sound energy.

Measurements of total drag with and without sound energy for a wooden wing of rectangular planform, aspect ratio of 6, chord length of 3 in., and maximum thickness of 15 percent at 0.6 chord length were made at the Catholic University of America.[1] The

* Aeronautical Research Engineers.

TABLE 1
Ratio of Power Reduction to Power Input

Angle of attack	Total C_D reduction	Velocity of air stream, ft/sec	Frequency of sound, cps	Strouhal number	Power reduction/power input
0°	0.007	35.7	1,500	17.52	6.7
15°	0.022	34.5	2,000	24.20	19.0

range of Reynolds numbers based on chord length and free-stream velocity was 8.34–8.7 × 10^4, the range of frequency was 500–2,000 cps, and angles of attack varied from −15° to +15°. Sound energy from a Hewlett-Packard audio-oscillator was injected into the air stream in the range of Strouhal numbers from 5.82 to 24.2. The location of sound source with respect to air stream is important, and in order to obtain the maximum effect of sound, the audio-oscillator was placed behind the airfoil, so that the sound was propagated against stream direction.

Some of the test results are shown in Figs. 1 and 2, the data being average values of several test runs. The curves show that the drag at various angles of attack can be reduced over a range of Strouhal numbers. Strouhal number is defined as $S = nc/V$, where n is the frequency of sound (cps), c is the chord length of an airfoil (ft), and V is the free-stream velocity (ft/sec). It should be noted that in these preliminary results the Strouhal number was varied by changing only the frequencies from 500 to 1,500 cps, but the flow velocity was 35.7 ft/sec for all frequencies of air flow tested. The minimum total drag was measured in the range of S = 11–18 at various angles of attack, and the maximum reduction, amounting to 21 percent of total drag, was attained at S = 17.5 and at zero angle of attack.

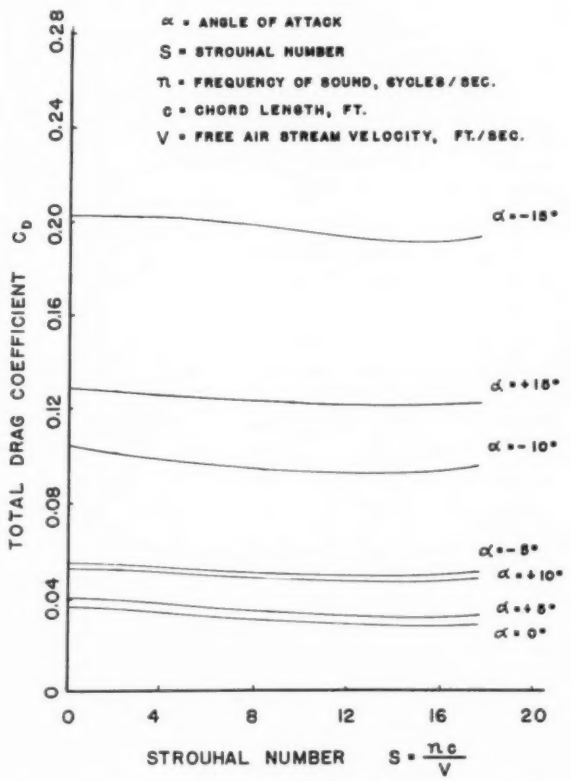

FIG. 1. Measured total drag coefficient of airfoil vs. Strouhal number.

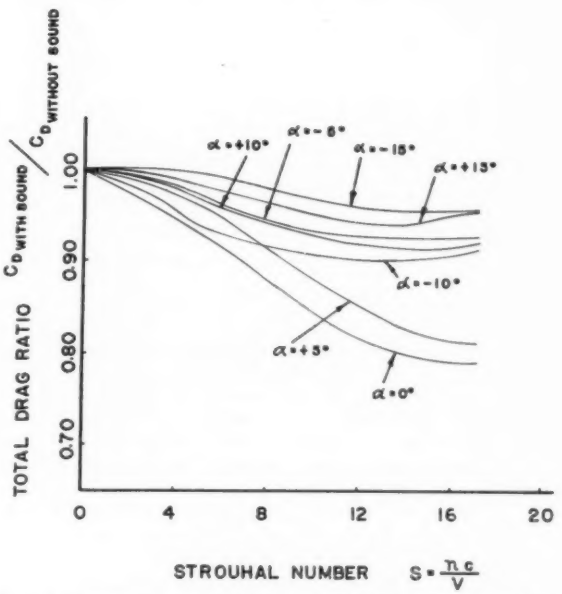

FIG. 2. Measured total drag ratio of airfoil vs. Strouhal number.

The ratios of power reduction to power input to the audio-oscillator are shown in Table 1.

REFERENCE

[1] Betz, A. J., Jr., Burke, P. J., Hendricks, C. M., Lawrence, J. T., and Rogers, L. W., *An Experimental Investigation of the Effect of Sound on the Drag Characteristics of a Finite Wing*, B.S. Thesis, Catholic Univ. of America, 1960.

Comment on "Shear-Lag Solutions for Sheet-Stringer Panels by Means of a Hydrodynamic Analogy"*

Martin Goland
President, Southwest Research Institute, San Antonio, Texas
December 24, 1960

Mr. M. Fine of Dowty Rotol Ltd. has kindly called my attention to a paper which he coauthored, entitled *A Method of Estimating the Direct Stress Concentration Round Holes in Reinforced Sheet*, by M. Fine and A. Pellew, A.R.C.R. and M. No. 2604 (Gt. Britain), May 1942. This earlier paper covers essentially the same material as my own treatment, and my apologies are due these authors and the readers of the JOURNAL for this duplication. My only excuse is the growing difficulty of conducting comprehensive searches of all literature sources.

My own version of the problem does include a more careful treatment of the boundary conditions, permitting a discussion of

* Journal of the Aero/Space Sciences, Vol. 27, No. 4, pp. 291–295, 303, April 1960.

cases when the cutout boundaries are rigidly fixed, as well as certain types of cutout reinforcements. In all other respects, the two papers show a remarkable similarity of approach.

EDITOR'S NOTE

The following communication has been received from Mr. Fine: "The authors of R. & M. No. 2604 feel that innocent duplication of prior work is unavoidable at present, and are grateful to Martin Goland for his acknowledgment of priority. The first such use of the Laplace equation, in effect, is possibly by Younger; see his *Mechanics of Aircraft Structures*, 2nd Ed., McGraw-Hill, on shear lag."

Comments on "On the Rotational Motion of a Body Re-Entering the Atmosphere"

Duane F. Dunlap
Aerodynamicist, Chrysler Corporation, Missile Division, Detroit, Mich.
December 27, 1960

METHODS HAVE BEEN DERIVED[1] to compute the angle-of-attack envelope of a body re-entering the atmosphere. Both spinning and nonspinning bodies were investigated. Several inconsistencies were noted in the derivations and discussion of this paper. These will be commented on in the following note.

In combining the aerodynamic moments with the rotational equations of motion, the damping terms K_M and K_N were not divided by a moment-of-inertia term. This results in the improper definition of the term A_{MN}. The definition should be

$$K_{MN} = -A_{MN}Ve^{kh}I_y \tag{1}$$

Without the moment-of-inertia term, the definition of A_{MN} would be dimensionally incorrect.

It was also discovered that the constants of integration involved in the solution of the coupled equations of motion were incorrectly derived. The correct constants are as follows:

$$A_1 = \frac{\dot\beta_0 - \dot\beta_f(0)}{I_x\omega_x/I_z} \qquad B_1 = \frac{\dot\alpha_f(0) - \dot\alpha_0}{I_x\omega_x/I_z}$$

$$A_2 = \frac{\dot\alpha_0 - \dot\alpha_f(0)}{I_x\omega_x/I_z} \qquad B_2 = \frac{\dot\beta_0 - \dot\beta_f(0)}{I_x\omega_x/I_z}$$

$$A_3 = \alpha_0 - \alpha_f(0) - A_1 \qquad B_3 = \beta_0 - B_f(0) - B_1$$

$$A_4 = \beta_f(0) - \beta_0 - A_2 \qquad B_4 = \alpha_0 - \alpha_f(0) - B_2$$

Another error which seems to compensate for the erroneous constants of integration was found in the integration of the damping terms associated with the coupled case. The integral

$$-\int_0^t \frac{(1/2)(d/dt)\sqrt{\omega_n^2 + (I_x\omega_x/2I_z)^2}\,dt}{\sqrt{\omega_n^2 + (I_x\omega_x/2I_z)^2}}$$

when properly carried out leads to the result

$$-(1/4)\ln\left[\omega_n^2 + (I_x\omega_x/2I_z)^2\right]_0^t$$

which must be evaluated for the limits of integration. Since $\omega_n = 0$ at $t = 0$, and $\omega_n = \omega_n$ at $t = t$, we are led to the result

$$-\int_0^{\omega_n} \frac{(1/2)(d/dt)\sqrt{\omega_n^2 + (I_x\omega_x/2I_z)^2}\,d\omega_n}{\sqrt{\omega_n^2 + (I_x\omega_x/2I_z)^2}} = \ln\left\{\frac{(I_x\omega_x/2I_z)^{1/2}}{[\omega_n^2 + (I_x\omega_x/2I_z)^2]^{1/4}}\right\} \tag{2}$$

Apparently the proper limits of integration were not applied to the coupled case as they were to the planar case. Substitution of this term and the A's and B's into the assumed solution will yield

$$\frac{A_{\alpha,\beta}}{A_{\alpha,\beta}(0)} = \left(\frac{I_x\omega_x}{2I_z}\right)^{1/2} \times \frac{e^{-[(A_L + A_{MN})/2k\sin\Phi]e^{kh}}}{[-(m/I_z)1_xV^2e^{kh}(A_L + A_D) + (I_x\omega_x/2I_z)^{1/2}]^{1/4}} \tag{3}$$

This equation is identical to the one published in Ref. 1 except for the A_{MN} term and the negative sign of the exponential. It appears, then, that there were compensating errors in the derivation of the A's and B's and in the integration of the damping terms. The negative sign which appears in the exponential of both the planar and the coupled cases seems to be an oversight, otherwise the envelope would diverge. (Both k and $\sin\Phi$ are negative.)

Some comments on parts of the discussion are also in order. The statement that A_{MN} is always positive, as well as the implication that $C_{L\alpha}$ can be negative, are incorrect. To the best experience of aerodynamicists A_{MN} is often negative and $C_{L\alpha}$ is never negative. Negative values of A_{MN} generally stem from pressure effects, rather than purely viscous effects.

Aside from these comments, the results of the article have been of great utility to the author.

REFERENCE

[1] Garber, T. B., *On the Rotational Motion of a Body Re-Entering the Atmosphere*, Journal of the Aerospace Sciences, Vol. 26, No. 7, pp. 443–449, July 1959.

Author's Reply

T. B. Garber
Electronics Department, The RAND Corporation, Santa Monica, Calif.
January 26, 1961

IN REF. 1, four specific criticisms are raised in connection with the writer's paper *On the Rotational Motion of a Body Re-Entering the Atmosphere*. These criticisms are discussed below in the order in which they appear in Ref. 1.

1. It is noted that the damping parameters, K_{MN} and K_M, were not divided by the moment of inertia, I_z, in Eqs. (46)–(50).[2] As pointed out,[1] this omission results in a dimensional inconsistency. As a consequence the proper definition of A_{MN}, Eq. (60) in Ref. 2, is

$$K_{MN}/I_z = -A_{MN}Ve^{kh}$$

Apparently the omission of I_z occurred as the result of a notational change which was made in writing the paper. The proper value of A_{MN} was used in the preparation of the curves presented in Ref. 2.

2. It is stated[1] that the constants of integration of Eqs. (74) and (75)[2] are incorrect. Then it is pointed out that the integrals of the exponential terms are apparently evaluated improperly[2] so that a compensating effect is achieved. These integrals, as they appear in Eqs. (74) and (75), are *indefinite*. Thus at very high altitudes,

$$e^{\int \sigma_1\,dt} \cong e^{\left[-\int \frac{A_{MN}e^{kh}\,dh}{\sin\Phi} - \frac{1}{2}\ln\sqrt{\omega_n^2 + \left(\frac{I_x\omega_x}{2I_z}\right)^2}\right]} \cong \frac{e^{-(A_{MN}e^{kh}/k\sin\Phi)}}{\left[\omega_n^2 + \left(\frac{I_x\omega_x}{2I_z}\right)^2\right]^{1/4}} \tag{1}$$

$$e^{\int \sigma_2\,dt} \cong e^{\left[-\int \frac{A_Le^{kh}}{\sin\Phi} - \frac{1}{2}\ln\sqrt{\omega_n^2 + \left(\frac{I_x\omega_x}{2I_z}\right)^2}\right]} \cong \frac{e^{-(A_Le^{kh}/k\sin\Phi)}}{\left[\omega_n^2 + \left(\frac{I_x\omega_x}{2I_z}\right)^2\right]^{1/4}} \tag{2}$$

where $\omega_x \gg \omega_n$ and $\dot h = V\sin\Phi$.

To illustrate the process involved in determining the constants of integration, let $\alpha_{h=h_0} = \alpha_0 - \alpha_f(0)$ where h_0 is very large—e.g., 500,000 ft. All other initial conditions are zero. At very large values of h, ω_n approaches zero, and the exponential terms of Eqs. (1) and (2) approach 1, since k is negative. It can be shown that, for the assumed conditions, Eq. (74) reduces to the following expression

$$\alpha_0 - \alpha_f(0) = A_3/\left[\left(\frac{I_x\omega_x}{2I_z}\right)^{1/2}\right] \tag{3}$$

Eq. (3) is consistent with the results of Ref. (2), In Ref. 1, limits of integration have been employed in evaluating Eqs. (1) and (2) above. Thus

$$e^{\int_0^t \sigma_1\,dt} \cong e^{\int_{h_0}^{h} \frac{\sigma_1}{V\sin\Phi}\,dh} =$$

$$\frac{(I_x\omega_x/2I_z)^{1/2}e^{-\frac{AMN}{k\sin\Phi}(e^{kh}-e^{kh_0})}}{[\omega_n^2+(I_x\omega_x/2I_z)^2]^{1/4}} \tag{4}$$

$$e^{\int_{h_0}^{h} \frac{\sigma_2}{V\sin\Phi}\,dh} = \frac{(I_x\omega_x/2I_z)^{1/2}e^{-\frac{AL}{k\sin\Phi}(e^{kh}-e^{kh_0})}}{[\omega_n^2+(I_x\omega_x/2I_z)^2]^{1/4}} \tag{5}$$

The corresponding expression for $\alpha_0 - \alpha_f(0)$ is

$$\alpha_0 - \alpha_f(0) = \frac{(I_x\omega_x/2I_z)^{1/2}}{(I_x\omega_x/2I_z)^{1/2}}A_3' = A_3' \tag{6}$$

However, because of the fact that a multiplicative constant is introduced when definite integrals are employed, one should not expect A_3 and A_3' to be identical. Indeed, they cannot be. Either approach to the evaluation of the A's and B's is valid. Thus it is not a mere coincidence that the final results obtained in Ref. 1 are in agreement with those of Ref. 2.

3. The absence of a minus sign in the exponents of Eqs. (60) and (79)[2] is definitely an error of omission.

4. The final comment of Ref. (1) is concerned with the aerodynamic parameters, C_{L_α} and A_{MN}. It is stated[1] that C_{L_α}, the lift curve slope, is never negative, and that the damping parameter, A_{MN}, is frequently negative.

To begin with it is stated[2] that the graphical results which are presented are limited to the case of a conical body and the assumption of Newtonian aerodynamics. For these conditions[3,4]

$$\left.\begin{aligned} C_{L_\alpha} &= 2(\cos^2 B - \sin^2 B) && \text{(a)}\\ C_{m_q} &= -\frac{1}{9\cos^2 B} - 2\cos^2 B\left(\frac{l_x}{l_{\text{ref}}}\right)^2 && \text{(b)}\\ C_{m_{\dot\alpha}} &= 0 && \text{(c)}\\ A_{MN} &= -\frac{(C_{m_q}+C_{m_{\dot\alpha}})}{2I_z}\rho_0 A_{\text{ref}} l^2_{\text{ref}} && \text{(d)} \end{aligned}\right\} \tag{7}$$

Where B is the cone half-angle, l_{ref} is the cone length, l_x is the static margin, and A_{ref} is the cone reference area.

An examination of Eq. (7a) indicates that for B greater than 45°, C_{L_α} is negative, even for small angles of attack. Eq. (7b) indicates that for any value of B or l_x, C_{m_q} is negative, and thus the damping parameter A_{MN} is always positive.

In general, the statement that C_{L_α} is never negative is incorrect. For example, at angles of attack beyond the stall point, the lift curve slope of any aircraft is negative.

The original work on which Ref. 2 is based has recently been declassified.[5] This report is recommended for a more comprehensive treatment of the problem of stability during re-entry.

Finally the writer would like to express his appreciation for the above comments. Their value is obvious in that points 1 and 3 above were overlooked by both the author and the technical referees.

References

[1] Dunlap, D. F., *Comments on "On the Rotational Motion of a Body Re-Entering the Atmosphere,"* Readers' Forum, Journal of the Aerospace Sciences, Vol. 28, No. 9, p. 744, Sept. 1961.

[2] Garber, T. B., *On the Rotational Motion of a Body Re-Entering the Atmosphere*, Journal of the Aero/Space Sciences, Vol. 26, No. 7, pp. 443–449, July 1959.

[3] Allen, H. J., *Motion of a Ballistic Missile Angularly Misaligned with the Flight Path Upon Entering the Atmosphere and its Effect Upon Aerodynamic Heating, Aerodynamic Loads, and Miss Distance*, NACA TN-4048, Oct. 1957.

[4] Tobak, M., and Wehrend, W. R., *Stability Derivatives of Cones at Supersonic Speeds*, NACA TN-3788, Sept. 1956.

[5] Garber, T. B., *An Analysis of the Rotational Motion of a Body During Re-Entry*, The RAND Corp., Research Memo. 1863–1, Jan. 28, 1957.

A Note on the Compressible Turbulent Boundary Layer With Surface Mass Transfer*

F. E. C. Culick
Naval Supersonic Laboratory,
Massachusetts Institute of Technology, Cambridge, Mass.

December 29, 1960

ONE POSSIBLE MEANS to alleviate the effects of aerodynamic heating is mass transfer or transpiration cooling. Practical considerations then require that one should investigate the behavior of turbulent boundary layers when gas is transferred through the surface. The most extensive analysis of the problem appears to be that of Rubesin and Pappas;[1] they fail, however, to find certain observed features of the effect of mass transfer, although the influence of fairly high injection rates on heat transfer was described correctly.[7] Relatively simple calculations outlined here tend to agree with expected and observed results.

The boundary layer is regarded as comprising two crudely defined regions: the "laminar sublayer" and an outer region in which turbulence is "fully developed." Accordingly, two sets of equations are treated and the solutions matched at the interface. Details of further assumptions are discussed in Ref. 2. The results are reasonable and permit an approximate assessment of the effects of thermal diffusion.

Only the flat-plate problem is considered here. In the absence of detailed information a simple description of the flow in the turbulent region is obtained by invoking a form of "Reynolds' analogy," assuming the "turbulent" Prandtl and Schmidt numbers to be unity. It follows as usual from the momentum and concentration equations for the turbulent region that the mean value of concentration, c_l, is linearly related to the velocity component u. Then a "solution" to the energy equation is obtained by assuming the temperature T to be a function of u. Variations in the specific heat with c_l are accounted for, and after satisfaction of the boundary conditions there results the useful relation:

$$f_l = \bar h_0 + \frac{\tilde u_l^2}{2} - \tilde u_l - f_l' c(1-\tilde u_l) \tag{1}$$

in which $\quad f = (C_{p_2}T)/u_e^2; \qquad f' = df/d\tilde u$

$$c = 1 + c_{1l}(C_{p_{12}} - 1); \qquad \tilde u = u/u_e$$

and $\bar h_0$ is the normalized free-stream stagnation enthalpy $C_{p_2}T_0/u_e^2$. Values at the edge of the laminar sublayer are denoted by $(\ )_l$. Subscripts e and w denote evaluation in the free stream and at the wall.

The problem in the sublayer region is treated roughly as a perturbation of the case when the Prandtl number (Pr) and Schmidt number (Sc) are equal to one, justified in part because these quantities are always of order unity. Temperature differences are assumed sufficiently small that Pr and Sc are functions of c_l only. This condition is fulfilled by the available

* This research was supported in whole or in part by the United States Air Force under Contract No. AF 49(638)-245, monitored by the Air Force Office of Scientific Research of the Air Research and Development Command.

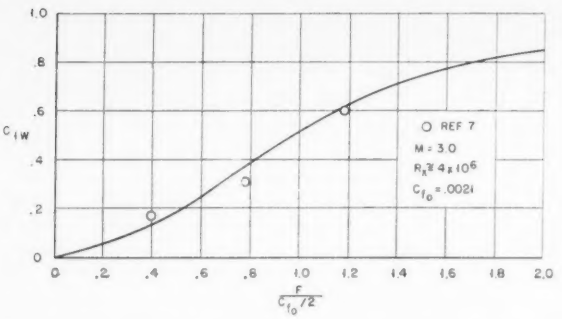

FIG. 1. Effect of injection on wall concentration of helium.

measurements. It appears from results in Ref. 3 that a good approximation in the concentration equation is to neglect the effects of thermal diffusion so that this equation takes the more usual form

$$\rho u(\partial c_1/\partial x) + \rho v(\partial c_1/\partial y) = \partial/\partial y[(\mu/Sc)(\partial c_1/\partial y)] \qquad (2)$$

Then assuming c_1 a function of u yields a total differential equation for c_1. This is further simplified by noting that in the sublayer region the shear stress is approximately constant, especially at low injection rates. The resulting equation can be integrated formally and solved by a simple iteration procedure to give

$$c_1/c_{1w} = 1 - \omega = 1 - (A\bar{u} - B\bar{u}^2) \qquad (3)$$

where $A = \dfrac{1+2\beta}{1+\beta}$; $B = \dfrac{\beta}{1+\beta}$; $\beta = \dfrac{j_2}{j_1}\dfrac{c_{1w}}{2}$

for which Sc varies linearly:[2]

$$Sc = j_1 + j_2 c_1$$

In a helium-air mixture $j_1 = 0.230$ and $j_2 = 1.549$.

The energy equation can be handled in a similar manner, assuming again that T is a function of u. When these computations are carried out, the Lewis number $L = Pr/Sc$ is quite accurately represented by

$$L = [k_1/(k_2 - K\omega)] + S; \quad k_1 = 0.852; \quad k_2 = K - 0.295$$
$$S = 0.210; \quad K = (C_{p_{12}} - 1)c_{1w} = 4.17c_{1w}$$

Then the energy equation can be integrated formally, yielding integrals which can be evaluated numerically without difficulty.

The influence of mass-transfer rate on skin friction and wall concentration of foreign gas may be calculated quite easily with a modified form of Covert's work,[4] based on an approximate integral method suggested by Liepmann.[5] Details of these calculations[2] will not be given here; the very simple formulas result:

$$\frac{C_f}{C_{f_0}} = \sqrt{\frac{\lambda_w}{I_1+1}} = \sqrt{\left(\frac{F}{C_{f_0}}\right)^2 + \lambda_w} - \frac{F}{C_{f_0}} \qquad (4)$$

$$c_{1w} = \frac{I_1}{I_1 + \left(1 + \dfrac{j_2}{2j_1}\right)} = \frac{F/C_{f_0}}{F/C_{f_0} + 2\left(1 + \dfrac{j_2}{2j_1}\dfrac{C_f}{C_{f_0}}\right)} \qquad (5)$$

where $I_1 = \dfrac{(\rho v)_w}{(\rho u)_e}\dfrac{2}{C_f} = \dfrac{2F}{C_f}$ and $\lambda_w = \dfrac{(\rho\mu)_w}{(\rho\mu)_e}$

C_{f_0} is the local skin friction coefficient with no mass transfer. The result (4) agrees very well with the measurements of Ref. 6 taken on a cone at a Reynolds number of 4×10^6 and $M_e = 3.24$. The data show virtually no changes in a Reynolds-number range 2.93×10^6 to 5.80×10^6. However, a serious failing of Eq. (4) is that it does not predict the strong influence of Mach number observed in the reference. Values of wall concentration from Eq. (5) are shown in Fig. 1.

Heat transfer (Stanton number) and the recovery factor are computed from the integrated energy equation and Eq. (1). It has been shown[3] that with mass transfer at the surface and thermal diffusion included, the proper "adiabatic wall" boundary condition is

$$[\kappa(\partial T/\partial y)]_{aw} = [\rho v(RTk_T/c_1)]_{aw}$$

which can be written in terms of previously defined quantities as

$$f_{aw}' = -Gf_{aw}; \qquad -G = 2I_1[(RPrk_T)/(c_1C_p)] \qquad (6)$$

where k_T is the thermal-diffusion ratio and R the gas constant for the mixture. The recovery factor and Stanton number are then given by

$$r = \frac{1}{(1-GW)}\left[r' + 2\frac{GW}{(\gamma-1)M_e^2}\right]$$

$$St = St'\frac{1-GW}{1+GW/(r'/2)(\gamma-1)M_e^2 + [1-(T_w/T_e)]}$$

with

$$W = \int_0^{\bar{u}_l}\frac{d\xi}{\chi} + \frac{c(1-\bar{u}_l)}{\chi_l}; \qquad \chi = \frac{1}{P_r}(k_2 - K\omega)$$

and r', St' are the values with mass transfer but no thermal diffusion.[2] For simplicity, effects of the latter appear here only through the boundary condition (6).

Fig. 2 shows some computed results for a helium-air mixture, and also the special case of air injection. The velocity at the sublayer edge has been left unknown so far as its variation with injection rate is concerned. Evidently the calculations are not excessively sensitive to its value. The dashed curves including the "correction" for thermal diffusion cannot be regarded as especially accurate, but the obvious trend appears to be true. The overshoot in r/r_0 at low injection rates in Fig. 2 can be ascribed to the factor k_T/c_1 in G; slight changes in this ratio can change the unsatisfactory behavior. There appears to be some uncertainty in the values of k_T.[3]

For the most part, the results are satisfactory, with two exceptions: the calculated skin friction does not exhibit the observed dependence on Mach number, and the predicted recovery factor lies considerably below measured values. It is perhaps an important result, although not truly conclusive, that if thermal diffusion is included, then the latter error is reduced while the heat transfer is only slightly affected. This might have been anticipated from estimates in Ref. 3 (pp. 76–80).

REFERENCES

[1] Rubesin, M. W., and Pappas, C. C., *An Analysis of the Turbulent Boundary Layer Characteristics on a Flat Plate with Distributed Light Gas Injection*, NACA TN 4149, Feb. 1958.

[2] Culick, F. E. C., *The Compressible Turbulent Boundary Layer with Surface Mass Transfer*, Mass. Inst. of Technology, Naval Supersonic Lab., TR 454, Aug. 1960.

[3] Baron, J. R., *The Binary Mixture Boundary Layer Associated with Mass Transfer Cooling at High Speeds*, Mass. Inst. of Tech., Naval Supersonic Lab. TR 160, May 1956.

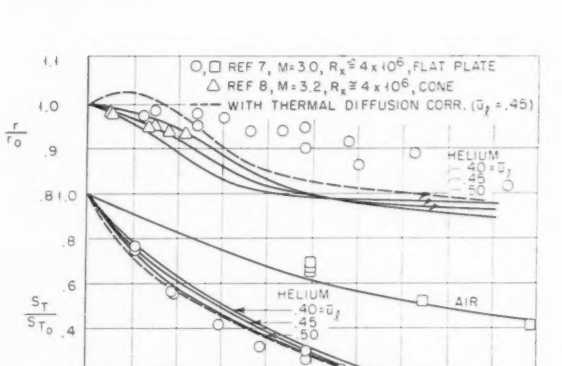

FIG. 2. Comparison of theory and experimental results for recovery factor and Stanton number: helium injection.

[4] Covert, E. E., *Some Approximations to the Solution to the Binary Boundary Layer Problem*, Mass. Inst. of Tech., Naval Supersonic Lab., TR 390, Sept. 1959.

[5] Liepmann, H. W., *A Simple Derivation of Lighthill's Heat Transfer Formula*, J. Fluid Mech., Vol. 3, Pt. 4, pp. 361–367, Jan. 1958.

[6] Pappas, C. C., and Okuno, A. F., *Measurements of Skin Friction of the Compressible Turbulent Boundary Layer on a Cone with Foreign Gas Injection*, Journal of the Aero/Space Sciences, Vol. 27, No. 5, pp. 321–333, May 1960.

[7] Leadon, B. M., and Scott, C. J., *Measurements of Recovery Factors and Heat Transfer Coefficients with Transpiration Cooling in a Turbulent Boundary Layer at M = 3 Using Air and Helium as Coolants*, Univ. of Minnesota, Heat Transfer Lab., Rosemount Aero. Lab., TR 126, 1956.

[8] Rockower, B., and Goelnick, A. F. Jr., *Mass Transfer Cooling of a Cone*, Mass. Inst. of Tech., Naval Supersonic Lab., TR 424, to be published.

The Epicyclic Analysis as Applied to Free-Flight Data

Peter J. Mantle
Graduate Student, Guggenheim Aeronautical Laboratory California Institute of Technology, Pasadena, Calif.
December 27, 1960

SYMBOLS

$\mathbf{K}_j$ $(j = 1, 2, 3)$	=	rotating vectors in amplitude plane
k	=	pitch radius of gyration
l_r	=	reference length
m	=	body mass
p_0	=	steady rate of roll
S_r	=	reference area
U	=	forward velocity of body c.g.
I_x	=	rolling moment of inertia about body axis
I	=	pitching moment of inertia about body axis
Δx	=	horizontal displacement between peaks in amplitude plane
α	=	pitch incidence relative to rolling body axes
$\tilde{\alpha}$	=	pitch incidence relative to nonrolling coordinates
β	=	sideslip angle relative to rolling body axes
$\tilde{\beta}$	=	sideslip angle referred to nonrolling coordinates
μ	=	complex angle of attack $(\beta + i\alpha)$
$\lvert\mu\rvert$	=	"total" angle of attack $\sqrt{\alpha^2 + \beta^2}$
$\nu_j (j = 1, 2)$	=	damping parameters in epicyclic solution
$\omega_j (j = 1, 2)$	=	angular rates of vectors $\mathbf{K}_j$

Subscript

p	=	evaluated at in-phase position—i.e., at peaks

AS A COMPLEMENTARY NOTE to Ref. 1 a short discussion is presented on the application of the epicyclic analysis to free-flight data of axisymmetric bodies, with particular reference to data obtained in an aeroballistic range.

After Fowler *et al.*[2] demonstrated the epicyclic behavior of spinning shells, Nicolaides[3] introduced the technique of analyzing the data in the complex amplitude plane where the coordinate and abscissa are pitch incidence $(\tilde{\alpha})$ and sideslip angle $(\tilde{\beta})$, respectively. Nicolaides' analysis was characterized by the use of a nonrolling body-axis system which resulted in the complex angle of attack being represented by the sum of three rotating vectors (the tricyclic form). If, however, by a rotation of axes we return to rolling coordinates, where the rotation is given by the integral of the roll rate, then the epicyclic form of the solution is obtained and we may write[4]

$$\beta + i\alpha = \mathbf{K}_1 e^{[\nu_1 + i(\omega_1 - p_0)]t} + \mathbf{K}_2 e^{[\nu_2 + i(\omega_2 - p_0)]t} + \mathbf{K}_3 \quad (1)$$

The quantities $\mathbf{K}_1$, $\mathbf{K}_2$, $\mathbf{K}_3$ are the initial values of the complex angle of attack, and specifically, $\mathbf{K}_3$ is the trim vector associated with body asymmetries and control inputs. The resonance phenomenon related to this trim vector has been considered by Murphy.[5]

The epicyclic analysis as presented here results in a particularly simple data-reduction technique and avoids the iterative procedures required in both Nicolaides' tricyclic analysis and Danis' epicycle method. The method is best described with the aid of an example. For this purpose the flight-data obtained from the trajectory of a flared-base projectile in the aeroballistics range at the Canadian Armament Research and Development Establishment (CARDE) will be used. The flight data of a typical trajectory are presented in Fig. 1.

Each experimental point in this amplitude plane corresponds to the value of the total angle of attack measured at a particular station. Proceeding from point to point along the curve describes the flight history—i.e., Fig. 1 represents the trace of the nose of the projectile during its flight downrange. The value of X at each point has been omitted for clarity. The development of the method is given in Ref. 4 but the pertinent results are summarized here. The technique is based on the condition that the loops in the amplitude plane (Fig. 1) correspond to the in-phase positions of the vectors $\mathbf{K}_1$ and $\mathbf{K}_2$ (note the vector $\mathbf{K}_3$ can be eliminated by a simple translation of the origin). From this the following important results are obtained which provide solutions for the static stability and damping parameters

$$C_{m_\alpha} = -[(\pi/\Delta x)^2 - (I_x/I)^2(p_0/U)^2](2I/\rho S_r l_r) \quad (2)$$

$$C_{N\alpha} - (l_r/k)^2(C_{m_q} + C_{m_{\dot{\alpha}}}) = -(2m/\rho S_r)(\nu_1 + \nu_2)_p \quad (3)$$

In Eq. (3) the result is limited by the condition that $\nu_1\nu_2 \ll 1$ which is satisfied by most conventional configurations. The value of the steady roll rate can be obtained from the rate of migration of the loops in the amplitude plane, but it is more usually obtained from the original free-flight data. For slender bodies rolling at moderate rates the second term in Eq. (2) can be neglected, giving the simple approximate value for the static stability coefficient

$$C_{m_\alpha} = -(\pi/\Delta x)^2(2I/\rho S_r l_r) \quad (4)$$

The reduction technique utilizes two quantities taken from the amplitude plane (Fig. 1). These are X_p, the distance flown to the peaks of each loop, and $\lvert\mu\rvert_p$, the total angle of attack measured at each peak. Plotting X_p versus the peak number (counted from the first convenient peak in the trajectory) gives a straight line of slope ΔX which is shown, for the cited example, in Fig. 2. The slope of this line and Eq. (2) or (4) give the value of the static-stability parameter.

Plotting the value of $\lvert\mu\rvert$ at each peak on a logarithmic scale against the linear distance to peak gives Fig. 3. The slope of

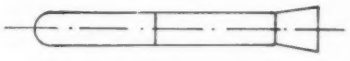

Flared Base Projectile

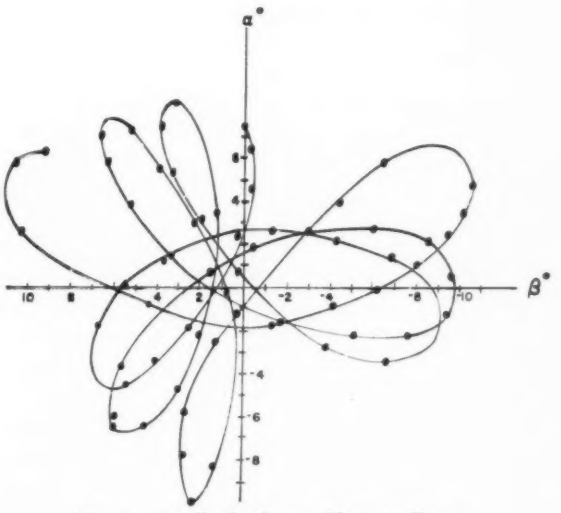

FIG. 1. Amplitude plane, rolling coordinates.

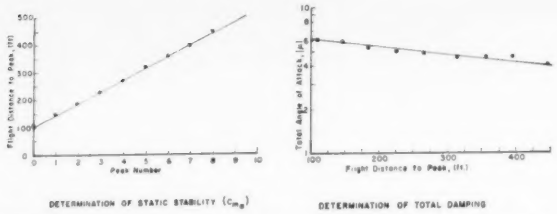
Flight Distance to Peak, (ft)
Peak Number
DETERMINATION OF STATIC STABILITY (C_{m_α})
Total Angle of Attack, (μ)
Flight Distance to Peak, (ft.)
DETERMINATION OF TOTAL DAMPING

FIG. 2. (*Left*) Determination of static stability (C_{m_α}). FIG. 3. (*Right*) Determination of total damping.

this straight line ($\nu_1 + \nu_2$) is directly proportional to the damping of the system as given by Eq. (3). This completes the reduction technique.

This epicyclic method has been applied successfully to many free-flight data obtained on axisymmetric bodies in the aeroballistic range at CARDE. These data pertained to configurations tested over a large range of flight Mach numbers and roll rates. Although this method is only applicable to the case of steady roll, it is obvious that the trajectory can be divided into regions over which a mean value of the roll rate is taken and the solutions superposed.

In conclusion, it is seen that this method is particularly simple to apply and avoids the iterative procedures previously employed and also the need for digital computers. A restriction on the method is that only a small portion of the available experimental data is actually used, which places a more stringent requirement on the accuracy of such data.

REFERENCES

[1] Danis, R. P., *The Epicycle Method for the Reduction of Flight-Test Data Using a Digital Computer*, Journal of the Aerospace Sciences, Vol. 27, No. 12, pp.913–920, Dec. 1960.

[2] Fowler, R. H., *et al.*, *The Aerodynamics of a Spinning Shell*, Phil. Trans. Roy. Soc. (London), 1920.

[3] Nicolaides, J. D., *On the Free-Flight Motion of Missiles Having Slight Configurational Asymmetries*, APC/BRL/R 858, 1953.

[4] Mantle, P. J., *Tricyclic and Epicyclic Analyses as Applied to Aeroballistics Range Data*, CARDE TM/AB-64, Aug. 1960.

[5] Murphy, C. H., *Advances in the Dynamic Analysis of Range Data*, APG/BRL/R 1005-1, 1957.

Shock Propagation in Time Department Ducts*

Roy Gundersen
Associate Professor of Mathematics, Illinois Institute of Technology, Chicago, Ill.
December 29, 1960

ALTHOUGH problems with ducts of time-dependent cross-sectional area are rare (one example would be a boundary layer growing with time), it is of interest that the pressure change behind a shock propagating through such a duct is given by the solution for the time-independent duct by making a simple change of the time variable.

The equations which govern the one-dimensional, unsteady flow of an inviscid, ideal compressible gas in a tube of varying cross-sectional area are:

$$u_t + uu_x + \frac{2}{\gamma - 1} cc_x = \frac{c^2}{\gamma(\gamma - 1)c_v} s_x$$

$$\frac{2}{\gamma - 1} Ec_t + \frac{2}{\gamma - 1} Euc_x + cEu_x + cE_t + ucE_x = 0$$

$$s_t + us_x = 0$$

where u, c, s, and E are, respectively, the particle velocity, the local speed of sound, the specific entropy, and the cross-sectional area. Partial derivatives are denoted by subscripts and γ is the ratio of specific heats at constant pressure c_p and at constant volume c_v.

If the cross-sectional area of the tube is expressed in the form $E(x,t) = E_0 + E_1(x,t)$, where E_0 is the original uniform area and $E_1(x,t)$ is the perturbation, and the above equations are linearized in the neighborhood of a known (isentropic) solution denoted by the subscript zero, the following system of linear equations, which govern the first approximation to the behavior of the disturbed flow (not assumed isentropic) is obtained:

$$\left.\begin{aligned} &A_t + (u_0 + c_0)A_x + \left[\frac{\gamma + 1}{2} A + \frac{\gamma - 3}{2} B\right]\alpha_x = \\ &\qquad -(1/2E_0)(u_0c_0E_{1x} + c_0E_{1t}) + (1/2)\, H_0 \\ &B_t + (u_0 - c_0)B_x + \left[\frac{3 - \gamma}{2} A - \frac{\gamma + 1}{2} B\right]\beta_x = \\ &\qquad -(1/2E_0)(u_0c_0E_{1x} + c_0E_{1t}) - (1/2)H_0 \end{aligned}\right\} \quad (1)$$

where $\dfrac{u_0}{2} + \dfrac{c_0}{\gamma - 1} = \alpha, \qquad -\dfrac{u_0}{2} + \dfrac{c_0}{\gamma - 1} = \beta$

$$\frac{u_1}{2} + \frac{c_1}{\gamma - 1} = A, \qquad -\frac{u_1}{2} + \frac{c_1}{\gamma - 1} = B$$

and $H_0c_v\gamma(\gamma - 1) = c_0^2 s_{1_x}$

The derivation closely parallels that of Ref. 1, which may be consulted for details.

For the case of an initially uniform flow, α and β are constants and the general solution to the system (1) is:

$$\left.\begin{aligned} H_0 &= 2R'(x - u_0t) \\ A &= F[x - (u_0 + c_0)t] + c_0^{-1}R(x - u_0t) - \\ &\qquad E_1[x, (u_0 + c_0)t/u_0]\, u_0c_0/2E_0(u_0 + c_0) \\ B &= G[x - (u_0 - c_0)t] + c_0^{-1}R(x - u_0t) - \\ &\qquad E_1[x, (u_0 - c_0)t/u_0]u_0c_0/2E_0(u_0 - c_0) \end{aligned}\right\} \quad (2)$$

When an originally uniform shock wave propagates through a tube of varying cross-sectional area, the shock is perturbed, the shock strength is altered, and the subsequent flow is nonisentropic. There are two contributions to the disturbance—viz., a permanent perturbation due to the area variations and a transient perturbation propagated downstream with sonic velocity relative to the flow behind the shock, due to reflections from the shock of the permanent perturbation.

Suppose the area variations are restricted to the region $x > 0$ and that the shock of arbitrary strength initially moves with constant velocity through the region $x < 0$. If the shock is generated by a piston moving with constant velocity, it is assumed that the piston is always sufficiently far to the left so that no reflections come back from it to interfere with the interaction under consideration.

Let the flow in front of the shock be denoted by the subscript 1 and the flow behind by the subscript 2. Let P denote the pressure, w the shock velocity, $v = w - u$, $m = u/c$, $M = v/c$ so that the following relations hold:

$$\left.\begin{aligned} u_2 &= u_1 + 2M_1c_1(1 - M_1^{-2})/(\gamma + 1) \\ c_1/c_2 &= (\gamma + 1)M_2/M_1(\gamma - 1 + 2M_1^{-2}) \\ P_2/P_1 &= 2\gamma M_1^2/(\gamma + 1) - (\gamma - 1)/(\gamma + 1) \\ M_2^2 &= (\gamma - 1 + 2M_1^{-2})/[2\gamma - (\gamma - 1)M_1^{-2}] \\ m_2 &= (\gamma + 1)M_2m_1/M_1(\gamma - 1 + 2M_1^{-2}) + \\ &\qquad 2(1 - M_2^2)M_2(\gamma + 1) \\ (\gamma + 1)v_2 &= M_1c_1(\gamma - 1 + 2M_1^{-2}) \end{aligned}\right\} \quad (3)$$

The present problem is identical with that solved in Ref. 2 save for the added dependence of E_1 on t. Hence the results may be given with only minor modifications. The perturbation of the shock will be obtained by the use of the general solution, Eqs. (2), by setting $F = 0$, since, from the formulation of the problem, the contribution given by F is not included, for there

* This work was supported by a grant from the National Science Foundation.

is no mechanism downstream of the shock which could give rise to such a term. Thus, denoting perturbations of a base quantity by a bar, setting $F = 0$ in the second of Eqs. (2), and utilizing the perturbation form of the relations (3) we obtain

$$\bar{P}_2 = -(\gamma+1)(P_2-P_1)\bar{u}_1/M_1c_1(1-M_1^{-2})(1+2M_2+M_1^{-2}) + (\gamma+1)(P_2-P_1)(1+M_1^{-2})\bar{P}_1/2\gamma P_1(1-M_2^2)(1+2M_2+M_1^{-2}) - 2(P_2-P_1)\bar{c}_1/c_1(1+2M_2+M_1^{-2}) - (\gamma+1)m_1(P_2-P_1)E_1[x,(1+m_2)t/m_2]/E_0(1+m_2)M_1(1-M_1^{-2})(1+2M_2+M_1^{-2}) - 2(P_2-P_1)E_1[x,(1+m_2)t/m_2]/E_0(1+m_2)(1+2M_2+M_1^{-2}) \quad (4)$$

To complete the present solution, the arbitrary function G of Eq. (2) must be determined. This is most easily obtained by adding the last two of Eqs. (2), evaluating the result on the shock, $x = wt$, and replacing $\bar{P}_2$ by its equivalent from Eq. (4). This yields:

$$G(\lambda)/c_2 = -\bar{u}_1[\tau\lambda,\lambda/c_2(1+M_2)]\,2(1-M_2^2)/M_1c_1(1-M_1^{-2})(1+2M_2+M_1^{-2}) - 4\bar{c}_1[\tau\lambda,\lambda/c_2(1+M_2)](1-M_2^2)/(\gamma+1)c_1(1+2M_2+M_1^{-2}) + \bar{P}_1[\tau\lambda,\lambda/c_2(1+M_2)](1+M_1^{-2})/\gamma P_1(1+2M_2+M_1^{-2}) + m_2E_1[\tau\lambda,(m_2-1)\lambda/m_2c_2(M_2+1)]/2E_0(m_2-1) + \{m_2/2(1+m_2) - 2m_1(1-M_2^2)/(1+m_2)M_1(1-M_1^{-2})(1+2M_2+M_1^{-2}) - 4(1-M_2^2)/(\gamma+1)(1+m_2)(1+2M_2+M_1^{-2})\}\{E_1[\tau\lambda,(m_2+1)\lambda/m_2c_2(M_2+1)]/E_0\} \quad (5)$$

where $\tau = (M_2+m_2)/(1+M_2)$ and $\lambda = x-(u_2-c_2)t$.

Thus, the complete solution for $\bar{P}_2$ is:

$$\bar{P}_2/(P_2-P_1) = -\{E_1[x,(1+m_2)t/m_2]/(m_2+1) + E_1[x,(m_2-1)t/m_2]/(m_2-1) - E_1[\tau\lambda,(m_2-1)\lambda/m_2c_2(M_2+1)]/(m_2-1)\}\{(\gamma+1)m_2/4E_0(1-M_2^2) + \{(\gamma+1)m_2/4(1+m_2)(1-M_2^2) - (\gamma+1)m_1/(1+m_2)M_1(1-M_1^{-2})(1+2M_2+M_1^{-2}) + -2/(1+m_2)(1+2M_2+M_1^{-2})\}E_1[\tau\lambda,(m_2+1)\lambda/m_2c_2(M_2+1)]/E_0 - \bar{u}_1(\gamma+1)/M_1c_1(1-M_1^{-2})(1+2M_2+M_1^{-2}) - \bar{c}_1 2/c_1(1+2M_2+M_1^{-2})\,\bar{P}_1(\gamma+1)(1+M_1^{-2})/2\gamma P_1(1+2M_2+M_1^{-2})(1-M_2^{-2}) \quad (6)$$

where the omitted arguments of $\bar{u}$, $\bar{c}_1$ and $\bar{P}_1$ are the same as in Eq. (5).

In the region directly behind the shock, the pressure change is given by Eq. (4). When the flow behind the shock is subsonic, a disturbance will be reflected downstream of the shock, and the pressure perturbation is given by Eq. (6). When the flow behind the shock is supersonic, this disturbance will propagate upstream of the shock, and the pressure perturbation is given by the entire Eq. (6).

It is easily seen that when there is no time dependence in the area variations, the present results reduce to those presented in Ref. 2.

References

[1] Gundersen, R., *The Flow of a Compressible Fluid with Weak Entropy Changes*, J. Fluid Mech., Vol. 3, Pt. 6, pp. 553–581, March 1958.

[2] Gundersen, R., *The Propagation of a Plane Shock Wave into a Moving Fluid*, Readers' Forum, Journal of the Aerospace Sciences, Vol. 28, No. 7, pp. 584, 585, July 1961.

Stagnation-Point Heat Transfer in Equilibrium Dissociated Air With Variable Prandtl and Lewis Numbers

Aemer D. Anderson*

Lockheed Aircraft Corporation, Missiles and Space Division, Sunnyvale, Calif.

January 3, 1961

Symbols

c_i = mass fraction of component i

c_{pi} = specific heat at constant pressure of component i

$\bar{c}_p = \sum_i c_i c_{pi}$

c_{pt} = total specific heat at constant pressure of mixture

D = diffusion coefficient

h_i^0 = heat of formation of component i at absolute zero

h = total enthalpy of mixture, $\sum_i \int_0^T c_{pi}\,dT + h_i^0$

h_d = chemical enthalpy at boundary layer edge, $\sum_i c_{ie} h_i^0$

k = ordinary thermal conductivity due to molecular collision

k_t = total equilibrium thermal conductivity

L_e = Lewis number, $\rho D\bar{c}_p/k$

p = pressure

Pr = Prandtl number $\mu\bar{c}_p/k$

q = heat flux

T = absolute temperature

u = velocity in x direction

v = velocity in y direction

x = surface coordinate

y = normal coordinate

ρ = density

μ = absolute viscosity

Subscripts

e = boundary-layer edge

w = wall

THE THEORY of stagnation-point heat transfer in dissociated air was set forth by Fay and Riddell in 1958.[1] They reported numerical solutions to the stagnation-region boundary-layer equations for air in equilibrium, which were obtained assuming constant Prandtl and Lewis numbers in each solution. These calculations were for $Pr = 0.71$ and $1.0 \leq Le \leq 2.0$. Their correlation of these solutions may be written as follows:

$$q = 0.76\,Pr^{-0.6}(\rho_e\mu_e\,du_e/dx)^{0.5}(\rho_w\mu_w/\rho_e\mu_e)^{0.1} \times [1+(Le^{0.52}-1)h_d/h_e](h_e-h_w) \quad (1)$$

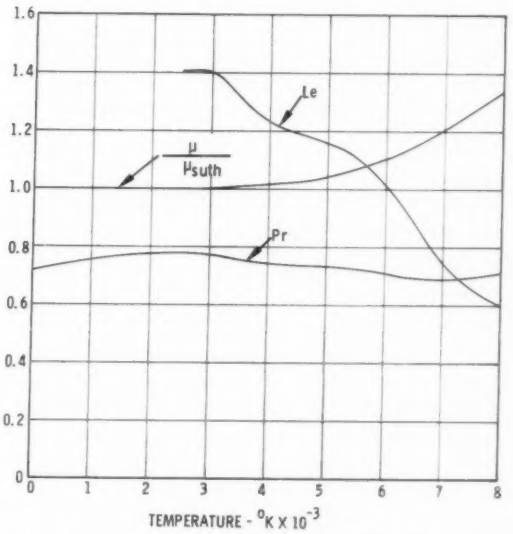

FIG. 1. Property values according to Ref. 2.

* Thermodynamicist.

TABLE 1

Numerical Solutions

P_{e}, atm	T_{w}, °R	T_{e}, °R	h_{e}, Btu/lb$_m$	h_{w}, Btu/lb$_m$	$\rho_w \mu_w / \rho_e \mu_e$	$\overline{Pr}$	$\overline{Le}$	$\frac{\overline{Pr}}{\overline{Le}}$	$\frac{q}{q(\text{Eq. 1})}$
0.1	3500	500	2935	217	2.56	0.77	1.32	0.34	1.00
0.1	6000	500	9536	217	3.84	0.73	1.11	0.64	0.98
1.0	2500	500	1261	217	1.92	0.76	1.40	0.02	1.00
1.0	2500	1000	1261	450	1.49	0.77	1.40	0.02	1.00
1.0	3500	500	2477	217	2.43	0.76	1.36	0.24	0.99
1.0	3500	1000	2477	450	1.89	0.77	1.36	0.24	1.01
1.0	5500	500	5140	217	3.25	0.75	1.26	0.39	0.98
1.0	5500	1000	5140	450	2.53	0.75	1.26	0.39	1.00
1.0	5500	2000	5140	967	1.89	0.75	1.26	0.39	1.03
1.0	5500	3000	5140	1705	1.53	0.75	1.26	0.39	1.03
1.0	5500	4000	5140	3314	1.20	0.73	1.17	0.39	1.04
1.0	6500	500	8511	217	3.78	0.73	1.14	0.56	0.97
1.0	6500	1000	8511	450	2.94	0.73	1.14	0.56	1.00
1.0	7000	500	11,140	217	4.12	0.73	1.07	0.64	0.98
1.0	7000	1000	11,140	450	3.20	0.73	1.07	0.64	1.00
1.0	7000	2000	11,140	967	2.39	0.73	1.07	0.64	1.03
1.0	7000	3000	11,140	1705	1.93	0.73	1.07	0.64	1.04
1.0	7000	4000	11,140	3314	1.51	0.72	0.99	0.64	1.07
1.0	8000	500	16,390	217	4.68	0.73	1.00	0.69	0.97
1.0	8000	1000	16,390	450	3.64	0.73	1.00	0.69	1.00
10.0	4000	500	2737	217	2.57	0.77	1.40	0.21	0.99
10.0	7000	500	7552	217	3.73	0.74	1.21	0.47	0.96
100.0	4500	500	2350	217	2.66	0.77	1.43	0.16	0.99
100.0	8000	500	8049	217	3.90	0.74	1.22	0.42	0.96

This expression defines the effect of the level of the density-viscosity product and the effect of its distribution through the boundary layer, at least for the Sutherland viscosity model used. It also indicates the influence of the level of the Prandtl and Lewis numbers.

In dissociated-air boundary layers the Prandtl number is in fact nearly constant; this is not true, however, of the Lewis number.[2, 3] The effect of Lewis-number distribution through the boundary layer is left undefined by Eq. (1) and could very well be important at high enthalpy levels. The purpose of this note is to show that Eq. (1), with its attendant simplicity, can be used in situations where the Prandtl and Lewis numbers do vary across the boundary layer, when representative values of these parameters are selected in a particular way.

The present uncertainty in the determination of the transport properties of dissociated air is considerable.[2, 3] The calculations of Hansen[2] were used in this study since they provide, in convenient form, a complete model for both the thermodynamic and the transport properties.

The solutions reported herein were carried out, primarily, for a pressure of 1 atm. The viscosity given in Ref. 2 for this pressure is shown normalized with the Sutherland viscosity in Fig. 1. The Prandtl and Lewis numbers from Ref. 2 are also shown in Fig. 1 for this pressure. These property values are not strongly pressure-dependent in the enthalpy and pressure ranges of interest here.

The total equilibrium thermal conductivity, k_t, as tabulated by Hansen, describes the overall energy transfer in the presence of a temperature gradient. This includes the energy transfer by diffusion as well as that by ordinary conduction due to molecular collision. The total specific heat is defined as

$$c_{pt} = (\partial h/\partial T)_p$$

where h includes both the sensible and the chemical enthalpies.

Using these properties, the boundary-layer conservation equations may be written for the stagnation region, as follows:

Mass:

$$(\partial/\partial x)(\rho u x) + (\partial/\partial y)(\rho v x) = 0 \qquad (2)$$

Momentum:

$$\rho u \frac{\partial u}{\partial x} + \rho v \frac{\partial u}{\partial y} = \frac{\partial}{\partial y}\left(\mu \frac{\partial u}{\partial y}\right) + \rho_e u_e \frac{du_e}{dx} \qquad (3)$$

Energy:

$$\rho u \frac{\partial h}{\partial x} + \rho v \frac{\partial h}{\partial y} = \frac{\partial}{\partial y}\left(\frac{k_t}{c_{pt}} \frac{\partial h}{\partial y}\right) \qquad (4)$$

Numerical solutions of these equations were obtained using the transformations and calculation procedure described in Ref. 4. A revision was made so that the effect of the compressibility, Z, was included in the calculation of the density.

The boundary conditions for which the various solutions were carried out are shown in Table 1. Also shown are the parameters used in the Fay-Riddell correlation [Eq. (1)] and a comparison of the correlation with the numerical solutions.

The quantity $\overline{Le}$ is the average of the maximum and minimum values of the Lewis number in the boundary layer. The representative Prandtl number, $\overline{Pr}$, was similarly evaluated. With this choice of these parameters, Eq. (1) is seen to correlate the numerical solutions within ±5 percent, with one exception at a very high wall temperature.

This agreement is somewhat to be expected since the use of either the maximum or minimum Lewis number in Eq. (1) would change the prediction by only 15 percent at the most (increasing the scatter to ±20 percent). These solutions do show, however, that neither the Lewis number nearest the wall nor the Lewis number at the edge of the boundary layer (where the chemical enthalpy is largest) is more representative of the entire boundary layer.

REFERENCES

[1] Fay, J. A., and Riddell, F. R., *Theory of Stagnation Point Heat Transfer in Dissociated Air*, Journal of the Aeronautical Sciences, Vol. 25, No. 2, pp. 73–85, 121, Feb. 1958.

[2] Hansen, C. F., *Approximations for the Thermodynamic and Transport Properties of High-Temperature Air*, NASA TR R-50, 1959.

[3] Bauer, E., and Zlotnick, M., *Transport Coefficients of Air to 8000°K*, ARS Jour., Vol. 29, No. 10, Pt. 1, pp. 721–728, Oct. 1959.

[4] Hoshizaki, H., and Smith, H. J., *Axisymmetric Stagnation Point Mass Transfer Cooling*, LMSD/48379, Dec. 1958.

Comparison of Flow-Direction Probes at Supersonic Speeds

Frank W. Barry

Measurements and Control Dynamics Section, Technical Services
Hamilton Standard Division, United Aircraft Corporation
Windsor Locks, Conn.

January 6, 1961

AERODYNAMICISTS working on flight instrumentation, wind-tunnel instrumentation and aircraft air-induction-system controls are concerned with measuring Mach number and flow direction. The selection of probes for measuring Mach number has been discussed.[1] Various wedge, conical, hemispherical and pitot probes which provide a pressure signal related to flow direction are compared here on the basis of theoretical and experimental sensitivity (rate of change of pressure difference or of pressure ratio with flow-direction angle) data.

THEORY

Static-pressure taps on a conical probe have been used to measure flow direction.[2] The theoretical sensitivity, if the flow is aligned with the cone axis, is

$$\Delta P/Q\epsilon = 0.034906(\bar{P}/Q)\eta/\bar{P} \qquad (1)$$

where ΔP is the difference between pressures at two diametrically opposite taps, Q is the free-stream dynamic pressure ($\gamma P_{s0} M^2/2$), ϵ is the flow angle in the plane of the taps in degrees, and $\eta/\bar{P}$ and $\bar{P}/Q$ may be computed from tables.[3, 4] The sensed pressures are larger for a probe with pitot tubes near the cone surface instead of static taps, and the sensitivity is

$$\Delta P/Q\epsilon = (0.034906 P_p/Q)(\eta/\bar{P} + KX) \qquad (2)$$

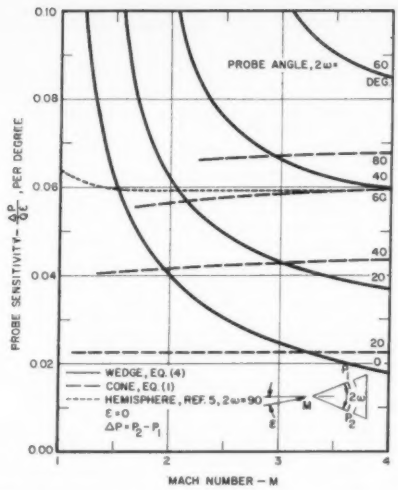

FIG. 1. Sensitivity of probes with static taps.

where the pitot pressure P_p is computed from $\bar{P}$ and M_s^2, X is tabulated,[4] and

$$K = \sqrt{\frac{8}{\gamma - 1}} \frac{(2M_s^2 - 1)\gamma\{1 + [(\gamma - 1)/2]M_s^2\}^{3/2}}{M_s(2\gamma M_s^2 - \gamma + 1)} \quad (3)$$

if the cone surface Mach number M_s exceeds one.

The theoretical sensitivity of a two-dimensional wedge probe at zero flow angle may be derived from an extension of the analysis of Ref. 1. In terms of the nomenclature of Ref. 1, the sensitivities are, for two surface static taps,

$$\Delta P/Q\epsilon = -(4t/\gamma M^2 c)c_\alpha/c \quad (4)$$
$$= 0.069813/\sqrt{M^2 - 1}$$

for a flat plate ($\omega = 0$); and, for two pitot tubes between the oblique shock and the surface,

$$\Delta P/Q\epsilon = -(4t/\gamma M^2 c)[d(c_\alpha/c) - d_{M1}M_\alpha] \quad (5)$$
$$= \frac{0.069813}{\sqrt{M^2 - 1}}\left[b - \frac{b_M\left(1 + \frac{\gamma - 1}{2}M^2\right)}{\gamma M}\right]$$

for $\omega = 0$.

COMPARISON OF PROBES

The theoretical sensitivities of wedge and conical probes using surface static taps and an empirical correlation (Ref. 5) for hemispherical probes are shown in Fig. 1. The theoretical sensitivities of probes using pitot tubes are shown in Fig. 2. Measurements with pitot tubes on a 26° included-angle cone for Hamilton Standard Division showed slightly lower sensitivities than were computed from Eq. (2). Comparison of Fig. 2 with Fig. 1 shows that greater sensitivities can be obtained with pitot tubes than with static taps on probes at Mach numbers exceeding roughly two. The measured sensitivities of a hemisphere with two short, projecting, pitot tubes at 45° to the axis (similar to the Douglas-Giannini probe[6]) and of a Y-shaped probe with an included angle of 120° between the two pitot arms are also shown in Fig. 2. The sensitivities of the latter probe were derived from tests of a pitot tube in the UAC Research Laboratory supersonic wind tunnel at flow angles from 5° to 80°.

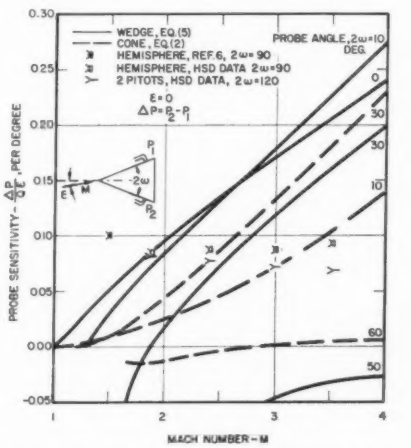

FIG. 2. Sensitivity of probes with pitot tubes.

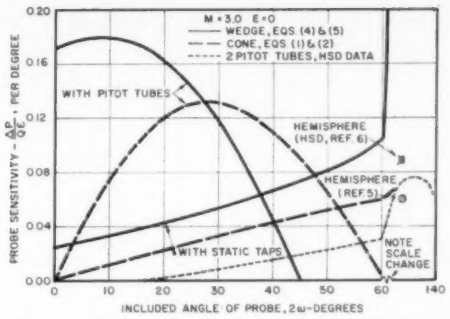
M=3.0 ε=0
WEDGE, EQS (4) & (5)
CONE, EQS (1) & (2)
2 PITOT TUBES, HSD DATA
WITH PITOT TUBES
HEMISPHERE (HSD, REF. 6)
HEMISPHERE (REF. 5)
WITH STATIC TAPS
NOTE SCALE CHANGE
PROBE SENSITIVITY - ΔP/Qε, PER DEGREE
INCLUDED ANGLE OF PROBE, 2ω-DEGREES

FIG. 3. Effect of geometry on probe sensitivity.

The variation of the sensitivity of several probes with included angle is shown in Fig. 3 for a Mach number of 3.0. The sensitivities of pitot tubes on a probe are a maximum for a 10° wedge and for a 28° cone and become negative at large included angles. The sensitivities of static taps on wedges and cones increase with included angle. The sensitivity of two pitot tubes is largest for an included angle of roughly 110° between the arms.

The probes discussed above are compared in Fig. 4 for applications where a sensed pressure ratio rather than a pressure difference is used to determine flow direction. As shown by the line labeled "typical locus of constant accuracy," friction and threshold effects in the sensor require that a probe providing signals with a lower pressure level have a larger sensitivity in order to maintain constant accuracy in sensed flow direction. Therefore, static taps on a 60° wedge can provide the same accuracy as pitot tubes on a flat plate.

Flow-direction angle in one plane can be determined at supersonic speeds by measuring a pair of pressures from a flow-direction probe. Selection of an appropriate probe geometry will optimize the pressure signal and thereby minimize errors in the derived flow direction.

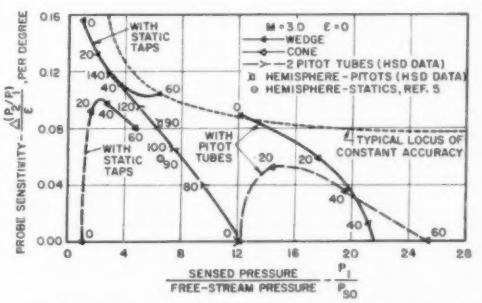

FIG. 4. Effect of geometry on pressure-ratio sensitivity and pressure level. Number beside symbol is included angle of probe (2ω) in degrees.

REFERENCES

[1] Barry, F. W., *Determination of Mach Number from Pressure Measurements*, Trans. of ASME, Vol. 78, No. 3, pp. 581–589, April 1956.

[2] Centolanzi, F. J., *Characteristics of a 40° Cone for Measuring Mach Number, Total Pressure, and Flow Angles at Supersonic Speeds*, NACA TN 3967, May 1957.

[3] Kopal, Z., *Tables of Supersonic Flow Around Cones*, Center of Analysis, M.I.T., Tech. Rep. No. 1, 1947.

[4] Kopal, Z., *Tables of Supersonic Flow Around Yawing Cones*, Center of Analysis, M.I.T., Tech. Rep. No. 3, 1947.

[5] Beecham, L. J., and Collins, S. J., *Static and Dynamic Response of a Design of Differential Pressure Yawmeter at Supersonic Speeds*, ARC (Great Britain), CP No. 414, 1958.

[6] Smetana, F. O., and Headley, J. W., *A Further Study of Angle-of-Attack Angle-of-Sideslip Pitot-Static Probes*, WADC Tech. Rep. 57-234, Pt. II June 1958.

✦ ✦ ✦

Torsional Analysis of Thin-Walled Shells (*Continued from page 731*)

References

[1] Kuhn, P., *Stresses in Aircraft and Shell Structures*, McGraw-Hill Book Co., Inc., New York, 1956, pp. 11–20.

[2] Timoshenko, S., *Strength of Materials, Part II*, 3rd Ed., D. Van Nostrand Co., Inc., New York, 1957 pp. 251–254.

[3] Benscoter, S. U., *Numerical Transformation Procedures for Shear-Flow Calculations*, Journal of Aeronautical Sciences, Vol. 13, No. 8, pp. 438–443, August 1946.

[4] Bruhn, E. F., *Analysis and Design of Aircraft Structures*, Vol. 1, Tri-State Offset Co., Cincinnati, 1958, pp. A6.10–A6.15.

[5] Rivello, R. M., and Bates, C. C., *Torsion of Rectangular and Triangular Cross-Section Honeycomb Sandwich Panels*, APL/JHU CF-2771, Applied Physics Laboratory, The Johns Hopkins University, September 1958.

[6] Fox, D. W., and Rivello, R. M., *Torsional Analysis of Thin-Walled Shells with Closely Spaced Spars*, APL/JHU CF-2754, Applied Physics Laboratory, The Johns Hopkins University, September 1958.

[7] Luber, J. L., *The Shear Distribution in a Multicell Section Due to an Applied Shear Force*, Master of Science Thesis, Department of Aeronautical Engineering, University of Maryland, June 1959.

[8] Niedenfuhr, F. W., *Torsion Analysis of Multicell Tubes*, Journal of the Aero/Space Sciences, Vol. 27, No. 4, pp. 308–309, April 1960.

[9] Seide, Paul, *On the Torsion of Rectangular Sandwich Plates*, J. Appl. Mech., Vol. 23, No. 2, June 1956.

[10] Cheng, Shun, *Torsion of Rectangular Sandwich Plates*, Forest Products Laboratory Report 1871, August 1959.

[11] McComb, H. G., Jr., *Torsional Stiffness of Thin-Walled Shells Having Reinforced Cores and Rectangular, Triangular, or Diamond Cross Sections*, NACA TN 3749, 1956.

[12] McLachlan, N. W., *Bessel Functions for Engineers*, Oxford, London, England, 1955.

✦ ✦ ✦

Orthotropic Sandwich Plates (*Continued from page 735*)

action with the surrounding medium (air, fluid); this effect will be discussed in a future publication. Also, another limitation of the present analysis should be indicated: since the strains and stresses in the z-direction have been neglected, the results do not seem to be applicable for frequencies and modes for which the distance between nodal lines is smaller than about twice the thickness of the plate.

References

[1] Mindlin, R. D., *Influence of Rotatory Inertia and Shear on Flexural Vibrations of Isotropic, Elastic Plates*, J. Appl. Mech., Vol. 18; also Trans. ASME, Vol. 73, pp. 31–38, 1951.

[2] Mindlin, R. D., *Flexural Vibrations of Elastic Sandwich Plates*, (ONR Report), Columbia University, Dept. of Civil Engineering and Engineering Mechanics, 1959.

[3] Freudenthal, A. M., and Geiringer, H., *The Mathematical Theories of the Inelastic Continuum, Encyclopedia of Physics*, Vol. VI, Springer Verlag, 1958.

✦ ✦ ✦

An Authorized Binding for
Journal of the Aerospace Sciences

Arrangements have been made by the Institute of the Aerospace Sciences for members and subscribers to have their Journals bound carefully and economically. Simply write for details to:

Publishers' Authorized Bindery Service Ltd., 430 West Erie St., Chicago 10, Ill.

REQUIREMENTS *for* CONTRIBUTIONS
to the publications of the
INSTITUTE *of the* AEROSPACE SCIENCES

The Institute of the Aerospace Sciences invites both members and nonmembers from any country to submit papers for publication in the JOURNAL OF THE AEROSPACE SCIENCES and AEROSPACE ENGINEERING. The Institute, following the practice of other societies, does not pay for contributions.

The following directions for the preparation of papers, if followed by authors, will save correspondence, avoid the return of papers for changes, minimize the work of preparation for the printer, and save the expense due to the charges made for "author's corrections."

MANUSCRIPTS: The original typewritten copy of the paper is desired. **To expedite review, an additional copy of both the manuscript and figures should be submitted.** The manuscript must be double or triple spaced on one side of white paper sheets, consecutively numbered. There should be wide margins to allow for the marking of directions to the printer. Correcting, changing, or adding to papers after they are in type is costly. It is, therefore, imperative that papers submitted be in final form. Typographical errors may be corrected on proofs, but if authors wish to add material, they may do so at their own expense. In mailing, drawings may be rolled, but manuscripts should be sent flat. Send by first-class mail (register if you wish for your own protection) to the Editorial Office, Institute of the Aerospace Sciences, 2 East 64th Street, New York 21, N.Y. All manuscripts will be examined by the Editorial Committee and by the Editor. Authors will be advised as promptly as possible whether the paper is acceptable for publication.

TITLES: The title of the paper should be brief. The name and initials of the author should be written as he prefers. The use of the full name of an author is advocated because of the frequent duplication of initials and surnames which sometimes makes it difficult to establish the identity of the author. This is particularly important for large annual indexing and abstracting services. All titles and degrees or honors are omitted. The name of the organization with which the author is associated should be placed after his name on a separate line. The date on which the paper is received will be inserted by the Editor. The author's title or position should be indicated in a footnote.

SUMMARIES OR ABSTRACTS: An abstract to be printed at the beginning should accompany each article. It should be adequate as an *index* and as a *summary*. It should contain a statement of major conclusions reached, since summaries in many cases constitute the only source of information used in compiling scientific reference indexes. Abstracts printed in other journals, especially foreign, in most cases consist of summaries from printed papers. The summary should explain as adequately as possible the major conclusions to a nonspecialist in the subject and should contain from 100 to 300 words, depending on the length of the paper.

SUBHEADINGS: Subheadings should be inserted by the author at frequent intervals. The work of editorial preparation will be simplified by the author's provision of many subheadings.

MATTER USUALLY DELETED: Photographs or illustrations of little technical interest and not showing advances in general practice. Too detailed tabular matter (general results of such tables may be included in the text). Lengthy descriptions of materials or processes or of preliminary experiments or theories that preceded final results; salient features only are of interest.

REFERENCES: References should be numbered consecutively and grouped together at the end of the manuscript, with only the corresponding number being mentioned in the text. The arrangement should be as follows. For books: [1]Durand, W. F., *Aerodynamic Theory*, 1st Ed., Vol. 1, p. 23; Julius Springer, Berlin, 1934. For magazines: [1]England, C. R., Crawford, A. B., and Mumford, W. W., *Some Results of a Study of Ultra-Short-Wave Transmission Phenomenon*, Proc. IRE, Vol. 20, No. 12, pp. 481–482, March, 1933. Please give author, title, edition, volume number, page, publisher, and place and date of publication as indicated. Omission of one required fact causes much extra editorial work and possible inaccuracies.

ILLUSTRATIONS: Illustrations should accompany manuscripts, and each should always be referred to in the text by number. Drawings or graphs should not be larger than 12 × 16 inches, and must be made with jet black India ink on white paper or tracing cloth, the latter being preferred. *Do not use typewriter for lettering.* The smallest lettering on 8 × 10 inch figures should be no less than $^1/_4$ inch high. Cross-section paper (white with black lines) may be used, but it should not have more than 4 lines per inch. If finer ruled paper is used, the major division lines should be drawn in with black ink, omitting the finer divisions. In the case of finely ruled paper, only blue-lined paper can be accepted. *Tracing paper and blueprints* are not acceptable. Lettering and all markings must be large enough to be readable after reduction to single-column width ($3^5/_{16}$ in.). Mail rolled or flat; never fold. Drawings that cannot be reproduced (including pencil drawings) will be returned to the author for redrawing, thus delaying publication of the paper. Photographs should be distinct and show clear black and white contrasts. They must be on glossy white paper. Avoid round or oval photographs.

CAPTIONS AND LEGENDS: Legends or captions must accompany each drawing or photograph submitted. If written on the drawing or photograph they should be placed below and well outside the part to be reproduced. Each table should have a caption such as Table 1, Table 2, Table 3, etc. Captions should be complete in themselves so as to make the data intelligible to the reader without reference to the text. A duplicate list of captions for figures should be included as the last page of the manuscript. Use "Fig. 1" (not Figure 1), "Figs. 3 and 4," etc., in both the text and the numbering of illustrations. In the text, "Eq. (1)" or "Eqs. (1) and (2)" is used, not "Equation (1)." In captions, legends, and in table headings, write all words in full; do not abbreviate, except for "Fig." and "Eq."

MATHEMATICAL WORK: Formulas may be typewritten or carefully written in pen and ink, the writing to be large enough so that it can be marked for the printer. Considerable space for marking should be allowed above and below all equations. All complicated equations should be repeated on separate sheets with adequate space left for marking. The solidus should be used for simple fractions appearing within the text. Make all expressions clear to the typesetter. Greek letters used in formulas should be clearly designated by name in the margin of the manuscript. The difference between capital and lower-case letters should be clearly distinguished and care taken to avoid confusion between zero (0) and the letter (o), between the numerical (one) and the letter (ell) and the prime (′), between alpha and a, kappa and k, u and mu, v and nu, n and eta. All subscripts and exponents should be clearly distinguished. Avoid complicated exponents and subscripts. Dots and bars over letters or mathematical expressions should also be avoided. When it is necessary to repeat a complicated expression, it should be represented by some convenient symbol.

SYMBOLS AND ABBREVIATIONS: The symbols recommended in the American Standard Association "Letter Symbols for Aeronautical Sciences," ASA Y10.7—1954, should be used wherever practicable. All symbols should be clearly written and carefully checked. Standard abbreviations should be used, and it should be noted that most abbreviations are lower case.

Corporate Members

of the

Institute of the Aerospace Sciences

AC SPARK PLUG DIVISION, GENERAL MOTORS CORPORATION

ACADEMY OF AERONAUTICS

AEROJET-GENERAL CORPORATION

AERONCA MANUFACTURING CORPORATION

AERONUTRONIC, DIVISION OF FORD MOTOR COMPANY

AEROSPACE CORPORATION

AGAWAM AIRCRAFT PRODUCTS, INC.

AIRBORNE INSTRUMENTS LABORATORY, DIVISION OF CUTLER-HAMMER, INC.

ALLIED RESEARCH ASSOCIATES, INC.

ALLISON DIVISION, GENERAL MOTORS CORPORATION

AMERICAN AIRLINES, INC.

AMERICAN BOSCH ARMA CORPORATION

AMERICAN OIL COMPANY

AMOCO CHEMICALS CORPORATION

ARDE ASSOCIATES

ARO, INC.

ASTRO-ELECTRONIC PRODUCTS DIVISION, RADIO CORPORATION OF AMERICA

AVCO-EVERETT RESEARCH LABORATORY

AVCO CORPORATION, RESEARCH AND ADVANCED DEVELOPMENT DIVISION

AVIEN, INC.

BEECH AIRCRAFT CORPORATION

BELL AEROSPACE CORPORATION

THE BENDIX CORPORATION

THE BOEING COMPANY

BOOZ, ALLEN APPLIED RESEARCH, INC.

BULOVA RESEARCH & DEVELOPMENT LABORATORIES, DIVISION OF BULOVA WATCH COMPANY, INC.

CANADAIR, LTD.

CHANCE VOUGHT CORPORATION

THE CHASE MANHATTAN BANK

CHICAGO AERIAL INDUSTRIES, INC.

CONTINENTAL MOTORS CORPORATION

CORNELL AERONAUTICAL LABORATORY INC.

COX & COMPANY, INC.

CURTISS-WRIGHT CORPORATION

DANIEL, MANN, JOHNSON, & MENDENHALL

THE DECKER CORPORATION

DEFENSE ELECTRONIC PRODUCTS DIVISION, RADIO CORPORATION OF AMERICA

DEFENSE SYSTEMS DIVISION, GENERAL MOTORS CORPORATION

DEL MAR ENGINEERING LABORATORIES

DELCO-RADIO DIVISION, GENERAL MOTORS CORPORATION

DELCO-REMY DIVISION, GENERAL MOTORS CORPORATION

DOAK AIRCRAFT COMPANY, INC.

DOUGLAS AIRCRAFT COMPANY, INC.

DZUS FASTENER COMPANY, INC.

EASTERN AIR LINES, INC.

EATON MANUFACTURING COMPANY

EDO CORPORATION

ELASTIC STOP NUT CORPORATION OF AMERICA

ENGINEERING SUPERVISION COMPANY

FAIRCHILD CAMERA AND INSTRUMENT CORPORATION

FAIRCHILD STRATOS CORPORATION

THE GARRETT CORPORATION

GENERAL APPLIED SCIENCE LABORATORIES, INC.

GENERAL DYNAMICS CORPORATION

GENERAL ELECTRIC COMPANY

GENERAL PRECISION, INC.

THE B. F. GOODRICH COMPANY

GOODYEAR AIRCRAFT CORPORATION

GRUMMAN AIRCRAFT ENGINEERING CORPORATION

HOFFMANN AIRCRAFT COMPANY

HUGHES AIRCRAFT COMPANY

INSURANCE COMPANY OF NORTH AMERICA COMPANIES

IBM SPACE GUIDANCE CENTER

THE INTERNATIONAL NICKEL COMPANY, INC.

ITT FEDERAL LABORATORIES, A DIVISION OF INTERNATIONAL TELEPHONE AND TELEGRAPH CORPORATION

ANITROL AIRCRAFT DIVISION, MIDLAND-ROSS CORPORATION

JOHNS-MANVILLE SALES CORPORATION

KOLLSMAN INSTRUMENT-CORPORATION

LAVELLE AIRCRAFT CORPORATION

LEAR, INCORPORATED

C. W. LEMMERMAN, INC.

THE LIQUIDOMETER CORPORATION

ARTHUR D. LITTLE, INC.

LOCKHEED AIRCRAFT CORPORATION

THE MARQUARDT CORPORATION

THE MARTIN COMPANY

McDONNELL AIRCRAFT CORPORATION

MELETRON CORPORATION

MINNEAPOLIS-HONEYWELL REGULATOR COMPANY

MOBIL OIL COMPANY

NATIONAL CREDIT OFFICE, INC.

NORTH AMERICAN AVIATION, INC.

NORTHROP CORPORATION

PAN AMERICAN WORLD AIRWAYS, INC.

THE RALPH M. PARSONS COMPANY

PIASECKI AIRCRAFT CORPORATION

POLY INDUSTRIES, INC.

REPUBLIC AVIATION CORPORATION

ROHR AIRCRAFT CORPORATION

RYAN AERONAUTICAL COMPANY

SHELL OIL COMPANY

SIMMONDS PRECISION PRODUCTS, INC.

SOLAR AIRCRAFT COMPANY

SOUTHWEST PRODUCTS COMPANY

SPACE TECHNOLOGY LABORATORIES, INC.

R. DIXON SPEAS ASSOCIATES

SPERRY GYROSCOPE COMPANY, DIVISION OF SPERRY RAND CORPORATION

STANDARD-THOMSON CORPORATION

STANLEY AVIATION CORPORATION

THERM, INCORPORATED

THIOKOL CHEMICAL CORPORATION

THOMPSON RAMO WOOLDRIDGE INC.

TRANS WORLD AIRLINES, INC.

UNION CARBIDE METALS COMPANY, DIVISION OF UNION CARBIDE CORPORATION

UNITED AIR LINES, INC.

UNITED AIRCRAFT CORPORATION

UNITED STATES AVIATION UNDERWRITERS, INC.

VEHICLE RESEARCH CORPORATION

WESTERN GEAR CORPORATION

WESTINGHOUSE ELECTRIC CORPORATION